Channel Modeling and Performance Analysis of Ultra Wideband In-Body Communication

Vom Promotionsausschuss der
Technischen Universität Hamburg

zur Erlangung des akademischen Grades

Doktor-Ingenieur (Dr.-Ing.)

genehmigte Dissertation

von

Jan-Christoph Brumm

aus

Hamburg

2024

Vorsitzende des Prüfungsausschusses:
Prof. Dr. habil. Sibylle Fröschle

1. Gutachter:
Prof. Dr.-Ing. Gerhard Bauch

2. Gutachter:
Prof. Dr.-Ing. Peter A. Höher

Tag der mündlichen Prüfung:
09.01.2024

doi: 10.15480/882.9047
ORCiD: 0000-0002-3623-4584

Für Nils und Levi

It's a dangerous business going out your door. You step onto the road, and if you don't keep your feet, there's no knowing where you might be swept off to.
J. R. R. Tolkien

Acknowledgements

The research work described in this thesis has been carried out during my time as research assistant at the Institute of Communications at Hamburg University of Technology. I would like to thank Prof. Gerhard Bauch for giving me the opportunity to work at the Institute of Communications and for his trust in my work, as well as his continuous support and guidance during the last years. Moreover, I would like to thank Prof. Peter Höher for his review of this thesis and Prof. Sibylle Fröschle for the pleasant handling of the examination process.

I would also like to thank all my colleagues at the Institute of Communications for creating such an enjoyable and great work atmosphere. All their input and help during the various discussions we had, helped a great deal to shape this thesis. Additionally, I would like to thank the students who did their Bachelor's or Master's thesis with me and contributed valuable information to this work.

Nicht zuletzt möchte ich mich bei meinen Eltern und Geschwistern dafür bedanken, dass sie mich immer unterstützt und an mich geglaubt haben. Nils und Levi danke ich ganz besonders für ihre neugierigen und interessierten Fragen und dafür, dass sie mich immer wieder zur richtigen Zeit abgelenkt haben. Maren danke ich von ganzem Herzen für einfach alles.

Hamburg, Januar 2024

Abstract

The usage of wireless capsule endoscopes to gain insights into the small intestine is a proven method for the diagnosis of certain gastrointestinal diseases. A capsule endoscope is a pill-sized device equipped with a camera and a radio transmitter that is used to transmit pictures from the inside of the digestive tract to an on-body receiver. Current devices are capable of transmitting images with a rather limited video quality. State of the art in-body communication systems are usually based on narrowband communication in frequency bands where only limited spectral resources are available. Much higher bandwidths are allowed in the ultra wideband frequency range from 3.1 GHz to 10.6 GHz. The feasibility of increasing the data rate using ultra wideband communication has been shown in various experiments in literature.

The main contribution of this thesis is a simplified channel model for ultra wideband communication which can easily be adapted to different setups and extended to different human body models. Similar as for well-established wireless communication channel models, it is not the target to model every detail of the physical channel. Instead, a channel model is built which captures the essential characteristics but is simple enough to allow for the design and simulation of the in-body communication system. The general idea is to model the propagation path of an electromagnetic wave by a multi-layered dielectric resembling the tissue structure on the path between transmitter and receiver. Hence, it is called the *layer modeling* approach. It is shown by a numerical simulation of the wave propagation that the proposed layer modeling approach fulfills the above requirements. The resulting path loss, power delay profile and the frequency dependency of the transfer functions are very well recreated by the layer modeling approach. Based on the layer modeling approach a channel model for ultra wideband in-body communication in a capsule endoscopy application is derived. This channel model is then utilized to determine fundamental limits of the communication by computing the channel capacity and investigate the bit error rate performance of an exemplary transmission scheme for a capsule endoscopy scenario.

The channel capacity is computed for twelve digital human phantoms, which are all based on medical imaging data of real human patients. The differences in channel capacity between the digital human phantoms are significant. For five optimally placed receive antennas on the abdomen the channel capacity varies between 217.5 Mbit/s and 1.5 Gbit/s. It is shown that the exact placement of the receive antennas on the abdominal surface plays a crucial role for the channel capacity. As soon as the optimum placement is not met exactly, the channel capacity deteriorates drastically by around one order of magnitude. Hence, a suboptimal placement scheme is investigated which needs much more receive antennas to achieve the same performance as for the optimized antenna positions. Furthermore, it is investigated how the physiological properties, e.g. the body mass index, of the digital human phantoms influence the channel capacity. Moreover, it is found that the values for the dielectric properties of human tissue have a drastic influence on the resulting channel capacity and may lead to a reduction by more than one order of magnitude.

Finally, an exemplary ultra wideband communication system using pulse position modulation is designed and its bit error probability is analyzed. It is shown that the effective discrete time equivalent baseband transfer function is frequency flat. Moreover, it is analyzed how the different receive antenna placements affect the transmitter coverage in the digestive tract. A coverage of 99.8 % of the digestive tract can be achieved with an uncoded bit error probability of less than 10^{-2} at a data rate of 3 Mbit/s for a specific antenna setup. The results also show that the influence of the combining scheme is negligible.

Contents

Chapter 1

Introduction

1.1 Motivation

Wireless communication with implanted or ingested devices is very common already in today's clinical routine. With these wireless connected devices inside the body, it is possible to observe the health status of a patient over a much longer period compared to a rather short hospital visit. Especially due to the aging society and the fact that more and more people suffer from chronic diseases, it will be necessary to monitor patients at home. In these situations where the patients do not need to be monitored in a hospital, a physician could be called automatically if the situation of the patient demands it. However, there are many challenges to be overcome for new generation in-body sensors to achieve higher data rates, e.g. for higher resolution video material, compared to currently used ones.

The use of inductive coupling for data transmission from implanted sensors has been well known for a long time [KN17]. Nevertheless, this technology works only in close proximity of the communicating devices. Moreover, the communication is prone to misalignment of the devices and the weight and size makes the usage difficult [KN14]. Only small data rates of 1 kbit/s to 30 kbit/s [KPN14] can be achieved, which limits the amount of information that can be collected by the sensor inside the human body.

The communication to and from implanted or ingested devices is commonly referred to as in-body communication. These devices usually consist of a power source, a sensor and a radio transceiver, which nowadays usually operates in the ultra high frequency (UHF) band because of the limitations of inductive coupling mentioned above. The most common application of in-body sensors is cardiac pacemakers,

which collect data of the heart's rhythm and may also help to control it [KN17]. Another application is an implanted sensor inside the brain that can measure the pressure of the brain liquids and automatically react on the situation [MHM11]. This makes the life of affected patients much easier as frequent surgeries are avoided. Other applications include deep brain sensors, cochlear implants, glucose monitors, drug delivery systems, and many more [KN17]. All these devices collect some physiological information and transmit them wirelessly to a node that is placed somewhere on the body surface.

Apart from these more common applications, in recent years the wireless capsule endoscope has generated an increased interest. A wireless capsule endoscope consists of a camera, LEDs for lightning, an RF transceiver and a battery. After being swallowed the camera inside the pill starts to take pictures and transmits them wirelessly to an on-body receiver [IMG+00]. This procedure allows to gain an insight into the small intestine, which is only partially explorable by classical endoscopy due to its length of 6 m to 8 m and its meandering nature [KCB10][CBB12]. Several capsule endoscopes are already approved and on the market. They are usually able to transmit 2 to 6 images per second where each image has a resolution ranging from 320×320 pixel to 512×512 pixel [KPN14][vdBdLH15]. The battery of these devices lasts around 8 h to 10 h, which is in most of the cases sufficient to pass through the small intestine. Most of them operate in the band from 430 MHz to 440 MHz, which is among others reserved for capsule endoscopy [Bun19b]. From the most current data that could be obtained, it can be concluded that these modern capsule endoscopes transmit at rates of several hundred kbit/s [Mic14].

However, from a medical point of view it is desired to increase the image quality and the image rate of the resulting video stream. This would allow the physicians to make more confident and accurate diagnoses as the pictures are of higher quality. Furthermore, the chance that there is image material missing of some parts of the small intestine is reduced drastically. For these improvements of the video quality it is necessary to transmit several Mbit/s [SW10][CKB+09]. To transmit data with this high rate, other possible frequency bands have to be considered. The usage of unlicensed ISM Band could be considered. However, most of the ISM bands are not internationally available and do not allow for a sufficient bandwidth. The only one that is internationally available around 2.4 GHz is crowded by WLAN and Bluetooth traffic [YD12]. Another alternative is ultra wideband (UWB) communication, which is already standardized in IEEE 802.15.6 for communication between sensor nodes on the body surface. It is expected that ultra wideband communication will be included in a future version of the standard also for in-body communication [CSK+13].

Ultra wideband communication is most commonly defined as communication with signals that occupy a bandwidth of more than 500 MHz [Mol06]. It is allowed in most countries worldwide with an equivalent isotropic radiated power spectral density of −41.3 dBm/MHz in a frequency range from 3.1 GHz to 10.6 GHz [Eur16a]. Due to the lower attenuation for the lower frequencies inside the human body, especially the low band from 3.1 GHz to 4.8 GHz is of interest for in-body communication [CBB+13][SAW12a][CKB+09].

Especially, the usage of impulse radio ultra wideband is advantageous for in-body communication as small and energy efficient transmitters can be built. Obviously, the attenuation in the ultra wideband (UWB) frequency band is much higher than for UHF frequencies. There have already been several experimental and numerical investigations that show the feasibility of UWB communication for capsule endoscopy scenarios, e.g. in [WWP10] and [CBB+13]. Nevertheless, apart from these feasibility studies only few publications on the performance of transmission schemes or the estimation of the channel capacity are available. Most of these performance simulations are either based on simplified path loss models or on completely unpublished models directly taken from numerical wave simulations.

1.2 Outline

In the light of the outlined prerequisites, the major objective of this thesis is to determine an idea of fundamental limits for ultra wideband in-body communication in the abdominal region and investigate the performance of an exemplary transmission scheme. To achieve this goal, in a first step a channel model needs to be created, as no comprehensible channel models exist in literature for this scenario. Similar as for well-established wireless communication channel models, it is not the target to model every detail of the physical channel. Instead, a channel model is needed which captures the essential characteristics but is simple enough to allow for the design and simulation of the in-body communication system. Secondly, the fundamental limits on the data rate in this very specific environment will be determined by utilizing the concept of channel capacity. In current literature, the channel capacity is rarely used as a performance metric for ultra wideband in-body communication. And if it is used, it is only used for specific setups and not systematically investigated. Finally, an appropriate transmission scheme is designed and analyzed in terms of its bit error rate performance and its coverage of the gastrointestinal tract. For the development of transmission and reception strategies the overall constraints on the

available energy, the transmit power, specific absorption rate (SAR) constraints and the required data rate for real time high definition video material will be considered.

The main contributions of this work can be summarized as follows:

1. A channel model is developed that can easily be adapted to different frequency bands, human body models, and a varying placement of transmit and receive antennas. Furthermore, the resulting transfer functions are validated using numerical wave simulations in digital phantoms of real human body models.

2. Based on the above channel model, the channel capacity for different ultra wideband communication scenarios is determined. This will give insights into how to best place the receive antennas on the abdominal surface, how many antennas are needed for a certain performance, and what happens if there are deviations from the optimum placement. Moreover, the channel capacities of different human body models are compared to show the dependence on certain physiological properties. Finally, the uncertainty about the actual dielectric properties of human tissues is investigated.

3. Based on the previous results a pulse position modulation (PPM) scheme is designed to simulate the coverage that can be obtained for a specific application. This includes again various placements of the receive antennas but also different space diversity schemes.

The remaining thesis is organized as follows. Chapter 2 introduces fundamental concepts of the propagation of electromagnetic waves in human tissue and introduces the human phantoms that are used as reference throughout the thesis. In Chapter 3 some information on the background of in-body communication systems is given. Moreover, the literature on ultra wideband channel models for in-body communication is reviewed. The channel model that is developed in the course of this thesis is presented in Chapter 4. Based on a simplified modeling technique, the channel model is derived and validated using numerical wave simulations. Furthermore, the channel characteristics are presented and compared to the channel models from literature presented in Chapter 3. Chapter 4 ends with the presentation of an easy to reproduce version of the initially developed channel model, which is used as basis for the remaining chapters. In Chapter 5 results of the channel capacity are presented. First the optimum transmission bandwidth is determined. Moreover, the effect of the placement of the receive antennas, the difference between the human phantoms, and the improvement to communication in the UHF frequency band are shown. Finally, in Chapter 6 a discrete time equivalent baseband channel model is derived for a specifically designed pulse position modulation (PPM) scheme. For this scheme

the bit error rate performance is simulated and it is shown how the placement of the receive antennas, the human phantoms, and the diversity scheme influence the resulting performance. The thesis concludes in Chapter 7 with a summary of the most important findings.

Chapter 2

Fundamentals of Wireless In-Body Communication

One major concern for medical applications is the safety of the patient. Especially, sick patients should not be exposed to an unnecessary amount of electromagnetic radiation. However, it is very difficult to investigate the behavior of electromagnetic radiation in actual human bodies. This chapter is organized as follows. First, the electromagnetic characteristics of human tissue will be investigated in Section 2.1. In the following Section 2.2 it will be shown how the effects of radio propagation can be modeled. These different methodologies can in turn be used to investigate the interaction between the electromagnetic radiation and the human tissue. In Section 2.3 it is described, which biological effects may occur and how the regulations limit the maximum allowable transmit power for an in-body sensor. Finally, in Section 2.4 the digital human phantoms used as reference throughout this thesis are introduced.

2.1 Electromagnetic Characteristics of Human Tissue

The human body is a large collection of various different tissue types. Each tissue has a different molecular structure. Hence, also the dielectric properties of each tissue are different. The most well-known characterization of the electromagnetic properties of human (and animal) tissue was done by Gabriel *et al.* in 1996 [Gab96].

The relative permittivity ε_r of human tissue varies over frequency in three dispersion regions [GGC96]. These regions differ in the underlying biological process that

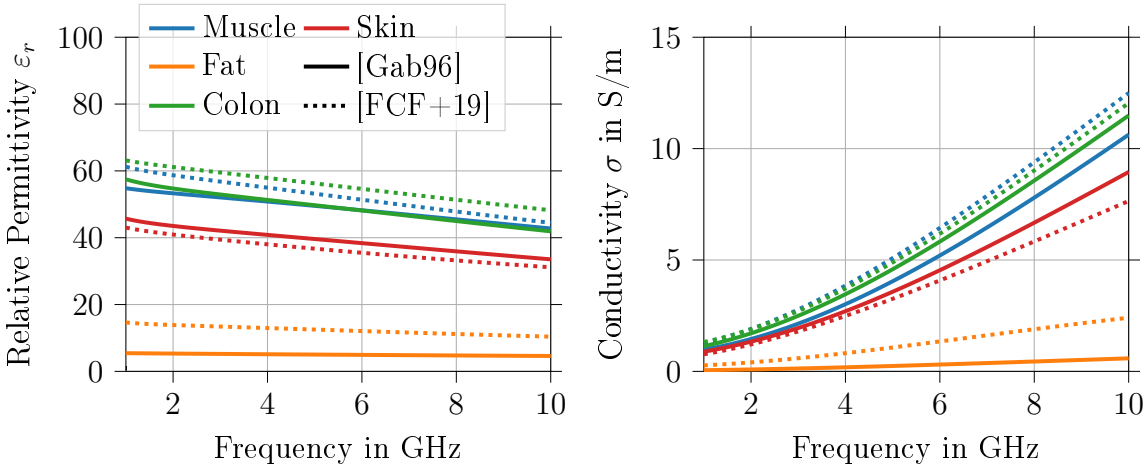

(a) Relative permittivity ε_r (b) Conductivity σ

Figure 2.1: The relative permittivity ε_r and the conductivity σ for different human tissues.

dominates the cause of a drop in relative permittivity. For low frequencies ionic diffusion processes are the dominant mechanisms. At frequencies of around 100 kHz polarization of the cell membranes takes over. Finally, in the gigahertz frequency range the polarization of the water molecules is the dominant effect.

A lossy dielectric material can in general be characterized by its complex relative permittivity

$$\varepsilon_r(f) = \varepsilon_r'(f) - j\varepsilon_r''(f) = \varepsilon_r'(f) - j\frac{\sigma(f)}{2\pi f \varepsilon_0}, \tag{2.1}$$

where ε_r' is the dielectric constant, ε_r'' is the loss factor, σ is the conductivity of the tissue, and ε_0 is the permittivity of vacuum.

Investigations by Gabriel *et al.* showed that the frequency dependent behavior of the relative permittivity can be modeled by the following Cole-Cole expression [GLG96b]:

$$\varepsilon_r(f) = \varepsilon_\infty + \sum_{n=1}^{4} \frac{\Delta\varepsilon_n}{1 + (j2\pi f \tau_n)^{1-\alpha_n}} + \frac{\sigma}{j2\pi f \varepsilon_0}, \tag{2.2}$$

where f is the frequency, ε_∞ is the permittivity for $f \to \infty$, σ is the static ionic conductivity , ε_0 is the permittivity of free-space, and $\Delta\varepsilon_n$, τ_n, α_n are tissue specific parameters for each dispersion region n. Details on the parameters can be found in [Gab96] and [GLG96b]. Please note that, although only three dispersion regions exist, a Cole-Cole model with four regions is used for the modeling to achieve a better fit [GLG96b]. The relative permeability of human tissue is assumed to be

$\mu_r = 1$. The resulting relative permittivity and conductivity for 4 exemplary tissues from [Gab96] are depicted in Figure 2.1 using solid lines. Tissues with higher water content, e.g. muscle, will have higher losses than tissues with low water content, e.g. fat, as their relative permittivity is larger.

As the relative permittivity is additionally dependent on the temperature it is important to note that all measurements in [Gab96] were done at 37 °C. In [Gab96] the parameters of (2.2) were determined for 44 different tissue types for frequencies from 1 MHz to 20 GHz. However, as there are much more than 44 tissues in the human body, some of the tissues can be mapped to similar behaving tissues. In this work mainly the mapping from [AFP97] is used to cover the dielectric properties of up to 61 tissues [And16]. Based on [ITI18] the dielectric properties of the content of the gastrointestinal tract were set to the properties of muscle. The mapping of all tissues used in this work is shown in Table A.1 in Appendix A.

Certain tissues, e.g. muscle, are anisotropic, i.e. their dielectric properties depend on the direction the electromagnetic radiation is passing through the tissue [JDM75]. However, this effect is not covered by Gabriel *et al.* in their final results [GLG96a]. Moreover, the available digital phantoms do not include information on the direction of the tissues. Hence, in this thesis all tissues are assumed to be isotropic.

In addition to the temperature dependency and possible anisotropy, human tissue itself varies between different humans, due to different physiological properties and possible diseases. Furthermore, they are also depending on the age of the subject because the water content in the tissues changes with age [WFW06]. In [SO19] and [SAL+18] the dielectric properties of human blood samples were investigated in great detail. A strong correlation between the hemoglobin concentration of the blood and the permittivity was found. A parameterized model for the relative permittivity depending on the hemoglobin concentration was derived. It can be derived from their results that the real part of the relative permittivity can vary by up to 15 % compared to the values from [Gab96]. For the conductivity the relative differences can even be up to a factor of 2 depending on the hemoglobin concentration. From this example it is clear that the complex relative permittivity of human tissues not only varies between the tissue types but also between humans. However, as the blood vessels take up only a negligible volume compared to other tissues (see Figure 2.2 for details) this specific dependency will not be covered in this thesis.

Recently, there has been an extensive measurement campaign reported by Fornes-Leal *et al.* in [FCF+19] on the dielectric characterization of abdominal tissue in

the ultra wideband frequency range. The measurement campaign used three anesthetized, female pigs of similar size and weight. They address several issues of previously reported results. First of all, the measurements were taken in-vivo in contrast to the measurements reported by Gabriel *et al.* and others that were mostly performed ex-vivo, i.e. using tissue removed from dead animals or humans. Doing ex-vivo measurements has the drawback that, due to dehydration of the tissue over time, the measured dielectric values decrease [MSP+19]. Moreover, all previously published models of dielectric tissue properties are based on a mixture of species or only on a small set of tissues. Hence, the results from [FCF+19] have the advantage that they were determined in natural conditions from three comparable specimen. Furthermore, it was noted by Fornes-Leal *et al.* that due to the inhomogeneity of some of the tissues the uncertainty of the measured values is quite high. In total, dielectric properties for 21 tissues in the frequency range from 0.5 GHz to 26 GHz are reported. These tissues are listed in Table A.1 in Appendix A. The authors also use a Cole-Cole expression as in (2.2) to model the complex permittivity. Their results are depicted in Figure 2.1 using dotted lines. How these dependencies affect the attenuation and propagation velocity is investigated in Section 4.3.1.

Apart from the research by Fornes-Leal *et al.*, there are some studies that show substantial deviations in the observed dielectric properties for some tissue types compared to the results from Gabriel *et al.* [KN14, p. 138]. However, as the results from [Gab96] are the most widely used, their results will be used for all following calculations unless noted otherwise.

2.2 Wave Propagation Inside the Human Body

As has been shown in the last section, each of the more than 50 different tissues has a different composition and for that reason different electrical properties. Thus, the human tissue can be described as a lossy dielectric with a frequency dependent complex permittivity. Due to this heterogeneous propagation medium, it is difficult to predict the propagation behavior of electromagnetic waves inside the human body. To investigate this behavior for in-body communication several different approaches are used in literature as it is not feasible to conduct experiments directly with human subjects. These approaches can roughly be distinguished in experimental and numerical approaches.

2.2.1 Experimental Approaches

Experiments are most often done by using a so-called phantom, which is a material that mimics the dielectric properties of the human tissue. The phantom can be made from a liquid, gel or a solid. Liquid phantoms are used for example in [TAH+09], [CGF+15], [WLS+15], [NAW18], and [ATT+08] for experiments on the effects of tissue on the path loss and on the design of antennas in various frequency ranges. The recipes for liquid phantoms are usually only valid for a narrow frequency range. Hence, they are unsuitable to imitate ultra wideband transmission. However, in [ACG+16] and [CGF+16] improved recipes for liquid phantoms are proposed, which are valid for the complete frequency range from 3 GHz to 18 GHz. These liquids are used e.g. in [PAG+19] for a two layer phantom of equivalent muscle and fat tissue. In [APG+18] even a three layer phantom was build with muscle, blood and fat tissue. Yet, most of the time only a single liquid is used as phantom.

Gel phantoms, as described e.g. in [KHT08] and [Dan11], have the advantage over liquids that they can be used to model a certain shape and it is easy to build multi-layered tissue structures [SRF+10]. Both liquid and gel phantoms are based to a large extend on deionized water. They are best at mimicking tissues with a high water content, e.g. muscle. Furthermore, they have the disadvantage that they are not stable over a long time, as the water evaporates and the mixture deteriorates [KN14, p. 155].

Solid phantoms are usually only used for investigating the propagation on and around the body as it is difficult to analyze the fields inside the solids [KN14]. Moreover, it is much more difficult to fabricate solid phantoms than liquids or gels.

Another possibility for phantom experiments is to use organs from animals to model the human body more realistically as described in [AHY+06]. In [TRY15] tissue samples from a pig are arranged in layers to model the propagation path.

Experiments with animals are only reported rarely, due to their complexity. However, in some recent publications a group from Oslo and a group from Valèncía published results from measurements with anesthetized pigs. Usually, pigs are used because their abdominal structure resembles the human abdomen very well [GMB15]. Animal studies were reported in [CBB+13], [AKC+14], [FCB+15], [GCC+15], [SAC+17], [FCP+18], and [WNN+18].

Usually the experiments incorporating liquid phantoms are using plastic containers to hold the liquid, anatomically correct shapes are used only rarely. This is an inherent advantage of animal experiments, as the gastrointestinal structure is recreated

very good. Additionally, the pigs are usually anesthetized. Hence, there is blood flowing and respiratory movement. However, the environment and positioning can be controlled much better using either a liquid or gel phantom. Furthermore, it has to be kept in mind that it was shown in some studies that homogeneous models overestimate the absorbed energy in the tissue [KN14][GFC+16].

2.2.2 Numerical Approaches

Numerical approaches to simulate the electromagnetic wave propagation inside the human body are based either on simple geometric shapes or on anatomical correct models that are derived from photographs, magnetic resonance imaging (MRI) or computer tomography (CT) scans [KN14].

More than 20 different so-called virtual human or voxel models are available today according to [MNY+17]. Many digital phantoms are based on data provided by the Visible Human project of the U.S. National Library of Medicine [Ack98]. Although, some of these models are anatomically very accurate, e.g. with a resolution of $1\,\mathrm{mm}^3$, they have one disadvantage over experiments in living animals: the models are static. There is no respiration or blood circulation included in these models. Due to the complex heterogeneous structure of the model, usually time domain approximations to Maxwell's equations either in integral or in differential form are used to simulate the electromagnetic wave propagation, i.e. the finite integration technique (FIT) or finite difference time domain (FDTD) method, respectively [SHI17].

Numerical simulations with anatomical correct digital phantoms combine the repeatability of phantom experiments with the anatomical exactness of animal experiments. However, they are limited by the computational complexity required and the fact that there might be effects in real bodies that is not captured in the numerical model.

2.3 Health Effects from Electromagnetic Radiation

2.3.1 Effects on Human Tissue

Several effects from electromagnetic radiation on human tissue can be observed. They can be categorized in thermal and non-thermal effects. If not noted otherwise

the source of the following discussion is [Fos00]. The dominant effects that are revealed in most studies are the thermal effects caused by conduction currents and polarization effects of the water molecules. The heating of tissue is also the easiest effect to observe. A recent study on rats of the National Toxicology Program in the USA showed that it is not only the heating one has to be concerned with when talking about health effects of electromagnetic radiation [Nat20]. In their 2-year-study published in [Nat18] 180 rats were exposed to GSM and CDMA modulated signals in repeated intervals. They found that the exposure with these signals indicates a coincidence with the development of heart tumors in male rats. However, there is an ongoing debate whether these results are significant enough and transferable to humans [Mel20][Int20]. Nevertheless, this study confirms the World Health Organisation (WHO) in categorizing radio frequency radiation as "possibly carcinogenic to humans" [Int13a]. Additionally, it is possible that also small and localized temperature changes already lead to certain stress reactions on the protein level [Nat18]. However, all these results are obtained from long-term exposure. Thus, it remains unclear which effects on the health of patients may occur from short-term exposure, i.e. from one-time treatments as e.g. from a capsule endoscopy. For that reason only the thermal effects will be considered in the following.

In general, the higher the field strength of the applied field the higher is the heating effect. However, there is also the so-called microwave hearing effect, which is caused by the sudden thermal expansion of water induced by transient electromagnetic pulses. These sudden expansion of the water molecules is auditory through the bones as clicking sounds and, hence, should be avoided. There are also other mechanisms, which act on the cell structures and the dipoles in the tissue. However, they are found to be very unlikely in [Fos00], as high external fields are needed to produce any observable effect.

To avoid adverse health effects, limits on the field strength of electromagnetic waves, that humans may be exposed to, were derived by the International Commission on Non-Ionizing Radiation Protection (ICNIRP) [Int98] and the IEEE [Ins05]. Both derive the limits of electromagnetic field strength such that a temperature increase of the whole body by more than 1 °C is strictly avoided. It has been shown in several studies mentioned in [Int98] and [Ins05] that an increase above this value can cause severe damage to the tissue. To derive limits on the electromagnetic field strength, the specific absorption rate (SAR) is defined as the rate at which the energy is absorbed from the tissue. Or in other words the absorbed power per unit mass. Its

relation to the electric field E is given by

$$\mathrm{SAR} = \frac{\sigma}{\rho} E^2 \,, \tag{2.3}$$

where σ is the conductivity of the tissue and ρ is the mass density [WW13]. The specific absorption rate can be related directly to the electric field strength in the tissue and the temperature increase [Ins05]. The whole body temperature will increase by more than 1 °C, if the complete body is exposed to electromagnetic radiation with a SAR of more than 4 W/kg for at least 30 min [Int98]. Thus, for general public exposure the whole body SAR limit was set to 0.08 W/kg including a certain safety margin. For communication applications inside the body the whole body SAR is not that meaningful, as the radiation only occurs localized around the transmit antenna. The thermoregulatory effects of blood flow and sweating control the overall body temperate very fast by distributing the heat from a localized heat source to the outside [Ins05]. For that reason the SAR limit for a localized exposure to electromagnetic waves was set to 2 W/kg averaged over 10 g of body tissue and 6 min of exposure [Ins05], [Int98].

In order to avoid the microwave hearing effect mentioned above, there are additional regulations for pulsed transmission. The limit on the absorbed energy, the specific absorption (SA), is set to 2 mJ/kg averaged over 10 g of tissue and 6 min of exposure. The specific absorption is the time integral of the specific absorption rate [Int98].

2.3.2 Maximum Transmit Power for an In-Body Sensor

To the best of our knowledge, the investigations in [TRY15] are the only to comprehensibly investigate the temperature increase of the tissue due to a transmit antenna placed in the digestive tract for ultra wideband transmission. For simulation of the specific absorption rate the authors transmitted an ultra wideband pulse in the frequency range of 3.5 GHz to 4.5 GHz. Their results show that the transmit power should not exceed 21.5 mW, as with this transmit power the SAR limit of 2 W/kg is reached. The absorbed energy per pulse, i.e. the specific absorption (SA), using their setup is only 4 nJ/kg. This is multiple orders of magnitude below the threshold of 2 mJ/kg set in the regulations to avoid the microwave hearing effect.

Furthermore, it was found in [TRY15] that the whole body temperature increased from 37 °C to 37.173 °C after 6 min of exposure and the maximum temperature increase by 0.438 °C is found close to the capsule located inside the colon. Hence,

it can be concluded from these investigations that a transmit power of 21.5 mW is safe for impulse radio ultra wideband communication inside the human body.

In general, it has to be noted that the absorption of electromagnetic energy depends on the antenna, the surrounding tissue and on the frequency band [XMR+09]. In the aforementioned study Xu *et al.* investigated the radiation characteristics of a capsule endoscope for frequencies from 430 MHz to 3 GHz and found that a transmit power of 25 mW does not lead to a specific absorption rate exceeding the regulatory limits. There are more investigations for narrowband communication in the range of 401 MHz to 406 MHz. However, for that frequency range only very diverse results could be found in literature. In [WW13, p. 213] it is stated (without any source) that a transmit power of 20 mW should be safe. Yazdandoost *et al.* even show in [YK07] SAR values that are well under the ICNIRP limits for a transmit power of 1 W. Furthermore, in [Cha14] it is found that the transmit power should stay below 60.4 mW. Hence, the resulting SAR seems to depend highly on the exact settings and methods.

Nevertheless, it can be concluded that the maximum transmit power should be in the range of some ten mW to be on the safe side. In addition to the heating of the tissue due to the radiation, the sensor node itself generates heat and has to be taken into consideration when evaluating the specific absorption rate [TRY14b]. However, no investigations on this matter could be found in literature so far.

2.4 Digital Human Body Phantoms

2.4.1 Overview

As discussed already in chapter 2.2, there are many ways of emulating the human body for measurements of the transmission and propagation characteristics of electromagnetic waves. Experiments can be conducted for example with anesthetized pigs, as their anatomy is similar to that of humans. Moreover, different kinds of either liquid or gel-like substances can be used for measurements. Another different approach is to use digital models of the human body and numerical simulation software to solve Maxwell's equations for this discrete structure. In this thesis all results will be obtained form digital human phantoms. Hence, in this section different phantoms are introduced and their physiological properties will be analyzed.

Table 2.1: All digital human phantoms investigated in this thesis and their properties.

Model Name	Source	Sex	Age	Height in cm	Weight in kg	Resolution in mm^3
Alvar	[Laa18]	♂	-	176	72	0.512×0.512×0.512
AustinMan 1	[MY20b]	♂	38	180	106.2	$1 \times 1 \times 1$
AustinMan 2	[MY20b]	♂	38	180	106.2	$2 \times 2 \times 2$
AustinWoman 1	[MY20b]	♀	59	173	84.8	$1 \times 1 \times 1$
AustinWoman 2	[MY20b]	♀	59	173	84.8	$2 \times 2 \times 2$
Donna	[Hel16]	♀	40	170	70	$1.875 \times 1.875 \times 10$
Golem	[Hel16]	♂	38	176	69	$2.08 \times 2.08 \times 8$
Hanako	[Nat17]	♀	22	160	53	$2 \times 2 \times 2$
Helga	[Hel16]	♀	26	170	81	$0.98 \times 0.98 \times 10$
Irene	[Hel16]	♀	32	163	51	$1.875 \times 1.875 \times 5$
Taro	[Nat17]	♂	22	173	65	$2 \times 2 \times 2$
VisibleHuman	[Hel16]	♂	38	180	103	$0.91 \times 0.94 \times 5$

A digital human phantom is usually represented by a 3D matrix indicating the position of different tissue types inside the body. Hence, the human body is discretized in small volume elements, so-called *voxels*. Inside these voxels, the properties of the tissue are assumed to be constant. There are numerous phantoms available today. However, not all of them are freely available to the public or for academic use. Table 2.1 shows all phantoms that will be covered in this thesis.

The digital phantoms Donna, Golem, Helga, Irene and VisibleHuman were created by the Helmholtz Zentrum München and are available online for academic use [Hel16]. Their construction is described in detail in [PZF+02] and [FZP+04]. All of them were segmented from computer tomography (CT) data. Donna, Golem, Helga and Irene were patients that for various reasons had to undergo whole-body examinations. VisibleHuman was constructed from the CT data available from the American National Library of Medicine in the Visible Human Project [Ack98][The20].

The data of the Visible Human Project is not only accessible as CT scans but also as high resolution images. These were taken from the cryosectioning of a donated male and female human body. Massey *et al.* of the University of Texas used these high resolution images of the Visible Human Male and Female dataset to create very detailed digital phantoms named AustinMan and AustinWoman, respectively [MY16]. These two models are open source and can be obtained in various resolutions and file formats from their website [MY20b]. The segmentation and labeling of the phantoms was done at the highest resolution of $1\,\text{mm} \times 1\,\text{mm} \times 1\,\text{mm}$. To obtain the lower

resolutions, neighboring voxels were combined into one voxel having the properties of "the most frequent material in a volume of voxels" [MY20a]. In this thesis the highest resolution and a coarser version with resolution of $2\,\text{mm} \times 2\,\text{mm} \times 2\,\text{mm}$ will be used to investigated the influence of the model resolution on the results.

Hence, the digital phantoms AustinMan and VisibleHuman are based on data from the same human body. However, due to the different data sources (CT scans and high resolution images) and different segmentation and labeling techniques the two phantoms are different. This can already be seen from the different height and weight in Table 2.1.

The Japanese National Institute of Information and Communications Technology (NICT) developed a male and a female digital phantom from CT scans of two volunteers, named Taro and Hanako [NWS+04]. The volunteers were chosen such that their height and weight were close to the average Japanese values. These two models can also be used for free for academic purposes and can be obtained from their website [Nat17].

Another open source digital phantom is Alvar. It has been developed at Aalto University [Laa18]. Alvar is based on the data provided from the BodyParts3D database for anatomy developed by the Database Center for Life Science at the University of Tokyo [MFT+09]. This database in turn is based on the Japanese digital phantom Taro described above. The authors of Alvar used the data from BodyParts3D and refined the structure at certain parts. Additionally, the proportions of the phantom were fitted to that of the reference man of the ICNIRP [Val02]. The reference man is a theoretical construct that is used in radiation dosimetry as reference for computing dose levels. It is basically a (Western European/North American) man with average size, weight and physiological properties. More details on the construction of Alvar can be found in [Laa18]. In other words, Alvar is a refined version of Taro with increased height and weight to fit it to Western European average values.

All of the aforementioned digital phantoms are discretized with different resolution of the underlying voxels (see Table 2.1). Moreover, the tissue types labeled in all of the phantoms differ slightly in the level of detail and the name itself. Hence, for each phantom a custom mapping to the 61 tissue types (see Section 2.1) used throughout this thesis had to be created. These mappings can be found in [Bru20].

2.4.2 Physiological Properties

As the given weight and height values are insufficient to properly draw conclusions on the physiological condition of the digital phantoms, in this section various physiological properties are computed from the phantoms. As the attenuation inside the body will increases with distance, especially measures of obesity are of interest. The body mass index (BMI), which is the ratio of body mass to squared height, is a very common measure of obesity. Recently, further measurements like the waist circumference (WC) and the waist-to-height ratio (WtHR) became more popular, because they offer a better estimate of body fat [Wor00][SFK+10].

A BMI of more than $25\,\mathrm{kg/m^2}$ indicates overweight. A BMI of more than $35\,\mathrm{kg/m^2}$ is considered as severe overweight [Wor00]. For the waist-to-height ratio a value above 0.5 is an indicator of overweight [Yoo16]. The waist circumference alone does not give a good indication of overweight. However, it might be interesting in our setup as waist circumference is correlated with transmission distance inside the abdomen.

As all the different tissues in the human body exhibit different propagation characteristics, it is also of interest how the various phantoms differ in their composition of different tissues. Figure 2.2 shows the relative volume of different tissues in the abdomen of each phantom. The eleven tissues with the highest total volume were selected for display. It can be seen that in nearly all phantoms the relative volume of fat is largest, except for Irene were muscle is the tissue with the largest volume in the abdomen. The tissue with the second-largest volume is muscle in all phantoms (except for Irene). All other tissues follow with a large gap. Moreover, it can be noted that there is different level of accuracy in the phantoms. For example, only AustinMan and AustinWoman have bone marrow labeled in their data. In the other phantoms it is not present at all. Overall, it can be noted that muscle and fat seem to be the dominant tissues in the abdomen. Hence, in addition to the aforementioned properties, we will compute the muscle mass to fat mass ratio $\frac{m_{\mathrm{muscle}}}{m_{\mathrm{fat}}}$ in the abdomen for each phantom.

All these properties are shown in Table 2.2[1]. The BMI ranges from $19.2\,\mathrm{kg/m^2}$ for Irene to $32.8\,\mathrm{kg/m^2}$ for AustinMan. Although, AustinMan and Visible Human are based on the same underlying human subject their weight was given with two different values. Hence, their BMI is also different.

[1]Please note that for some phantoms the physiological parameters were published already in [BB19]. However, due to a bug in the calculation of the waist circumference, some of the values differ substantially.

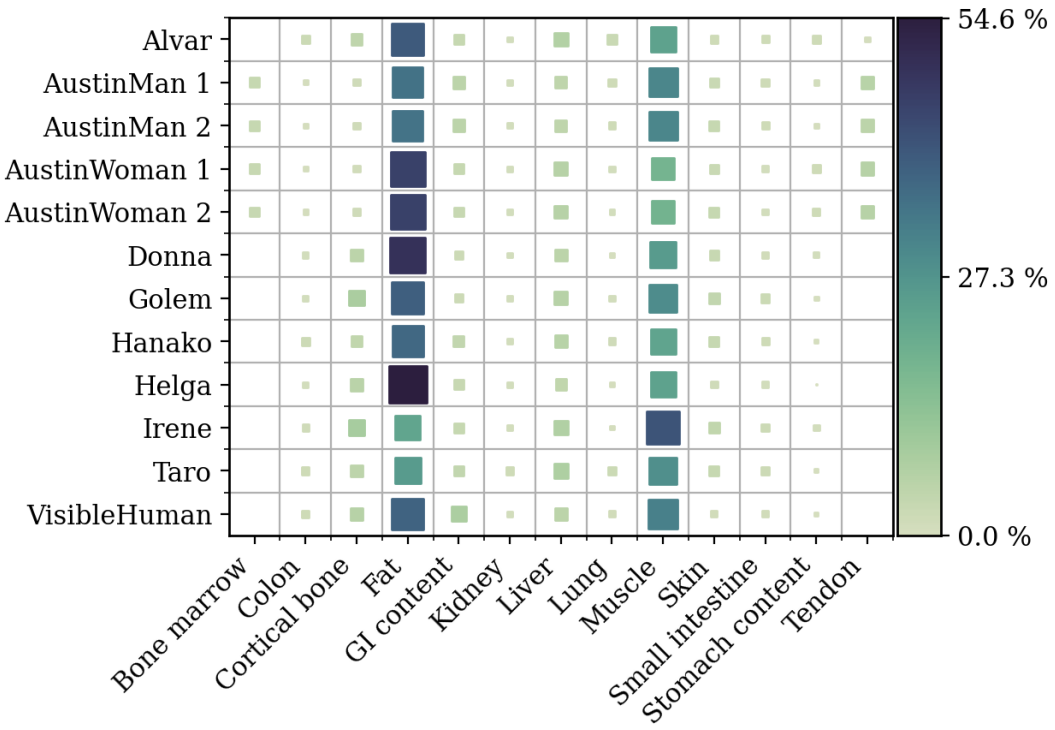

Figure 2.2: The relative volume of various tissues in the abdomen for all phantoms from Table 2.1. The eleven tissues with the highest total volume are shown. The size of the markers is proportional to the values.

Table 2.2: The physiological properties of the digital phantoms. Shown are the body mass index (BMI), the waist circumference (WC), the waist-to-height ratio (WtHR), and the muscle mass to fat mass ratio $\frac{m_{\text{muscle}}}{m_{\text{fat}}}$.

Model Name	BMI in kg/m^2	WC in mm	WtHR	$\frac{m_{\text{muscle}}}{m_{\text{fat}}}$
Alvar	23.2	967	0.55	0.70
AustinMan 1	32.8	1387	0.77	1.38
AustinMan 2	32.8	1444	0.80	1.43
AustinWoman 1	28.3	1318	0.76	0.57
AustinWoman 2	28.3	1323	0.76	0.60
Donna	24.2	1238	0.73	0.62
Golem	22.3	1070	0.61	0.95
Hanako	20.7	851	0.53	0.92
Helga	28.0	1245	0.73	0.51
Irene	19.2	838	0.51	2.64
Taro	21.7	890	0.51	1.55
VisibleHuman	31.8	1406	0.78	1.30

It can be seen that after the definition of the WHO 50 % of all phantoms are overweight in terms of the BMI [Wor00]. The value of the waist-to-height ratio indicates a possible overweight for all the phantoms. The waist circumference and the waist-to-height ratio are correlated to the BMI. The ratio of muscle mass to fat mass in the abdomen ranges from 0.51 for Helga to 2.64 for Irene. However, it can be recognized from the table that the ratio for Irene is much higher than for any other phantom. It is unclear where this severe difference in muscle mass comes from.

Chapter 3

Background on In-Body Communication Systems

This chapter gives an overview over existing solutions for in-body communication systems. Most commonly three different scenarios for communication of medical equipment in and around the human body are considered. If at least one of the communication partners is placed inside the body, i.e. it is either implanted or ingested, this is called *in-body* communication. For *on-body* communication the transceivers are placed on the skin or in the direct vicinity. While communication to devices that are further away is called *off-body* communication.

A classical solution for the communication with implants is inductive coupling. However, data transmission using inductive coupling is highly orientation dependent. Inductive coupling has the great advantage that data and power can be transmitted simultaneously. In general, the permeability of human tissue is constant [MRF+12][Dum20]. Thus, the effects on the magnetic field are drastically smaller than on the electric field in the human body. In most research papers only low data rates are assumed for inductive coupling, e.g. in [KPN14] and [KN17]. Recent research in [Dum20] shows that for large arrays of transmit and receive coils data rates up to several Mbit/s in depths up to 5 cm are possible. However, this performance degrades severely for larger depths due to the attenuation caused by the tissue. As for capsule endoscopy applications greater depth occur inevitably, inductive coupling is not considered any further in this work.

By far the most common technology used for in-body communication today is radio transmission in the UHF band. Especially for high data rate capsule endoscopy applications UWB transmission is an upcoming research interest.

This chapter is structured as follows. First, the evolution of wireless capsule endoscopy is summarized. Secondly, state of the art standards for in-body communication are presented. Finally, ultra wideband communication is introduced.

3.1 Evolution of Capsule Endoscopy

The earliest reports on ingestible wireless sensor capsules date back to 1957 [Mac59]. The invention of the transistor made it possible to produce small radio transmitters that could transmit pressure, temperature or acidity values from within the gastrointestinal tract [Mac59]. Deploying an analog frequency modulation scheme at a carrier frequency of about 500 kHz the capsule described in [Mac59] could transmit temperature and pressure readings for about two weeks. Their device had a diameter of 9 mm and a length of 28 mm, which is about the same as today's capsules.

From thereon, a multitude of different systems was developed. However, these devices were rarely used in clinical practice due to their high cost and limitations due to the level of integration of the electronics at that time [PW12]. In 1992 a first commercial capsule which could measure the pH level was presented. It could work for up to 6 h in the gastrointestinal tract and was 7.1 mm in diameter and 15.4 mm in length [PW12]. Although there have been some improvements in these capsules that measure physiological parameters, the physicians had to rely on indirect diagnoses with these devices which has a low reliability [PW12]. All of these first capsules were lacking the ability to actually see the tissue of the gastrointestinal tract.

Already in 1868, the first wired endoscope has been invented [CMD11]. These were usually equipped with some sort of imaging device that allowed the physician to visually inspect the gastrointestinal tract [CMD11]. In today's endoscope systems these imaging systems are usually based on fiber-optic cables [PW12]. However, to the date wired endoscopes have the disadvantage that they can only reach the large intestine and the stomach. Only the beginning and the end of the small intestine between these two can be reached and this already causes pain for the patient [IMG+00]. However, as the small intestine is the largest part of the gastrointestinal tract, with a length of about 6 m to 8 m [CMD11], there is a high chance that some diseases cannot be monitored using classical endoscopy.

In 2000 Iddan *et al.* published their ground-breaking paper describing the first wireless capsule endoscope in Nature [IMG+00]. Their device was the first to not only transmit physiological parameters but also image data from within the gastrointestinal tract. Moreover, it was the first device to allow imaging the complete

small intestine. Due to improvements in microelectronic technology their capsule was only slightly larger than the ones previously mentioned. Its dimensions were 11 mm × 30 mm. Iddan *et al.* used the UHF-band for radio transmission. Thus, they could transmit up to 6 h of video material by taking 2 images per second [MMD+09].

Already in 2001 the US Food and Drug Administration (FDA) approved their device. And only 9 years later, in 2009, capsule endoscopy using the PillCam SB developed by Iddan *et al.*, is considered to be the standard approach for certain gastrointestinal diseases [MMD+09]. Especially, for detecting bleeding sources in the small intestine [vdBdLH15]. However, these first versions of capsule endoscopes of course also had their limitations. Mainly, the low resolution and frame rate of the image material made it difficult for the physician to come to a diagnosis. Additionally, a limited battery duration, the fixed viewpoint of the camera, and the missing ability to take biopsy samples are mentioned in [MMD+09]. Moreover, the capsules lack the ability to be moved at specific locations as they depend on the natural peristalsis of the intestines. However, for all of these limitations active research is ongoing.

Advances in optical and electronic research lead to the development of improved versions of the first capsule endoscopes addressing some of the issues mentioned above. Table 3.1 shows commercially available capsule endoscopy systems for the inspection of the small intestine. Some of the companies offer specialized capsules for other applications, e.g. the inspection of the esophagus or the colon. The preparation for the patient usually is the same as for a conventional wired endoscopy, which means fasting for up to 24 h before the examination [CMD11]. Depending on the manufacturer, there is either an array of sensors directly attached to the skin of the patient or a sensor belt is put around the waist [vdBdLH15].

In general the frame rate and the image resolution of all the capsules in Table 3.1 are similar. In this context the frame rate describes the rate at which the images are taken. Although the actual image quality also depends on the optical properties of the lenses used. As can be seen from the table there are two capsules that do not use radio frequency (RF) transmission. Rather, IntroMedic uses human body communication (HBC), which utilizes the conduction of the human body as the communication medium. That means the transmission signal is coupled to the body tissue by capacitive electrodes.

A totally different approach is the CapsoCam by CapsoVision. This capsule does not use any wired or wireless transmission technology but instead stores all the images taken on an internal flash memory [Cap16a]. Moreover, their device is the only that

Table 3.1: Overview over commercially available capsule endoscopy systems. Unless otherwise noted the data is taken from [KPN14][YD12].

Model	Olympus Endocapsule 10	GivenImaging PillCam SB 3	IntroMedic MiroCam	CapsoVision CapsoCam Plus
Transmission	RF @ 433 MHz	RF @ 433 MHz	HBC	Flash Memory
Frame rate	2 frames/s	2 to 6 frames/s	3 frames/s	4×5 frames/s
Resolution	512×512 px	340×340 px	320×320 px	212×896 px
No. RX	8	8	8	None
Battery	12 h	> 8 h	11 h	15 h
Add. Sources	[Oly13]	-	[Int15]	[Cap16b]

has four cameras all around the side of the capsule and not in the front and/or the back as have the capsules from the other vendors. Due to this design the CapsoCam has a longer battery duration compared to the other capsules and they can take 5 frames/s with four cameras, i.e. in total 20 frames/s. However, this approach has the disadvantage that no localization of the capsule inside the gastrointestinal tract is possible, which is a feature that is included for the three capsules from Olympus, GivenImaging and IntroMedic. All of them claim that they can at least locate the capsule to an unknown degree of accuracy in two dimensions [Int13b], Olympus states they are able to track the capsule in all three dimensions [Oly13]. In addition to the missing possibility of localization, the CapsoCam also does not have any feedback link. For example, the PillCam Colon 2 of GivenImaging uses the feedback link to adapt the frame rate of the imaging device depending on the movement of the capsule [AM11]. Furthermore, one could think of a receiver device that analyses the images right after they are received and uses the feedback link to not only adjust the frame rate but also steer the capsule in the right direction. The only capsule of these four that supports locomotion other than the natural peristalsis is the MiroCam that can be controlled externally by a magnet [Int13b].

Regarding the parameters used for communication, not much information is available. The only information that is available is from Olympus and GivenImaging. Their capsules use the UHF band employing narrowband communication using carrier frequencies of 433 MHz. This frequency band from 430 MHz to 440 MHz is standardized by the European Telecommunications Standards Institute (ETSI) standard 303 520 for wireless capsule endoscopes. In this band wireless capsule endoscopes are allowed to use the complete bandwidth with an effective radiated power (ERP) spectral density of -40 dBm/10 MHz [Eur19][Bun19b]. Moreover, it is reported in [YD12] that the PillCam is based on the RF Transceivers built by Microsemi that allow a maximum raw data rate of 800 kbit/s [Bra07][Mic14] using 4-FSK. However,

it is unclear if this also relates to the newest models. But no other information could be retrieved.

As stated above, current devices have resolutions of about 340×340 pixel at a frame rate of 2 to 6 frames per second. In the following, the required data rate for an improved capsule endoscope is derived based on reasonable assumptions. Already a VGA resolution image with 640×480 pixel improves the quality of the diagnostics for the physician significantly. Additionally, a frame rate of at least 10 frames per second is desired for proper diagnostics [TP05]. Assuming 8 bit/pixel in total, a net data rate of 24.6 Mbit/s would be required. Because images of the insides of the intestines have a similar coloring, it is possible to compress the images drastically. In [KRB11] a low complexity image encoding algorithm specifically designed for capsule endoscopy is presented. It is shown by simulations using real endoscopic images that compression rates of up to 98 % are possible by retaining a peak signal to noise ratio of around 40 dB. The algorithm in [KRB11] is based on the work in [TP05]. There a hardware implementation of an enconding agorithm shows that a compression by 95 % is achievable using a CMOS chip with only 4 mm^2 and power consumption of 7.5 mW. Hence, in this thesis a compression rate of 95 % will be assumed for all following computations. The harsh in-body channel conditions will require proper error correction codes to be applied to the transmit signal. Assuming a code rate of $\frac{1}{2}$ a gross data rate of

$$R = 24.6\,\text{Mbit/s} \cdot 0.05 \cdot 2 = 2.46\,\text{Mbit/s} \tag{3.1}$$

results. To account for some additional signaling overhead, the target data rate that will be used in later parts of this thesis will be set to $R_{\text{target}} = 3\,\text{Mbit/s}$. Especially, in Chapter 6 this value will be used as basis for the parameter selection.

3.2 State of the Art In-Body Communication

Wireless body area networks (BANs) are networks that – according to IEEE 802.15.6 – realize "short-range, wireless communication in the vicinity of, or inside, a human body" [Ins12]. In IEEE 802.15.6 multiple physical layers are defined for different medical applications using one common medium access control (MAC) layer. In-body communication is intended only in the Medical Implant Communication Service (MICS) band from 402 MHz to 405 MHz with an information data rate of up to 455.4 kbit/s. The MICS band may be used only for bi-directional communication to and from implants inside the human body. Each user is allowed to use a

bandwidth of at most 300 kHz and the transmit power is limited to 25 µW effective isotropic radiated power (EIRP) [Eur16c]. According to [WW13] it would be save to use transmit powers up to 20 mW from a medical point of view. However, as the MICS band is only secondary user in that frequency range, it has to adhere to more strict limitations [Int02].

In addition to the in-body specifications in the MICS band, IEEE 802.15.6 also defines narrowband communication in various industrial, scientific and medical (ISM) bands, i.e. 860 MHz and 2.4 GHz, for on- and off-body communication. Moreover for on-body communication, ultra wideband communication and human body communication (HBC) are standardized. Human body communication is a technology that uses the body tissues as propagation medium. The signal is coupled to and from the tissue using capacitive electrodes. Ultra wideband communication is implemented as a variant of pulse position modulation (PPM), which is called On-Off Signaling in [Ins12]. For in-body communication in the MICS band differential phase shift keying is used as modulation scheme. Although, initially also M-ary frequency shift keying (FSK) was proposed [GZ11]. Forward error correction is handled by a BCH (63,51) code for all modulation schemes.

During development of the standard, a channel model for communication in the MICS band was derived in [SYH+09] and [YS10]. The channel model was determined from numerical simulations of one phantom using a specifically designed multi-thread loop antenna [SYH+09]. Different sample locations for sensors were considered for the channel models, e.g. pacemaker, nerve stimulation and motion sensors in the limbs. Moreover, two deep-tissue implant positions were investigated. These are the ones that are relevant for a capsule endoscopy application. From these two locations the power loss to arbitrary on-body positions is considered. The resulting log-distance path loss model will be described in more detail in Section 5.5. This channel model was verified using a different phantom (from Korea) in a numerical wave simulation software by Kim *et al.* [KLP+08]. However, Kim *et al.* used more in-body locations (eight) and more thoughtfully placed receive antennas. Still, there resulting path loss model is similar to that of [SYH+09].

Another channel model that was also part of the standardization, but did not make it into the final documents is from Aoyagi *et al.* [ATT+08]. It shows a linear trend of the path loss over the distance and was published in [ATK+09] with experimental verification in [TAH+09]. Numerical wave simulations from a total of 11 in-body locations were conducted to a coordinator node placed above the navel using the phantom Taro (cf. Section 2.4). Hence, there were only 11 measurements taken, which is not that much considering the heterogeneity of the human body.

Due to the bandwidth limitation in MICS band, today's capsule endoscopes use the specifically reserved band at 433 MHz for their communication, as already mentioned in the previous section. Another alternative is the use of the 2.4 GHz ISM band, which is proposed by some groups. However, these have the problem of interference from WiFi, Bluetooth and other technologies that use this band. To improve the image resolution and frame rate of the resulting video stream even further, ultra wideband communication has been proposed in recent years [CSK+13]. The potentially very large bandwidth promises a large increase in the data rate. For that reason ultra wideband communication will be the main focus of this thesis.

3.3 Ultra Wideband Communication

3.3.1 General

Ultra wideband (UWB) signaling is the oldest form of wireless communication, dating back to the first experiments by Hertz and Marconi in 1886 and 1901, respectively [For07]. Their transmitters were based on so-called spark-gap radios which could transmit pulsed electromagnetic waves, i.e. signals with very large bandwidth [Mol06]. Due to the spectral inefficiency of these early receivers, ultra wideband technology was not considered for communication for a long time. Especially, after the first amplitude modulation radios allowed the transmission of voice signals, the focus for radio communication shifted. Only in the 2000s ultra wideband transmission became popular again, after the US Federal Communications Commission (FCC) allowed the unlicensed use of ultra wideband signals in the frequency range of 3.1 GHz to 10.6 GHz [SM04][MCC+06]. Shortly after that decision most countries worldwide followed this proposal and implemented similar regulations. More details on the history of ultra wideband and radio transmission in general can be found in [Mol06], [For07], [SM04] and the references therein.

The most common definition from the FCC of ultra wideband signals is that of systems using an absolute -10 dB bandwidth of more than 500 MHz or a relative bandwidth of 20 % [Mol06][Di 06]. The relative bandwidth B_f is determined from

$$B_f = 2\frac{f_H - f_L}{f_H + f_L}\,, \tag{3.2}$$

where f_H and f_L are the upper and lower -10 dB points in the spectrum [Di 06]. The above definition is from the FCC and applicable in the USA and, thus, used in many standards. However, in the European Union the European Conference of Postal and Telecommunications Administrations (CEPT) set the minimum bandwidth for a signal to be classified as ultra wideband to 50 MHz and there is no criterion for a relative bandwidth [Bun19a], [EU 19]. To retain comparability with other studies and publications, we will stick with the most widely used definition of the FCC and consider a signal with more than 500 MHz bandwidth as ultra wideband. Moreover, the regulations regarding the maximum EIRP spectral density are different in the USA and the EU. The spectral mask is much stricter in Europe as can be seen from Figure 3.1. In Europe only the band from 3.1 GHz to 4.8 GHz can be used with a maximum EIRP spectral density of -41.3 dBm/MHz. Additionally to these strict spectral limits, it is required that the transmitter employs either a low-duty-cycle or

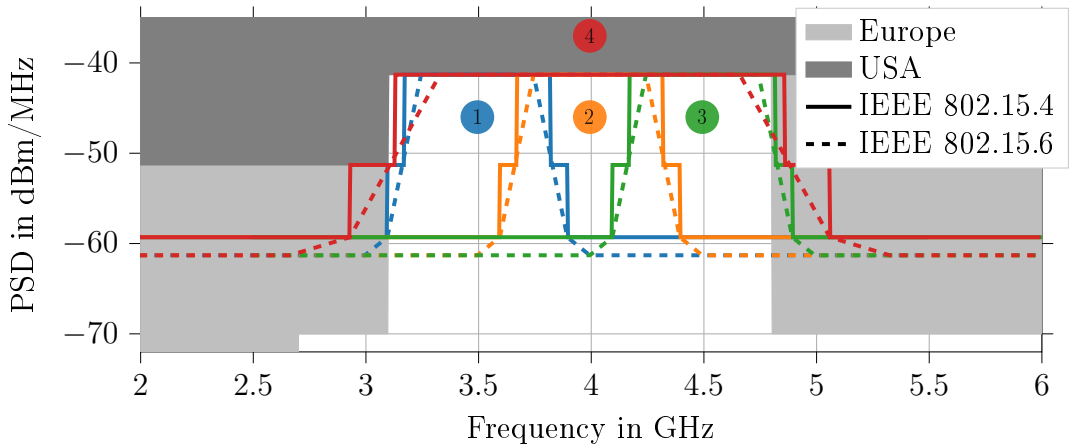

Figure 3.1: The power spectral density masks from European and US regulations. Additionally, the spectral masks for the UWB low band channels from IEEE 802.15.4 and IEEE 802.15.6 are shown as defined in Table 3.2.

detect-and-avoid scheme [Bun19a], which are further specified in [Eur16b]. Whereas in the USA there is no further restriction, other than the power spectral density mask, which extents from 3.1 GHz to 10.6 GHz with a limit of −41.3 dBm/Hz. It has to be noted that ultra wideband communication is also possible for frequencies as low as several MHz. However, the spectral regulations are much tighter for these frequencies. For that reason, most commonly the frequencies from 3.1 GHz to 4.8 GHz are being used. This so-called lower UWB band is preferred for body area networks and especially in-body communication because the attenuation is lower for the lower UWB frequencies [WW13][CKB+09]. As stated in [WS06] the energy contribution of an UWB pulse above 5 GHz to the received signal is negligible for in-body communication. Thus, we will focus in our work on the ultra wideband transmission in the frequency range of 3.1 GHz to 4.8 GHz.

There are two IEEE standards defining ultra wideband communication. One is the already introduced IEEE 802.15.6 for Body Area Networks. In this standard ultra wideband is standardized for the communication between on-body sensors. The second standard is IEEE 802.15.4 for Low-Rate Wireless Networks, where ultra wideband is standardized as part of the high rate pulse repetition frequency physical layer. In both, the channel allocation for the UWB low band is defined according to the data given in Table 3.2. The spectral masks required for the standards, however, are slightly different and shown in Figure 3.1. The channel definitions from Table 3.2 will be used throughout this thesis, e.g. to determine the channel characteristics in Section 4.3 and the computation of the channel capacity in Chapter 4. In both standards a variant of pulse position modulation (PPM) is deployed. More details on the modulation method will be covered in Chapter 6.

Table 3.2: Ultra wideband channel allocation in IEEE 802.15.4 [Ins20] and IEEE 802.15.6 [Ins12].

Channel	f_c in MHz	Bandwidth in MHz	IEEE 802.15.4	IEEE 802.15.6
1	3494.4	500	Optional	Optional
2	3993.6	500	Optional	Mandatory
3	4492.8	500	Mandatory	Optional
4	3993.6	1331.2	Optional	Not available

3.3.2 In-Body Communication

The use of ultra wideband signaling for medical applications is driven by several aspects that are advantageous compared to narrowband communication at other frequencies. First of all, it is difficult to eavesdrop on UWB signals as they operate close to the noise floor, which makes any complex encryption algorithms in this sensitive medical environment unnecessary [CB14]. Additionally, it allows the system to be robust against frequency selective fading as the signal is spread very wide in frequency domain [Mol06]. Different techniques to generate a UWB signal exist, e.g. spread spectrum or OFDM, which can be extended from conventional wideband signals to UWB signals [OHI04]. However, one of the easiest possibilities to generate an UWB signal is to use very short pulses. This is the so-called impulse radio (IR)-UWB. By using appropriate pulses these can be sent directly from the antenna without any up- or downconversion to a carrier frequency. For that reason, ultra wideband transmitters employing impulse radio technique can be built extremely simple and small [Mol06], [YHM09], [BMR+14]. A complete impulse radio UWB transmitter can be built with today's CMOS technology as small as $1.7\,\text{mm} \times 1.7\,\text{mm}$ [TRY14b], [KCB10], [AKC+14]. Hence, no power consuming RF stage is needed and the overall power consumption is reduced. The reduction in power consumption compared to narrowband transmitters can be up to a factor of 30 [TRY15]. Additionally, the short pulses allow much easier localization of the capsule inside the digestive tract [SCB10a] than with narrowband communication.

For the reasons mentioned above, impulse radio ultra wideband communication is very attractive for in-body communication. There are also some disadvantages compared to narrowband communication. One major disadvantage is the much higher attenuation of human tissue in the frequency bands assigned to UWB compared to the attenuation for lower frequencies used by common narrowband communication systems [TTT+12]. Additionally, the transmit power is limited by safety concerns as described in Section 2.3. Hence, the received power is very low and very low

noise amplifiers and high speed analog-to-digital converters are needed at the receiver [TRY14b]. However, as the receiver operates outside of the body, the energy consumption of the receiver is not that critical compared to the in-body sensors.

3.3.3 Feasibility Studies

To the best of our knowledge, the first feasibility study for UWB transmission from implants was done in 2006 by Wang et al. [WS06]. This study is based on a simple homogeneous human torso model that is used for numerical electromagnetic wave simulation. The torso was modeled as a cube shaped container consisting only of the tissue properties of muscle. A specifically designed elliptic disc dipole antenna was then placed in 2 cm depth inside the torso model to find the path loss. Using this path loss, the bit error rate of an UWB transmitter inside the torso was determined. It was concluded that the transmission using impulse radio UWB with uncoded BPSK is feasible inside the human body with a bit error rate (BER) of 10^{-5} for an SNR of 13.5 dB. However, these results were obtained by a simple model in an implantation depth of only 2 cm. In [WWP10] a liquid phantom, representing average tissue dielectric properties, was used for experimental verification of VGA video transmission. A specifically designed antenna for capsule endoscopy was incorporated into the liquid and used as transmit antenna for a wireless USB to VGA kit. This kit was designed for transmission in air with a data rate of 480 Mbit/s. It was found that the video transmission was successful up to an implantation depth of 10 cm.

Another experimental study in [CBB+13] showed that it is possible to transmit high definition video data with 80 Mbit/s from an implanted depth of 3 cm. In this study, a wireless USB hub was inserted into an anesthetized pig's abdominal cavity. The hub used a UWB multiband orthogonal frequency divison multiplex (OFDM) transmission in the 4.2 GHz to 4.8 GHz band. For higher depths, the quality of the video degraded drastically and no link could be established. However, the used UWB system was designed for use in free space. Thus, better results are expected with a specifically designed in-body antenna. Further investigations were done in [AKC+14] with a custom UWB impulse radio system. An antenna specifically designed by the authors for capsule endoscopy applications was used (the same as described in [WWP10]). The authors in [AKC+14] used an anesthetized pig for experimental evaluation of the bit error rate performance. In this case a data stream of 1 Mbit/s was transmitted up to a depth of 12 cm with a bit error rate of 10^{-2}. This shows that a higher penetration depth inside the human body

is possible by using a specific antenna and a lower data rate. Another hardware implementation of a capsule endoscope is shown in [TRY14a]. The authors develop a capsule endoscope, which they say can transmit 30 frames per second from inside a piece of pork meat. However, they do not specify the thickness of the meat.

All of these experiments show that it is feasible to increase the data rate compared to narrowband communication by using ultra wideband impulse radio techniques for in-body communication. To design new communication schemes for high data rate in-body communication using UWB technology for capsule endoscopy, it is necessary to have well designed and comprehensive channel models. For that reason, in the next section available channel models from literature will be reviewed.

3.4 Existing Ultra Wideband Channel Models in Literature

3.4.1 Overview

In this section the most comprehensible channel models that could be found in literature will be reviewed. These models will be used as reference for the channel characteristics from our proposed modeling approach in Section 4.3.3. Although the comparability of the different publications is limited, due to the use of different phantoms, methodologies and frequency ranges, comparing the channel characteristics yields valuable insights on the applicability of the proposed channel model. Moreover, it is usually not possible to remove the effect of the transmit antenna from the propagation behavior in in-body communication as the body becomes part of the antenna [SML+13], [DAA+16].

Table 3.3 shows an overview over ultra wideband channel models that could be found in literature and that are comprehensible to rebuild the resulting model. Moreover, only those channel models were selected that cover ultra wideband transmission in a similar frequency range as the one investigated in this thesis (3.1 GHz to 4.8 GHz) and that describe the propagation in the abdominal area.

In general most of the channel models from literature describe path loss models. There is only one publication [SAW12a] in which a tapped delay line channel impulse response model is described.

Table 3.3: Overview of ultra wideband channel models from literature.

Methodology	Label	Frequency in GHz	Distance in cm	Path Loss Model	Scenario	Source
Simulation	S1	3.4 – 4.8	5 – 24	Logarithmic	Abdominal Region	[SW10]
	S2	3.4 – 4.8	5 – 24	Logarithmic	Abdominal Region	[SAW12a]
	S3	3.5 – 4.5	0 – 10	Exponential	Abdominal Region	[TRY15]
	S4	4.5 – 6.5	3.2 – 10	Logarithmic	Liver Region	[LIS+18]
	S5	3.1 – 5.1	2.8 – 7.5	Logarithmic	Abdominal Region	[Per19]
Phantom	P1	3.1 – 8.5	6 – 20	Logarithmic	Muscle Tissue	[ACG+16]
	P2	3.1 – 5.0	3 – 11	Linear	Muscle Tissue	[GFC+16]
	P3	3.1 – 5.1	2.8 – 8	Logarithmic	Muscle Tissue	[AGC+18]
	P4	3.1 – 5.1	2.8 – 7.5	Logarithmic	Muscle-Fat Tissue	[Per19]
In-Vivo	V1	3.1 – 4.8	4.5 – 16	Logarithmic	Pig	[FCB+15]
	V2	3.1 – 5.0	3 – 11	Linear	Pig	[GFC+16]
	V3	3.4 – 4.8	3.6 – 11.3	Logarithmic	Pig	[SAC+17]
	V4	3.1 – 4.8	4.5 – 16	Logarithmic	Pig	[FCK+19]
	V5	3.1 – 5.1	2.8 – 7.5	Logarithmic	Pig	[Per19]

Most commonly the path loss models will be described with a logarithmic dependency on the distance between transmitter and receiver as

$$\mathrm{PL}_{dB}(d) = \mathrm{PL}_0 + 10 \cdot n \log_{10}\left(\frac{d}{d_0}\right) + \mathcal{N}(\mu, \sigma)\,, \tag{3.3}$$

where PL_0 is the path loss in dB at the reference distance d_0, n is the path loss exponent ($n = 2$ in air), d is the distance between transmit and receive antenna, and $\mathcal{N}(\mu, \sigma)$ describes the Gaussian-distributed shadowing. In some of the models an exponential/linear dependency on the distance is proposed as

$$\mathrm{PL}_{dB}(d) = \mathrm{PL}_0 + \alpha \cdot \left(\frac{d}{d_0}\right)^{\gamma} + \mathcal{N}(\mu, \sigma)\,, \tag{3.4}$$

where α and γ are model dependent scalar parameters. All channel models that will be reviewed are listed in Table 3.3. Each of the models will be explained in more detail in the following sections distinguished by the modeling approach. The average path loss for each presented channel model will be shown in the respective Figures 3.2, 3.3, and 3.4.

3.4.2 Numerical Simulations

One of the first ultra wideband channel models for capsule endoscopy was published by Shi *et al.* in [SW10], which is labeled as S1 in Table 3.3 and Figure 3.2. The authors simulated the wave propagation in the frequency range from 3.4 GHz to 4.8 GHz using the finite difference time domain (FDTD) method numerically. They used a dipole as transmit antenna at 33 different locations in the small intestine (at each of them in three different orientations) and an elliptic disc dipole antenna as receive antenna at five locations on the abdomen. The digital phantom used was Taro and the resulting path loss model shows a logarithmic behavior as in (3.3).

The same authors published results of the same simulation setup[1] also in [SAW12a] and [SAW12b], which is labeled as S2 in Table 3.3 and Figure 3.2. However, in the two latter publications the parameters of the (logarithmic) path loss model were substantially different. It is unclear were these differences come from. Additionally, the authors derive a channel impulse response model with two paths, i.e. $N = 2$,

[1] It is unclear if the underlying data is also from the same simulation run.

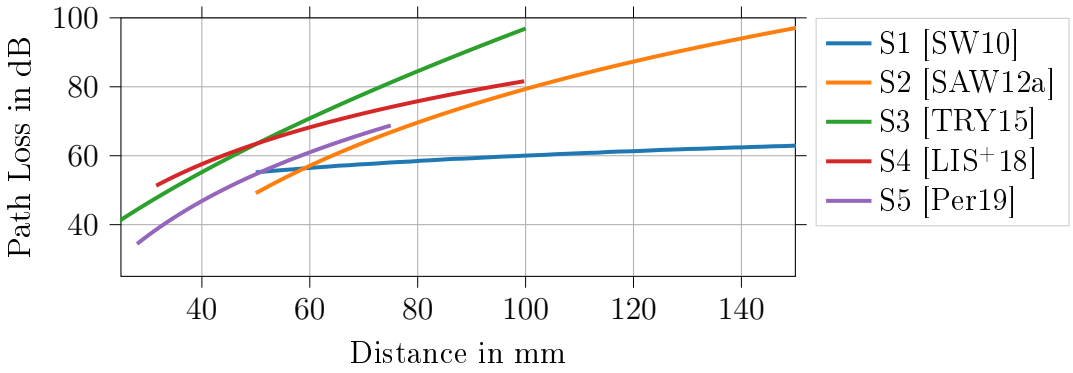

Figure 3.2: The average path loss of all the path loss models from literature based on numerical wave simulations.

based on the popular Saleh-Valenzuela model [SV87] in the following form

$$h(t) = \sum_{k=0}^{N-1} \alpha_k \delta(t - \tau_k)\,, \tag{3.5}$$

where the weights α_k are log-normal distributed and the distribution of the delays τ_k follows an inverse Gaussian distribution.

Another study that derives a path loss model from a numerical simulation for capsule endoscopy is from Thotahewa *et al.* [TRY15], which is labeled as S3 in Table 3.3 and Figure 3.2. The authors conducted a numerical simulation with an unknown digital phantom using a custom build U-shaped slot antenna as transmitter. The received power is derived from the electric and magnetic field using 512 field probes located equally spaced in the main lobe of the transmit antenna. Hence, these field probes are located inside the body as well as on the body surface. The resulting path loss model follows an exponential form as described in (3.4) with $\gamma = 0.611$. Moreover, results from measurements in a layered meat-phantom confirm the trend of the path loss equation from their simulations.

In [LIS+18] Leelatien *et al.* investigate the ultra wideband communication channel between a sensor on the liver and a receiver on the abdominal surface. This is labeled as S4 in Table 3.3 and Figure 3.2. Although, this study covers a sensor on the liver surface, the resulting path loss model is included here as the transmission happens in the abdominal area as well. The authors simulate the wave propagation using CST Microwave Studio for the digital phantom Taro. They use a low-profile tapered-slot antenna that is optimized for transmission in the frequency range from 4.5 GHz to 6.5 GHz. The resulting path loss model follows a logarithmic behavior as described in (3.3).

Finally, in [Per19] an improved version of the path loss model – initially proposed in [PAG+19] and [PBG+18] – for numerical simulations, as well as phantom and in-vivo measurements is published. The path loss model from numerical simulations is labeled as S5 in Table 3.3 and Figure 3.2. The simulations were done with a digital phantom called Nelly, which is available as add-on for CST Microwave Studio. For the ultra wideband simulations the voxel model was modified to contain only muscle tissue, with a layer of fat and skin on top. Hence, the original heterogeneity of the model was not taken into consideration. A coplanar waveguide antenna was used at six different locations in the abdomen and a patch antenna was placed at three different positions on the body surface. Hence, in total 18 communication links were investigated. The resulting path loss model has again the form of a logarithmic model as in (3.3).

It can be seen from Figure 3.2 that most of the resulting path loss models from literature show the same trend. That is, only the model S1 is deviating significantly from the others. However, observe the scaling of the axes. Even between these models that agree on the same trend, differences in path loss of 10 dB for the same distance are common. At most a difference of 27 dB can be observed for a distance of 100 mm between S2 and S3.

3.4.3 Phantom Experiments

Building realistic phantoms to emulate the propagation inside the human body is challenging for ultra wideband frequencies. However, recently an interdisciplinary team at the Universitat Politècnica de València published work on the development of a liquid phantom solution based on acetonitrile. It was found in [CGF+16] that these solutions can mimic the dielectric properties of different human tissues over a wide frequency range. Hence, they are suitable for ultra wideband phantom experiments. There are different studies from that same group that result in different path loss models. These will be summarized in the following.

In [ACG+16] a polypropylene container of $30 \times 30 \times 15\,\mathrm{cm}^3$ was filled with an acetonitrile solution mimicking muscle tissue. This setup was used to recreate a cross section of the human torso. Using a vector network analyzer the path loss was determined for frequencies from 3.1 GHz to 8.5 GHz. Measurements were taken from 1083 different transmit antenna locations inside the liquid to one static receive antenna mounted on the wall of the container. The same antennas as in [Per19] have been used. The resulting path loss model is logarithmic and labeled as P1 in Table 3.3 and Figure 3.3.

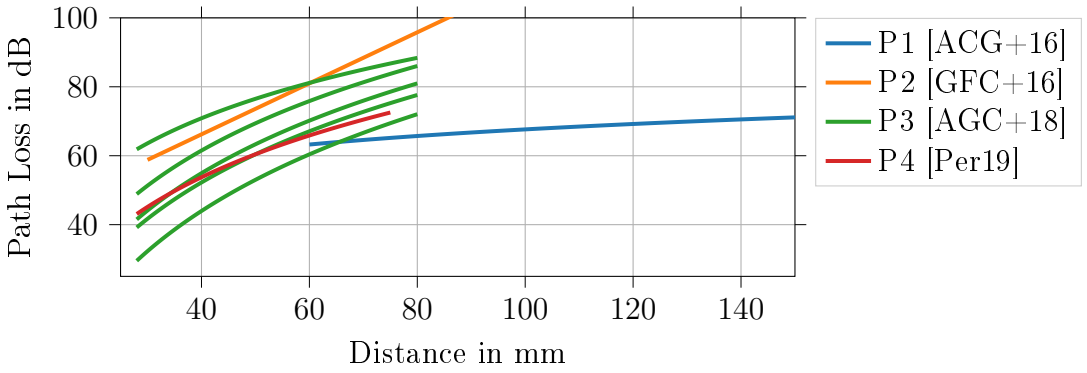

Figure 3.3: The average path loss of all the path loss models from literature based on phantom experiments. For P3 the carrier frequency increases from bottom to top.

The same setup from [ACG+16] was used in [AGC+18] to determine the frequency dependency of the path loss for five different subbands in the frequency range from 3.1 GHz to 5.1 GHz. In this work the authors show also that the logarithmic path loss model provides a better fit than the linear model for all subbands. These results are labeled as P3 in Table 3.3 and Figure 3.3. The average path loss is shown for all five subbands in Figure 3.3, where the carrier frequency increases from bottom to top.

Furthermore, in [GFC+16] the path loss in the frequency range from 3.1 GHz to 5 GHz was determined in a $22 \times 22 \times 16\,\mathrm{cm}^3$ Styrofoam container. The container was filled with a sucrose solution that is supposed to mimic the dielectric properties of muscle tissue in this case. In this experiment the patch antenna from [ACG+16] and [Per19] was used as transmit and receive antenna. The path loss was measured only in six different depths, resulting in a linear path loss model, which is labeled as P2 in Table 3.3 and Figure 3.3.

In [Per19] multiple phantom measurements based on the acetonitrile solutions from [CGF+16] are described. The path loss was determined in the frequency range from 3.1 GHz to 5.1 GHz using the same coplanar waveguide antenna as transmit antenna and the same patch antenna as receive antennas as for the numerical simulations from [Per19] mentioned above. Three different phantom containers were used, two square containers and one hexagonal container. All of them were filled with a phantom mimicking muscle tissue. Additionally, in all of them a 1.5 cm to 2 cm layer of fat-mimicking solution was placed between the muscle tissue and the receive antenna. This was done to more accurately imitate the human abdomen. In total 594 path loss measurements were taken. From these three measurements a logarithmic path loss model was obtained. This model is labeled as P4 in Table 3.3 and

Figure 3.3.

It can be seen from Figure 3.3 that, except P1, all the resulting path loss models show a similar trend. However, differences of around 20 dB can occur between the different results. The results from P3 also show that there is a detrimental impact on the path loss for higher carrier frequencies.

3.4.4 In-Vivo Experiments

In-vivo experiments for ultra wideband capsule endoscopy are usually conducted in anesthetized pigs. To the best of our knowledge only two groups work on these kind of in-vivo experiments, one group at the Universitat Politècnica de València and another at the Oslo University Hospital.

The first path loss model results from in-vivo experiments were reported by Floor *et al.* in [FCB+15]. The dielectric resonator transmit antenna was implanted in five different depths inside the abdominal cavity of an anesthetized pig. A bowtie dipole was used as receive antenna and placed at 26 different positions on the abdominal surface. A total number of 26 distinct measurements were taken. The resulting logarithmic path loss model is valid in the frequency range from 3.1 GHz to 4.8 GHz. This model is labeled as V1 in Table 3.3 and Figure 3.4.

In [GFC+16] in-vivo experiments were done in addition to the phantom experiments described in the previous section. The same patch antennas were used as transmit and receive antennas. The implanted transmit antenna was fixed at a reference location in the abdominal cavity of a pig and only the receive antenna on the abdominal surface was moved to six different locations. The path loss was computed for a frequency range from 3.1 GHz to 5 GHz. It was found that there is a linear dependency of the path loss on the distance. This model is labeled as V2 in Table 3.3 and Figure 3.4.

Shimizu *et al.* developed a dual-polarized planar elliptical loop antenna that allows for transmit diversity employing two different polarizations. They give a path loss model from their in-vivo experiments in [SAC+17]. Again the transmit antenna was fixed inside the abdominal cavity and the receive antenna (a planar dipole) was moved to eight different positions on the body surface. The path loss was computed for the frequency range of 3.4 GHz to 4.8 GHz. From this setup two logarithmic path loss models were obtained, one for each polarization. The results of the two polarizations are different because the signal of each of the two transmit antennas

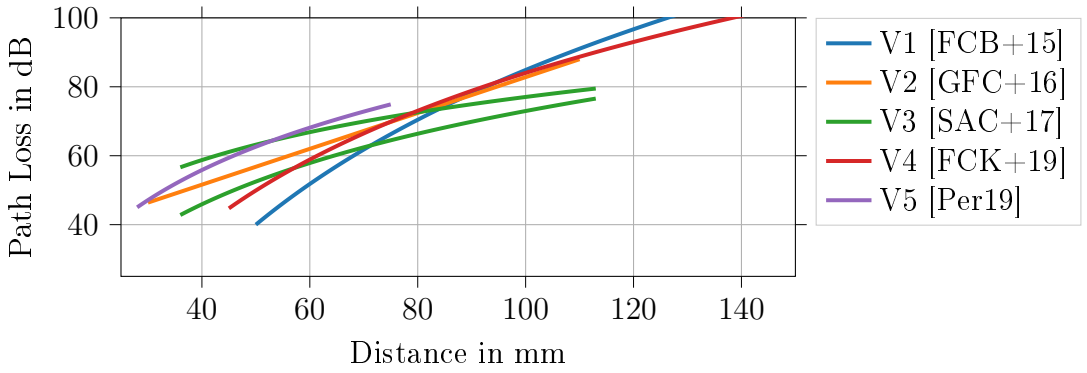

Figure 3.4: The average path loss of all the path loss models from literature based on in-vivo experiments. For V3 two differently polarized antennas were used.

was received by the same single dipole antenna. Both models are shown in Figure 3.4 and are labeled as V3 in Table 3.3.

In [FCK+19] the experiments from [FCB+15] and [SAC+17] are combined to a new logarithmic path loss model for frequencies from 3.1 GHz to 4.8 GHz. The resulting model is labeled as V4 in Table 3.3 and Figure 3.4. It is based on the data from V1 and V3.

Furthermore, in [Per19] two in-vivo experiments with in total three different receive antennas were conducted. The same coplanar waveguide antenna is used as transmit antenna, as mentioned already in the sections on the simulation and phantom models. As no relevant difference between the three receive antennas was found, all of the results were combined into one logarithmic path loss model, which is valid in the frequency range from 3.1 GHz to 5.1 GHz. From the description in [Per19] it is unclear how many different transmit and receive antenna locations have been investigated. However, from the plots it can be deduced that approximately 50 to 70 communication links have been taken into consideration. This model is labeled as V5 in Table 3.3 and Figure 3.4.

Figure 3.4 shows that for the in-vivo experiments all resulting path loss model operate somehow in the same range of values. Although the methodology for all of these experiments was similar, still differences of approximately 23 dB occur between the resulting path loss models, e.g. between V1 and V5 at 50 mm distance. And not only the absolute values differ but also the slope of the path loss models is significantly different.

3.4.5 Summary

From Figures 3.2, 3.3, and 3.4 it can be seen that most of the resulting path loss models that could be found in literature cover the same range of values. However, there are significant differences between the individual models, depending on the exact setup, the methodology and the underlying model. Hence, it is difficult based on these results to predict the path loss for in-body communication. As it could be seen for all three methodologies, the resulting path loss models may differ by up to 27 dB for the same distance between transmitter and receiver. Thus, large variations in the resulting channel capacity between different phantoms are to be expected.

Chapter 4

Communication Channel Modeling

As shown in Section 3.4, some channel models exist in literature for ultra wideband in-body communication in the abdominal area. However, in most of them only a path loss model is given, which does not seem feasible as a channel model for the simulation of transmission through a highly dispersive medium with bandwidths of more than 500 MHz. Moreover, these models are only valid in a certain frequency range. Furthermore, it is not possible to extend these results to other digital human phantoms, which is necessary to capture the differences in physiological conditions of different humans. Additionally, all the wave simulations and experiments are based on the usage of a certain transmit and receive antenna. This means that all results from simulations with one type of antenna are only valid for the use of that antenna. Thus, these path loss models are not suitable to draw general conclusions on the channel characteristics that originate from the human tissue properties. Furthermore, they cannot be used to compare the channel capacity for different human phantoms.

In this chapter a novel channel model is presented, which is based on treating the propagation path as a multi-layered dielectric. It will be referred to as *layer model* in the following. This layer model will be derived from the digital human phantoms presented in Section 2.4. The goal is to make it possible to investigate arbitrary locations of transmit antennas inside the body and receive antennas on the abdominal surface. The developed layer model is then validated using numerical wave simulations in CST Microwave Studio and compared to the path loss models from literature introduced in Section 3.4. Furthermore, the channel characteristics, i.e. the path loss and delay spread are determined. Finally, elementary basis functions are fitted to the transfer functions determined by the layer modeling approach to generate an easy to reproduce channel model.

4.1 Development of a Simplified Modeling Technique

4.1.1 General Idea

The general idea is to model the propagation path of an electromagnetic wave by a multi-layered dielectric resembling the tissue structure on the path between transmitter and receiver as shown in Figure 4.1. The inspiration for this procedure originates from [TTT+12], where the idea of using a multi-layered dielectric for channel modeling was first investigated systematically. Figure 4.1 shows one example mapping from the digital phantom Alvar to a layer model. In Figure 4.1a the location of the horizontal slice shown in Figure 4.1b is indicated by a red line. A transmitter is placed at $\mathbf{t}_i$ inside the gastrointestinal tract and a receiver is placed at $\mathbf{r}_j$ on the abdominal surface. Both $\mathbf{t}_i$ and $\mathbf{r}_j$ are having the same z-coordinate in this example for simplicity reasons. The tissues along the solid red line between $\mathbf{t}_i$ and $\mathbf{r}_j$ are mapped to the layer model shown in Figure 4.1c. The colors in all three plots are identically colored based on the tissue type. The gastrointestinal content is abbreviated with GI content. The tissues along the dashed red line are used for the calculation of the source impedance η_s for the communication link from $\mathbf{t}_i$ to $\mathbf{r}_j$.

By assuming that a plane wave is passing through this multi-layered dielectric, the transfer function can be calculated analytically based on equations from transmission line theory. Of course, the real wave inside the human body will not be a plane wave, this is only assumed for the calculation of the transfer function. Moreover, the boundaries between tissues are not perpendicular to the transmitted wave in reality and will lead to small-scale diffraction and scattering, which is not included in the layer modeling approach. It will be shown in Section 4.2 on the validation of the proposed model that these simplifications lead to differences between the transfer functions from the layer model and numerical wave simulations. However, considering the average transmission characteristics the layer modeling approach resembles the real wave propagation very well. The important channel characteristics are covered by the layer modeling approach.

This simplification makes the channel modeling for different digital human phantoms feasible. Additionally, it allows to determine the path loss for many more communication links compared to studies based on electromagnetic wave propagation or experiments. In those studies, typically only up to 100 different communication links are considered (cf. Section 3.4). However, especially the small intestine is long and there are many different locations and propagation paths to the outside possible.

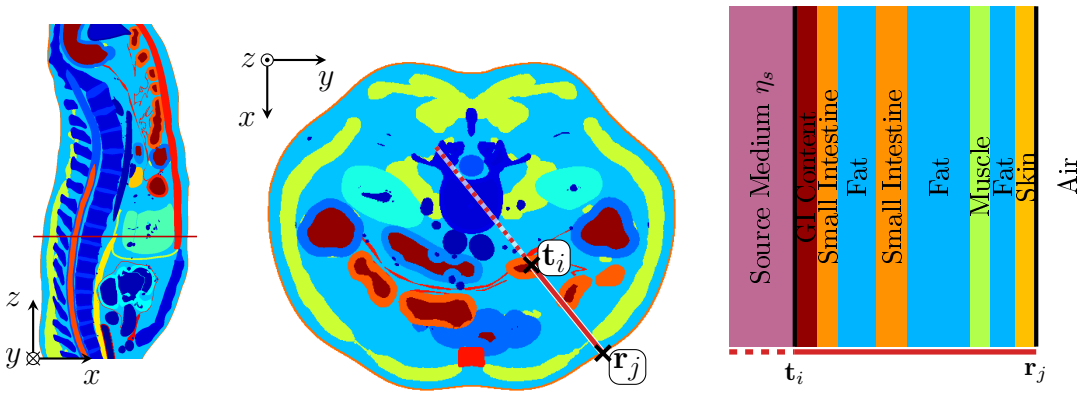

(a) (b) (c)

Figure 4.1: Example of a layer model mapping from the digital phantom Alvar. (a) Sagittal slice viewed from the right side of the body. (b) Horizontal slice viewed from top (location indicated in (a) by red line). The tissues along the solid red line between $\mathbf{t}_i$ and $\mathbf{r}_j$ are mapped to the layer model shown in (c).

The transfer function for a multi-layered dielectric will be derived step-by-step in the following Sections 4.1.2, 4.1.3, and 4.1.4. In Section 4.1.5 additional losses that need to be taken into account are discussed. Finally, in Section 4.1.6 the final layer model consisting of a direct and an indirect path will be presented.

4.1.2 Transmission of Electromagnetic Plane Waves Through Multi-Layered Dielectrics

The propagation of an electromagnetic plane wave propagating through a linear, homogeneous medium without any sources is described by Maxwell's equations

$$\nabla \times \vec{E} = -j\omega\mu\vec{H} \qquad (4.1) \qquad \nabla \cdot \vec{E} = 0 \qquad (4.3)$$

$$\nabla \times \vec{H} = j\omega\varepsilon\vec{E} \qquad (4.2) \qquad \nabla \cdot \vec{H} = 0\,, \qquad (4.4)$$

where $\vec{E}$ is the electric field vector, $\vec{H}$ is the magnetic field vector, ω is the angular frequency, ε is the complex permittivity of the medium, and μ is the permeability of the medium. Considering a transverse electromagnetic plane wave propagating in z-direction, this wave has only E_x and H_y components unequal to zero. Then (4.1) and (4.2) reduce to

$$\frac{\mathrm{d}E_x}{\mathrm{d}z} = -j\omega\mu H_y, \qquad (4.5) \qquad \frac{\mathrm{d}H_y}{\mathrm{d}z} = -j\omega\varepsilon E_x\,. \qquad (4.6)$$

It should be noted that phasor notation is used. That means E_x and H_y are phasors rotating in the complex plane with angular frequency $\omega = 2\pi f$. Thus, in the following derivations all quantities are in general functions of frequency. However, this dependency is omitted for the sake of readability.

By taking the derivative of (4.5) and using (4.6) the one-dimensional Helmholtz equation results as

$$\frac{\mathrm{d}^2 E_x}{\mathrm{d}z^2} = -k^2 E_x \,, \tag{4.7}$$

where $k = \omega\sqrt{\mu\varepsilon}$ is the wave number. A possible solution to (4.7) using the propagation constant $\gamma = jk = \alpha + j\beta$ is

$$E_x = E_+ e^{-\gamma z} + E_- e^{\gamma z} \,, \tag{4.8}$$

where E_+ is denoting a wave traveling in positive z-direction and E_- a wave traveling in negative z-direction. Substituting (4.8) into (4.5) yields the solution for the magnetic field as

$$H_y = H_+ e^{-\gamma z} - H_- e^{\gamma z} = \frac{1}{\eta}\left(E_+ e^{-\gamma z} - E_- e^{\gamma z}\right) \,, \tag{4.9}$$

where $\eta = \sqrt{\frac{\mu}{\varepsilon}}$ is the wave impedance of the medium. A wave with frequency f will propagate with a phase velocity of

$$c = \frac{2\pi f}{\beta} = \frac{2\pi f}{\mathrm{Im}\{\gamma\}} \,. \tag{4.10}$$

In the following the subscript of E_x and H_y will be dropped for easier readability, hence $E = E_x$ and $H = H_y$.

From (4.8) and (4.9) the *transmission parameters* (also known as ABCD-parameters) for a plane electromagnetic wave traveling through a lossy dielectric can be derived. The transmission parameters relate the electric and magnetic field at a boundary $(i+1)$ to the fields at the boundary i as

$$\begin{bmatrix} E_i \\ H_i \end{bmatrix} = \mathbf{T}_i \begin{bmatrix} E_{i+1} \\ H_{i+1} \end{bmatrix} = \begin{bmatrix} A_i & B_i \\ C_i & D_i \end{bmatrix} \begin{bmatrix} E_{i+1} \\ H_{i+1} \end{bmatrix} \,. \tag{4.11}$$

The advantage of using the transmission parameters to determine the propagation behavior of a wave through a multi-layered structure as depicted in Fig. 4.2 is that the matrices can be computed for all of the L individual layers and concatenated

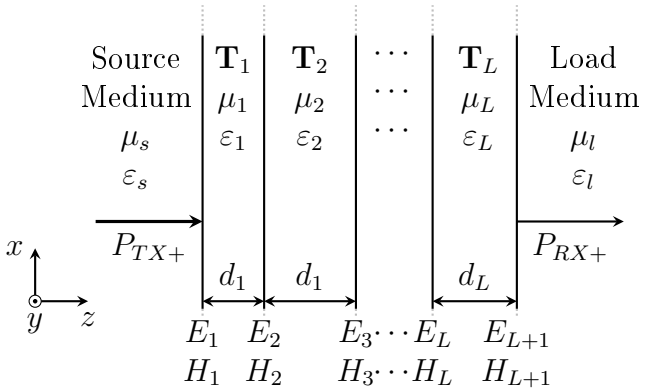

Figure 4.2: A plane wave with power P_{TX+} propagating through a multi-layered dielectric. The wave propagates along the positive z-direction and has a power of P_{RX+} at the receiver side.

afterwards to form the total transmission matrix

$$\mathbf{T} = \prod_{i=1}^{L} \mathbf{T}_i \,. \tag{4.12}$$

Arranging the setup depicted in Fig. 4.2 such that $z = 0$ is at the boundary between layer 1 and 2, it is clear from (4.8) and (4.9) that

$$E_2 = E_+ + E_- \tag{4.13}$$

$$H_2 = H_+ - H_- = \frac{1}{\eta}(E_+ - E_-) \,. \tag{4.14}$$

Furthermore, it holds that

$$E_1 = E_+ e^{\gamma_1 d_1} + E_- e^{-\gamma_1 d_1} \tag{4.15}$$

$$H_1 = \frac{1}{\eta}\left(E_+ e^{\gamma_1 d_1} - E_- e^{-\gamma_1 d_1}\right) \,. \tag{4.16}$$

Combining (4.11) and (4.13) up to (4.16), the entries A_i, B_i, C_i, D_i of the matrix $\mathbf{T}_i$ can be determined as

$$\mathbf{T}_i = \begin{bmatrix} A_i & B_i \\ C_i & D_i \end{bmatrix} = \begin{bmatrix} \cosh(\gamma_i d_i) & \eta_i \sinh(\gamma_i d_i) \\ \frac{1}{\eta_i}\sinh(\gamma_i d_i) & \cosh(\gamma_i d_i) \end{bmatrix} \,. \tag{4.17}$$

With (4.17) the relation of electric and magnetic field before and after each individual layer can be computed. Using (4.12) the relation of the fields after the L-th layer can be related to the fields at the first layer as the concatenation of all transmission

matrices $\mathbf{T}_i$. Now the transmission parameter matrix $\mathbf{T}$ can be used to determine the transfer function of a plane wave propagating through this multi-layered dielectric. This is shown in the next section.

4.1.3 From Transmission Parameters to Transfer Function

The transmission parameter matrix $\mathbf{T}$ relates the electric and magnetic field at the receiver side to the fields at the transmitter side of the dielectric. However, from a communication engineering perspective a transfer function relating the transmitted signal to the received signal is needed. These signals are usually assumed to have units of the square-root of power. This can be obtained by the scattering parameters $\mathbf{S}$ of the presented setup. When the inbound and outbound waves are defined accordingly, the squared magnitude of the scattering parameters describes the power flow through the structure.

As discussed in [TTT+12], most textbooks only give the transformation between transmission parameters $\mathbf{T}$ and scattering parameters $\mathbf{S}$ for purely real valued source and load impedances. However, as in the investigated scenario the impedance of the source material η_s inside the digestive tract is not real, another approach is needed. Theilmann *et al.* derive the transformation from transmission parameters to scattering parameters for arbitrary source and load impedances in [TTT+12] based on results from [MW92]. However, their derivation has some small inconsistencies. These were addressed already in [BB17b]. Nevertheless, a more detailed derivation will be provided here.

The setup shown in Fig. 4.3 will be used for the derivation of the scattering parameters. The source medium has a wave impedance of η_s and the load medium has a wave impedance of η_l. How these impedances are obtained will be discussed in Section 4.1.4. For the definition of the scattering parameters, inbound and outbound waves a_i and b_i are defined as

$$a_1 = \sqrt{\mathrm{Re}(\eta_s)} H_{TX+} \tag{4.18}$$

$$b_1 = \sqrt{\mathrm{Re}(\eta_s)} H_{TX-} \tag{4.19}$$

$$a_2 = \sqrt{\mathrm{Re}(\eta_l)} H_{RX-} \tag{4.20}$$

$$b_2 = \sqrt{\mathrm{Re}(\eta_l)} H_{RX+}\,. \tag{4.21}$$

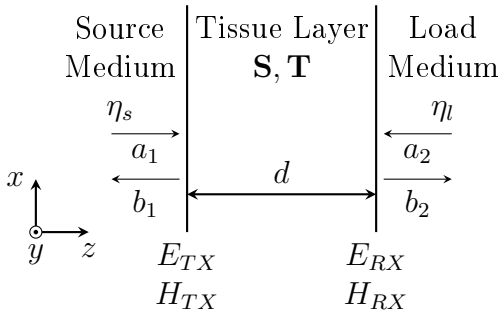

Figure 4.3: Equivalent setup of the multi-layer structure from Fig. 4.2 used for the computation of the S-parameters.

These are connected by the scattering parameter matrix $\mathbf{S}$ as

$$\begin{bmatrix} b_1 \\ b_2 \end{bmatrix} = \mathbf{S} \begin{bmatrix} a_1 \\ a_2 \end{bmatrix} = \begin{bmatrix} S_{11} & S_{12} \\ S_{21} & S_{22} \end{bmatrix} \begin{bmatrix} a_1 \\ a_2 \end{bmatrix} . \tag{4.22}$$

With these definitions the entries in the scattering matrix $\left|S_{ij}\right|^2$ give the power relationship from port i to port j. This can be seen using Poynting's theorem from which follows that the time average power of a linearly polarized plane wave can be computed as

$$P = \frac{1}{2} \operatorname{Re}(EH^*) . \tag{4.23}$$

Hence, the path loss from port 1 to port 2, i.e. from transmitter to receiver, can be calculated from (4.18), (4.21), (4.22), and (4.23) as

$$|S_{21}|^2 = \left| \left. \frac{b_2}{a_1} \right|_{a_2=0} \right|^2 = \frac{\operatorname{Re}(\eta_l) \left|H_{RX+}\right|^2}{\operatorname{Re}(\eta_s) \left|H_{TX+}\right|^2} = \frac{\operatorname{Re}\left(E_{RX+} H_{RX+}^*\right)}{\operatorname{Re}\left(E_{TX+} H_{TX+}^*\right)} = \frac{P_{RX+}}{P_{TX+}} . \tag{4.24}$$

Likewise, the reflected power at the transmitter can be obtained from

$$|S_{11}|^2 = \left| \left. \frac{b_1}{a_1} \right|_{a_2=0} \right|^2 = \frac{P_{TX-}}{P_{TX+}} . \tag{4.25}$$

Using all of the relationships and definitions above, it follows that

$$S_{21} = \left. \frac{b_2}{a_1} \right|_{a_2=0} = \frac{\sqrt{\operatorname{Re}(\eta_l)}}{\sqrt{\operatorname{Re}(\eta_s)}} \frac{2\eta_s}{\eta_l A + B + \eta_l \eta_s C + \eta_s D} \tag{4.26}$$

describes the transfer function of a plane wave propagating through a multi-layered dielectric defined by the matrix $\mathbf{T}$ as $|S_{21}|^2$ gives the relation ship of input to output power. The complete derivation of (4.26) is given in Appendix A.2.

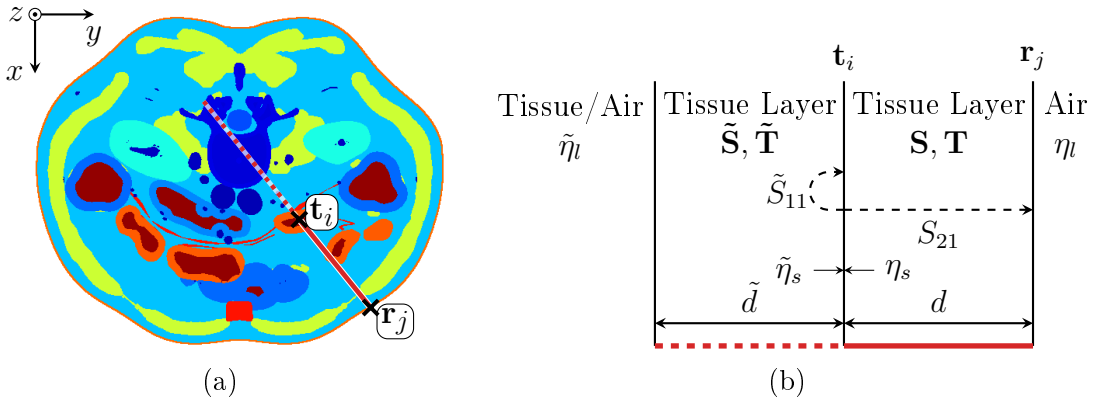

Figure 4.4: Setup for the calculation of the source impedance. The tissue layers along the red lines indicated in (a) are mapped to the layer model in (b).

4.1.4 Determination of Source and Load Impedance

As the receive antenna will always be placed on the abdominal surface, it is surrounded by air. Hence, the load impedance η_l is the wave impedance of free space, i.e. $\eta_l = \eta_0 = 376.73\,\Omega$.

The transmit antenna, however, is placed inside the digestive tract and, thus, surrounded by different tissue types depending on the exact location. For the derivation of the layer model it was assumed that the wave from transmitter to receiver only propagates on the direct line connecting the two points as indicated by the solid red line in Figure 4.4a. Furthermore, it will be assumed that reflections inside the phantom at the transmitter location are influenced only by the tissues along the opposite of the propagation direction as shown by the dashed red line in Figure 4.4a. The schematic setup is shown in Figure 4.4b.

Reflections at the transmitter tissue boundary will be included into the reflection coefficient $\tilde{S}_{11}$. In turn, $\tilde{S}_{11}$ determines the input impedance η_s of the tissue layers $\tilde{\mathbf{T}}$. S_{21} describes the transfer function of the tissue layers under investigation. The matrix $\tilde{\mathbf{T}}$ contains the transmission parameters of all tissue layers up to a certain depth in the opposite direction of propagation along the dashed red line indicated in Figure 4.4a. The entries of $\tilde{\mathbf{T}}$ can be determined from the tissue types and their thickness using (4.17) and (4.12). By utilizing the transmission parameter matrix $\tilde{\mathbf{T}}$, the reflection coefficient $\tilde{S}_{11}$ of the respective layer model can be computed with the following relationship:

$$\tilde{S}_{11} = \frac{\tilde{\eta}_l \tilde{A} + \tilde{B} - \tilde{\eta}_s \tilde{\eta}_l \tilde{C} - \tilde{\eta}_s \tilde{D}}{\tilde{\eta}_l \tilde{A} + \tilde{B} + \tilde{\eta}_s \tilde{\eta}_l \tilde{C} + \tilde{\eta}_s \tilde{D}}, \tag{4.27}$$

where $\tilde{\eta}_l$ is the load impedance of these tissue layers, and $\tilde{\eta}_s$ is their source impedance, i.e. the input impedance of $\mathbf{T}$. $\tilde{A}, \tilde{B}, \tilde{C}$ and $\tilde{D}$ are the entries of the transmission matrix $\tilde{\mathbf{T}}$. The derivation of (4.27) is shown in detail in Appendix A.2.

As the attenuation of the tissues is very high in the ultra wideband frequency range, only tissue layers up to a total distance of $\tilde{d} = 10\,\text{cm}$ or until the body surface is reached will be considered. The last tissue type that is found in this direction will determine the value of $\tilde{\eta}_l$.

From Fresnel's equations it is known that the reflection coefficient at the transmitter location $\mathbf{t}_i$ can also be expressed as

$$\tilde{S}_{11} = \frac{\eta_s - \tilde{\eta}_s}{\eta_s + \tilde{\eta}_s}\,. \tag{4.28}$$

Combining (4.27) and (4.28) leads to

$$\begin{aligned} \eta_s &= \tilde{\eta}_s \frac{1 + \frac{\tilde{\eta}_l\tilde{A} + \tilde{B} - \tilde{\eta}_s\tilde{\eta}_l\tilde{C} - \tilde{\eta}_s\tilde{D}}{\tilde{\eta}_l\tilde{A} + \tilde{B} + \tilde{\eta}_s\tilde{\eta}_l\tilde{C} + \tilde{\eta}_s\tilde{D}}}{1 - \frac{\tilde{\eta}_l\tilde{A} + \tilde{B} - \tilde{\eta}_s\tilde{\eta}_l\tilde{C} - \tilde{\eta}_s\tilde{D}}{\tilde{\eta}_l\tilde{A} + \tilde{B} + \tilde{\eta}_s\tilde{\eta}_l\tilde{C} + \tilde{\eta}_s\tilde{D}}} \\ \eta_s &= \frac{\tilde{\eta}_l\tilde{A} + \tilde{B}}{\tilde{\eta}_l\tilde{C} + \tilde{D}}\,. \end{aligned} \tag{4.29}$$

Thus, using (4.29) the source impedance η_s for the transfer function calculation of S_{21} can be determined from the transmission parameter matrix $\tilde{\mathbf{T}}$.

4.1.5 Spherical Radiation Loss

With (4.26) the propagation of a plane wave through a multi-layered dielectric, which extends to infinity in x and y direction, is described. Using this transfer function alone to describe the propagation of an electromagnetic wave from a small antenna in a capsule in the digestive tract to a receiver on the body, would mean that all the radiated power of the antenna is propagating only in the direction of the receiver. In other words, it would be assumed that the transmit antenna is highly directive and perfectly aligned to the receive antenna, as no transmitted power is lost in other directions. However, in a real capsule endoscopy scenario the orientation of the capsule relative to the receive antenna is unknown. Hence, an isotropic transmit antenna would be the best solution. To incorporate the additional losses due to the

omni-directional propagation the radiation loss

$$\mathrm{RL}(f, d; c) = \left(\frac{4\pi f d}{c}\right)^2 \tag{4.30}$$

will be included. Equation (4.30) is based on Friis transmission equation [Fri46]. It describes the power loss between two isotropic antennas in free space at a frequency f, with a phase velocity c, and with sufficient spacing d, such that a plane wave front can be assumed at the receiver.

It has to be noted that applying (4.30) to the in-body transmission is supposed to serve as an approximation to the spatial distribution of the radiation that occurs with a real antenna inside the body. Most probably, the antennas are not placed far enough from each other to justify reception in the far field [KB09]. However, it was found in [KKS14] and [WFP16] that by tuning the antenna parameters or as described in [KSS13] by reducing the bandwidth of the ultra wideband signal it is possible to reduce the near field effects on the human body surface. Moreover, the original equation was derived for propagation in free space and it is stated in [Fri46] that using the "formula [in] other conditions may require corrections [...] for absorption in the transmission medium" [Fri46].

To correct for the influence of the human tissue in (4.30) the effective phase velocity through multiple layers of tissue will be used. The phase velocity c_i for each layer i can be determined using (4.10). The effective phase velocity c_e through L layers of tissue of thickness d_i can then be computed as

$$c_e = \frac{\sum_{i=1}^{L} d_i}{\sum_{i=1}^{L} \frac{d_i}{c_i}}\,. \tag{4.31}$$

The results of comparing the layer modeling approach to numerical simulations in Section 4.2.4 showed that using (4.30) as an additional frequency dependent loss leads to a good approximation. Moreover, it is shown that using the effective phase velocity c_e in $\mathrm{RL}^{(e)} = \mathrm{RL}(f, d; c_e)$ overestimates the actual path loss and using $\mathrm{RL}^{(0)} = \mathrm{RL}(f, d; c_0)$ underestimates the path loss compared to the numerical wave simulation. Hence, in the following $\mathrm{RL}^{(e)}$ and $\mathrm{RL}^{(0)}$ will be used as upper and lower bounds to determine the communication performance.

4.1.6 The Layer Model

It has been found in an extensive numerical simulation of the actual wave propagation in CST Microwave Studio that it is not sufficient to approximate the in-body to on-body link with just one direct path. The results presented in Section 4.2 show that especially for larger distances between transmitter and receiver a second more dominant indirect path can be observed. This indirect path is made up out of two parts. The first part is the shortest way from the transmitter to the outside of the body and the second part is the path along the body surface to the actual receive antenna. Using the direct and indirect path is still a strong simplification to the real propagation in human tissue, as of course there will be many more paths the wave can travel.

Figure 4.5a depicts one example communication link from a transmit antenna located at $\mathbf{t}_i = [t_x, t_y, t_z]^T$ in the digestive tract to a receive antenna placed at $\mathbf{r}_j = [r_x, r_y, r_z]^T$ on the abdominal surface. Moreover, the two paths and their construction are indicated.

4.1.6.1 The Direct Path

The direct path contains all tissues along the red solid line of the direct connection from $\mathbf{t}_i$ to $\mathbf{r}_j$ in Figure 4.5a. The tissues along the red dotted line are used to determine the wave impedance η_s of the source medium for the direct link. Hence, the transfer function for the direct link is

$$\mathcal{H}^{\text{direct}}_{\mathbf{t}_i \to \mathbf{r}_j}(f; c) = \frac{S^{\text{direct}}_{21}(f)}{\sqrt{\text{RL}(f, d_{\mathbf{t}_i, \mathbf{r}_j}; c)}}\,, \tag{4.32}$$

where $S^{\text{direct}}_{21}(f)$ is the transfer function determined from the multi-layered dielectric of the direct connection between $\mathbf{t}_i$ and $\mathbf{r}_j$ and $\text{RL}(f, d_{\mathbf{t}_i, \mathbf{r}_j}; c)$ is the additional radiation loss introduced in the previous section.

4.1.6.2 The Indirect Path

For the indirect path, first, the closest point on the body surface $\mathbf{m}_i$ with respect to $\mathbf{t}_i$ is determined. Second, the path between $\mathbf{m}_i$ and $\mathbf{r}_j$ is approximated by a circle along the body surface. This circle is constructed from $\mathbf{m}_i$, $\mathbf{r}_j$, and the closest point on the abdominal surface along the perpendicular bisector of the line from $\mathbf{m}_i$ to $\mathbf{r}_j$ (green cross in Figure 4.5a). The tissues along the purple dotted line are

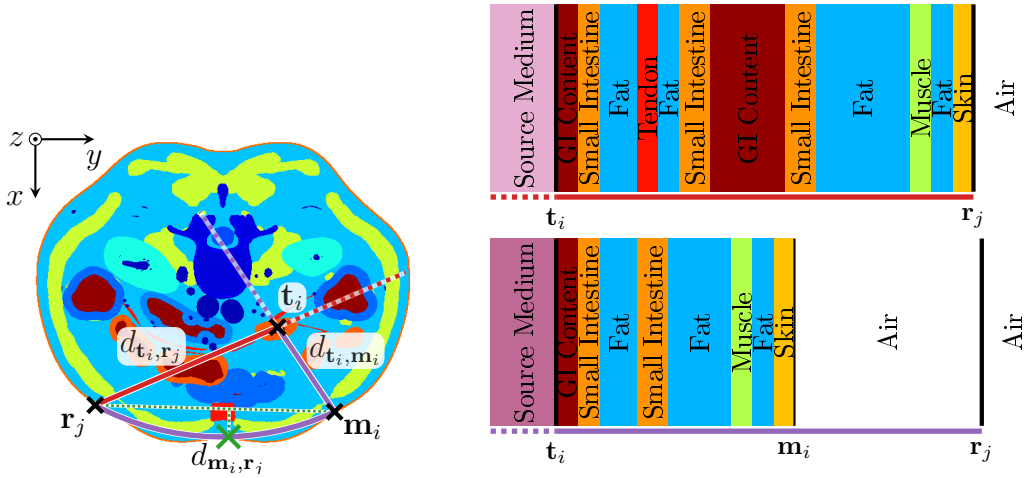

(a) (b)

Figure 4.5: Construction of the layer model. (a) Horizontal slice viewed from top (same as in Figure 4.1). The communication link from $\mathbf{t}_i$ to $\mathbf{r}_j$ is considered. The direct path is colored red and the indirect path purple. The point $\mathbf{m}_i$ is the point on the abdominal surface with shortest distance from $\mathbf{t}_i$. (b) The equivalent multi-layered dielectrics of the direct path (top) and the indirect path (bottom).

used to determine the wave impedance η_s of the source medium for the indirect link. The transfer function $\mathcal{H}^{\text{indirect}}_{\mathbf{t}_i\to\mathbf{r}_j}(f;c)$ of the indirect path is determined from the transfer function $S^{\text{indirect}}_{21}(f)$ of the multi-layered dielectric constructed from the path $\mathbf{t}_i \to \mathbf{m}_i \to \mathbf{r}_j$ and the corresponding radiation losses. For the first part of the propagation from $\mathbf{t}_i \to \mathbf{m}_i$ the radiation loss from (4.30) is applied. For the second part from $\mathbf{m}_i \to \mathbf{r}_j$ the path loss for a wave propagating on the body surface needs to be applied. A path loss model for ultra wideband signals propagating around the body on the surface is published in IEEE 802.15.6 [YS10]. It is defined as

$$\text{PL}_{\text{on}}(d) = 10^{4.46} \cdot \left(\frac{d}{0.1\,\text{m}}\right)^{3.1}, \tag{4.33}$$

where d is the distance measured along the body surface. With this, the transfer function for the indirect path yields

$$\mathcal{H}^{\text{indirect}}_{\mathbf{t}_i\to\mathbf{r}_j}(f;c) = \frac{S^{\text{indirect}}_{21}(f)}{\sqrt{\text{RL}(f, d_{\mathbf{t}_i,\mathbf{m}_i};c)\cdot \text{PL}_{\text{on}}(d_{\mathbf{m}_i,\mathbf{r}_j})}}. \tag{4.34}$$

4.1.6.3 The Overall Transfer Function

The overall transfer function is the sum of the direct and the indirect path. Hence,

$$\mathcal{H}_{\mathbf{t}_i\to\mathbf{r}_j}(f;c) = \mathcal{H}^{\text{direct}}_{\mathbf{t}_i\to\mathbf{r}_j}(f;c) + \mathcal{H}^{\text{indirect}}_{\mathbf{t}_i\to\mathbf{r}_j}(f;c) \tag{4.35}$$

gives the transfer function of the layer model from $\mathbf{t}_i$ to $\mathbf{r}_j$. To distinguish between the two different ways of computing the radiation loss, c may either be set to c_0 or c_e:

- The usage of $\mathcal{H}_{\mathbf{t}_i \to \mathbf{r}_j}(f; c_0)$ indicates that the transfer function is determined using the radiation loss based on the phase velocity in free space. In short, this will be called the *transfer function including free space losses.*
- The usage of $\mathcal{H}_{\mathbf{t}_i \to \mathbf{r}_j}(f; c_e)$ indicates that the transfer function is determined using the radiation loss computed from the effective phase velocity through the tissue layers. In short, this will be called the *transfer function including effective tissue losses.*

The complete Python source code to compute arbitrary layer models is available from [Bru20].

4.2 Validation of the Proposed Model

The goal of this section is to compare the transfer functions determined using the proposed layer modeling approach from the last section to the results of a numerical wave simulation. By using the same digital phantoms in both environments and placing the transmit and receive antennas at the exact same locations the results of both approaches are comparable. The transfer functions will not be identical in a one-to-one comparison, due to the simplifications introduced. However, similar as for well established wireless communication channel models, it is not the target to model every detail of the physical channel. Instead, a channel model is needed which captures the essential characteristics but is simple enough to allow for the design and simulation of the in-body communication system. Hence, the focus is not on comparing the transfer functions individually, rather the most important characteristics that can be derived from the frequency domain and time domain representations will be compared.

In a second step, the proposed layer model will also be compared to the different channel models from literature reviewed in Section 3.4. However, as these channel models are usually based on different assumptions and using different phantoms than our model they are not strictly comparable. Nevertheless, a comparison gives valuable insights about the similarity of the results that are to be expected.

4.2.1 General Setup of the Numerical Wave Simulations

The simulation of the electromagnetic wave propagation was done in CST Microwave Studio [Das20]. This software solves Maxwell's equations in integral form on a discretized grid based on the finite integration technique (FIT), i.e. the solver works on the integral equations in time domain. The algorithm is especially well suited for heterogeneous structures [SHI17]. Most of the simulation results available in literature for in-body propagation are based on this technique, e.g. in [KCL+10], [SCB10b], and [TRY15]. In [TRY15] it has been shown that their simulation using finite integration technique estimates the path loss obtained by measurements accurately. An extensive review of different numerical approaches to solve Maxwell's equations can be found in [SHI17].

For simulations in CST Microwave Studio using the finite integration technique, a short pulse is transmitted from the transmit antenna. Then the distribution of the electromagnetic waves in the simulation domain is determined using the integral form of Maxwell's equation in time domain. The pulse for the simulations in this thesis is selected such that the frequency band from 1 GHz to 6 GHz is covered as this includes the band of interest from 3.1 GHz to 4.8 GHz. The boundary conditions are set to a perfectly matched layer with a reflection coefficient of 10^{-8}. Not all digital phantoms could be considered for complexity reasons. AustinMan 2, AustinWoman 2, Hanako, and Irene are chosen as representatives as their physiological properties are quite different (cf. Table 2.2). To reduce the computational load of the simulation, the phantoms are truncated around the area of interest before being imported into CST Microwave Studio. The slices which have been cut out from the digital phantoms are shown in Figure 4.6 by the dashed black lines. Initial simulations were executed to determine the extent of these slices such that the effect on the scattering parameters is negligible. It was found that a height of the slice in z-direction of 14 cm is sufficient. Additionally, it was found that for AustinMan 2 and AustinWoman 2 it is sufficient to cut off the slice such that there are around 7 cm spacing from the edge of the slice to the next receive antenna on the body surface.

Only dipole antennas are used for the simulation. Details on the antennas are given in the next Section 4.2.2. All antennas are placed in the same xy-plane and oriented in z-direction. Hence, all dipoles are perfectly aligned to each other. In each of the investigated phantoms the xy-plane with the highest number of possible locations for the placement of the transmit dipole is chosen for the simulations. The transmit antenna is placed at $N_{\mathrm{TX}} = 11$ random locations in the small intestine and in the colon. $N_{\mathrm{RX}} = 21$ receive antennas are placed on the abdominal surface

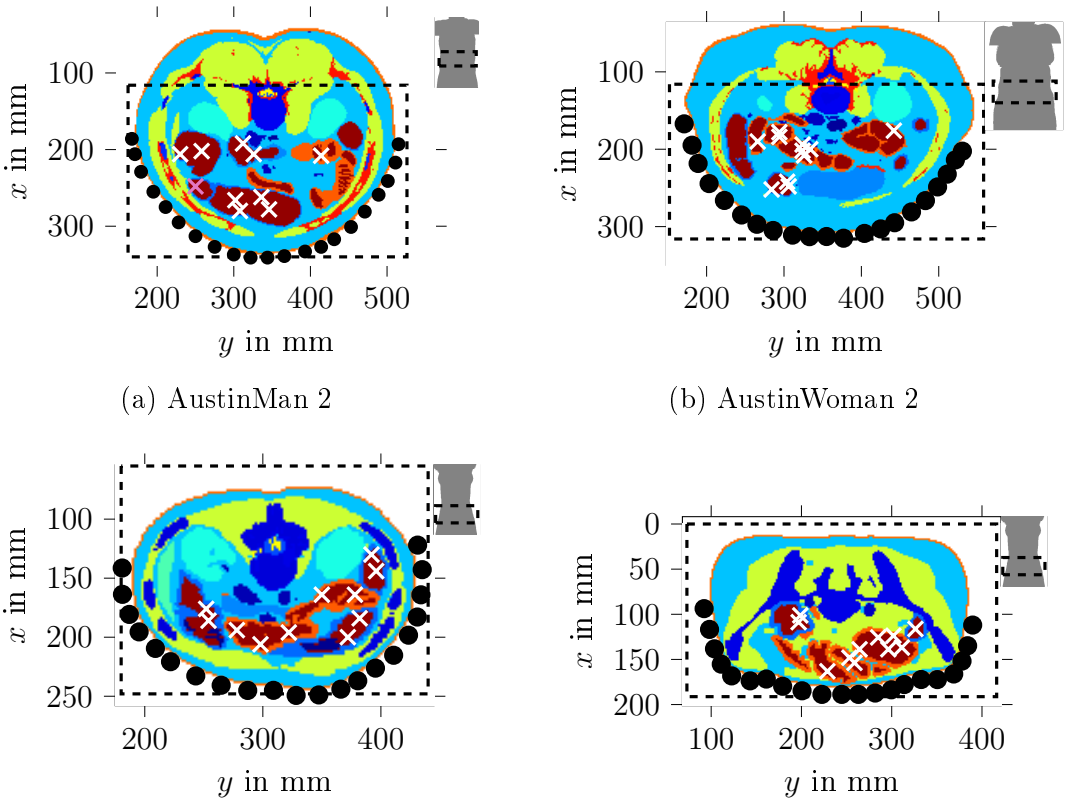

(a) AustinMan 2

(b) AustinWoman 2

(c) Hanako

(d) Irene

Figure 4.6: Setup for the numerical simulations of (a) AustinMan 2, (b) AustinWoman 2, (c) Hanako, and (d) Irene. The dashed black line depicts the border of the slice that has been cut out of the phantom for import into CST Microwave Studio. The crosses denote the locations of the transmit antenna and the black circles the receive antennas. In the top right corner of each plot the digital phantom is shown from the front.

approximately equidistantly. The exact locations of transmit and receive antennas are indicated by crosses and circles, respectively, in Figure 4.6.

Some initial results of this comparison have been published in [BB20] and show a good agreement between the simulation an the layer modeling approach. However, the simulation setup has been improved for this thesis. Especially, the stopping criterion of the finite integration technique (FIT) solver is refined to increase the accuracy. The default stopping criterion of the FIT solver is determined by the remaining overall energy in the simulation domain. The simulations in [BB20] were stopped at an energy decay of 60 dB, i.e. the simulation terminated once the overall energy of the electromagnetic waves in the simulation domain was 60 dB smaller than the maximum value. It was found later that this caused the simulation to stop too early, i.e. before the time domain pulse that was transmitted could be received completely as the attenuation of the tissue is so large. Hence, for the simulations

presented in this thesis, the stopping criterion is refined to take the change of the scattering parameters into account instead. The simulation is stopped when the difference between two consecutive computations of the scattering parameters drops below 0.004.

Moreover, in contrast to the simulation setup described in [BB20], it is made sure here that the transmit antennas are placed more widely and uniformly at random locations in the complete digestive tract and not only near the front of the abdominal wall (cf. Fig. 4 in [BB20]). It will be shown later that the choice of the transmit antenna locations has a huge impact on the channel characteristics.

For each of the $N_{\mathrm{TX}} \cdot N_{\mathrm{RX}} = 231$ communication links simulated in each phantom the transfer functions between transmit and receive antenna $\mathcal{H}^{\mathrm{SIM}}_{\mathbf{t}_i \to \mathbf{r}_j}(f)$ are obtained from the numerical simulation by evaluating the scattering parameters. The same transmit and receive antenna locations are used in the same phantom to determine the transfer function $\mathcal{H}^{\mathrm{LM}}_{\mathbf{t}_i \to \mathbf{r}_j}(f; c)$ from the proposed layer modeling approach for each communication link using (4.35).

To compare the layer modeling approach with the simulation results at first the general wave propagation is investigated on two example communication links in Section 4.2.3. In a second step the statistical properties of the two modeling approaches are compared.

4.2.2 Antenna Design

To simulate the scattering parameters between two ports in CST Microwave studio, at each port an antenna has to be designed. For the layer modeling approach it is assumed – by introducing the radiation loss in (4.30) – that the transmit and the receive antennas are isotropic antennas. To rebuild this scenario as close as possible, in the numerical simulations dipole antennas are used, as they exhibit a quasi-isotropic radiation pattern in the plane perpendicular to the antenna elements. The following antenna characteristics were published already in [BB20].

The transmit antenna is placed in the gastrointestinal tract. As there is a great difference between the relative permittivity of the content of the gastrointestinal tract to the relative permittivity in air, the antenna has to be designed specifically for placement inside the digestive tract. Based on the information from [SAW12a] on using a dipole for simulations in the UWB frequency range, the transmit antenna is optimized to radiate efficiently in the gastrointestinal tract. It was found that a dipole with a length of 8.5 mm, a radius of 57.2 µm, and a dielectric coating

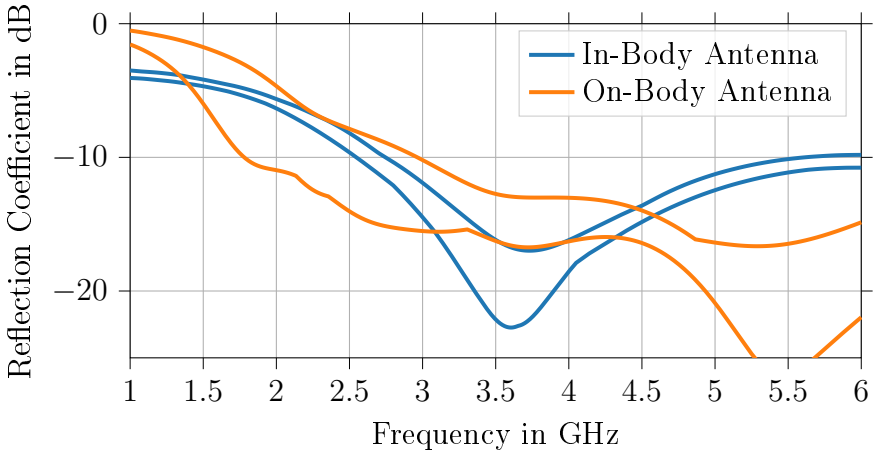

Figure 4.7: The upper and lower bound of the reflection coefficient of the in-body and on-body antennas over all possible locations.

of 10 µm thickness with relative permittivity $\varepsilon_r = 10$ achieves good propagation characteristics. The dimensions of the antenna are chosen for transmission in the frequency range of 3.1 GHz to 4.8 GHz. As the surrounding tissue changes also the reflection coefficient changes depending on the exact location inside the body. The upper and lower bound of the reflection coefficient for the in-body antenna over all possible locations are shown in Figure 4.7.

Due to the placement on the abdominal surface, the on-body antenna has different parameters. The length is set to 33.73 mm and the radius is determined to be 3.73 mm. These dimensions are optimized such that the reflection coefficient is smaller than −10 dB for frequencies between 3.1 GHz to 4.8 GHz in free space. However, the antenna characteristics change due to the placement in close proximity to the human body. But still, the reflection coefficient is smaller than −10 dB in the relevant frequency range as can be seen from Figure 4.7. Figure 4.7 shows the upper and lower bound of the reflection coefficient for the on-body antenna over all possible locations.

4.2.3 Exemplary Analysis of the Wave Propagation

Before any comparison of the statistical properties between the layer modeling approach and the numerical simulations can be made, the wave propagation mechanisms in the human body have to be investigated in more detail to understand the underlying mechanisms. To determine how the transmitted power is distributed in space, the power flow monitor of CST Microwave Studio is utilized. A transmit antenna is placed at the pink cross indicated in Figure 4.6a. The resulting output of

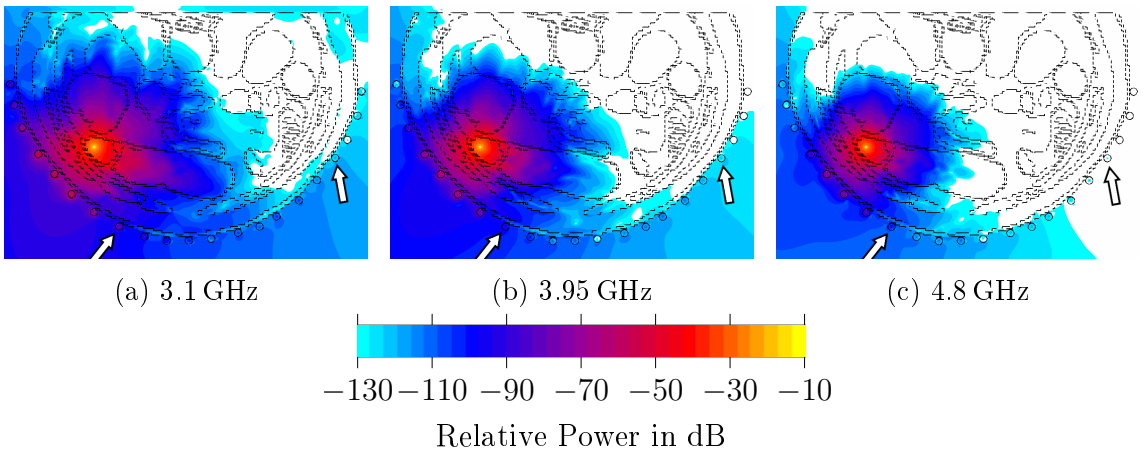

Figure 4.8: The power flow for 3.1 GHz, 3.95 GHz and 4.8 GHz inside AustinMan 2 simulated in CST Microwave Studio. The transmit antenna is placed at the bright yellow spot. Values smaller than −130 dB are colored in white. The receive antennas on the abdominal surface are marked by black circles. The two arrows indicate the receive antennas that are used for comparison of the transfer functions in Figure 4.9.

the power flow monitor for three selected frequencies is shown in Figure 4.8. There the transmit antenna location can be identified by the bright yellow spot. The power flow monitor records the peak power at every spatial point within the simulation time, which is shown color coded in Figure 4.8. All white colored areas correspond to a power level smaller than −130 dB relative to the maximum occurring power. The black lines indicate the outline of the phantom and its inner organs. The receive antennas on the abdominal surface are marked by black circles. It can be seen that the receive antennas that are further away receive only a small amount of the transmitted power. Moreover, the blue shaded area around the abdominal surface indicates, that the wave that arrives at these far-away receive antennas actually travels as a surface wave on the body surface and partially through the fat layer beneath the skin. For example, for the antenna indicated by the right arrow in Figure 4.8b the relative power is larger than −130 dB. However, the only possible way how the wave travels to that location is around the body on the outside as the attenuation inside the body is even higher. Parts of the wave also travel directly under the skin in the outermost fat layer. This is in line with observations from [SPB+19] and [JKK+10].

In Figure 4.9 the magnitude response and the group delay to two of the receive antennas (indicated by the arrows in Figure 4.8) are shown. The group delay is shown instead of the phase response for easier comparison and to better understand the propagation mechanisms. For each of the two communication links the transfer functions from simulations in CST and from the direct and indirect paths using the

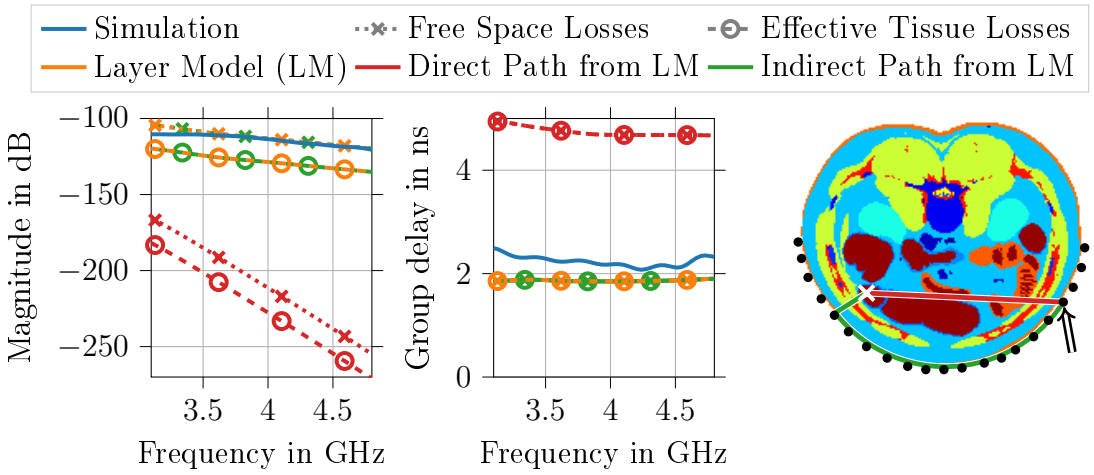

(a) Example of a communication link with a long distance between TX and RX antenna.

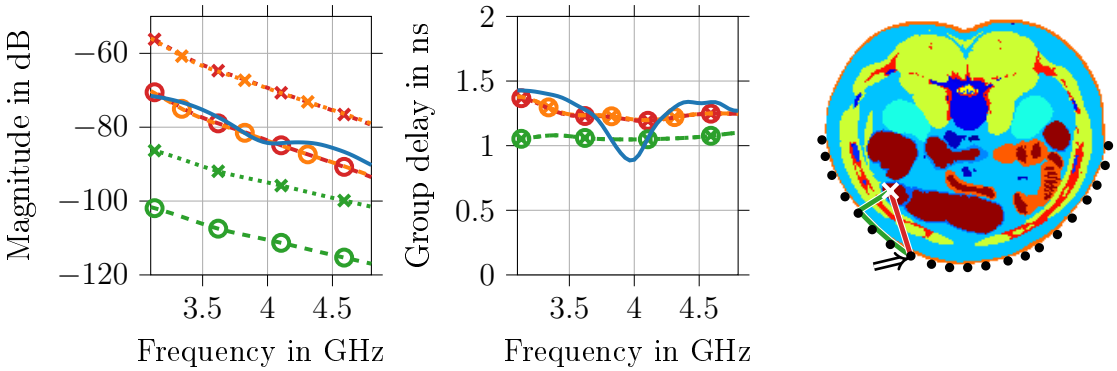

(b) Example of a communication link with a short distance between TX and RX antenna.

Figure 4.9: The magnitude and the group delay of the transfer functions of two example communication links inside AustinMan 2. The TX antenna is marked with a white cross and the RX antenna with an arrow in the rightmost plot. The transfer functions including free space losses are marked with crosses and the ones including effective tissue losses with circles.

layer modeling approach are shown. Moreover, the total transfer function of the layer model, i.e. the sum of the two paths is depicted. The transfer functions based on the layer modeling approach are either including free space losses or effective tissue losses as discussed in Section 4.1.5. The rightmost drawing in the Figures 4.9a and 4.9b shows the spatial setup of the two communication links – the direct path in red and the indirect in green.

It can be seen in Figure 4.9a that for the rather long communication link the magnitude and the group delay of the transfer function of the indirect path are matching very well to the result from the numerical simulation. The transfer function of the direct path largely overestimates the real path loss between the two antennas and

the group delay is more than twice as high. Due to this, the sum of the direct path and indirect path transfer functions is nearly identical to the transfer function of the indirect path. Moreover, it can be seen that using the transfer function including free space losses approximates the transfer function resulting from the numerical simulation very well. Whereas using the transfer function including effective tissue losses, the attenuation is overestimated by approximately 15 dB.

For the shorter communication link in Figure 4.9b the direct path estimates the magnitude and the group delay of the simulation very well. The indirect path has a much higher path loss than the direct path. In this case the sum of the direct and indirect transfer functions is nearly identical to the transfer function of the direct path. Furthermore, it can be seen that the magnitude response including free space losses has a magnitude which is approximately 15 dB larger than the magnitude response from simulation. Whereas, the transfer function including effective tissue losses gives a precise approximation of the transfer function from simulation.

These two examples show that the transfer function can indeed be approximated by the sum of the direct and indirect path. It was tested for the indirect path not to use the shortest path out of the body but instead that with the lowest attenuation. However, it turned out that the resulting transfer functions were very similar to the ones determined by just selecting the shortest path. Hence, the much less complex approach by using the shortest path was kept.

In case of the shorter communication link in Figure 4.9b, using the transfer function including free space losses gives a good approximation. Whereas for the farther receive antenna in Figure 4.9a, the transfer function including effective tissue losses gives a better approximation. Further investigations could not show any general rule in which case using free space losses gives a better approximation than using effective tissue losses. Hence, both values will be used for analysis in the following. By comparing different communication links, it was found that the transfer functions will not in all cases be as well-approximated as for these two examples above. Nevertheless, it will be shown in the following sections that the properties of the transfer functions and impulse responses are estimated very accurately by the proposed layer modeling approach.

4.2.4 Comparison of the Transfer Function Properties

In this section the comparison of the previous section is extended to all 231 communication links under investigation in all four digital phantoms. In the following, the path loss, the correlation of the transfer functions, and the power delay profile will be compared.

4.2.4.1 Path Loss

To compute the path loss, it is assumed that the transmit power spectral density $S_{xx}(f)$ is constant in the frequency range from 3.1 GHz to 4.8 GHz. Thus, the path loss $\mathrm{PL}_{\mathbf{t}_i \to \mathbf{r}_j}$ between transmitter $\mathbf{t}_i$ and receiver $\mathbf{r}_j$ can be determined from the transfer function as

$$\mathrm{PL}_{\mathbf{t}_i \to \mathbf{r}_j}(f_L, f_U) = \frac{f_U - f_L}{\int_{f_L}^{f_U} \left| \mathcal{H}_{\mathbf{t}_i \to \mathbf{r}_j}(f; c) \right|^2 \mathrm{d}f}, \tag{4.36}$$

where $f_L = 3.1\,\mathrm{GHz}$ and $f_U = 4.8\,\mathrm{GHz}$. The argument of $\mathrm{PL}_{\mathbf{t}_i \to \mathbf{r}_j}(f_L, f_U)$ will be omitted in the following if it is clear from the context which two frequencies are used. The path loss computed from the transfer functions resulting from numerical simulations is denoted as $\mathrm{PL}^{\mathrm{SIM}}_{\mathbf{t}_i \to \mathbf{r}_j}$ and the path loss using the layer modeling approach as $\mathrm{PL}^{\mathrm{LM}}_{\mathbf{t}_i \to \mathbf{r}_j}$.

In Figure 4.10 these path loss values are shown in a scatter plot to visualize their similarity. As mentioned in the last section, it is unclear if applying free space losses or effective tissue losses to the transfer function is more suitable. Hence, both are compared in a single plot to determine their correlation. The orange dots in Figure 4.10 show the path loss of the layer modeling approach including free space losses. Whereas, the green dots show the path loss of the layer modeling approach including effective tissue losses. The black line shows the ideal model with a perfect match of the resulting path loss. Hence, all results that are above that line are underestimating the path loss compared to the numerical simulation and all results that are below the line are overestimating the path loss. The legend of Figure 4.10 also shows the correlation ρ of the respective path loss values. It can be seen from the Figure that in general there is a high correlation between the path loss determined from the layer modeling approach to the path loss determined from the numerical simulation. The correlation is at least 0.84 in case of AustinWoman 2 and goes up to 0.95 for Irene and Hanako. For AustinMan 2, Hanako, and Irene it is clear from the plot that using additional free space losses gives a lower bound on the path loss and

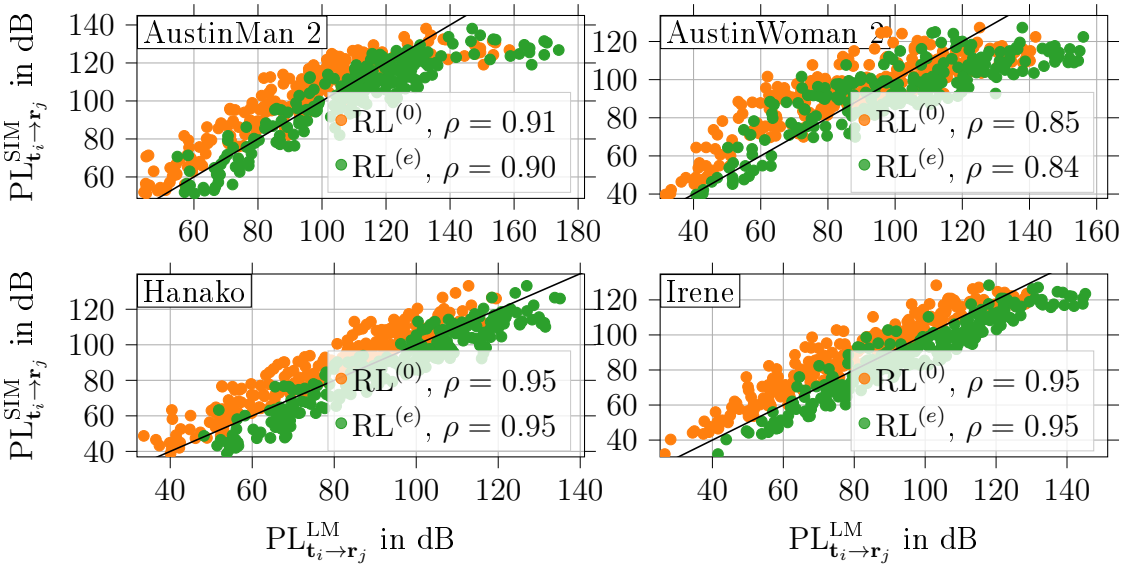

Figure 4.10: The path loss from the numerical simulations $\mathrm{PL}^{\mathrm{SIM}}_{\mathbf{t}_i \to \mathbf{r}_j}$ vs. the path loss from the layer modeling approach $\mathrm{PL}^{\mathrm{LM}}_{\mathbf{t}_i \to \mathbf{r}_j}$. The radiation loss is either computed using free space loss $\mathrm{RL}^{(0)}$ or effective tissue loss $\mathrm{RL}^{(e)}$. The correlation ρ of the path loss values is given in the legend. The black line shows the ideal case for a correlation of $\rho = 1$.

using effective tissue losses yields an upper bound. In the case of AustinWoman 2 there is still a tendency of the green dots being below the line and the orange ones above. However, the black line does not separate the two cases as well as in the other three plots of AustinMan 2, Irene, and Hanako. It was also tested if the effective tissue losses and free space losses could be combined for a better agreement with the simulation results. However, no solution could be found that is based on reasonable theoretic assumptions. Thus, in the following both approaches will be used. It can be concluded that transfer functions including free space losses tend to underestimate the path loss compared to numerical wave simulations and the effective tissue losses tend to overestimate the path loss.

4.2.4.2 Correlation of Transfer Functions

As it has been shown in the last section, the path loss can be well approximated by the layer modeling approach. Due to the frequency selective nature of the channel transfer function, not only the path loss is of interest but also how well the frequency dependency is recreated by the layer modeling approach. This similarity of the frequency dependency between the transfer functions from the two approaches will be determined by the correlation of the transfer functions. The correlation

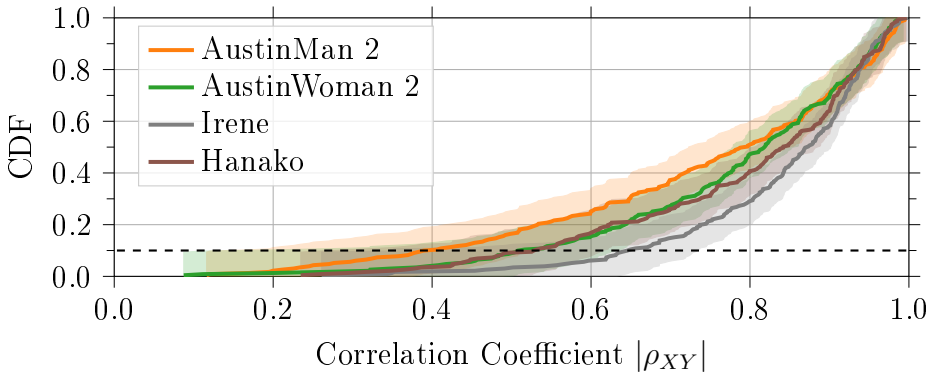

Figure 4.11: The empirical cumulative distribution function (CDF) of the magnitude of the correlation coefficient of the transfer functions. The dashed black line indicates the 10^{th} percentile. The 95 % confidence interval of the empirical cumulative distribution function (CDF) is indicated by the light-colored area.

between two complex functions is determined by the magnitude of the complex correlation coefficient ρ_{XY}. For more details on the correlation of complex data see Appendix B.1 and [SS10]. The correlation coefficient ρ_{XY} is computed for all 231 transfer functions of each phantom by setting $X = \mathcal{H}^{\text{SIM}}_{\mathbf{t}_i \to \mathbf{r}_j}(f)$ and $Y = \mathcal{H}^{\text{LM}}_{\mathbf{t}_i \to \mathbf{r}_j}(f; c)$. It was found that the choice of the radiation loss, using either free space losses or effective tissue losses, has no observable influence on the correlation of the transfer functions.

Figure 4.11 shows the empirical cumulative distribution function (CDF) of $|\rho_{XY}|$ with the corresponding 95 % confidence interval. The confidence interval is computed based on the Dvoretzky-Kiefer-Wolfowitz inequality which is described in more detail in Appendix B.2. It can be seen that there is a high correlation between the transfer functions for all models. Although, due to the small sample size, the 95 % confidence interval is quite large. Only for AustinMan 2 the correlation is significantly worse compared to the other curves. However, $|\rho_{X,Y}|$ is still larger than 0.39 in 90 % of all cases. For AustinWoman 2, Hanako, and Irene the correlation coeffcient is larger than 0.51, 0.53, and 0.65 in 90 % of all cases, respectively. Hence, it can be concluded that there is a high correlation between the transfer functions for most of the communication links and the frequency dependency of both modeling approaches is similar.

4.2.4.3 Power Delay Profile

A commonly used measure to compare channel models is to compare their power delay profile (PDP). The power delay profile of a channel with impulse response

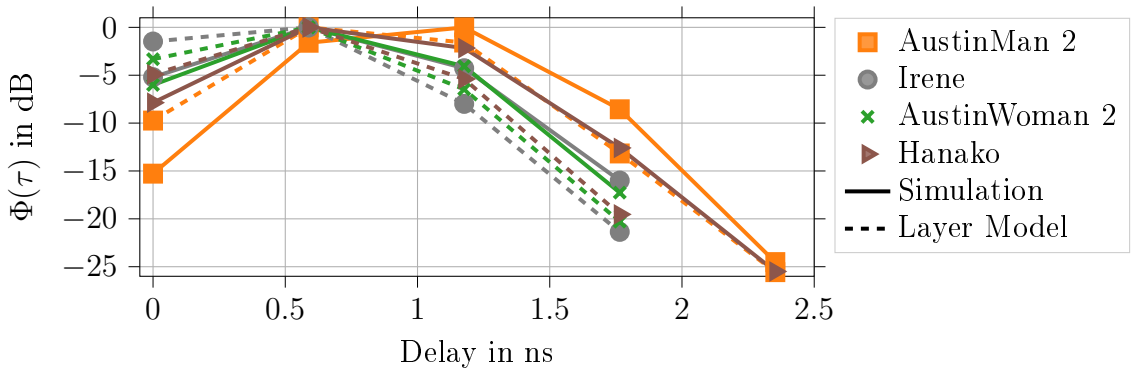

Figure 4.12: The power delay profile $\Phi(\tau)$ resulting from the layer modeling approach and the numerical simulations.

$h(\tau)$ is defined as

$$\Phi(\tau) = \mathrm{E}\left\{\left|h(\tau)\right|^2\right\}, \tag{4.37}$$

where the expectation operation $\mathrm{E}\{\cdot\}$ is taken over all channel realizations. From the power delay profile the mean delay $\bar{\tau}$ and the root mean square (RMS) delay spread τ_{rms} can be determined as

$$\bar{\tau} = \frac{\int_0^\infty \tau \cdot \Phi(\tau)\,\mathrm{d}\tau}{\int_0^\infty \Phi(\tau)\,\mathrm{d}\tau} \tag{4.38}$$

and

$$\tau_{\mathrm{rms}} = \sqrt{\frac{\int_0^\infty (\tau-\bar{\tau})^2 \cdot \Phi(\tau)\,\mathrm{d}\tau}{\int_0^\infty \Phi(\tau)\,\mathrm{d}\tau}}, \tag{4.39}$$

respectively.

The power delay profiles resulting from the numerical simulation and the layer modeling approach are compared in Figure 4.12 for the four digital phantoms. They are computed using (4.37) from the sampled impulse responses $h[n]$. The resulting power delay profile is truncated at a relative power level of $-30\,\mathrm{dB}$. The sampled impulse response $h[n] = h(\tau = nT_s))$ is determined by computing the inverse discrete Fourier transform of the downconverted and bandlimited transfer function in the frequency range from 3.1 GHz to 4.8 GHz, where the sampling period is set to

$$T_s = \frac{1}{B} = \frac{1}{1.7\,\mathrm{GHz}} = 0.588\,\mathrm{ns}\,. \tag{4.40}$$

For the bandlimitation a rectangular filter of bandwidth B is applied before downconversion as at this stage no knowledge about the transmission scheme should be included in the computation. It was found that the choice of the radiation loss has

Table 4.1: Mean delay and RMS delay spread from numerical simulations (SIM) and the layer modeling approach (LM).

Phantom	τ_{rms}		$\bar{\tau}$	
	SIM	LM	SIM	LM
AustinMan 2	0.37 ns	0.35 ns	0.99 ns	0.83 ns
AustinWoman 2	0.34 ns	0.34 ns	0.70 ns	0.59 ns
Hanako	0.37 ns	0.33 ns	0.80 ns	0.64 ns
Irene	0.35 ns	0.34 ns	0.68 ns	0.51 ns

no significant influence on the power delay profile. The resulting values of the mean delay $\bar{\tau}$ and the RMS delay spread τ_{rms} can be found in Table 4.1. It can be seen from Figure 4.12 that there are differences between the power delay profiles computed from simulation and the ones from the layer modeling approach. Especially for AustinMan 2, the difference between layer modeling approach and simulation is clearly visible. This might be related to the lower correlation between the transfer functions of the two approaches found in the previous section. However, the general trend is the same for both approaches. Moreover, the RMS delay spread is nearly identical for both approaches for all four digital phantoms.

4.3 Channel Characteristics

After deriving the layer modeling technique and validating it with appropriate numerical simulations in the previous section, in this section the characteristics of the propagation will be investigated. First, the basic propagation properties through a single layer of human tissue are analyzed. Secondly, it is explored how the path loss, the power delay profile and the correlation between communication links behave for the different digital human phantoms. Finally, the resulting path loss models will be compared to the channel models from literature which were presented in Section 3.4.

4.3.1 Transmission Behavior in Single Human Tissues

In this section the propagation of a plane wave through an infinitely extended tissue layer in x, y, and z direction is considered. This is done to investigate basic propagation parameters like the attenuation and speed of light inside human tissue.

Figure 4.13a shows the path loss of the eleven most common tissue types in the abdomen of all of the investigated human phantoms for a sinusoidal wave at 4 GHz.

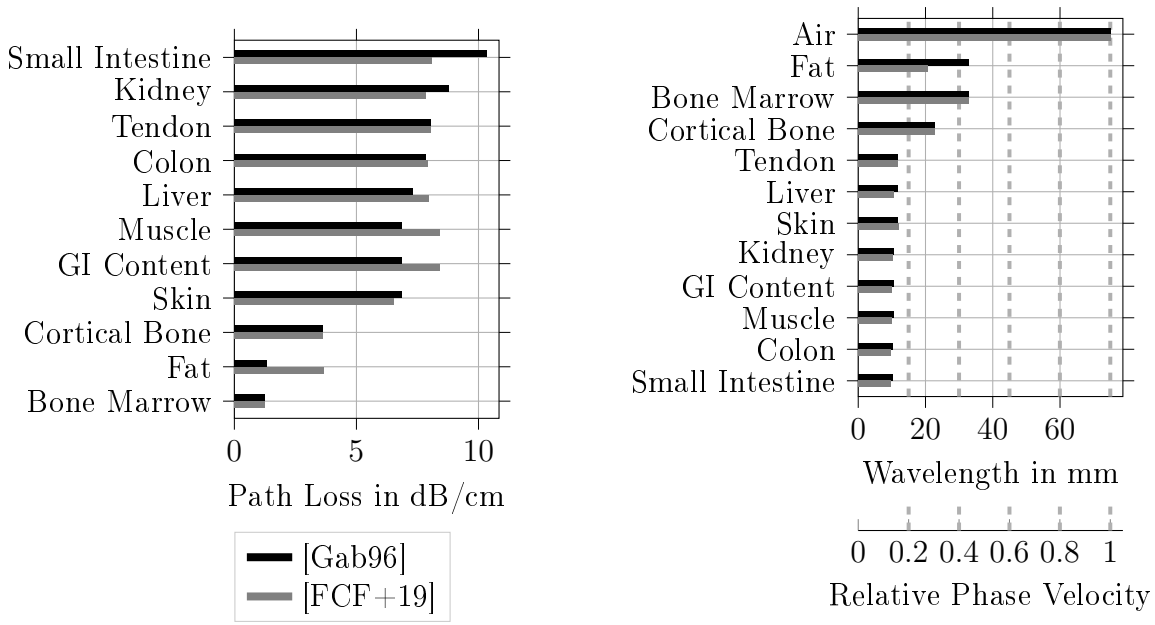

(a) Path loss in dB per cm

(b) Wavelength and rel. phase velocity

Figure 4.13: Properties of the most common tissue types in the abdomen for a sinusoidal wave with a frequency of 4 GHz.

The most common tissues are determined from Figure 2.2. It can be seen that there are huge variations from 1.26 dB/cm up to 10.32 dB/cm. Moreover, for some tissues the path loss per cm differs largely depending on the source of the dielectric properties. Bars in black show the path loss using the dielectric properties from Gabriel *et al.* [Gab96] and the ones in gray the results using the dielectric properties from Fornes-Leal *et al.* [FCF+19]. How these different values for the dielectric properties are obtained was discussed in Section 2.1. The most important differences between the properties refer to muscle and fat. Based on the measurements from [FCF+19] the path loss in dB in fat is 2.7 times as large as using Gabriels results. Furthermore, for muscle tissue the path loss in dB is larger by a factor of 1.2. Nevertheless, the results from [FCF+19] also show smaller path loss values for some tissues, e.g. for small intestine and kidney. However, as muscle and fat are by far the most dominant tissue types in the abdomen, it is expected that also the resulting performance of the communication is severely effected by this uncertainty of the dielectric properties. The influence on the channel capacity will be investigated further in Section 5.4.

The wavelength also varies inside the different tissues. This is shown in Figure 4.13b. The wavelength varies from 11.28 mm in muscle up to 34.83 mm in fat for a sinusoidal wave at 4 GHz. In air the wavelength at the same frequency is 74.95 mm. Thus, the wavelength in human tissue is smaller by a factor of 2 up to 6.6. In Figure 4.13b

Table 4.2: The number of transmit antenna locations N_{TX} in the digestive tract and the maximum possible number of receive antennas $N_{\mathrm{RX,max}}$ for each digital Phantom.

Model	N_{TX}	$N_{\mathrm{RX,max}}$	Model	N_{TX}	$N_{\mathrm{RX,max}}$
Alvar	2000	135	Golem	1048	152
AustinMan 1	2000	162	Hanako	2000	137
AustinMan 2	2000	156	Helga	1567	205
AustinWoman 1	2000	152	Irene	1685	115
AustinWoman 2	2000	147	Taro	2000	109
Donna	781	160	VisibleHuman	2000	203

also the phase velocity relative to the phase velocity in free space is shown. There is a reduction of the phase velocity inside muscle tissue to 15 % of the value in air. The tissue with the largest phase velocity is fat with 46 % of the speed of light in air. Despite of fat, the wavelength or phase velocity does only change a little when comparing the two different sources for the dielectric properties.

4.3.2 Transmission in Digital Human Phantoms

The digital human phantoms that are investigated in this thesis were presented in Section 2.4. For a proper analysis of all of them, in the following up to $N_{\mathrm{TX}} = 2000$ transmitter locations $\mathbf{t}_i$ in the digestive tract are drawn randomly. It is made sure that the distance between the locations is at least 4 mm. Due to the different resolutions of the voxel models and deviating physiological conditions, the actual number of possible transmit antenna locations in the digestive tract varies between 781 to 2000. Details are listed in Table 4.2. The receive antennas should only be placed on the abdominal surface. Placing antennas on the back or on the side of a patient will not be considered, as the distance to the digestive system is then much higher than to the front of the body.

For each phantom the abdominal area, where possible receive antennas can be placed, is identified individually. These areas are indicated in gray in Figure 4.14. The surface of all of the phantoms is discretized to account for a certain physical size of the receive antennas. There is a multitude of studies on the design of ultra wideband on-body antennas and their dimensions vary a lot. In [AGF+17] and [BMA+16] planar antennas with outer dimensions of approximately 3 cm × 3 cm were developed. Whereas in [AKC+14] and [KSK+19] antennas with outer dimensions in the range of 10 cm × 10 cm are proposed. In this work we chose the grid size to be approximately 3 cm × 3 cm to allow for a finer placement of the receive

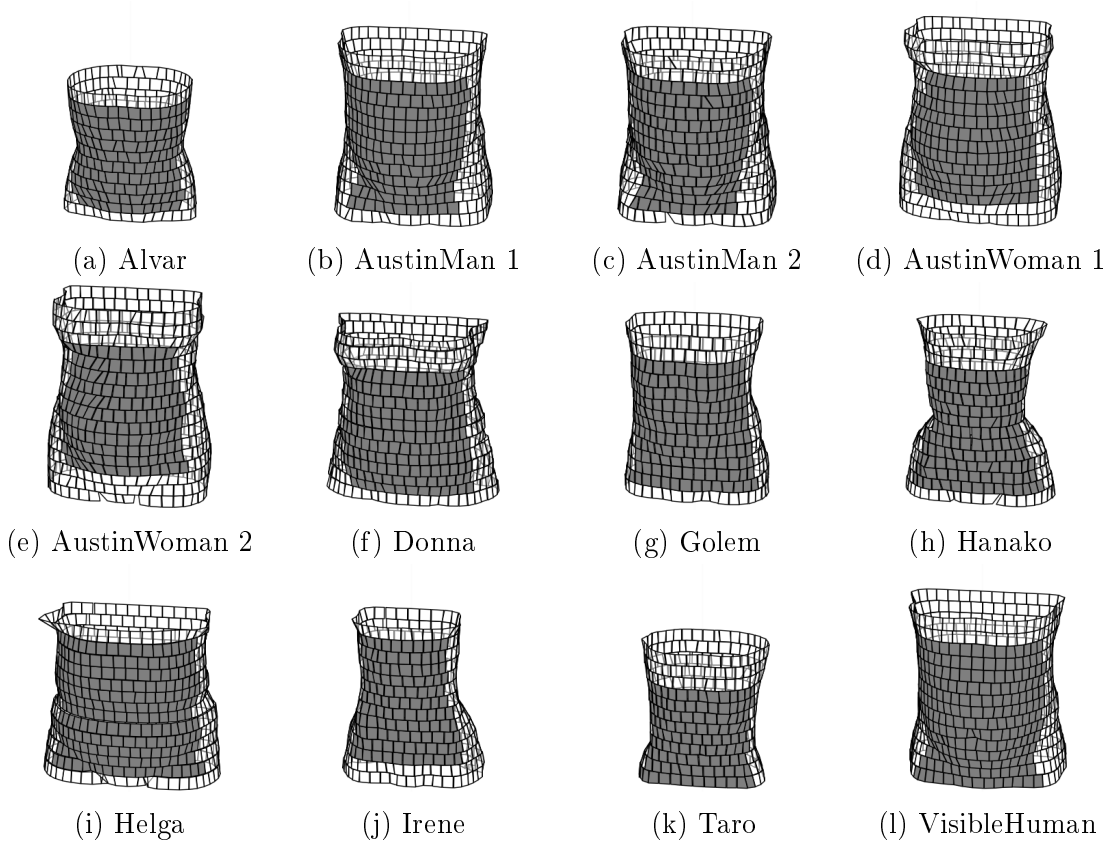

(a) Alvar (b) AustinMan 1 (c) AustinMan 2 (d) AustinWoman 1

(e) AustinWoman 2 (f) Donna (g) Golem (h) Hanako

(i) Helga (j) Irene (k) Taro (l) VisibleHuman

Figure 4.14: The discretized skin layer of all the digital phantoms from Table 2.1. Indicated in gray is the area on the abdomen that is considered for placing possible receive antennas.

antennas. With this discretization, a receive antenna could be placed on one of 109 to 205 possible locations, depending on the physiology of the phantom.

All following results in this Section include all possible communication links, i.e. one receive antenna is placed at an arbitrary location on the abdomen and the transmit antenna is placed at any position in the digestive tract. For each possible communication link $\mathbf{t}_i \rightarrow \mathbf{r}_j$ the transfer function $\mathcal{H}_{\mathbf{t}_i \rightarrow \mathbf{r}_j}(f; c)$ will be computed using (4.35). The path loss and the power delay profile will be computed for different frequency bands in the ultra wideband low band from 3.1 GHz to 4.8 GHz. The channel allocation is made based on the specifications for ultra wideband communication in IEEE 802.15.4 and IEEE 802.15.6 shown in Table 3.2, which is replicated as Table 4.3 with the addition of channel number 5 covering the complete bandwidth from 3.1 GHz to 4.8 GHz.

Table 4.3: Ultra wideband channel allocation used for channel characterization. Based on the allocation from IEEE 802.15.4 [Ins20] and IEEE 802.15.6 [Ins12].

Channel No.	Center frequency f_c	Bandwidth
1	3494.4 MHz	500 MHz
2	3993.6 MHz	500 MHz
3	4492.8 MHz	500 MHz
4	3993.6 MHz	1331.2 MHz
5	3950.0 MHz	1700.0 MHz

4.3.2.1 Path Loss Model

The path loss $\mathrm{PL}_{\mathbf{t}_i \to \mathbf{r}_j}(f_L, f_U)$ of the communication links will be computed using (4.36). This equation assumes a constant transmit power spectral density $S_{xx}(f)$ in the frequency range from f_L to f_U. The resulting path loss for AustinMan 2 using the radiation loss in free space is plotted in Figure 4.15. Each dot represents the value of the path loss for one communication link $\mathbf{t}_i \to \mathbf{r}_j$ and the black line is a logarithmic fit through these values.

Path loss models usually follow a logarithmic or exponential behavior over the distance. The corresponding equations (3.3) and (3.4) were already introduced in Section 3.4. It was found that a logarithmic path loss model as described in (3.3) yields a better fit than an exponential or linear model as described in (3.4). The logarithmic path loss model used for fitting is

$$\mathrm{PL}_{dB}(d) = \mathrm{PL}_0 + 10 \cdot n \log_{10}\left(\frac{d}{d_0}\right), \tag{4.41}$$

where PL_0 is the path loss in dB at the reference distance $d_0 = 5\,\mathrm{cm}$, n is the path loss exponent, and d is the distance between transmit and receive antenna. As can be seen from Figure 4.15 there is a large amount of variation around the fitted path loss model. This was also observed in initial investigations published in [BB17c].

The path loss model (4.41) is fitted to the path loss data from all digital human phantoms using the radiation loss in free space and in the effective tissue. The parameters of the fitting functions are obtained by non-linear least squares minimization based on the Levenberg-Marquardt algorithm using the Python library lmfit [NON+20]. All resulting fitting parameters are summarized in Table C.1 in Appendix C. Figure 4.16 shows the values of PL_0 and n for all the digital phantoms for the 5 different channels from Table 4.3 including free space losses. It can be seen that both parameters differ largely between the different phantoms. For

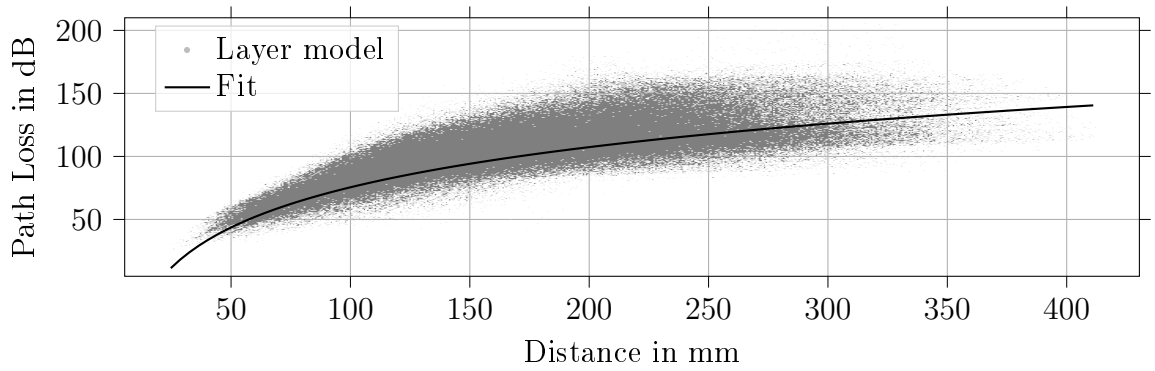

Figure 4.15: The path loss from the layer modeling approach for AustinMan 2. The transfer function is computed including free space losses.

Taro, PL_0 is in the range of 56.4 dB to 70.8 dB and for Helga it is between 28.9 dB to 46.9 dB. Thus, depending on the channel index, the difference of PL_0 between Taro and Helga, which have the highest and lowest values of PL_0, respectively, is 24 dB to 28 dB. The values of PL_0 for AustinMan 1 and AustinMan 2 differ by only around 1.3 dB. And the same holds for AustinWoman 1 and AustinWoman 2 approximately. Moreover, the path loss at reference distance PL_0 shows a strong dependence on frequency. It increases from channel 1 to channel 3 as the center frequency increases. For channel 4 the center frequency remains the same as for channel 2. However, the bandwidth is increased. Hence, also smaller frequencies are included and PL_0 gets smaller than in the case of channel 2 as also the band of channel 1 is included. Channel 5 consists of the complete band from 3.1 GHz to 4.8 GHz. Thus, the average path loss decreases compared to channel 4 again as lower frequencies are included in the computation.

Looking at the path loss exponent n in the lower part of Figure 4.16, it can be seen that Helga has the largest value n of 11.8 dB to 12 dB and Irene has the smallest values of n in range of 7.2 dB to 7.4 dB. Hence, the difference between the smallest and the largest path loss exponent is approximately 4.6 dB. The path loss exponent of AustinMan 1 and AustinMan 2 are nearly identical. For AustinWoman 1 and AustinWoman 2 there is a maximum difference of 0.5 dB for channel 3. The path loss exponent n shows only a small dependence on the frequency. For Hanako the largest difference of 0.4 dB can be observed between channel 1 and channel 3. For all other phantoms it shows nearly no dependency on the frequency.

Comparing the path loss model parameters of the different digital phantoms it can be concluded that there are large variations because of the different physiological properties of the underlying human body. Furthermore, the phantoms that are

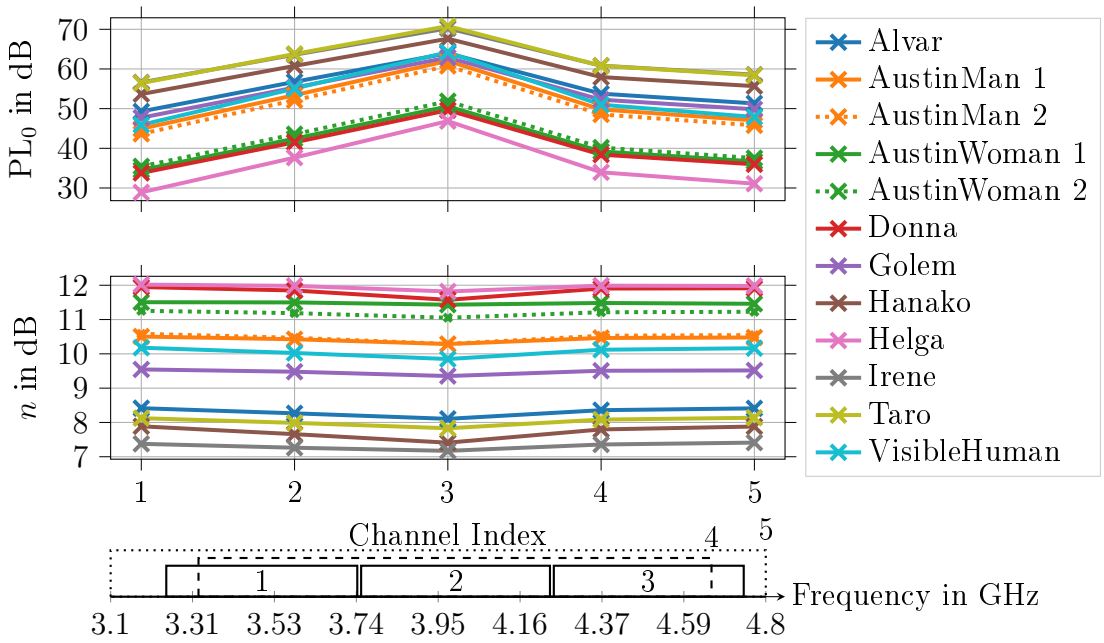

Figure 4.16: The path loss model parameters for the digital phantoms based on the transfer function including free space losses. The lower most plot visualizes the frequency bands corresponding to the channel indices from Table 4.3.

based on the same human body, e.g. AustinMan 1 and AustinMan 2, show only a very small difference in path loss modeling parameters.

Up to now, only the path loss model including free space losses was considered. However, there will be an increase in path loss if the transfer function is computed including effective tissue losses instead of free space losses. This increase is shown in Figure 4.17. There, it can be seen that the path loss increases by around 12.5 dB for Donna and by up to 15.8 dB for Irene. However, for most of the phantoms the increase is smaller than 14.3 dB. Moreover, the effect of the radiation loss on PL_0 is nearly constant for the different UWB channels. One reason to explain the large difference of Irene to the other phantoms is that Irene contains much more muscle tissue in the abdomen than all the other phantoms (see Table 2.2). Hence, there is a high concentration of tissue with a relatively low phase velocity (see Figure 4.13b). As the effective tissue losses are computed based on the phase velocity inside the tissue (see Section 4.1.5), the path loss inside Irene is increasing more than for the other phantoms. Finally, it can be seen from the lower plot in Figure 4.17 that the path loss exponent n does not substantially change whether free space losses or effective tissue losses are included.

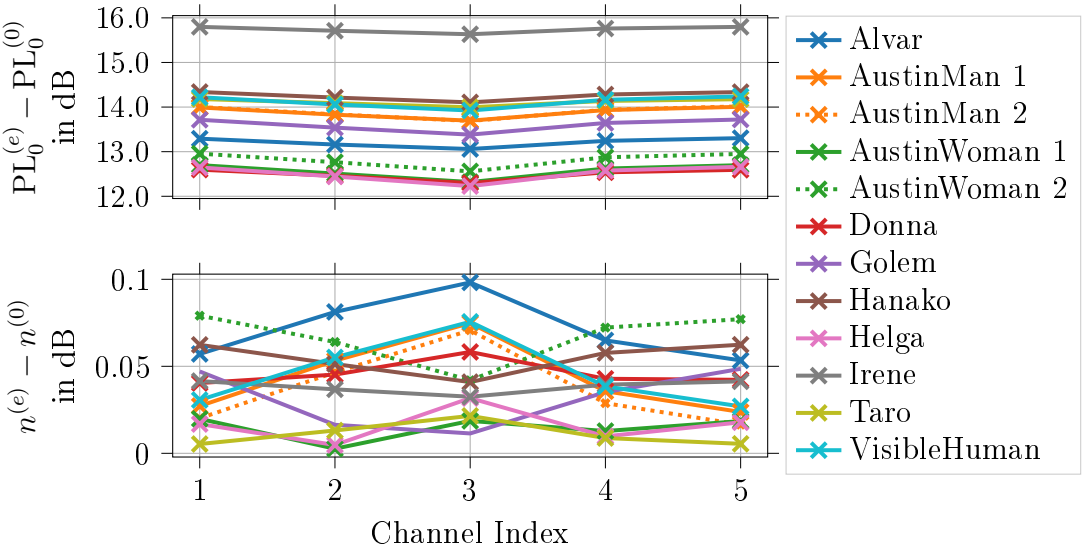

Figure 4.17: The difference in PL_0 (top) and path loss exponent n (bottom) when using free space losses (0) compared to effective tissue losses (e). The frequency bands for the channel indices are visualized in Figure 4.16.

4.3.2.2 Power Delay Profiles

The power delay profiles of the different communication channels in all of the digital human phantoms are computed as described in Section 4.2.4 using (4.37). Only the bandwidth and the center frequency for the downconversion are adjusted according to the specific UWB channel defined in Table 4.3. This means the sampling rate for channels 1 to 3 is 500 MHz, for channel 4 it is 1.33 GHz and for channel 5 it is 1.7 GHz. The power delay profiles are truncated at a relative power level of −30 dB.

Figure 4.18 shows the power delay profiles of UWB channel 1 and channel 5. It can be seen from the upper plot in Figure 4.18 that there are only minor differences in-between the power delay profiles of the digital phantoms for channel 1. The power delay profiles for channel 2 and 3 are similar to the one from channel 1 and all of them consist of 3 channel taps. There is a maximum deviation between channel 1 and channel 3 of 0.66 dB and 2.6 dB for the second and third tap, respectively. For that reason the power delay profile for channel 2 and 3 are not shown.

A much larger difference can be found when the bandwidth of the transmission is increased. This can be observed in the lower plot in Figure 4.18 for channel 5. First of all, the power delay profile for channel 5 is much shorter in time than the one for channel 1. Moreover, there is a clear difference between the power delay profiles, e.g. between Helga and Taro. Due to the comparable bandwidth, channel 4 is similar to channel 5. In general the power delay profile of channel 4 and 5 consist of 4 to 5

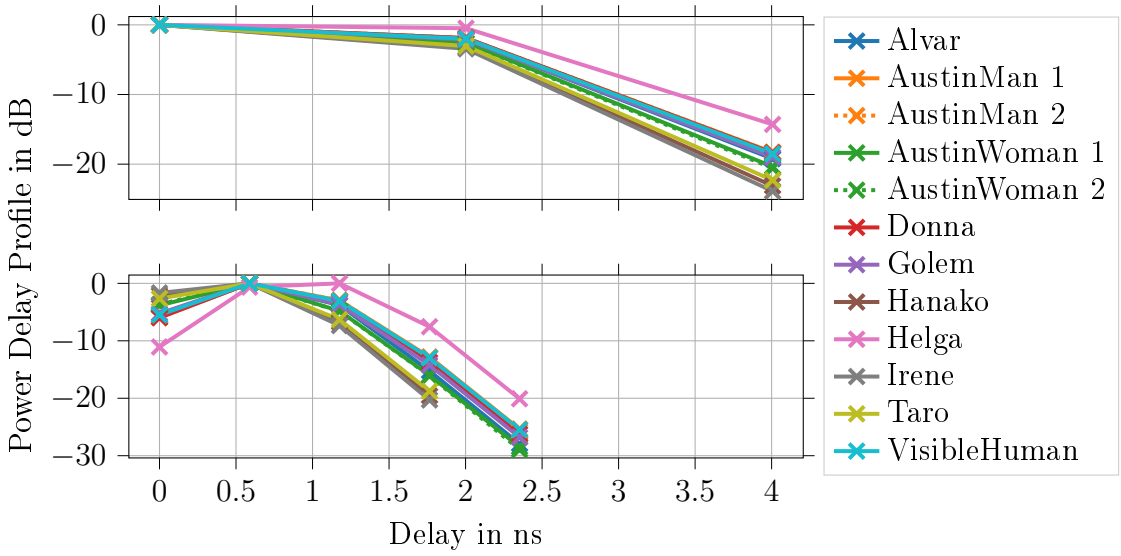

Figure 4.18: The power delay profiles for UWB channel 1 (top) and channel 5 (bottom). The crosses mark the channel taps. Whereas, the lines are only drawn to increase the readability of the plot.

channel taps. Although the power delay profile is shorter in time than for channels 1 to 3, the smaller sample spacing of $\frac{1}{1.7\,\mathrm{GHz}} = 0.588\,\mathrm{ns}$ leads to more channel taps in a shorter period of time.

The differences of the temporal behavior can also be seen from the RMS delay spread, which is shown as a boxplot for each UWB channel in Figure 4.19. For each channel the RMS delay spread is computed from all phantoms. A boxplot shows the spread of the underlying data based on its quartiles. The box spans from the first to the third quartile, where the median is indicated by the orange line inside the box. The whiskers extending from the box reach to the minimum and maximum values in the data set. It is clear from this plot that there is only a small deviation in the RMS delay spread between the phantoms as the difference between the first and the third quartile is small. For the channels 1 to 3 the median RMS delay spread is between 1.01 ns to 1.02 ns. Although, the value of the first quartile is getting slightly smaller. By increasing the bandwidth, the median RMS delay spread is decreasing to 0.43 ns for channel 4 and even further to 0.37 ns for channel 5.

4.3.2.3 Correlation Between Transfer Functions

In addition to the aforementioned channel parameters it is of interest how similar the transfer functions from one transmitter location to different receiver locations are. The similarity between the transfer functions is measured using the magnitude of the complex correlation coefficient ρ_{XY} as explained in Appendix B.1. As a first example

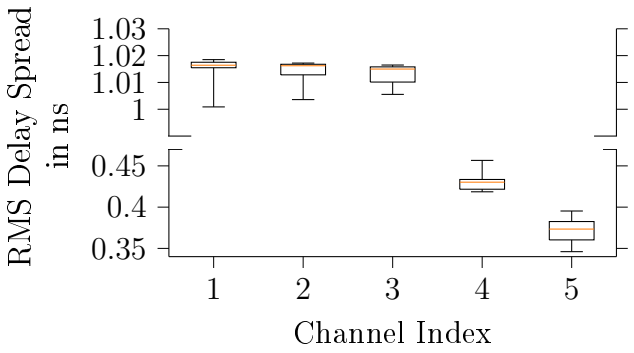

Figure 4.19: Boxplot of the RMS delay spread from all digital phantoms for channels 1 to 5.

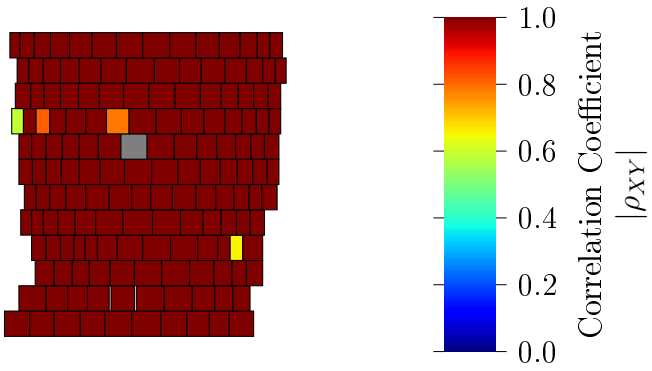

Figure 4.20: Correlation between one reference transfer function $\mathcal{H}_{\mathbf{t}_0\to\mathbf{r}_{50}}(f;c)$ to all other transfer functions $\mathcal{H}_{\mathbf{t}_0\to\mathbf{r}_j}(f;c), j = 1,\ldots,49,51,\ldots,N_{\mathrm{RX}}$ starting from the same transmit location $\mathbf{t}_0$. $\mathbf{r}_{50}$ is marked in dark gray, the other receiver locations are colored according to the magnitude correlation coefficient. The phantom AustinMan 2 has been used exemplarily in this figure.

the correlation between one reference transfer function $\mathcal{H}_{\mathbf{t}_0\to\mathbf{r}_{50}}(f;c)$ to all other transfer functions $\mathcal{H}_{\mathbf{t}_0\to\mathbf{r}_j}(f;c), j = 1,\ldots,49,51,\ldots,N_{\mathrm{RX}}$ from the same transmitter location $\mathbf{t}_0$ is shown in Figure 4.20. The transmit location $\mathbf{t}_0$ is chosen arbitrarily, whereas the reference receiver location $\mathbf{r}_{50}$ is chosen because it is close to the center of the abdomen. Each receiver location is colored according to the magnitude of the correlation coefficient ρ_{XY}, where $X = \mathcal{H}_{\mathbf{t}_0\to\mathbf{r}_{50}}(f;c)$ and $Y = \mathcal{H}_{\mathbf{t}_0\to\mathbf{r}_j}(f;c)$. The reference location $\mathbf{r}_{50}$ is marked in dark gray. It is evident that most of the transfer functions exhibit a high correlation near 1 with respect to $\mathcal{H}_{\mathbf{t}_0\to\mathbf{r}_{50}}(f;c)$. Only for some locations smaller correlations can be seen by the different colors. It was observed that this behavior occurred for most of the reference locations in all of the digital phantoms independent of the selection of the transmit antenna location.

Hence, the cumulative distribution function (CDF) of the magnitude of all correlation coefficients is determined and is shown in Figure 4.21. It can be seen from Figure 4.21 that most transfer functions exhibit a high correlation between each

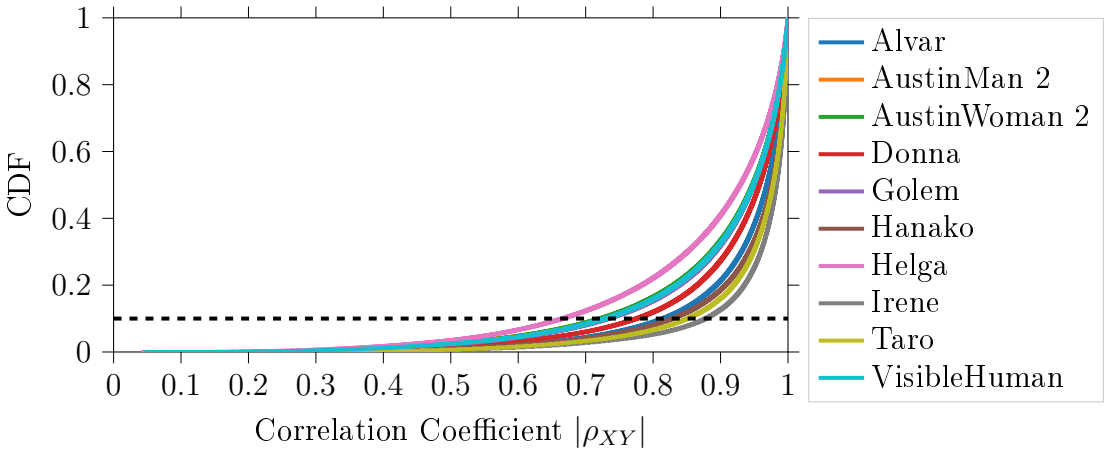

Figure 4.21: Cumulative distribution function (CDF) of the correlation coefficient $|\rho_{XY}|$ between all transfer functions from 100 randomly selected transmitter locations to all possible receive locations.

other. There are only few with a correlation smaller than 0.5. The 10^{th} percentile is larger than 0.67 for all digital phantoms. Hence, it can be concluded that there are some differences between the transfer functions, but their general behavior over frequency is more or less the same for all communication links. Thus, the main difference between different communication links is their path loss.

4.3.3 Comparison with Channel Models from Literature

Existing comprehensive channel models for UWB capsule endoscopy have been reviewed in detail in Section 3.4. After deriving the path loss model parameters for the layer modeling approach in Section 4.3.2.1, the proposed model can be compared to results from these literature sources. Please keep in mind that due to different frequency ranges, methodologies, and phantoms a one-to-one comparison of the path loss models is limited. However, it is still possible to compare the general trend and the order of magnitude of the path loss.

Figure 4.22 shows the comparison of the path loss models of AustinMan 2, Helga, and Irene in channel 5 with the path loss models from literature. Channel 5 is selected in this case as it covers the complete range form 3.1 GHz to 4.8 GHz, which is also used in most of the literature. These three digital phantoms are selected as reference because Helga shows the lowest path loss and Irene the highest of all phantoms (see Figure 4.16). Moreover, the path loss values for AustinMan 2 are between the values of the two. For these three, the path loss model including free space losses

and effective tissue losses are shown as the lower and upper line, respectively. The area between the two corresponding curves is colored for easier visibility.

It can be seen from all three plots in Figure 4.22 that in general all of the path loss models operate on the same range of values. However, there are of course differences between them. The comparison with path loss models based on numerical simulations is shown in Figure 4.22a. Except for S1 and S2 all numerical simulations are based on different antennas, frequencies and digital phantoms. A large variety of path loss values can be observed depending on the literature source. As mentioned already in Section 3.4 it is unclear why the two path loss models of S1 and S2 are substantially different although they are based on the same simulation setup. In general differences between the literature models of around 20 dB can be observed. However, the general trend of the literature models fits quite well to the proposed layer modeling approach.

Path loss models resulting from phantom measurements are shown in Figure 4.22b. All these liquid phantoms are supposed to mimic muscle tissue. Only in P4 an additional layer of a fat-mimicking substance was included in the measurement setup. The path loss model P3 contains results for multiple sub channels in the frequency range of 3.1 GHz to 5.1 GHz for each of these channels one curve is plotted in Figure 4.22b.

The path loss models from in-vivo experiments are shown in Figure 4.22c. All in-vivo experiments were conducted in anesthetized pigs using different antennas and frequency ranges. However, also in this case a wide variety of average path loss values was determined.

All three comparisons show that in general the trend and the range of values of the path loss predicted with the layer modeling approach agrees to results from literature. However, already the path loss models from literature show a large difference in path loss.

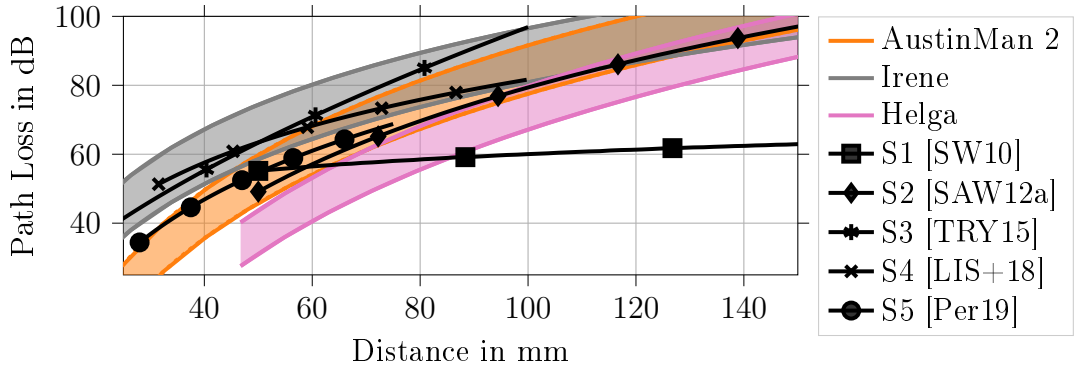

(a) Literature models from numerical simulations

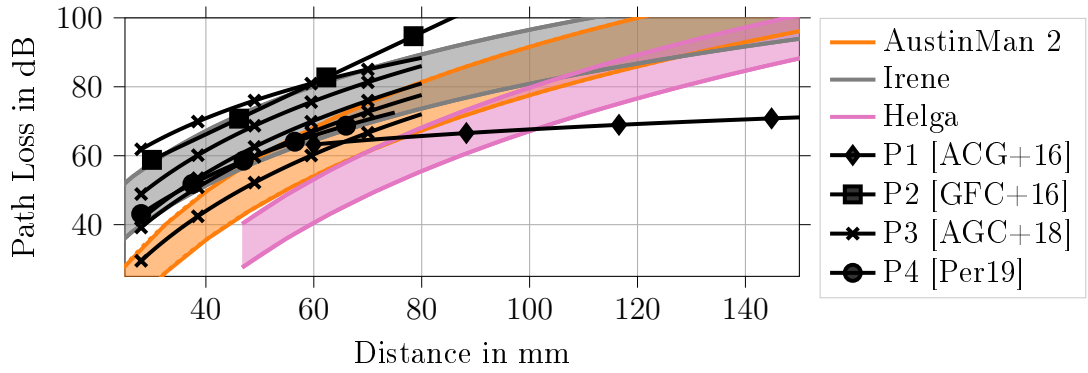

(b) Literature models using phantom measurements

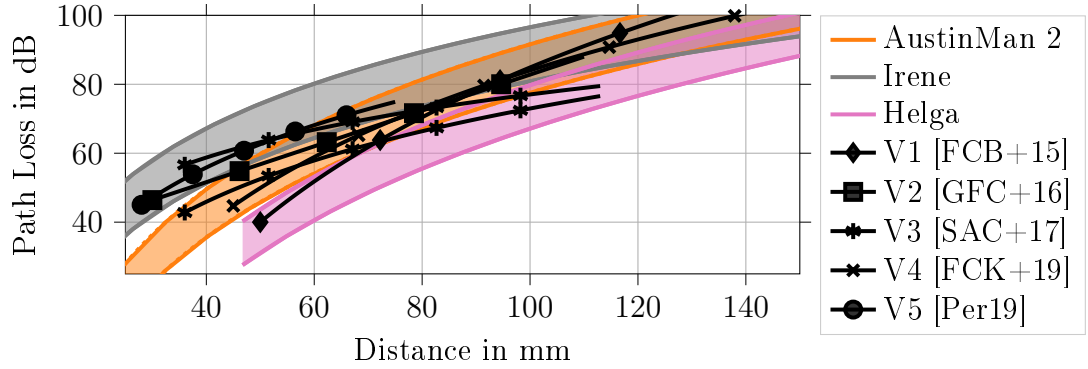

(c) Literature models from in-vivo experiments

Figure 4.22: The average path loss in channel 5 (3.1 GHz to 4.8 GHz) for AustinMan 2, Helga, and Irene compared to various path loss models from literature. More details on the models from literature can be found in Table 3.3. For AustinMan 2, Helga, and Irene the average path loss including effective tissue losses and free space losses is plotted as upper and lower line, respectively. The area between these two curves is colored only for better visibility.

4.4 An Easy-to-Reproduce Channel Model

In this section, it is investigated how the transfer functions computed using the layer modeling approach can be represented by simple parameterized functions for easier reproducibility. Up to now the layer modeling approach described in (4.35) was used to compute the transfer functions. This involves determining the tissue layers between transmitter and receiver each time and solving several matrix multiplications to determine the scattering parameters. Additionally, the equations to determine the transfer function depend on many parameters, which are all frequency dependent. Furthermore, for each calculation the respective digital phantom needs to be loaded into memory. Depending on the voxel size this can result in memory requirements of up to 1.4 GB, e.g. for Alvar. The drawback of this is twofold. First, simulations based on the layer modeling equations are time consuming if the transfer functions has to be computed again in each run. Secondly, it is difficult for others, who want to investigate in-body ultra wideband communication and build on the results of this thesis, to reproduce the channel model.

Thus, it would be a good alternative to use simple parameterized functions that could easily be reproduced instead of computing (4.35) every time. In communication engineering usually stochastic channel models are employed. In [BSB19] a stochastic channel model was created based on the transfer functions of the layer modeling approach. However, the only way to introduce randomness with the layer modeling approach is over the transmit or receive antenna locations. The underlying layer modeling approach does not introduce any randomness apart from different placements of transmit and receive antenna, i.e. the transfer function between two coordinates $\mathbf{t}_i$ and $\mathbf{r}_j$ is deterministic and always the same. Furthermore, to model a complete transit of the capsule through the gastrointestinal tract, it is necessary to include each transmit antenna location exactly once. Additionally, the correlation of neighboring receive antenna locations is close to 1 as shown in Section 4.3. For this reasons, instead of a stochastic model a deterministic channel model will be build in the following. This deterministic channel model will consist of simplified functions which approximate the transfer function for each communication link in the corresponding digital phantom. Hence, it is possible to share just the parameters to these functions and use them for further computations and simulations.

In the following, suitable candidate functions for the approximation are identified and it is investigated which of them fit best to the transfer functions computed using the layer modeling approach. Furthermore some examples on the accuracy are given. The resulting channel model parameters are available from [Bru20].

4.4.1 Suitable Candidate Functions

In the previous work done in [BSB19] it was found that the magnitude of the transfer functions is best approximated by a sum of three exponential functions. Moreover, a linear function was determined as best fit for the phase of the transfer functions. However, in that publication it was assumed that the direct link is dominant in the propagation. It was shown in Section 4.2 that the transfer function is composed of the sum of a direct and an indirect path. Hence, it is reasonable to assume that especially the shape of the magnitude of the transfer function changes compared to the previous approach. Furthermore, the complete ultra wideband frequency range from 3.1 GHz to 10.6 GHz was covered in [BSB19]. Whereas in this thesis only the frequency range from 3.1 GHz to 4.8 GHz is investigated because the attenuation for higher frequencies prevents any useful communication. It was found in an initial evaluation that indeed the behavior of the magnitude over frequency is more similar to a higher order polynomial than to a sum of exponential functions. The behavior of the phase over frequency was found to be approximately linear. Thus, in addition to fitting a sum of exponential functions to the magnitude of the transfer functions also polynomials of different degree are evaluated. For the phase only polynomials of different degrees are considered.

The investigated candidate functions are a sum of K exponential functions

$$\exp_K(f) = \sum_{i=0}^{K} a_i \cdot e^{f\tau_i} \tag{4.42}$$

and polynomials of degree K

$$p_K(f) = \sum_{i=0}^{K} c_i \cdot f^i \,. \tag{4.43}$$

All coefficients a_i, c_i and τ_i in (4.42) and (4.43) are real valued.

It was also tested to fit a sum of complex exponential functions to the complex transfer function. It became clear after a few trial runs, that it is in principle possible to fit complex exponential functions directly. However, finding a good fit seemed to be very sensitive on the correct initial values. As these varied for different communication links, it was not feasible to automate the procedure of setting the initial values. Hence, this approach was not pursued any further.

4.4.2 Index of Agreement as Error Metric

As the path loss for different communication links may vary by around 100 dB, cf. Figure 4.15, comparing an absolute error metric, e.g. the mean-squared error (MSE), between the communication links would not be meaningful. Instead, a relative error metric – the so-called *index of agreement* – introduced by Willmott *et al.* in [WW80] and refined in [WRM12] will be used. The index of agreement d_{IA} between observed samples O_i and their prediction $P_i, i = 1, 2, \ldots, N_s$ is defined as[1]

$$d_{\mathrm{IA}}(P, O) = 1 - \frac{\sum_{i=1}^{N_s} |P_i - O_i|}{\sum_{i=1}^{N_s} \left(\left| P_i - \bar{O} \right| + \left| O_i - \bar{O} \right| \right)} . \tag{4.44}$$

The index of agreement takes on values between 0 and 1. A value of 1 means that the prediction P_i perfectly estimates the samples O_i. Whereas, a value of 0 means that the prediction fails completely. It was found already in [BSB19] that the index of agreement is well suited to compare the goodness-of-fit for magnitude and phase of the transfer functions.

4.4.3 Determination of the Best Fitting Functions

To evaluate the goodness-of-fit of the different fitting functions AustinWoman 2 is used. The transfer functions are computed for $N_{\mathrm{RX}} \cdot N_{\mathrm{TX}} = 2000 \cdot 147 = 294\,000$ communication links. All $N_{\mathrm{RX}} = 2000$ transmitter locations have been drawn randomly inside the digestive tract with a minimum distance of 4 mm between each other. These are the same transmitter locations that have been used in Section 4.3.2. All results shown in the following are based on the transfer functions including free space losses $\mathcal{H}_{\mathbf{t}_i \to \mathbf{r}_j}(f; c_0)$ according to (4.35). It was found that there is no difference in the fitting accuracy whether free space losses or effective tissue losses are assumed. The fitting for the magnitude of the transfer function is done according to (4.42) and (4.43) with $\exp_2(f)$, $\exp_3(f)$, and $p_K(f), K = 3, 4, \ldots, 9$, respectively. The phase of the transfer function is fitted with $p_K(f), K = 1, 2, \ldots, 5$. The coefficients for the polynomials $p_K(f)$ are determined by a linear least squares fit. Whereas the coefficients for the exponential functions $\exp_K(f)$ are computed by a non-linear least squares fit using the Levenberg-Marquardt algorithm.

The resulting cumulative distribution functions (CDFs) of the index of agreement for the fitting of magnitude and phase are shown in Figures 4.23a and Figure 4.24a,

[1] This version is denoted as d_1 in [WRM12].

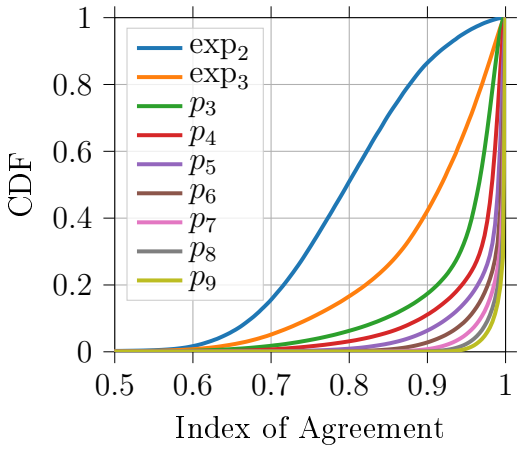

(a) The CDF of the index of agreement for fitting the candidate functions to the magnitude response.

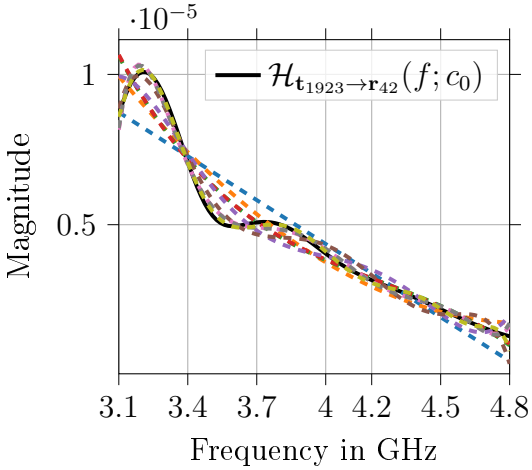

(b) Example fit for the magnitude of the transfer function closest to the 10^{th} percentile of the index of agreement for p_7.

Figure 4.23: Comparisons to determine the best fitting function for the magnitude of the transfer functions. The legend in (a) also applies for (b).

respectively. One example for the magnitude and one for the phase of two different transfer functions are shown in Figures 4.23b and Figure 4.24b. At first the fitting to the magnitude response is discussed and afterwards the fitting of the phase response is investigated.

Fitting a sum of exponential functions to the magnitude of the transfer functions does results in a rather poor performance compared to fitting even a polynomial of degree 3 to these functions. This can be seen from Figure 4.23a, as the probability for a larger index of agreement increases from $\exp_3$ to p_3. Additionally, the example in 4.23b indicates clearly that using a polynomial as fitting function is the better solution. Moreover, when fitting $\exp_2$ or $\exp_3$ to the transfer functions, there are transfer functions which result in an index of agreement of 0. By using a polynomial this does not happen anymore, even for a polynomial of degree 3 the minimum index of agreement is 0.3 and raises to 0.69 for p_7 and 0.84 for p_9.

Furthermore, fitting polynomials has the advantage that determining the coefficients is a linear optimization problem. For the sum of exponential functions non-linear optimization is necessary, which is also dependent on the initial values of the parameters.

The 10^{th} percentile for the index of agreement when fitting p_3 to the magnitude of the transfer functions is 0.846. Hence, in 90 % of all cases the index of agreement is

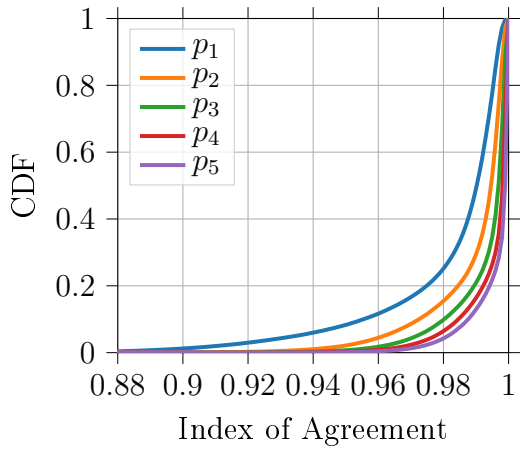

(a) CDF of the index of agreement for fitting the candidate functions to the phase response.

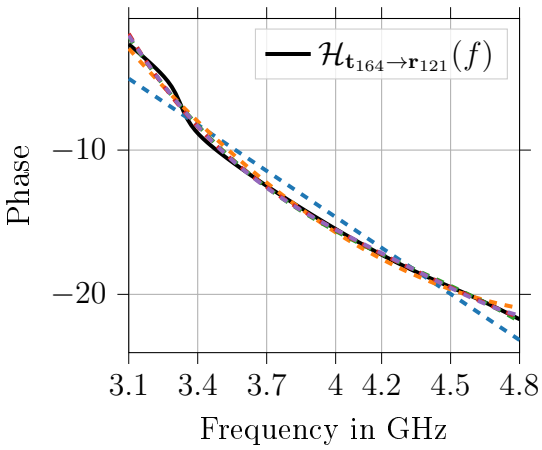

(b) Example fit for the phase of the transfer function closest to the 10^{th} percentile of the index of agreement for p_3.

Figure 4.24: Comparisons to determine the best fitting function for the phase of the transfer functions. The legend in (a) also applies for (b).

larger than this value. For a polynomial of degree 9 the 10^{th} percentile increases to 0.985. Thus, the higher the degree of the polynomial the better the fit gets. To allow for an accurate approximation using the polynomial fitting functions, a polynomial of degree 7 will be used in the following for the magnitude. From $p_6(f)$ to $p_7(f)$ the 10^{th} percentile of the index of agreement increases only slightly from 0.95 to 0.97. However, the minimum value that is attained is 0.57 for $p_6(f)$ and 0.69 for $p_7(f)$. So there is a rather large increase in the minimum index of agreement from degree 6 to degree 7. Although the increase of the 10^{th} percentile is only minuscule, it was decided to use a polynomial of degree 7 as the minimum value increases quite a bit. Moreover, the comparison of the different fitting functions is only done for AustinWoman 2. To be on the safe side, there might be effects occurring in the other digital phantoms for which it is beneficial to use a degree of 7. In Figure 4.23b the magnitude of the transfer function closest to the 10^{th} percentile of the index of agreement for p_7 is shown. Hence, for 90 % of all transfer functions the fitted polynomial with degree 7 resembles the actual magnitude response better than the depicted example.

Next, a suitable fitting function for the phase response is to be found. Fitting a polynomial of degree 1 to the phase of the transfer function results in values of the index of agreement which are always larger than 0.77. However, as it was observed that not all the phase responses are purely linear, also polynomials with higher degree are investigated. It can be seen from Figure 4.24b that at least some of

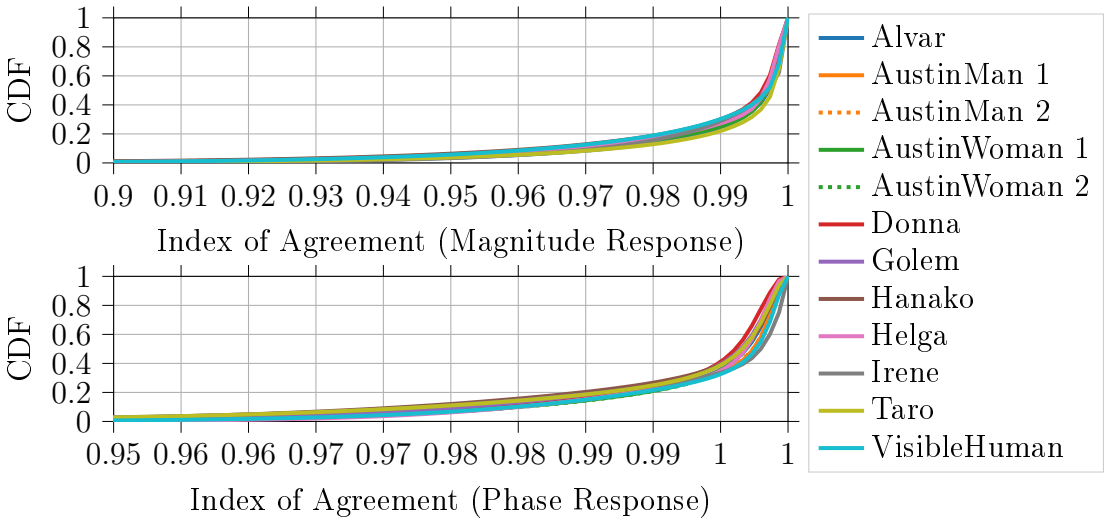

Figure 4.25: The CDF of the index of agreement for magnitude (top) and phase (bottom) of the transfer functions for the 12 digital phantoms using $p_7(f)$ for the magnitude response and $p_3(f)$ for the phase response.

the phase responses have a non-linear behavior at certain frequencies. The CDF in Figure 4.24a shows that the fitting accuracy increases significantly from degree 1 to 3. The further improvement by using a polynomial of degree 4 is only very small. In numbers this means that the 10^{th} percentile increases from 0.96 for $p_1(f)$ to 0.98 for $p_3(f)$. For $p_4(f)$ the 10^{th} percentile is 0.99. Hence, as a trade off between fitting accuracy and memory usage it is decided to use a polynomial of order 3 for approximation of the phase response.

The best fitting function is derived only from AustinWoman 2. In Figure 4.25 the CDFs of the index of agreement are shown for all 12 digital phantoms. The index of agreement is computed using a polynomial of degree 7 for the magnitude response and using a polynomial of degree 3 for the phase response. It is clear from Figure 4.25 that there are some deviations in the fitting accuracy between the different phantoms. However, in general using the said approximation is very accurate for all of them. Moreover, it was found that the path loss computed using the approximation does not deviate more than 0.34 dB from the results of the layer modeling approach over all 12 digital phantoms.

4.4.4 The Resulting Model

In conclusion, the transfer function will be approximated by

$$\tilde{\mathcal{H}}_{\mathbf{t}_i \to \mathbf{r}_j}(f; c) = p_7(f) \cdot e^{j \cdot p_3(f)}\,, \tag{4.45}$$

where the coefficients of $p_7(f)$ and $p_3(f)$ will be determined either including free space losses or effective tissue losses. Hence, the transfer function will be denoted as $\tilde{\mathcal{H}}_{\mathbf{t}_i \to \mathbf{r}_j}(f; c_0)$ or $\tilde{\mathcal{H}}_{\mathbf{t}_i \to \mathbf{r}_j}(f; c_e)$, respectively. The coefficients of $p_7(f)$ and $p_3(f)$ are obtained for each possible transmit and receive antenna combination $\mathbf{t}_i \to \mathbf{r}_j$ for each of the phantoms. Thus, there are around $3 \cdot 10^5$ sets of coefficients for each phantom (cf. Table 4.2). The resulting coefficients for all the 12 digital phantoms can be obtained from [Bru20].

4.5 Summary

In this chapter a new channel modeling approach for ultra wideband capsule endoscopy based on a multi-layered dielectric was introduced. The modeling approach was validated using a numerical simulation employing the finite integration technique. Furthermore, the characteristics of the channel model were investigated and compared to results from literature.

The general idea is to model the propagation path of an electromagnetic wave by a multi-layered dielectric resembling the tissue structure between transmitter and receiver. By assuming that a plane wave is passing through this multi-layered dielectric, the transfer function can be calculated analytically based on equations from transmission line theory. This way the channel modeling can be adjusted dynamically to different setups and constraints. Moreover, it allows to investigate many more communication links in different human phantoms than using state-of-the-art numerical simulations as the computational complexity is reduced drastically.

It has been found in an extensive numerical simulation of the actual wave propagation in CST Microwave Studio that it is not enough to approximate the in-body to on-body link with just one direct path. Rather, it was shown that the transfer function is a combination of a direct path and an indirect path. The direct path is the direct connection between transmit and receive antenna. The indirect path consists of two parts. The first part is the shortest way from the transmitter to the outside of the body and the second part is the path along the curved body surface to the actual receive antenna.

For each of these two paths, the propagation behavior through the tissue is determined from the transfer function of a plane wave through an equivalent multi-layered dielectric. First, the equations needed to compute the transfer function based on the scattering parameters were derived in detail. As the permittivity of human tissue is complex-valued the transformation into scattering parameters could not be based

upon common textbook results, which usually require real permittivity values. Instead, an approach from [TTT+12] and [MW92] has been refined to be used in this scenario. Additionally, a radiation loss term based on Friis transmission equation is added to the transfer function to incorporate the spherical radiation losses caused by an isotropic antenna. This additional radiation loss can either be computed based on the phase velocity in free space or on the effective phase velocity through the tissue layers. These two variants will both be considered in the following investigations and will be called to include free space losses or effective tissue losses, respectively.

In the following, the proposed layer modeling approach was validated using a numerical wave simulation in CST Microwave Studio. The simulation was conducted for 231 communication links in each of four digital human phantoms. As comparison the same transmit and receive antenna locations were used for the layer modeling approach. In a first step, it could be shown that the transfer function of the layer model shows a good resemblance to the transfer function obtained by simulation. It could be seen from two exemplary communication links that indeed the transfer function consists of two paths, i.e. it is the sum of a direct and an indirect path. In addition to this exemplary analysis, the correlation coefficient between the transfer functions computed from both approaches was determined. The cumulative density function of the correlation coefficient showed there is a high correlation between the transfer functions of most of the communication links. Thus, the frequency dependency of both modeling approaches is similar. Moreover, it could be shown that the path loss predicted by the layer modeling approach fits well to the values obtained by simulation. It was found that using the transfer function including free space losses underestimates the path loss and the one including effective tissue losses overestimates the path loss. For that reason, both variants will be used in the following chapters as lower and upper bounds, respectively. Additionally, the power delay profile showed a good agreement and the RMS delay spread is nearly identical for both approaches.

Afterwards, the channel characteristics, i.e. the path loss and power delay profile, were investigated for all twelve phantoms. It was found for single human tissue layers that there are huge differences in path loss in the order of 9 dB/cm between different tissue types. Moreover, it could be observed how the differences in the dielectric properties shown in Section 2.1 lead to path loss values which are different by a factor of 2.7 on a dB scale. Computing the path loss vs. the transmission distance for all the phantoms, it was found that the best fit is achieved using a logarithmic path loss model. The general behavior of the path loss model for different frequency bands was observed to be approximately the same for all phantoms. However, for

one specific frequency band there are huge variations. The path loss at the reference distance PL_0 differs by up to 28 dB and the path loss exponent n differs by up to 4.6 dB between different phantoms. Nevertheless, the power delay profile showed only minor differences between phantoms. The RMS delay spread is nearly the same for all phantoms. Moreover, it could be shown that the correlation between transfer functions of the same phantom using different transmit and receive antenna locations is high. Thus the main difference between different communication links is their path loss and not the exact shape of the frequency dependency.

Having obtained path loss models for each phantom, these could be compared to the path loss models that have been found in the course of the literature review described in Section 3.4. Comparing the path loss models obtained from the layer modeling approach to path loss models from numerical simulation, phantom experiments and in-vivo measurements, it could be seen that the general trend and order of magnitude is well predicted by the layer model. The difference between the path loss from the layer modeling approach to the literature results is on the same scale as the differences between the various literature sources themselves.

Finally, an easy-to-reproduce channel model is presented which eliminates the computational complexity of the layer modeling approach and makes it easier for others to use the channel model presented in this thesis. This model was determined from the layer modeling approach by fitting polynomial functions to the magnitude and phase of the transfer functions. Hence, only the parameters of the polynomials are needed to reproduce the results of the channel capacity computations and bit error rate simulations presented in the following chapters.

Chapter 5

Channel Capacity

In the last section a channel model for ultra wideband capsule endoscopy was derived. That model will be used in this chapter to determine the fundamental limits on the data rate in this specific environment. The fundamental limits on the data rate in any communication channel are determined by the channel capacity as derived by Claude Shannon in [Sha48]. The channel capacity C in a real-valued additive white Gaussian noise (AWGN) channel is defined as

$$C = B \cdot \log_2 \left(1 + \frac{P_R}{P_N}\right) , \tag{5.1}$$

where B is the bandwidth of the transmission system, P_R is the received signal power, and P_N is the noise power in the band B. This rate C is the largest possible data rate in bit/s at which it is possible to transmit with an arbitrarily low error probability.

The capacity of a frequency selective channel is determined by dividing the transfer function $\mathcal{H}(f)$ in infinitesimally small sub-bands. The channel capacity then becomes [BLM04]

$$C = \int_0^\infty \log_2 \left(1 + \frac{S_{xx}(f) \left|\mathcal{H}(f)\right|^2}{S_{NN}(f)}\right) \mathrm{d}f \, , \tag{5.2}$$

where $S_{xx}(f)$ is the power spectral density of the transmit signal, $\mathcal{H}(f)$ is the channel transfer function, and $S_{NN}(f) = \frac{N_0}{2}$ is the power spectral density of the noise. Unless noted otherwise, the noise power spectral density N_0 is computed for 37 °C as in (5.3). The noise figure $N_{f,dB}$ for receiver in body area networks is reported to range from 6 dB to 20 dB [WW13][Ins12][Int02]. Hence, the noise power spectral

density, including $N_{f,dB} = 20\,\mathrm{dB}$ as a worst case approximation, yields

$$N_0 = k_B T N_f = 1.38 \times 10^{-23}\,\mathrm{J/K} \cdot 310.15\,\mathrm{K} \cdot 100 = 4.282 \times 10^{-19}\,\mathrm{W/Hz}\,. \quad (5.3)$$

In the following sections, the power spectral density of the transmit signal $S_{xx}(f)$ is assumed to be constant in the frequency band B unless noted otherwise. Actually, the channel capacity would be achieved by distributing the transmit power using a water filling scheme. However, this would mean that $S_{xx}(f)$ needs to change for each location in the digestive tract because the transfer function changes. Thus, the power spectral density of the transmit signal $x(t)$ will be set to

$$S_{xx}(f) = \begin{cases} \frac{P_{\mathrm{TX}}}{2B} & f_L \leq |f| \leq f_U \\ 0 & \text{else} \end{cases}\,, \quad (5.4)$$

where P_{TX} is the transmit power and the transmission takes place in the band $B = f_U - f_L$ between the lower frequency f_L and the upper frequency f_U. Unless noted otherwise, the transmit power in this chapter will be set to the maximum value of $P_{\mathrm{TX}} = 21.5\,\mathrm{mW}$ for safe transmission as described in Section 2.3.2.

For all following capacity calculation the transfer function $\mathcal{H}_{\mathbf{t}_i \to \mathbf{r}_j}(f; c_0)$ including free space losses according to (4.35) will be used. It was shown in Section 4.2 that using free space losses always results in smaller path loss values than using effective tissue losses. The channel capacity is an upper bound on the achievable data rate. To make sure that the values determined in this chapter can still serve as an upper bound, only the free space losses will be included. Hence, the achievable data rate in any practical scenario will always be below the values obtained in this chapter.

The remainder of this chapter is organized as follows. First, the behavior of the channel capacity for increasing bandwidth is determined. Second, the behavior of the capacity for multiple receive antennas and their optimum placement is examined. Third, it is investigated how the physiological properties of the digital phantoms affect the channel capacity. Fourth, the impact of the accuracy of the measured dielectric properties is analyzed. Finally, the channel capacity for ultra wideband communication is compared to the channel capacity for transmission in the Medical Implant Communication Service (MICS) band.

5.1 Transmission Bandwidth

In this section the behavior of the channel capacity for increasing transmission bandwidth is investigated. A similar investigation was already published in [BB17a]. However, as the approach and the underlying layer modeling technique were improved in this thesis, the results are not comparable.

The investigations in this section are based on AustinWoman 2 using the same 2000 randomly drawn transmitter locations as described in Section 4.3.2. All $N_{\mathrm{RX}} = 147$ locations as shown in Figure 4.14 are considered for placing a single receive antenna. For a constant transmit power P_{TX}, the dependency of the channel capacity on the occupied bandwidth is non-linear. This can be seen immediately when (5.4) is inserted into (5.2). It follows that

$$C = \int_{f_L}^{f_U} \log_2 \left(1 + \frac{P_{\mathrm{TX}} \left| \mathcal{H}_{\mathbf{t}_i \to \mathbf{r}_j}(f; c_0) \right|^2}{(f_U - f_L) N_0} \right) \mathrm{d}f \,. \tag{5.5}$$

The channel capacity is evaluated for each possible communication link for an increasing bandwidth. The lower frequency f_L is fixed to 3.1 GHz. Whereas, the upper frequency f_U increases in 30 steps to 6 GHz, i.e. $f_U = f_L + k \cdot 96.\overline{6}\,\mathrm{MHz}, k \in [1, 2, \ldots, 30]$.

In Figure 5.1 the mean, the median and the 10 %-outage channel capacity computed over all investigated communication links are shown for an increasing upper frequency f_U. The 10 %-outage capacity is 105.5 kbit/s for a bandwidth of $96.\overline{6}$ MHz and decreases to 13.0 kbit/s for the maximum bandwidth. Similarly, the median of the capacity is decreasing from 34.2 Mbit/s to 5.3 Mbit/s. Only the mean of the capacity is increasing from 272.8 Mbit/s to 1.4 Gbit/s with increasing bandwidth. This indicates that there are only a few communication links that benefit from an increase of the bandwidth.

Having a closer look at the behavior of the channel capacity over the upper frequency shows that for most of the communication links an increase in bandwidth leads to a reduction of the channel capacity as the attenuation is so high that it counteracts the benefit of increasing the bandwidth. From all communication links, only for 22.4 % the channel capacity is increasing with the bandwidth. For 77.6 % it is decreasing. From these 77.6 % communication links with decreasing channel capacity for most of them (64.9 %) the capacity is monotonically decreasing, only for 35.1 % the capacity is increasing to a maximum before it is decreasing again.

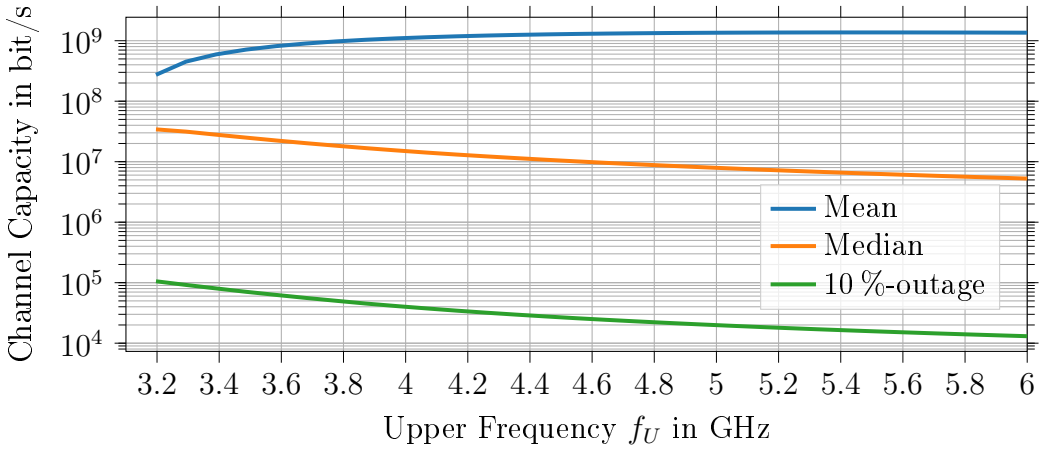

Figure 5.1: Behavior of the channel capacity for increasing transmission bandwidth. The computations are based on all possible transmit and receive antenna locations in and on AustinWoman 2.

Thus, it can be concluded that it is generally important to keep the bandwidth as small as possible for optimizing communication performance based on the channel capacity. Of course, the bandwidth cannot be reduced to arbitrarily small values as each communication scheme requires a certain minimum bandwidth. For ultra wideband communication a minimum bandwidth of 500 MHz is required. For that reason, in all upcoming discussions regarding the channel capacity UWB channel 1 (see Table 3.2) will be used for the computations. Channel 1 has a nominal bandwidth of 500 MHz and is centered around $f_c = 3494.4\,\text{MHz}$.

5.2 Multiple Receive Antennas and Their Placement

As has been seen in the previous section, the channel capacity when using just one randomly placed receive antenna is rather small. The maximum 10 %-outage channel capacity is just 105.5 kbit/s, which is much lower than the target data rate of $R_{\text{target}} = 3\,\text{Mbit/s}$ that was identified in Section 3.1. Therefore, it is important to use multiple antennas and an appropriate combining scheme to increase the data rate sufficiently. In the following section the influence of the number of antennas and their position on the abdominal surface on the channel capacity will be investigated. This extends the results already published in [BB16] and [BB17b] for the more accurate channel model derived in this thesis.

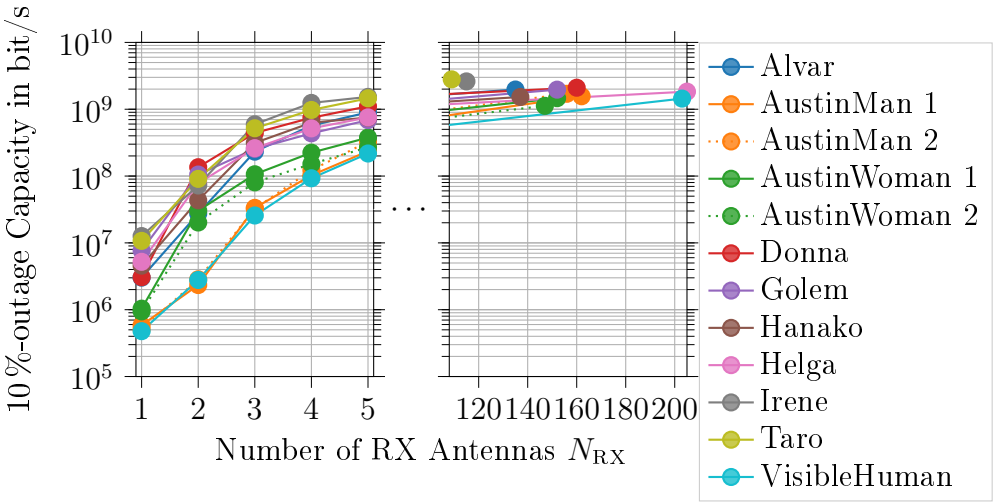

Figure 5.2: The maximum 10 %-outage channel capacity obtained for a certain number of receive antennas N_{RX} placed on the abdominal surface. The right part of the plot shows the maximum number of receive antennas that can be placed on the respective phantom.

5.2.1 Optimum Placement

In this section, the placements of the receive antennas that maximize the 10 %-outage channel capacity will be determined. The channel capacity is computed for all digital phantoms using the same number of randomly drawn transmitter locations as described in Section 4.3.2. For each phantom the maximum number of receive antenna locations $N_{RX,max}$ as shown in Figure 4.14 is considered for placing the receive antennas. The optimum placement for multiple receive antennas will be determined based on maximizing the 10 %-outage channel capacity, i.e. for 90 % of all communication links the channel capacity will be larger as the given value. Moreover, it will be shown later in Section 6.3.3 that selection combining performs nearly as good as maximum ratio combining. Due the high attenuation inside the body, there is usually only one dominant link to the on-body antennas. Hence, selection combining will be used prior to the determination of the 10 %-outage capacity. Due to the fast growth of possible combinations of the number of receive antennas N_{RX}, it is only possible to determine the optimum placement of up to $N_{RX} = 5$ receive antennas.

Figure 5.2 shows the resulting 10 %-outage capacity and Figure 5.3 the corresponding optimum placement of the receive antennas. The 10 %-outage capacity for $N_{RX} = N_{RX,max}$ is determined additionally as an upper bound and is shown in the right part of the plot of Figure 5.2. In this case all possible receive antenna locations are occupied and no further optimum placement has to be found. It can be seen

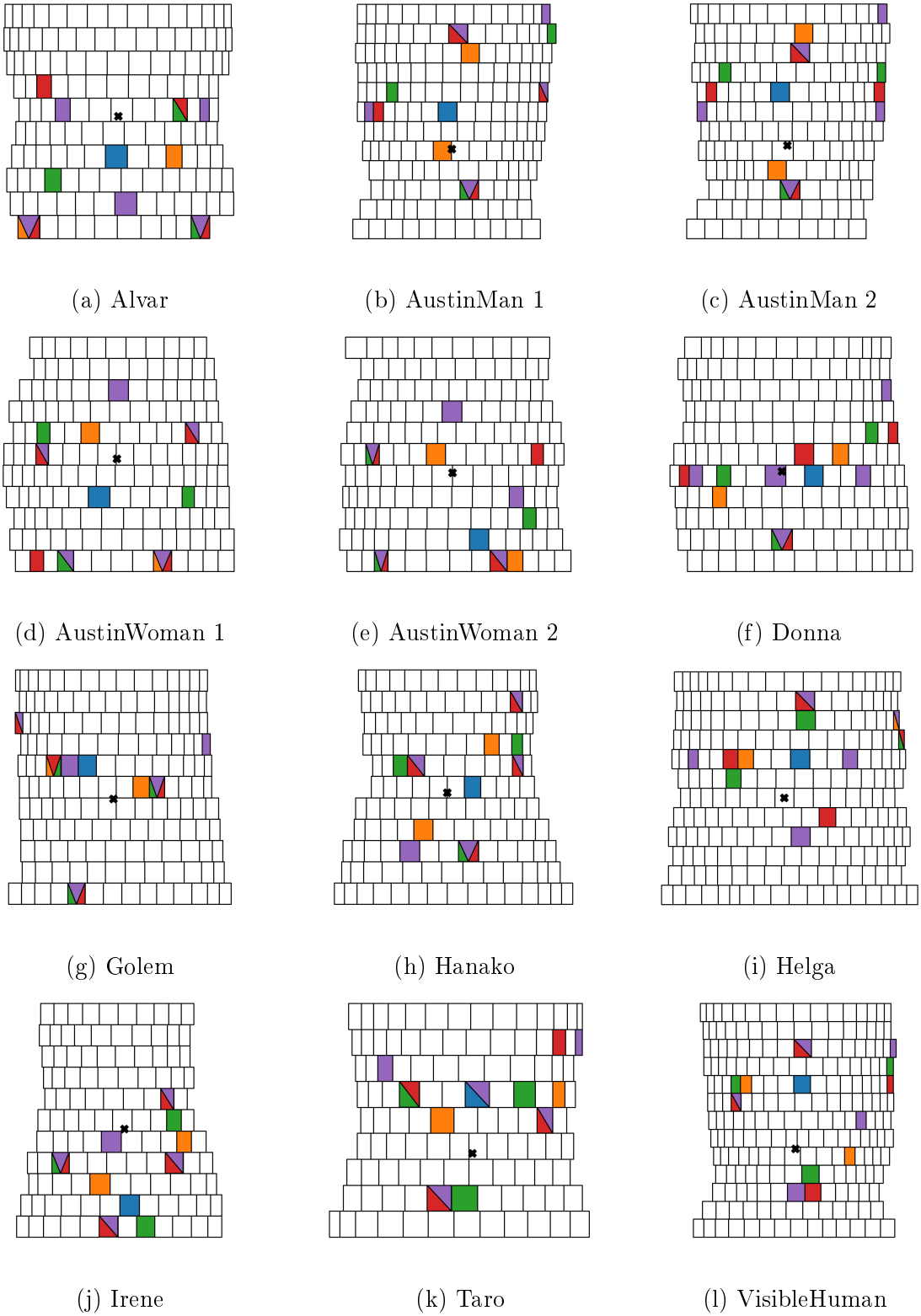

(a) Alvar (b) AustinMan 1 (c) AustinMan 2

(d) AustinWoman 1 (e) AustinWoman 2 (f) Donna

(g) Golem (h) Hanako (i) Helga

(j) Irene (k) Taro (l) VisibleHuman

Figure 5.3: The optimum placement for up to five receive antennas based on the 10 %-outage channel capacity. The black cross indicates the location of the navel. Different colors are used to indicate the number of receive antennas:
1 2 3 4 5

that increasing N_{RX} from 1 to 5 increases the 10 %-outage capacity for all digital phantoms by approximately two orders of magnitude. The results for AustinMan 2, AustinMan 1 and VisibleHuman are all similar, which again verifies that these three phantoms are all based on the same human. For all other phantoms huge variations can be observed. For one receive antenna, the 10 %-outage capacity ranges from 477.3 kbit/s for VisibleHuman to 12.6 Mbit/s for Irene. Furthermore, for five receive antennas it ranges from 217.5 Mbit/s for VisibleHuman to 1.5 Gbit/s for Irene. For all phantoms, the slope of the capacity over N_{RX} is declining, i.e. the first additional antennas have a larger impact on the 10 %-outage capacity than the later. For placing the maximum number of receive antennas, a 10 %-outage channel capacity between 1.1 Gbit/s to 2.8 Gbit/s results for all digital phantoms. Hence, in some of the digital phantoms already five antennas are sufficient to get close to this upper limit.

In Figure 5.3 the optimum placements for all 12 digital phantoms is depicted. Having a close look at the figure it can be seen that even for one antenna the optimum location (marked with ■) is not in the same area on the abdomen for all the phantoms. For AustinMan 1&2 the optimum location is somewhere in the middle of the abdomen. Whereas for Alvar this optimum is clearly further down in the area of the navel and for Irene it is even further down on the abdominal surface. These differences increase with the number of investigated antennas. When placing five antennas (marked with ■) optimally according to the 10 %-outage capacity, three of them are placed on the same horizontal line for Donna. However, for AustinWoman 1 they are placed approximately on an equidistant circle around the middle of the abdomen.

5.2.2 Deviation from the Optimum Placement

As has been seen in the previous section, the optimum placement of up to five receive antennas differs significantly from phantom to phantom. To obtain a general guide on how to place the receive antennas optimally, it is of interest how the channel capacity behaves if the antennas are not placed at their exact optimum positions. Two different scenarios will be considered. First, the optimum placement of receive antennas on one phantom will be transferred to all the others with respect to a common reference point. Second, the antennas will be placed around the optimum positions with a certain deviation.

To transfer the optimum receive antenna placements from one phantom to another, the relative location to a common reference needs to be known. Here, the navel will

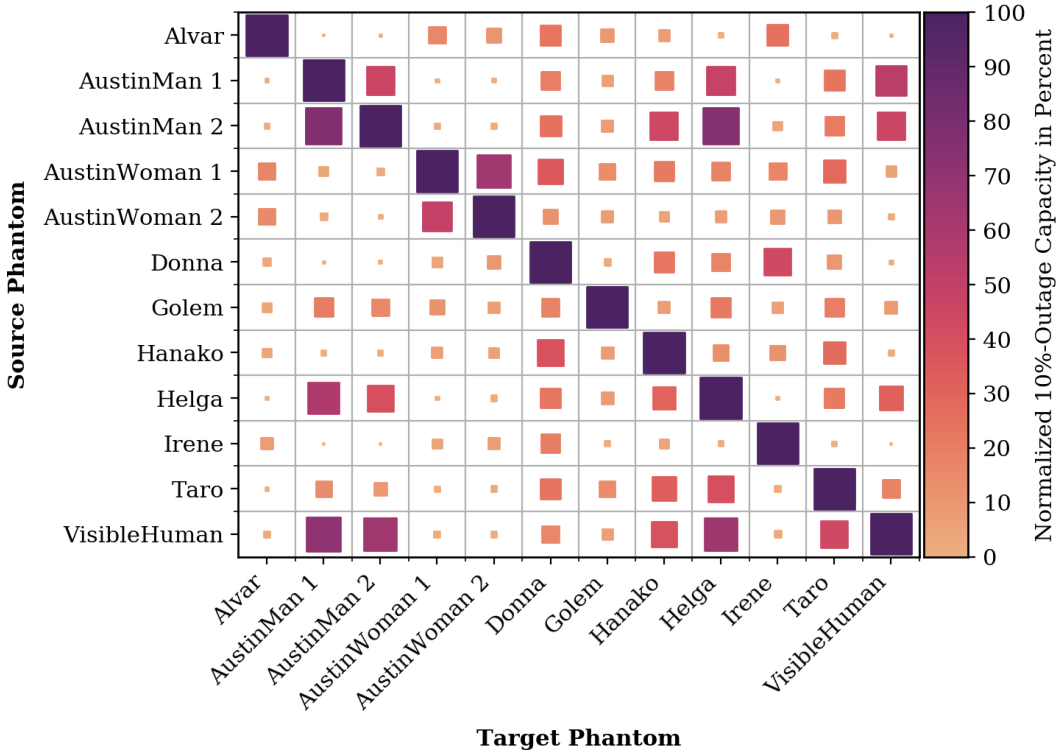

Figure 5.4: The normalized 10 %-outage capacity in percent when applying the optimum receive antenna placement for five antennas of the source phantom to the target phantom. The capacity is normalized with respect to the optimum value of the target phantom. The size of the markers is proportional to the values.

be considered as a common reference point. The location of the navel is determined manually using different cross-sectional views of the phantoms and is indicated by a black cross in Figure 5.3. Using the relative location of the optimum antenna positions the 10 %-outage channel capacity is determined as in the previous section. Figure 5.4 shows the normalized 10 %-outage capacity in percent when applying the optimum placement for five receive antennas of a source phantom on any of the other phantoms as a target. The capacity is normalized with respect to the optimum value of the target phantom. Both, size and color of the markers in Figure 5.4 are proportional to the normalized capacity as indicated in the legend.

For example, using the optimum placement determined for Alvar on Irene (first row, third-from-last column), the 10 %-outage capacity of Irene decreases to 25.4 % of the optimum value for Irene. Using the placement from Alvar on any other phantom, the reduction is even higher. Transferring the optimum placement to another phantom drastically reduces the 10 %-outage capacity for most of the phantoms. Only for approximately 10 % of the entries in Figure 5.4 the normalized capacity is larger than 40 %. Moreover, the resulting values are not symmetric. For example, using the placement from AustinMan 1 on AustinMan 2 the capacity is reduced to 46 %, but

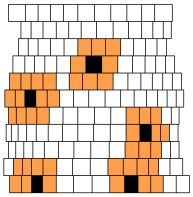

Figure 5.5: All possible receive antenna locations for AustinWoman 2 within a maximum distance of 50 mm (in orange) around the optimal location (marked in black).

only to 77 % for using the placement from AustinMan 2 on AustinMan 1. Moreover, for using the optimum placement of these two phantoms on Helga or VisibleHuman also leads to a reduced capacity of at least 46 % of their respective optimum values.

When the optimum placement of two to four antennas is analyzed, the magnitude of normalized capacity is similar to the ones shown in Figure 5.4. Only the optimum position for one receive antenna can be transferred to other phantoms with much less losses. However, as the 10 %-outage capacity with one receive antenna is very low anyway this is not a relevant scenario.

Additionally, when comparing the results from Figure 5.4 with the optimum locations on the corresponding phantoms from Figure 5.3, it becomes clear that the normalized capacity is large in cases when the optimum positions of the receive antennas agree with each other anyway. For example, compare the purple colored locations for five receive antennas in Figure 5.3 for AustinMan 1 and AustinMan 2 or Helga and VisibleHuman. They all have similar optimum positions. Hence, the degradation when using the optimum placement of one of these phantoms on another with a similar optimum placement, is relatively small.

In addition to the fact that it was not possible to find a general rule on how to place the receive antennas equally good on all phantoms, it won't be possible for a physician to place the receive antennas exactly at their desired position. Hence, there will be an uncertainty in the exact placement. The question that will be answered in the following is: how much does a small deviation of the placement affect the 10 %-outage channel capacity? The average distance between the receive antennas in their optimum location is larger than 100 mm for most of the phantoms. To avoid overlap of the possible regions around the optimum positions, the maximum deviation around the optimum is set to 50 mm. Only for Irene, the optimum receive antenna locations are so close together, that the maximum deviation had to be set to 40 mm. Figure 5.5 shows the investigated receive antenna positions in orange together with the optimum positions in black for AustinWoman 2. Because not all of the discretized surface elements are exactly of size 30 mm $\times$ 30 mm (the width of

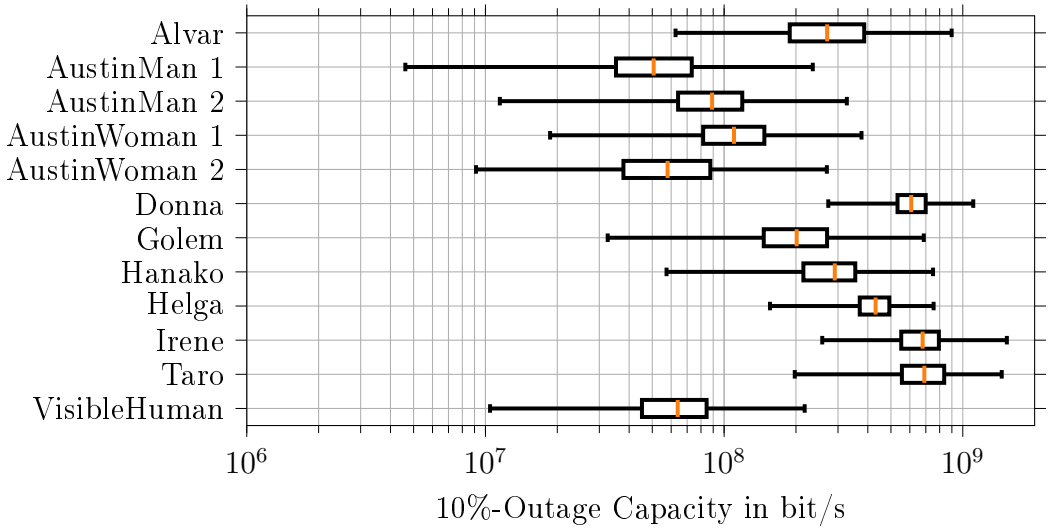

Figure 5.6: Boxplot of the 10 %-outage capacity for any possible combination of receiver locations within a maximum distance of 50 mm from the optimum (40 mm for Irene). The left and right whisker show the minimum and maximum value, respectively.

some of the elements is smaller than 30 mm due to the curvature of the body), there are different numbers of neighboring receive antenna locations considered. There are between 12 348 and 105 300 possible combinations of receive antenna locations to investigate for each phantom.

In Figure 5.6 a boxplot of the resulting 10 %-outage channel capacity is shown. It can be seen that there are huge variations between the phantoms. The rightmost whisker shows the 10 %-outage capacity for the optimum position and the leftmost the minimum achieved capacity. For most of the phantoms the capacity can decrease by approximately one order of magnitude, depending on the exact placement. However, for AustinMan 1 the capacity is reduced by nearly two orders of magnitude in the worst case – from 235 Mbit/s to 4.62 Mbit/s. On the other hand for Donna and Helga the maximum degradation is rather small. For them the reduction is less than one order of magnitude in the worst case. But the degradation is not only large in the worst case. Already for the median of the resulting 10 %-outage capacity values, a degradation to 21.5 % of the optimum capacity for AustinMan 1 and 57.2 % for Helga is observed.

Hence, already small deviations may lead to detrimental decrease of the outage capacity. This supports the previous findings, that using the optimum placement from one phantom on another leads to severe degradation in capacity. Moreover, no general rule could be obtained for the general placement of receive antennas on the abdomen as it varies unpredictably between the phantoms. Nevertheless, the

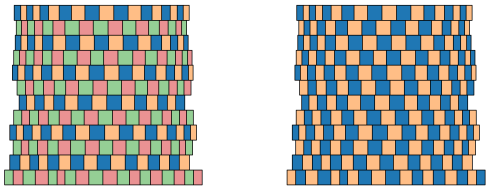

(a) Regular grid (b) Check pattern

Figure 5.7: Example of the antenna grid for Helga. In (a) the four possibilities for a grid with a distance of $d_{\text{grid}} = 60\,\text{mm}$ and in (b) the two check patterns are shown. The placement of each antenna grid is indicated by a different color.

optimum placement of the receive antennas calculated above gives valuable insights into the channel capacity that could be achieved in theory. However, it does not seem to be a practical solution for clinical routine.

5.2.3 Placement of an Antenna Grid

A more practical approach is using a rectangular grid with a fixed distance between the receive antennas. This could be manufactured as a vest or belt for the patient which is then placed arbitrarily on the abdomen. This grid of antennas will be placed with some random variations to reflect the uncertainty of placement in a realistic scenario.

As the distance between neighboring receive antenna locations on the discretized abdominal surface is approximately 30 mm, the distances between the antennas of the antenna grids will be set to multiples of 30 mm. Hence, distances of $d_{\text{grid}} \in \{30\,\text{mm}, 60\,\text{mm}, 90\,\text{mm}, \text{and } 120\,\text{mm}\}$ between the receive antennas are investigated. For $d_{\text{grid}} = 30\,\text{mm}$ this means that an antenna is placed at every possible receive antenna location as indicated in Figure 4.14 and summarized in Table 4.2. If that distance is increased to 60 mm, only each second location of the aforementioned possible receive antenna location will be used for placing an antenna. This is shown in Figure 5.7a for Helga. In this case, antennas are placed either at all the blue, orange, red or green marked locations. Hence, there are four possible ways to place the antenna grid with $d_{\text{grid}} = 60\,\text{mm}$ on the abdominal surface. In case of Helga this leads to 50 to 53 antennas placed on the abdominal surface. The number of antennas varies because for placing the antenna grid only the abdominal surface as indicated in Figure 4.14 is considered. Table 5.1 shows the number of receive antennas that are placed on each phantom for each grid distance. If the antenna grid distance is increased even further to 90 mm or 120 mm, only every 3^{rd} or 4^{th} possible receive

Table 5.1: Minimum and maximum number of receive antennas placed on the respective phantom for a given grid distance and the check pattern. In each column the maximum number of antennas is highlighted in bold.

Phantom	d_{grid} in mm				Check pattern
	30	60	90	120	
Alvar	135	32–37	13–19	6–12	66–69
AustinMan 1	162	38–43	16–19	8–11	80–82
AustinMan 2	156	37–40	15–19	8–12	77–79
AustinWoman 1	152	35–42	13–20	6–12	75–77
AustinWoman 2	147	33–40	13–19	6–11	73–74
Donna	160	35–45	15–21	6–12	80–80
Golem	152	33–43	13–20	6–12	76–76
Hanako	137	29–40	11–18	6–11	68–69
Helga	**205**	50–53	21–24	11–15	102–**103**
Irene	115	26–32	9–16	4–9	57–58
Taro	109	24–31	10–13	5–10	54–55
VisibleHuman	203	45–**56**	19–**28**	11–**17**	101–102

antenna location is used to place an actual antenna. In these cases there are 9 and 16 possible placements of the antenna grid on the abdominal surface, respectively. As the distance between the antennas increases, the number of antennas that can be placed on the body is decreasing. For the example of Helga this means that for $d_{\text{grid}} = 90\,\text{mm}$ and $d_{\text{grid}} = 120\,\text{mm}$ only 21 to 24 and 11 to 15 antennas can be used, respectively. Moreover, a check pattern as shown in Figure 5.7b is investigated. For the check pattern two possible placements, indicated in blue and orange, are considered.

For each grid configuration on each phantom, the 10 %-outage capacity is determined. The results are shown in Figure 5.8 The figure shows the minimum and maximum values of the 10 %-outage capacity over all phantoms for the different distances between receive antennas. For a better overview of the plot, the names of the phantoms have been omitted and all values are sorted in ascending order. The graph can be read as follows. The dashed red curve for a grid distance of 120 mm shows that there is only one phantom in which the worst case 10 %-outage capacity is 5.51 Mbit/s. Hence, if an antenna grid with 120 mm spacing is placed arbitrarily on any of the 12 phantoms, the 10 %-outage capacity is at least 5.51 Mbit/s. Whereas, the 10 %-outage capacity is larger than 174.6 Mbit/s for all phantoms if the grid is placed in its optimal position on each of them. This is shown by the lowermost marker on the red solid line in Figure 5.8. Hence, the 10 %-outage channel capacity for each grid distance varies significantly depending on the exact placement on the abdominal surface. Especially, for large grid distances, variations of more than one

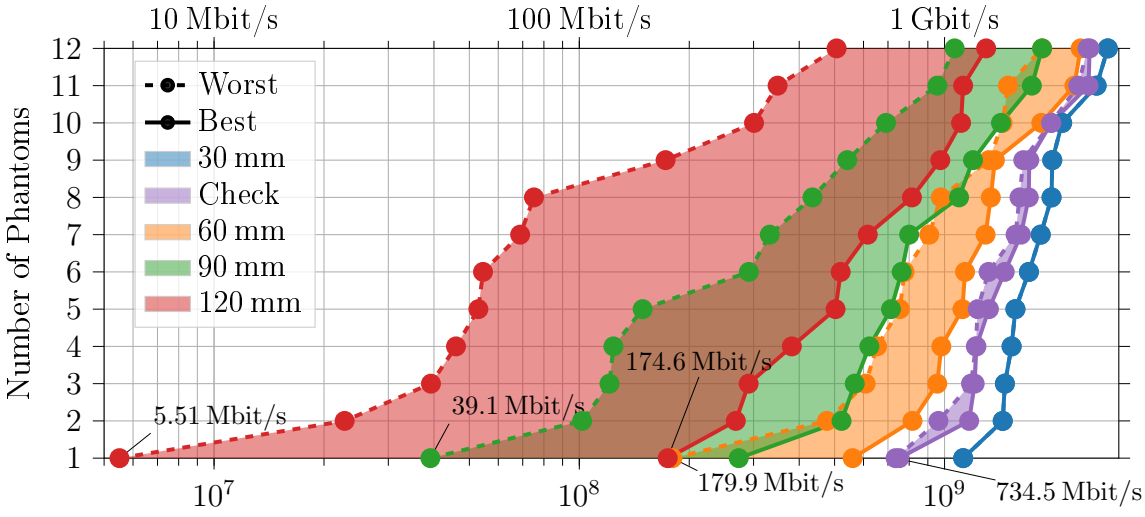

Figure 5.8: Number of phantoms that have a 10 %-outage capacity that is smaller or equal to the value shown on the abscissa. The dashed line shows the 10 %-outage capacity for the worst placement of each grid and the solid line the best.

order of magnitude are possible.

Moreover, the 10 %-outage capacity for every phantom is at least, i.e. for the worst case placement, 39.1 Mbit/s, 179.9 Mbit/s, and 734.5 Mbit/s for an antenna grid with distance of 90 mm, 60 mm, and the check pattern, respectively. The blue line indicates the maximum 10 %-outage channel capacity for all phantoms by using an antenna grid with $d_{\text{grid}} = 30\,\text{mm}$. These are the same values as shown in Figure 5.2. The higher the number of antennas, the lower is the chance of misalignment and poor performance. However, for smaller distances between the receive antennas more antennas are needed.

To achieve at least the same performance as with five optimally placed receive antennas, the grid distance would have to be set to 60 mm. In that case nearly any placement of the receive antenna grid would result at least in the same performance on any digital phantom with five optimally placed receive antennas. Only for Alvar, AustinWoman 2 and Irene the worst case placement of the grid leads to a 10 %-outage capacity slightly below the capacity for the optimized positions shown in Figure 5.2. Thus, 26 to 56 antennas would be needed, depending on the surface area of the abdomen, to achieve the same performance. These are a lot more antennas compared to the number of receive antennas in current products, which usually utilize eight receive antennas (cf. Table 3.1).

5.3 Physiological Properties

The results in the previous section showed that there is a large difference in 10 %-outage capacity between the best and the worst placement of an antenna grid on the abdominal surface. Especially, as there is a great difference between the different phantoms, it is interesting to know how the physiology of the phantoms influences the channel capacity. Hence, in this section it will be evaluated how the physiological parameters of the digital phantoms influence the channel capacity. The physiological properties of the phantoms were summarized in Table 2.2. They will be used here to investigate possible correlations to the 10 %-outage channel capacity. The following extends the results already published in [BB19] for the more accurate channel model derived in this thesis.

Figure 5.9 shows the 10 %-outage channel capacity of all the 12 digital phantoms vs. the waist circumference, the waist-to-height ratio, the ratio of abdominal muscle mass to fat mass, and the body mass index. In the figure, each phantom is represented by a distinct marker and the number of receive antennas is indicated by the color of the lines and markers. Next to the lines the correlation coefficient ρ between the respective property and the 10 %-outage capacity is denoted. For the 10 %-outage capacity the results from the previous section on the optimum placement of $N_{\mathrm{RX}} = 5$ and the maximum number of receive antennas were used. It can be observed that the trend over any of the properties shown in Figure 5.9 does not change significantly if the number of receive antennas is increased. However, the correlation ρ between the outage capacity and the physiological properties is changing slightly. The same could be observed for smaller values of N_{RX}, although these values are not shown here for clearness of the figure.

For all physiological properties it can be noted that there is no strict linear relationship between the 10 %-outage capacity and any of the properties. However, the general trend of the graphs for the waist circumference, the waist-to-height ratio and the body mass index shows that an increase in their value leads to a decrease of the 10 %-outage capacity. This behavior is supported by the correlation coefficient ρ which is smaller than -0.64 for all the aforementioned properties.

For Hanako a rather low 10 %-outage capacity can be observed compared to Taro and Irene which have a similar waist circumference, waist-to-height ratio and body mass index. This can be seen, for example, from the first three markers in the waist circumference plot of Figure 5.9. One reason might be that for Hanako also parts of the rectum are considered for placing a transmit antenna. However, the rectum

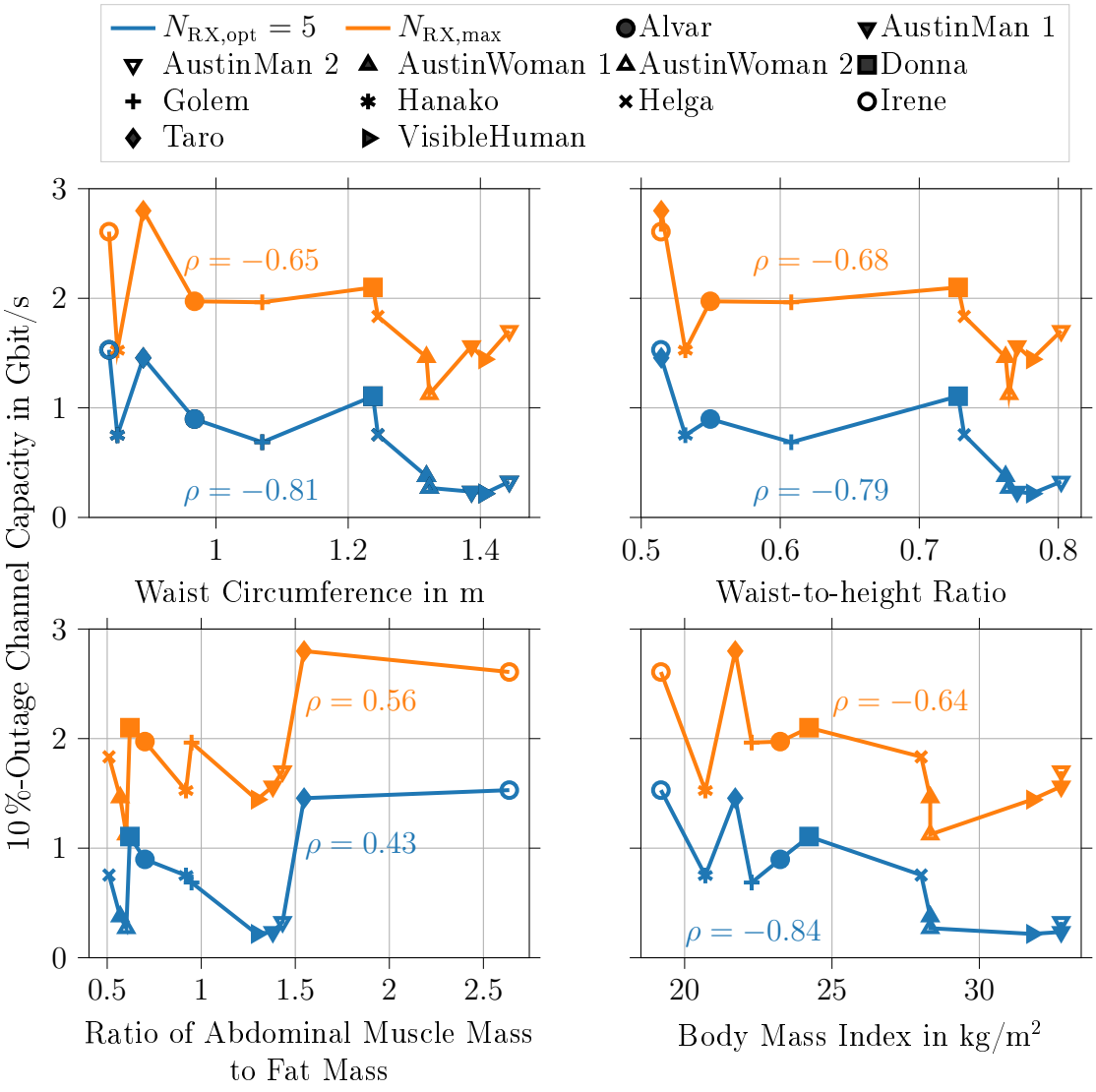

Figure 5.9: The 10 %-outage channel capacity obtained for $N_{RX} = 5$ and $N_{RX,max}$ receive antennas vs. various physiological properties of the digital phantoms.

is deep inside the abdominal cavity and obstructed by the uterus and the bladder. Hence, the channel capacity of these links is low. For Taro and Irene, the rectum is not labeled as detailed as for Hanako. Hence, no transmit antennas are placed that far inside the body for them.

In general, there is a negative influence of the waist circumference, the waist-to-height ratio and the body mass index on the 10 %-outage capacity. This is an expected result as the radio wave needs to propagate through more layers of tissue due to the larger volume of the abdomen. In contrast to the other properties, the 10 %-outage capacity gets larger for an increase of the ratio of abdominal muscle mass to fat mass. One reason might be that the phantoms with a large muscle-to-fat ratio (e.g. Taro and Irene) are more likely to be non-overweight. Hence, the propagation paths are shorter with fewer losses although muscle tissue itself has a higher attenuation than fat.

The data basis of 12 phantoms is too small to derive more precise relationships between the channel capacity and the physiological properties. Nevertheless, it can be stated that from the obtained results that, as expected, overweight has a serious negative effect on the channel capacity.

5.4 Dielectric Properties

As discussed in Section 2.1 there has been a recent and comprehensive study from Fornes-Leal *et al.* concerning the dielectric properties of tissues in the abdominal region [FCF+19]. Their results show that there is a huge uncertainty in the measurement of the tissue properties compared with the most used database from Gabriel *et al.* [Gab96]. Figure 4.13a shows these variations in terms of the path loss in dB/cm. For most of the tissues the path loss is higher than using the measurements from Gabriel *et al.*, which were used for the results presented so far in this thesis. In [FCF+19] the dielectric properties for the 21 most common tissues were measured. For the calculations in this section, we replaced all the dielectric properties for which new values were obtained in [FCF+19]. The dielectric properties of the remaining tissues are kept at the values from Gabriel *et al.* [Gab96]. A detailed overview over the exact tissue mapping can be found in Appendix A.1

As in Section 5.2 the optimum placement of up to five receive antennas in terms of the 10 %-outage channel capacity is determined. For multiple receive antennas a selection combining scheme is implemented. Apart from the tissue properties the setup for the computations is the same as in Section 5.2.

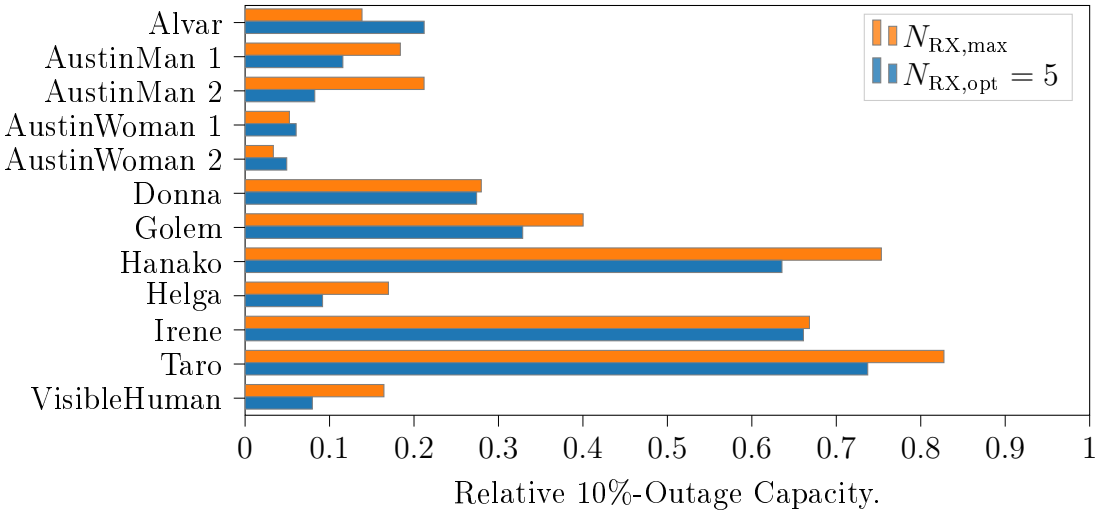

Figure 5.10: Relative 10 %-outage channel capacity when using the tissue properties from Fornes-Leal *et al.* [FCF+19] instead of the ones from Gabriel *et al.* [Gab96].

Figure 5.10 shows the relative 10 %-outage channel capacity for 5 receive antennas at their optimum locations and for $N_{\mathrm{RX,max}}$ receive antennas. It can be seen that the influence of the modified tissue properties varies tremendously between the phantoms. For Taro the maximum 10 %-outage capacity, achieved using $N_{\mathrm{RX,max}}$ antennas, is reduced to only 0.83 times the value compared to using the tissue properties from [Gab96]. This means a reduction from 2.80 Gbit/s to 2.32 Gbit/s. For AustinWoman 2 the capacity using $N_{\mathrm{RX,max}}$ antennas is even reduced by a factor of more than 30. Moreover, the same antenna setup is affected differently for each phantom. For most of them, the relative 10 %-outage capacity for five antennas is smaller than for all $N_{\mathrm{RX,max}}$ antennas. However, for some this is the other way around.

In general, the outage capacity is reduced more for those phantoms which have a large amount of fat in their abdomen. This is an expected result because the path loss per cm is more than doubled on a dB scale for fat as shown in Figure 4.13a. The increase in path loss for, e.g., muscle is not as large. Whereas for other less common tissues a lower path loss is predicted by Fornes-Leal *et al.* [FCF+19].

The optimum placement of the five receive antennas also changes slightly compared to the results based on the dielectric properties from Gabriel *et al.* [Gab96]. On average the optimum placement for one to five antennas is shifted only by 34.6 mm. However, in one case the antenna placement is shifted by 138 mm.

It can be concluded from this section that it is of vital importance to obtain more data on the dielectric properties of tissues in the human abdomen. Especially, the heterogeneity and the deviations between humans needs to be investigated further.

Moreover, as proposed in [MSP+19] special care has to be taken to avoid the dehydration of the tissue samples in the measurement process. For exact reproduction, the exact conditions of the measurement procedures should be published along with the resulting data. However, this is not considered in most of the publications regarding dielectric tissue properties.

From the outage capacity calculations in this section, differences up to a factor of 30 in the 10 %-outage channel capacity can be observed. This uncertainty comes on top of the uncertainty due to the physiological condition of the patient. Hence, from these computations a rather large safety margin needs to be incorporated to actually build a capsule endoscope deploying ultra wideband transmission working in an arbitrary patient. When placing $N_{\mathrm{RX,max}}$ antennas on the abdomen, i.e. in a grid with distance of $d_{\mathrm{grid}} = 30\,\mathrm{mm}$ between the antennas, the 10 %-outage capacity is 287.4 Mbit/s for VisibleHuman using the dielectric properties from [FCF+19]. However, in the other extreme it could be up to 2.80 Gbit/s using the dielectric properties from [Gab96] based on Taro. Hence, there is a huge uncertainty of one order of magnitude concerning the 10 %-outage channel capacity.

As derived in Section 3.1 a gross data rate of 3 Mbit/s needs to be guaranteed to substantially improve state of the art capsule endoscopes. Furthermore, it can be seen from Figure 5.8 that using an antenna grid with distance of 60 mm between the antennas results in a 10 %-outage capacity of 179.9 Mbit/s. Combining this with the uncertainty due to the tissue properties found in this section, the capacity might be reduced to just 6.0 Mbit/s, which is just above the required data rate of 3 Mbit/s from above. This would mean that 24 to 56 antennas – depending on the geometry of the body – would need to be placed on the abdomen (see Table 5.1 for details on the number of antennas for each of the antenna grids).

5.5 Comparison to Transmission in MICS Band

Communication with implanted sensors may take place in the Medical Implant Communication Service (MICS) band from 402 MHz to 405 MHz. Each user is allowed to occupy a bandwidth of 300 kHz. One possibility to communicate in this frequency range is using the IEEE 802.15.6 standard [Ins12]. The details of this standard are discussed in Section 3.2. Throughout the standardization a channel model for in-body communication in the MICS band was developed [YS10]. In contrast to the ultra wideband channel modeling, it was observed that the proposed layer modeling approach is not suitable for channel modeling in the MICS band. For that reason,

the following investigation uses the channel model from [YS10]. The development of the channel model is described in [SYH+09], the results of the channel modeling were confirmed by complementary simulations during the standardization described in [KLP+08].

The channel model developed by Sayrafian-Pour *et al.* in [SYH+09] is a pure path loss model with log-normal distributed shadowing term. The path loss model is derived from numerical simulations of one male digital phantom, whose origin is not specified any further. A custom designed antenna was used as the implant antenna. This antenna was placed at two deep tissue locations (ca. 100 mm below the skin) in the abdomen. From these locations the path loss was computed for a receiver placed on any point within 20 mm above the body surface. The resulting path loss model was found to be

$$\mathrm{PL}_{dB}^{\mathrm{MICS}}(d) = 47.14\,\mathrm{dB} + 4.26\,\mathrm{dB} \cdot 10 \cdot \log_{10}\left(\frac{d}{50\,\mathrm{mm}}\right) + \mathcal{N}(0, 7.85\,\mathrm{dB})\,. \tag{5.6}$$

Due to European regulations a single system is only allowed to use a bandwidth of at most 300 kHz in the MICS frequency range [Eur16c]. To investigate the potential in the MICS band, also the complete bandwidth of 3 MHz will be considered in the following computations. Although, it is not allowed by current regulations it can give valuable insights on the potential for in-body communication in the MICS band. Using the path loss model from (5.6) the channel capacity is computed for a bandwidth of 300 kHz and 3 MHz.

Again the same setup of transmit and receive antenna locations as described in 4.3.2 is used. For multiple antennas a selection combining scheme is implemented since only a path loss model is available. As (5.6) only depends on the distance between transmitter and receiver, only the respective distances between transmit and receive antennas are taken into account. Hence, the only difference between the phantoms that is considered here is a different distribution of the distances between transmitter and receiver.

Figure 5.11 shows the 10 %-outage capacity for the two bandwidths in MICS band for different receive antenna configurations based on the path loss model from (5.6). Additionally, the minimum 10 %-outage capacity from all phantoms for ultra wideband communication is displayed for the same receive antenna configurations. The values of the ultra wideband transmission are taken from the results in Sections 5.2 and can be found in Figures 5.2 and 5.8 as well. They are based on the dielectric properties from [Gab96]. First, the optimum placement of one and two antennas

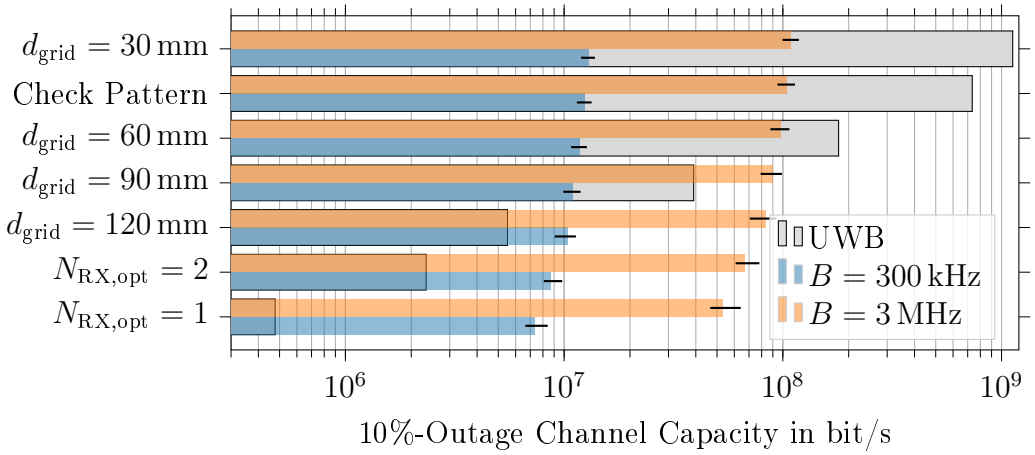

Figure 5.11: The blue and orange bars show the average 10 %-outage channel capacity over all phantoms obtained for the given antenna configuration in MICS band for a bandwidth of 300 kHz and 3 MHz, respectively. The small black error bars on top of them indicate the minimum and maximum value obtained for any phantom. The gray bars show the minimum 10 %-outage capacity for UWB transmission in UWB channel 1 centered at 3.49 GHz for any phantom. These are the values obtained in the last sections from the layer modeling approach.

Table 5.2: Minimum and maximum number of receive antennas placed on any phantom for a given grid distance and the check pattern. This is a summary of Table 5.1.

d_{grid} in mm	30	60	90	120	Check pattern
No. of Antennas	109–203	24–56	9–28	4–17	54–103

concerning the 10 %-outage capacity is shown. Second, the placement of an antenna grid with varying distance between the antennas as discussed in Section 5.2 is considered. Finally, the 10 %-outage capacity using all possible receive antenna locations ($d_{\text{grid}} = 30\,\text{mm}$) is depicted. The minimum and maximum number of antennas for each grid distance are given in Table 5.2 which is a summary of Table 5.1.

For one optimally placed receive antenna the average 10 %-outage capacity in MICS band is 7.3 Mbit/s and 53.1 Mbit/s for 300 kHz and 3 MHz of bandwidth, respectively. These values increase to 12.9 Mbit/s and 109.1 Mbit/s when using the maximum number of receive antennas. In the ultra wideband case a 10 %-outage capacity of only 476.9 kbit/s can be guaranteed for one optimum receive antenna in an arbitrary phantom. However, this value increases to at least 1.1 Gbit/s for the maximum number of receive antennas.

The error bars on top of the blue and orange bars of MICS band results indicate the minimum and maximum values obtained for any phantom in any of the given configurations. The deviation from the average is approximately ±1 Mbit/s for

$B = 300\,\text{kHz}$ and approximately $\pm 10\,\text{Mbit/s}$ for $B = 3\,\text{MHz}$. Hence, the variation of the channel capacity for different phantoms is small compared to the ultra wideband results. However, it has to be kept in mind that the channel model (5.6) does not account for any physiological differences between the phantoms. Whereas, for the ultrawide band results in Figure 5.11, the layer modeling approach is used.

It can be seen from Figure 5.11 that, with increasing number of antennas, i.e. smaller grid distance, the 10 %-outage capacity increases in both frequency bands. However, compared to the increase using ultra wideband transmission, the increase in capacity for transmission in MICS band is only small. In MICS band the 10 %-outage capacity is just approximately doubled when the number of receive antennas increases from one optimally placed antenna to $N_{\text{RX,max}}$ antennas. For the same increase in receive antennas, an increase over up to three orders of magnitude can be observed for ultra wideband communication.

The maximum achievable channel capacity in MICS band is much lower than for ultra wideband communication. For example, for a bandwidth $B = 300\,\text{kHz}$ the maximum 10 %-outage capacity for $N_{\text{RX,max}}$ receive antennas is 13.8 Mbit/s, which is indicated by the right end of the error bar in Figure 5.11. Comparing this to the ultra wideband results, it can be seen that already an antenna grid with $d_{\text{grid}} = 90\,\text{mm}$ leads to a higher 10 %-outage capacity on any phantom. Thus, in the UWB case at most 28 antennas placed on an arbitrary phantom perform better than more than 100 antennas used in MICS band. Moreover, a grid of receive antennas with $d_{\text{grid}} = 120\,\text{mm}$ would lead to a higher channel capacity in eleven of the twelve digital phantoms for ultra wideband transmission compared to MICS band transmission. This can be seen from the red dashed line in Figure 5.8, where the marker for two phantoms shows a value larger than 20 Mbit/s. Thus, there are 11 phantoms with a 10 %-outage capacity larger than 20 Mbit/s. To put this into perspective, this would mean to use up to 109 or 205 receive antennas in MICS band and still achieve a worse performance than using just 9 to 28 antennas in ultra wideband communication.

Hence, to achieve a 10 %-outage capacity of well above 10 Mbit/s it is necessary to use ultra wideband communication. However, it is only possible to outperform transmission in MICS band with $B = 300\,\text{kHz}$ by ultra wideband communication if the antennas of a receive antenna grid are placed at most $d_{\text{grid}} = 90\,\text{mm}$ apart, which would result in about 9 to 28 receive antennas depending on the physiology of the patient.

If one could use the complete MICS bandwidth of 3 MHz, in the best case a 10 %-outage capacity of 118.4 Mbit/s could be achieved. This is shown by the right end of

the error bar in Figure 5.11 for $N_{\mathrm{RX,max}}$ antennas. In this case an antenna grid with a distance of $d_{\mathrm{grid}} = 60\,\mathrm{mm}$ (24 to 56 antennas) would be required to outperform the channel capacity of the MICS band using ultra wideband transmission.

In general, it can be said that for small numbers of antennas the 10 %-outage capacity in MICS band is larger than for ultra wideband communication. However, if it is feasible to place many antennas on the abdominal surface a significant performance gain may be expected from ultra wideband transmission.

5.6 Summary

This chapter dealt with the computation of the channel capacity for ultra wideband in-body communication based on the layer modeling approach introduced in Chapter 4. The channel capacity was chosen as it allows to determine the theoretic fundamental limits on the data rate of any communication channel. In this chapter different influences on the channel capacity were discussed.

It was shown that the 10 %-outage channel capacity of an ultra wideband system decreases with the transmission bandwidth of the system, when the constant transmit power is distributed uniformly over frequency. Only for a few communication links it could be observed that the 10 %-outage capacity increases with increasing bandwidth. For most of the communication links the high attenuation counteracts the benefit of using a larger bandwidth. As a conclusion the bandwidth should be kept at the minimum value of 500 MHz for ultra wideband communication. Thus, the ultra wideband channel 1 with a nominal bandwidth of 500 MHz centered around 3494.4 MHz was used for all following investigations.

Furthermore, it was observed that the channel capacity strongly depends on the placement of the receive antennas on the abdominal surface. The optimum placement of up to five receive antennas regarding the 10 %-outage capacity was determined. First of all, it was observed that by increasing the number of receive antennas from one to five the 10 %-outage capacity increases by two or even three orders of magnitude depending on the digital human phantom. The 10 %-outage capacity for one receive antenna ranges from 477.3 kbit/s to 12.6 Mbit/s, for five optimally placed receive antennas this values is in the range of 217.5 Mbit/s to 1.5 Gbit/s. Using the optimum placement of receive antennas found for one phantom on another phantom results in a considerable degradation of the performance. Doing this, the 10 %-outage capacity is rarely larger than 40 % of the capacity using the optimum placement on that phantom. This is mainly caused by the fact that already small

deviations from the optimum position may lead to detrimental reductions of the 10 %-outage capacity. When placing the receive antennas with a tolerance of 50 mm around the optimum position, the 10 %-outage capacity may be reduced by up to approximately one order of magnitude compared to the optimum.

In addition to the high accuracy requirements on the placement, also no clear general pattern could be derived that is valid for all phantoms. Hence, a different sub-optimal, but more practical approach was considered. The 10 %-outage capacity was computed for a regular grid of antennas with a given distance between the antennas. This grid was then placed randomly on the abdominal surface. Thus, the worst-case and best-case placement regarding the 10 %-outage capacity could be determined. The smaller the grid distance, the smaller are the variations between best and worst case placement because less variations in the placement are possible. To achieve at least the same performance as with five optimally placed receive antennas, the grid distance would have to be set to 60 mm. In that case nearly any placement of the receive antenna grid would result at least in the same performance on any digital phantom as five optimally placed receive antennas. However, instead of only five antennas up to 56 receive antennas would be needed.

In the next step, the relationship of the 10 %-outage capacity to various physiological properties that were assumed to influence the communication performance was investigated. It could be shown that there is a strong negative correlation between the 10 %-outage capacity and the waist circumference, the waist-to-height ratio as well as the body mass index. Hence, all investigated indicators for obesity cause a decrease in channel capacity when they are increasing. For the ratio of abdominal muscle mass to fat mass a positive correlation was found. However, this is most likely due to the fact that two of the digital phantoms, namely Taro and Irene, are rather muscular but also slim.

As the last effect on the channel capacity of the ultra wideband communication, the dependency on the dielectric properties used in the computations is investigated. A recent in-vivo measurement campaign on anesthetized pigs [FCF+19] revealed that there is – depending on the tissue – a huge gap to the most commonly used values from Gabriel *et al.* [Gab96]. Especially the path loss of fat and muscle increases drastically by using these new measurements. As these are two of the most common tissues in the abdomen, the effect on the channel capacity is quite large. It was found that due to the change in the dielectric properties, the 10 %-outage capacity is reduced by a factor between 1.2 and 30 depending on the phantom. Thus, more detailed data is needed on the actual dielectric properties of human tissue and their variation, as the value has a large impact on the channel capacity. Taking this

additional uncertainty into account, the most dense grid of receive antennas could result in a 10 %-outage capacity of 287.4 Mbit/s on one phantom using the newly obtained dielectric properties or up to a capacity of 2.8 Gbit/s on another using the most common dielectric properties. Hence, there is an uncertainty of one order of magnitude in 10 %-outage capacity over all phantoms.

Finally, the channel capacity for communication in the Medical Implant Communication Service (MICS) band was computed based on a channel model from the IEEE 802.15.6 standardization. The layer modeling approach was found to be not feasible for this frequency range. It was shown that the variation between different phantoms is negligible, which is mostly due to the simple path loss model. However, depending on the target data rate for a capsule endoscopy application it could be beneficial to use the MICS band if only a small number of receive antennas are to be deployed on the abdominal surface. In general, for small numbers of antennas the 10 %-outage capacity in MICS band is larger than for ultra wideband communication. By just using one receive antenna in its optimum position the 10 %-outage capacity in a 300 kHz MICS band is still larger than it is for ultra wideband transmission using up to 17 receive antennas, which is equivalent to a grid distance of 120 mm. But, for larger numbers of antennas, the use of ultra wideband communication leads to significant performance gains. Already the usage of an antenna grid with 9 to 28 antennas results in a larger 10 %-outage capacity in any configuration for ultra wideband communication compared to communication in MICS band.

Chapter 6

Bit Error Rate Performance

After deriving the channel capacity for various configurations in the previous chapter, in this chapter the bit error rate performance of a specific transmitter and receiver configuration will be investigated. An ultra wideband impulse radio transmitter will be simulated on its way through the digestive tract. The communication channel between the transmitter in the capsule and multiple receive antennas on the abdominal surface will be modeled by the layer modeling approach introduced in Chapter 4.

Ultra wideband impulse radio does not use any quadrature modulator or demodulator. The transmission takes place in the passband without any explicit upconversion. The transmit pulses are designed in such a way that they can directly propagate from an antenna. Pulse position modulation (PPM) is the modulation scheme that is most commonly used for ultra wideband impulse radio. Although the bandwidth efficiency of PPM is rather small, the power efficiency increases with the modulation order [BLM04]. This effect will be investigated in more detail in the following Section 6.1. Asymptotically it is even possible to reach channel capacity as the modulation order $M \to \infty$ [Gol49][Tur59]. However, this cannot be achieved in practice as in this case the bandwidth would also go to infinity and the delay between subsequent pulses as well. These arguments make PPM the preferred modulation scheme for ultra wideband in-body communication, which is investigated in most of the related publications, e.g. in [KFR+12], [KLN+07], [NRB12], and [WMW09].

This chapter is structured in the following way. First, fundamentals for pulse position modulation are summarized. Second, the communication channel model determined in Chapter 4 in conjunction with the spectral regulations for UWB communication will be used to determine a suitable pulse shape for the present scenario. Based on that pulse shape an equivalent baseband channel model will be derived.

This equivalent baseband channel model will be used to determine the bit error probability that may be achieved using a practical implementation in contrast to the computations of the channel capacity in Chapter 5. The performance of different receive antenna setups will be compared by evaluating the coverage, i.e. the percentage of all the transmitter locations at which a communication with a given receiver is possible at a certain target bit error rate (BER). Finally, an overview over further influences on the quality of service is presented.

6.1 Pulse Position Modulation

In a pulse position modulation (PPM) system the information carrying symbols are distinguished according to their position in time. A reference pulse $p(t)$ is transmitted in one of M time slots of duration T_{slot} to modulate the information. PPM is an orthogonal modulation scheme.

The transmit signal for PPM can be written as

$$x(t) = \sum_{n=-\infty}^{\infty} \alpha_n \cdot p\left(t - nT_s - d_n T_{\text{slot}} - \frac{T_{\text{slot}}}{2}\right), \tag{6.1}$$

where $p(t)$ is the pulse shape of the transmitted pulse, T_s is the symbol duration, T_{slot} is the duration of one slot, $d_n \in \{0, 1, \ldots, M-1\}$ is the transmitted symbol, which in our case is the same as the slot number, and α_n is a random variable that takes the values ± 1 with equal probability. The regular pattern of the pulses in the transmit signal leads to comb lines in the spectrum. One way to reduce these is to use a so-called pseudo-random polarity sequence α_n [NM03]. Figure 6.1 shows an exemplary transmit signal $x(t)$ for a 4-PPM using a rectangular pulse shape $p(t)$. The pulse shape $p(t)$ has to be chosen depending on the channel characteristics and spectral requirements. More details on the selection of the pulse shape will be given in Section 6.2.2. It is assumed in the following that the pulse shape, once determined, is kept constant, i.e. T_{slot} will not change when the modulation order is changed. In IEEE 802.15.4, a guard interval is defined to cope with interference from multipath propagation [Ins20]. Depending on the channel conditions the length T_G of the guard interval can be varied. To ensure a constant sampling rate at the receiver, T_G is an integer multiple of T_{slot}. Hence, the total symbol duration is $T_s = M \cdot T_{\text{slot}} + T_G$.

One major advantage of PPM is that coherent as well as non-coherent demodulation is possible. The receiver may use either a correlation or an energy detector to determine the slot numbers of the received pulses. A correlation receiver uses a

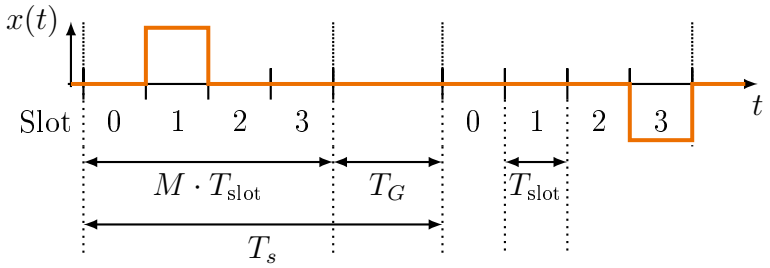

Figure 6.1: The timing of pulse position modulation for the example of a 4-PPM using a rectangular pulse $p(t)$.

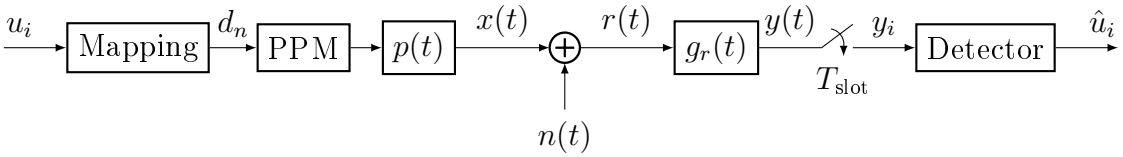

Figure 6.2: The transmission chain for pulse position modulation in a real valued AWGN channel.

receive filter that is matched to the transmit pulse shape and decides for the slot with the maximum correlation. The energy detector decides for the slot with the maximum received energy. Previous investigations in [BKB19] have shown that using an energy detector leads to a drastic increase in the bit error rate. Thus, only the correlation receiver will be covered in this thesis.

The transmission chain considered in the following is depicted in Figure 6.2. The transmit bits u_i are mapped to symbols d_n, which indicate the slot number of the pulse. The receive filter $g_r(t)$ is matched to the transmit filter $p(t)$, i.e. $g_r(t) = p^*(T_{\text{slot}} - t)$. The transmit filter $p(t)$ is assumed to be non-zero only in the interval $\left[-T_{\text{slot}}/2, T_{\text{slot}}/2\right]$. Hence, the 1. Nyquist condition is satisfied after sampling at a rate of $f_{\text{slot}} = \frac{1}{T_{\text{slot}}}$. Thus, the noise $n(t)$ remains white after sampling. Moreover, it is assumed that the receiver is perfectly synchronized to the transmit signal. For each PPM symbol a total of M samples $y_i, i \in \{0, 1, \ldots, M-1\}$, are fed into the detector. The detector decides for the index i of the largest sample and maps this to the estimated received bit vector $\hat{u}_i$. As the sampling rate $\frac{1}{T_{\text{slot}}}$ is not the same as the symbol rate $\frac{1}{T_s}$, the relationship of $\frac{E_b}{N_0}$ to the signal to noise power ratio $\frac{P_x}{P_N}$ depends not only on the modulation order M but also on T_{slot} and T_s. This will be shown in the following.

To avoid adverse health effects, regulations concerning ultra wideband communication in the human body refer to the average transmit power and the energy of the pulses. As discussed in Section 2.3, the constraints regarding the pulse energy are

much easier fulfilled than the constraints concerning the average transmit power, to limit the heating of the tissue. Moreover, it will be shown in Section 6.2.2 that by limiting the transmit power to $P_{\mathrm{TX}} = 21.5\,\mathrm{mW}$, the pulse energy is multiple orders of magnitude below the limits imposed by the ICNIRP. Thus, we focus on a constant average transmit power in the following. As the symbol duration T_s increases with the modulation order, the energy per symbol E_s has to increase as well in order to keep the average power constant. The average power of the signal $x(t)$ is then defined as

$$P_x = \frac{E_s}{T_s} = \frac{1}{T_s} \int_{-\infty}^{\infty} \left| p(t; M) \right|^2 \mathrm{d}t \,, \tag{6.2}$$

where the modulation order M is added as a second argument to $p(t)$ here to highlight the dependence of E_s and the pulse shape on M. As discussed above, the 1. Nyquist condition is satisfied after sampling. Hence, the noise power is

$$P_N = N_0 B = N_0 f_{\mathrm{slot}} \,, \tag{6.3}$$

where $B = f_{\mathrm{slot}}$ is the sampling rate of the signal at the detector input. Thus, the SNR of a PPM signal can be expressed in terms of $\frac{E_b}{N_0}$ as

$$\frac{P_x}{P_N} = \frac{E_s}{T_s} \cdot \frac{1}{N_0 f_{\mathrm{slot}}} = \frac{\log_2(M)}{T_s \cdot f_{\mathrm{slot}}} \cdot \frac{E_b}{N_0} \,. \tag{6.4}$$

Moreover, T_s is also a function of M. Hence,

$$\frac{P_x}{P_N} = \frac{\log_2(M)}{(M T_{\mathrm{slot}} + T_G) f_{\mathrm{slot}}} \cdot \frac{E_b}{N_0} \tag{6.5}$$

$$\Leftrightarrow \frac{E_b}{N_0} = \frac{M}{\log_2(M)} \cdot \frac{P_x}{P_N}\bigg|_{T_G=0} \,. \tag{6.6}$$

It can be seen from (6.6) that for a fixed signal to noise power ratio $\frac{P_x}{P_N}$ the energy per bit to noise density ratio $\frac{E_b}{N_0}$ increases proportional to $\frac{M}{\log_2 M}$ for $T_G = 0$. Thus, the bit error probability is reduced for higher order modulations at the same $\frac{E_b}{N_0}$. This will be shown in the following.

The symbol error probability for M-PPM in an additive white Gaussian noise (AWGN) channel using a correlation receiver is given by [BLM04]

$$\Pr(\hat{d}_n \neq d_n | d_n) = 1 - \int_{-\infty}^{\infty} f_Y(y) \left(1 - \frac{1}{2} \operatorname{erfc}\left(\frac{y}{\sqrt{2}\sigma_N} \right) \right)^{M-1} \mathrm{d}y \,, \tag{6.7}$$

where

$$f_Y(y) = \frac{1}{\sqrt{2\pi\sigma_N^2}} e^{-\frac{(y-1)^2}{2\sigma_N^2}} . \tag{6.8}$$

The average energy $E\left\{\left|y(t)\right|^2\right\}$ of the output $y(t)$ of the correlation receiver is normalized to 1 such that the noise variance is $\sigma_N^2 = \frac{N_0}{2E_s}$. Each y_i at the detector input is an independent Gaussian distributed random variable with zero mean except for the correct y_i, which has a mean of 1. Hence, under the assumption of perfect synchronization, all $M-1$ erroneous detections are equally likely. The bit error probability for M-PPM can then be written as [BLM04]

$$P_b = \Pr(\hat{d}_n \neq d_n | d_n) \cdot \frac{M/2}{M-1} . \tag{6.9}$$

Figure 6.3 shows the bit error probability of M-PPM in an AWGN channel. It can be seen that the bit error probability decreases for larger modulation order M. For a constant slot duration T_{slot}, the symbol duration T_s increases linearly with M. Hence, for an average transmit power constraint, the energy of one symbol increases linearly with M. On the other hand the number of bits in one symbol increases only logarithmic in M. Hence, the energy that is available per bit is getting larger.

As can be seen from Figure 6.3, pulse position modulation is getting more and more energy efficient the larger M gets. On the other hand the bandwidth efficiency η_M

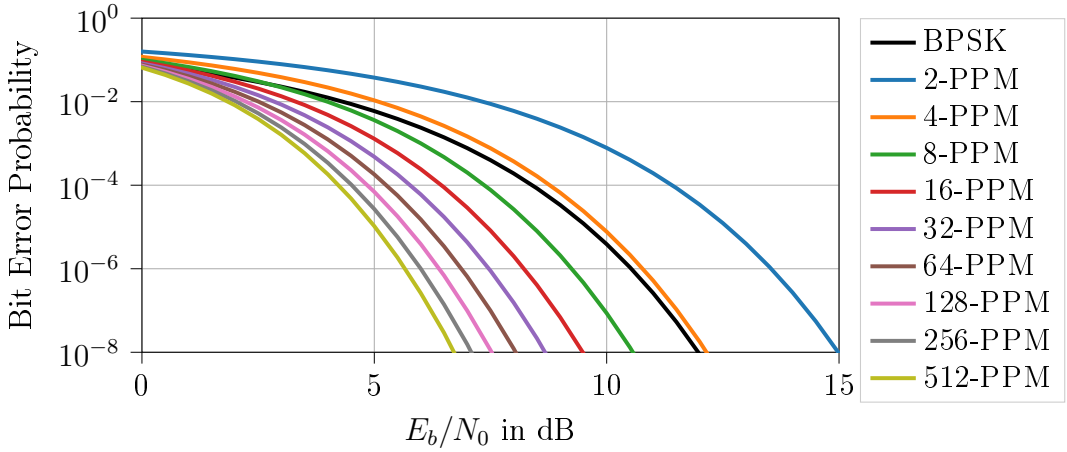

Figure 6.3: The bit error probability of M-PPM in an AWGN for different modulation orders M.

in bit/(s Hz) for PPM decreases with M as follows

$$\begin{aligned}\eta_M &= \frac{\frac{1}{T_s}\log_2(M)}{f_{\text{slot}}} = \frac{\log_2(M)}{(MT_{\text{slot}} + T_G)\cdot f_{\text{slot}}} \\ &= \left.\frac{\log_2(M)}{M}\right|_{T_G=0} . \end{aligned} \tag{6.10}$$

For common quadrature modulation schemes like quadrature amplitude modulation (QAM) or phase shift keying (PSK) the bandwidth efficiency increases with the modulation order whereas the energy efficiency decreases [BLM04]. Nevertheless, for ultra wideband communication the main restriction is the average power limit, where the occupied bandwidth is of minor concern. Hence, pulse position modulation is the favorable choice in this scenario given the above restrictions.

6.2 Development of an Equivalent Baseband Channel Model

6.2.1 Overview

Usually, ultra wideband communication systems are simulated in the real valued passband as there is no natural relation to the equivalent baseband as it is for narrowband signals and systems. However, in some scenarios, e.g. in [MBC+05], the equivalent baseband approach is considered to reduce the computational load of the simulation which arises from the large sampling rate in passband. A similar approach will be considered in this chapter. However, the transformation from bandpass to equivalent baseband and vice versa is only used as a tool for the simulation.

Figure 6.4 shows the transmission chain of an ultra wideband PPM system in the real passband. The transmit bits u_i are mapped and modulated according to the pulse position modulation explained in Section 6.1. This signal is then filtered with the pulse shaping filter $p(t)$ and transmitted via the transmit antenna. The choice of the pulse shaping filter will be discussed in the next Section 6.2.2. For ultra wideband signals the antenna behaves approximately like a derivation device [GMK07][Höh13][MKP+04]. Hence, the transmit and the receive antennas will be modeled by a derivative operation $\frac{\mathrm{d}}{\mathrm{d}t}$. The received signal is then the second derivative of the transmitted signal [Höh13].

In this chapter, the approximated channel transfer function $\tilde{\mathcal{H}}_{\mathbf{t}_i \to \mathbf{r}_j}(f; c)$, i.e. (4.45) derived in Section 4.4, is used. The additive noise $n(t)$ is assumed to be white and Gaussian with variance $\sigma_N^2 = \frac{N_0}{2}$.

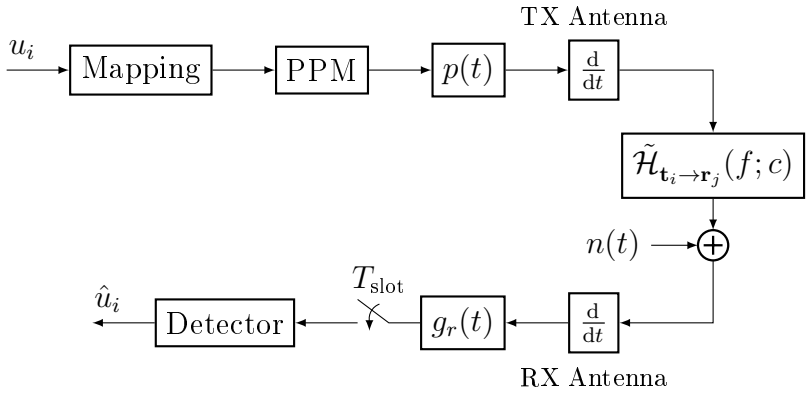

Figure 6.4: The ultra wideband transmission chain in the real valued passband from a transmitter at $\mathbf{t}_i$ to a receiver at $\mathbf{r}_j$.

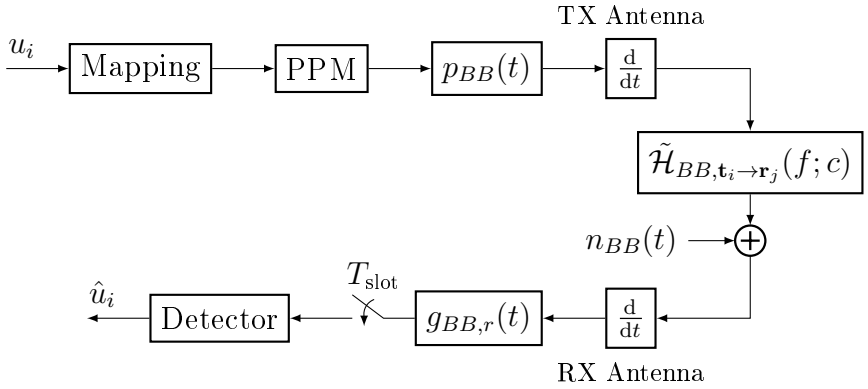

Figure 6.5: The ultra wideband transmission chain in equivalent baseband from a transmitter at $\mathbf{t}_i$ to a receiver at $\mathbf{r}_j$.

A coherent correlation receiver is assumed. Thus, the receive filter $g_r(t)$ is matched to the second derivative of $p^*(T_{\mathrm{slot}}/2 - t)$, i.e. $g_r(t) = \frac{\mathrm{d}^2}{\mathrm{d}t^2} p^*(T_{\mathrm{slot}}/2 - t)$. The correlator output is sampled at the slot rate $\frac{1}{T_{\mathrm{slot}}}$. Finally the transmitted bits are estimated using a hard-decision detector.

To generate the equivalent baseband channel model, it is assumed that the received signal is downconverted using a carrier frequency f_c before sampling at the receiver. The upconversion at the transmitter is included in the choice of the pulse shape. Only pulses which can directly propagate from an antenna will be considered. The carrier frequency should be selected based on the pulse shape such that most of the signal energy is captured inside the passband of the receive filter. As the down-conversion itself and all other components of Figure 6.4 are linear they can be recombined and simplified to the equivalent baseband model shown in Figure 6.5. The equivalent baseband pulse shape is then computed as

$$p_{BB}(t) = \frac{1}{2}\left[p(t) + j\mathbb{H}\{p(t)\}\right] e^{-j2\pi f_c t}, \tag{6.11}$$

where $\mathbb{H}\{f(x)\}$ is the Hilbert transform of $f(x)$. Likewise, the equivalent baseband channel impulse response $h_{BB,\mathbf{t}_i\to\mathbf{r}_j}(t;c)$ and the corresponding transfer function $\tilde{\mathcal{H}}_{BB,\mathbf{t}_i\to\mathbf{r}_j}(f;c)$ as well as the equivalent baseband receive filter $g_{BB,r}(t)$ can be obtained.

The equivalent baseband model from Figure 6.5 is now converted into a discrete time equivalent baseband model as depicted in Figure 6.6. Under the assumption that the matched filter condition mentioned above is fulfilled and that the pulse $p(t)$ is only non-zero in the interval $\left[-T_{\mathrm{slot}}/2, T_{\mathrm{slot}}/2\right]$, the 1. Nyquist condition is satisfied. Hence, the noise $n_{BB}[n]$ remains white after sampling. The overall impulse response $h_{BB}[n]$ includes transmit and receive filter, as well as the antennas and the channel

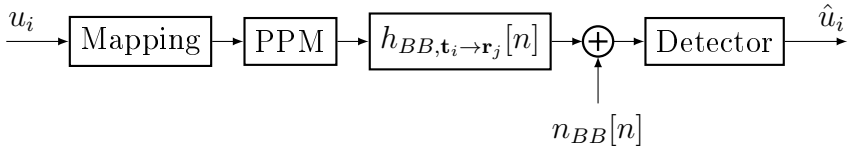

Figure 6.6: The discrete time equivalent baseband transmission chain from a transmitter at $\mathbf{t}_i$ to a receiver at $\mathbf{r}_j$.

transfer function sampled at a rate of $\frac{1}{T_{\text{slot}}}$. Now, to completely determine $h_{BB}[n]$ only the pulse shaping filters are missing. Hence, in the next section an appropriate set of parameters for the pulse shaping filters will be determined. Afterwards, the characteristics of the resulting discrete time equivalent baseband channel model will be analyzed.

6.2.2 Pulse Shaping

A variety of different pulse shapes are investigated in literature to be used for impulse radio signaling [Di 06][Wen07]. The most important property of an ultra wideband pulse is that it should not contain any DC component as the pulse is supposed to be radiated directly from the antenna without upconversion. The Gaussian monocycle, which is the first derivative of the Gaussian function, is especially easily generated by a switching circuit [GMH+02][Wen07]. Also higher order derivatives of a Gaussian pulse can be generated using relatively simple circuitry [Wen07]. For that reason, most commonly pulses based on a Gaussian shape are implemented [GMK07][BMR+14].

The general shape of a Gaussian pulse truncated to a duration of T_{slot} is given by

$$g_0(t) = \begin{cases} e^{-\left(\frac{t}{\tau}\right)^2} & -\frac{T_{\text{slot}}}{2} \leq t \leq \frac{T_{\text{slot}}}{2} \\ 0 & \text{else} \end{cases}, \tag{6.12}$$

where τ is the time-scaling factor. The n-th derivative of a Gaussian pulse is then given by

$$g_n(t) = \begin{cases} \frac{(-1)^n}{\tau^n} H_n\left(\frac{t}{\tau}\right) \cdot e^{-\left(\frac{t}{\tau}\right)^2} & -\frac{T_{\text{slot}}}{2} \leq t \leq \frac{T_{\text{slot}}}{2} \\ 0 & \text{else} \end{cases}, \tag{6.13}$$

where $H_n(t) = (-1)^n e^{t^2} \frac{\mathrm{d}^n}{\mathrm{d}t^n} e^{-t^2}$ is the physicists Hermite polynomial of order n. For example, in [KCB10], [CWB13], and [CKB+09] the 5^{th} and 2^{nd} derivatives

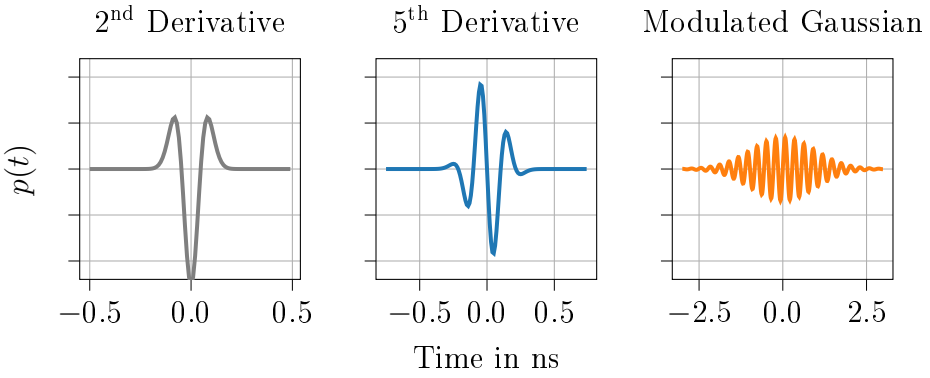

Figure 6.7: Three examples of Gaussian pulse shapes with equal energy. The 5$^{\text{th}}$ derivative and the modulated Gaussian correspond to the power spectral densities shown in Figure 6.8.

of a Gaussian pulse are used for bit error rate simulations of ultra wideband in-body systems. These are plotted exemplary in Figure 6.7. In general the order of the derivative increases the frequency of the maximum in the spectrum and the bandwidth is determined by τ [BMR+14]. However, the frequency of the spectral maximum is related to the time-scaling factor τ by

$$f_{\max} = \frac{\sqrt{n}}{\sqrt{2}\pi\tau}\,. \tag{6.14}$$

A different approach that is used in various scenarios, e.g. in [SW10] and [SAW12a], is a modulated Gaussian pulse, i.e. a Gaussian pulse that is multiplied by a sine wave. The resulting pulse is then

$$g_{0,m}(t) = \begin{cases} \sin\left(2\pi f_c t\right) \cdot e^{-\left(\frac{t}{\tau}\right)^2} & -\frac{T_{\text{slot}}}{2} \leq t \leq \frac{T_{\text{slot}}}{2} \\ 0 & \text{else} \end{cases}\,. \tag{6.15}$$

where f_c is the carrier frequency.

The Power spectral densities (PSDs) of two approaches, namely a 5$^{\text{th}}$ derivative and a modulated Gaussian, are compared in Figure 6.8. Of the Gaussian derivatives, the 5$^{\text{th}}$ is the one that can be placed closest to the ultra wideband mask. For that reason the power spectral density of the other derivatives is not shown in Figure 6.8. The slot duration T_{slot} is computed such that 99.99 % of the pulse energy is preserved. Otherwise the side lobes of the power spectral density of the modulated Gaussian would raise and cross the UWB spectral mask. This leads to a slot duration of 0.7 ns for the 5$^{\text{th}}$ derivative Gaussian and 5.3 ns for the modulated Gaussian. Due to the wide bandwidth of the 5$^{\text{th}}$ derivative pulse, the transmit power needs to be

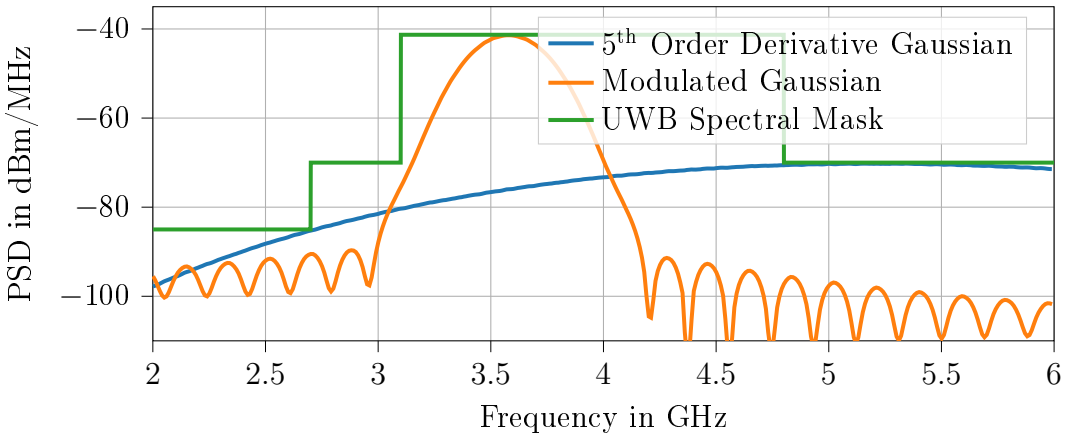

Figure 6.8: The power spectral density (PSD) of a 5$^{\text{th}}$ order derivative Gaussian pulse with $\tau = 106.0\,\text{ps}$ and $T_{\text{slot}} = 0.7\,\text{ns}$ as well as a modulated Gaussian pulse with $f_c = 3.575\,\text{GHz}$, $\tau = 1.35\,\text{ns}$ and $T_{\text{slot}} = 5.3\,\text{ns}$.

reduced to comply with the regulations. Whereas, the modulated Gaussian can be placed precisely in that region of the mask that allows the highest transmit power. Hence, the modulated Gaussian pulse will be used for all the following investigations. However, keep in mind that the modulated Gaussian is a specific pulse shape and does not imply that any kind of mixer is used at the transmitter.

The parameters f_c and τ will now be optimized for the modulated Gaussian. These parameters need to be determined such that the spectral characteristics of the received signal outside of the body of the phantoms comply with the UWB spectral mask. Thus, for each phantom the transfer function of that communication link with the smallest path loss was taken to determine the power spectral density outside of the body. Furthermore, the parameters will be chosen such that the resulting spectrum lies as close as possible inside the spectral mask for channel 1 of the IEEE 802.15.6 standard (cf. Table 4.3). It was shown in Section 4.3 that channel 1 has the smallest attenuation among all the standardized channels. The desired 10 dB bandwidth will be set to the minimum of 500 MHz as the channel capacity evaluations in Section 5.1 showed that increasing the bandwidth does not increase the capacity. With these boundary conditions, a value of $\tau = 1.35\,\text{ns}$ and a carrier frequency of $f_c = 3.575\,\text{GHz}$ were determined empirically. Figure 6.9 shows the resulting power spectral density (PSD) for all phantoms with their respective maximum transmit power, which is either limited by the specific absorption rate or the UWB mask. It can be seen from Figure 6.9 that the influence of the transfer function differs, i.e. the distortions caused are slightly different for each phantom. For some of the phantoms even a carrier frequency smaller than $f_c = 3.575\,\text{GHz}$ would have been possible without crossing the spectral mask. However, for the sake

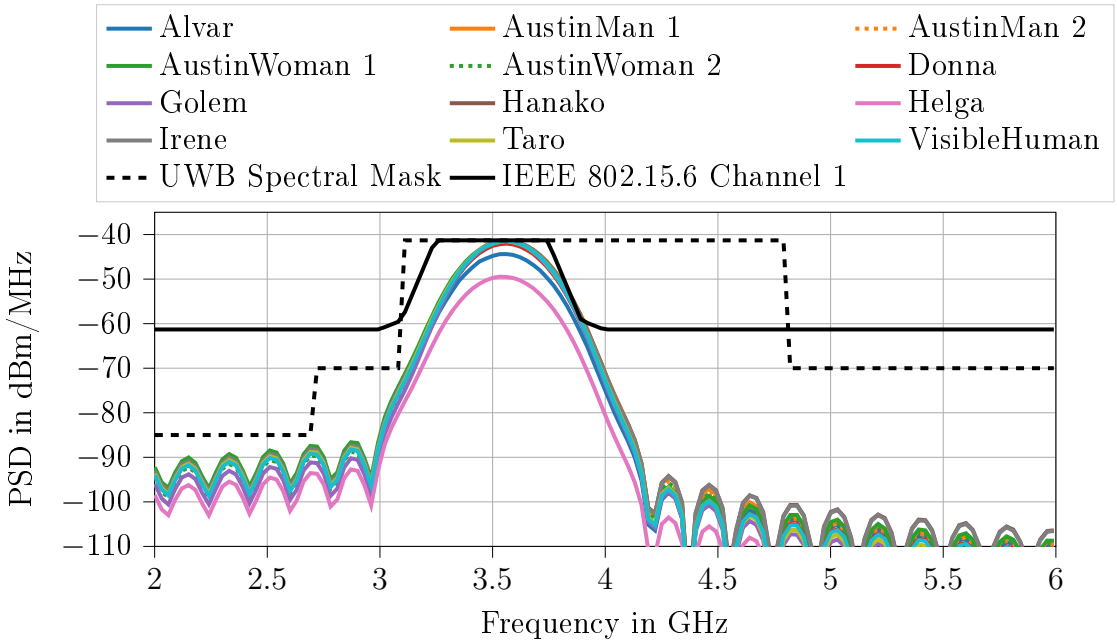

Figure 6.9: The power spectral density (PSD) of the final modulated Gaussian pulse transmitted through the channel with the lowest attenuation of each phantom.

of consistency one value was chosen that allows the transmission for all phantoms.

As discussed in Section 2.3.2, the transmit power inside the body has to be limited to at most $P_{\mathrm{TX,max}} = 21.5\,\mathrm{mW}$ for health reasons. Moreover, the ultra wideband mask has to be considered for setting the maximum average transmit power in each phantom. The maximum values of the transmit power for each phantom are listed in Table 6.1. For Alvar, Donna, and Helga, the transmit power is limited by the maximum specific absorption rate allowed inside the human body. Additionally, there is a difference of at nearly two orders of magnitude between the smallest and the largest maximum transmit power allowed. For example, in Hanako only a transmit power of 0.279 mW is possible because of the small attenuation.

In addition to the restriction on the average transmit power there is also a limit on the specific absorption for pulse based transmission (cf. Section 2). The specific absorption depends on the energy of the pulse [Int98]. Hence, the modulation order of the pulse position modulation needs to be taken into account as this determines the energy per pulse for a given pulse shape and average transmit power.

As mentioned above the pulse duration was set to $T_{\mathrm{slot}} = 5.3\,\mathrm{ns}$. The highest data rate achievable with these settings is

$$R_{\max} = \frac{\log_2 M}{M \cdot T_{\mathrm{slot}}} = \frac{1\,\mathrm{bit}}{2 \cdot 5.3\,\mathrm{ns}} = \frac{2\,\mathrm{bit}}{4 \cdot 5.3\,\mathrm{ns}} = 94.3\,\mathrm{Mbit/s} \tag{6.16}$$

Table 6.1: The maximum transmit power for all digital human phantoms.

Phantom	$P_{\mathrm{TX,max}}$ in mW	Phantom	$P_{\mathrm{TX,max}}$ in mW
Alvar	21.5	Golem	10.6
AustinMan 1	17.4	Hanako	0.279
AustinMan 2	11.9	Helga	21.5
AustinWoman 1	4.69	Irene	1.37
AustinWoman 2	3.66	Taro	0.951
Donna	21.5	VisibleHuman	6.14

Table 6.2: Ultra Wideband Simulation Scenarios. For both a modulated Gaussian pulse $g_{0,m}(t)$ with $\tau = 1.35\,\mathrm{ns}$ and $f_c = 3.575\,\mathrm{GHz}$ is used.

Scenario	T_{slot}	Data Rate	M	T_G/T_{slot}	T_s
A	5.3 ns	94.3 Mbit/s	4	0	21.2 ns
B	5.3 ns	3.0 Mbit/s	512	54	2999.8 ns

for a 2-PPM and a 4-PPM, respectively. However, using a 4-PPM results in a lower bit error probability. In this case no guard interval will be used, i.e. $T_G = 0\,\mathrm{s}$. This is the first simulation scenario that will be investigated further in the following sections. It is named scenario A in Table 6.2 and represents the scenario with the maximum achievable data rate with the aforementioned pulse shaping settings.

An ultra wideband system should at least support a data rate of 3 Mbit/s (see Section 3.1). As shown in the previous Section 6.1, the bit error rate of pulse position modulation decreases with an increasing modulation order. Hence, the maximum modulation order M for the given data rate needs to be found. The transmission of one symbol using M-PPM takes at least $M \cdot T_{\mathrm{slot}}$ for a guard interval length $T_G = 0$. The symbol duration for a given modulation order M and rate R is

$$T_s = \frac{\log_2 M}{R}\,. \tag{6.17}$$

Now to achieve a desired rate R, the symbol duration computed from (6.17) needs to be larger than $M \cdot T_{\mathrm{slot}}$ to fit in all the M slots. Hence, it has to hold that

$$\frac{\log_2 M}{R} \geq M \cdot T_{\mathrm{slot}} \tag{6.18}$$

$$\Leftrightarrow \frac{\log_2 M}{3\,\mathrm{Mbit/s}} \geq M \cdot 5.3\,\mathrm{ns}\,. \tag{6.19}$$

The largest M that fulfills (6.19) is 512. With this the symbol duration is $\tilde{T}_s = \frac{\log_2 512}{3\,\mathrm{Mbit/s}} = 3\,\mu\mathrm{s}$. To allow for uniform sampling at the receiver, the symbol duration

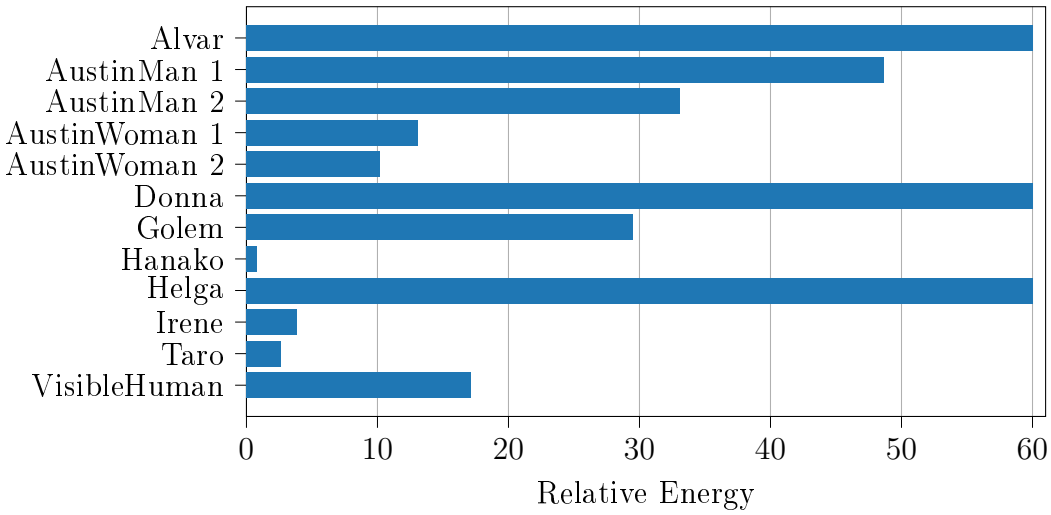

Figure 6.10: The energy per pulse for all the phantoms in scenario B relative to the energy of the setup from Thotahewa *et al.* [TRY15].

should be an integer multiple of T_{slot}. Hence, the symbol duration has to be set to

$$T_s = \left\lfloor \frac{\tilde{T}_s}{T_{\text{slot}}} \right\rfloor \cdot T_{\text{slot}} = 566 \cdot 5.3\,\text{ns} = 2.9998\,\mu\text{s}\,. \tag{6.20}$$

This means that there are 512 slots that will be used for the placement of a transmit pulse and 54 empty slots to achieve the desired data rate. It was clear already from initial investigations that the guard interval is not needed to compensate any channel effects. Thus, the 54 slots of the guard interval could be omitted to increase the data rate. However, then the symbol duration is decreased and by keeping the average transmit power constant, the energy that could be spent per pulse has to be reduced. Thus, they are kept and this set of parameters will be called scenario B in the following. The parameters are summarized in Table 6.2.

As now the modulation orders for scenarios A and B are fixed, the specific absorption for these setups can be investigated. The energy per pulse increases with the modulation order, as the average transmit power is fixed in our scenario. Hence, only scenario B with $M = 512$ needs to be considered as it leads to the highest energy per pulse. As shown in Section 2, the specific absorption using a maximum transmit power of $P_{\text{tx}} = 21.5\,\text{mW}$ is $4\,\text{nJ/kg}$ based on results from [TRY15], which is six orders of magnitude below the limit imposed by the ICNIRP. Figure 6.10 shows the pulse energy for scenario B relative to the result from [TRY15]. For the computations the maximum average transmit powers from Table 6.1 are used. It can be seen from the figure that the maximum energy per pulse is 60 times larger than the energy of the setup from [TRY15]. However, as their resulting specific

absorption was six orders of magnitude below the regulated limit, a pulse energy that is 60 times higher will most likely not exceed this threshold either. Thus, both scenarios A and B are save to use inside all the investigated phantoms.

6.2.3 Analysis of the Equivalent Baseband Channel Characteristics

The overall equivalent baseband channel impulse response $h_{BB}(t)$, consisting of transmit and receive filter and antennas as well as the channel transfer function from the layer modeling approach, is now evaluated for a perfectly synchronized transmission. It is assumed that the detector works with a sampling rate of $\frac{1}{T_{\text{slot}}} = 188.68\,\text{MHz}$. In a first step the time discrete impulse response $h_{BB}[n]$ is truncated such that 99.99 % of the energy is preserved. It is found that the resulting channel does not cause inter-symbol interference for the vast majority of communication links. These results differ from the power delay profiles shown in Sections 4.2.4 and 4.3.2.2 because there a rectangular bandpass filter was applied prior to the downconversion due to the missing knowledge of the tranmission scheme. Whereas, in this chapter the actual pulse shaping filter is included. Table 6.3 shows the number of impulse responses $h_{BB}[n]$ that have one or two taps, respectively. There were no impulse responses with three or more taps. For example, 270 000 communication links have been investigated in Alvar. Out of these only one channel consists of two channel taps, the rest consist of one channel tap. At most 24 two-tap channel impulse responses were found for AustinMan 2. However, it has to be noted that for all phantoms the second tap, if it occurred at all, was at least 30 dB smaller than the first tap. From this it was concluded that the transmission between the capsule endoscope and an on-body receiver can be well approximated with a pure AWGN channel for the scenarios in Table 6.2. Thus, the bit error probability can be determined from (6.9) using the received $\frac{E_b}{N_0}$.

The probability density function (PDF) of the received $\frac{E_b}{N_0}$ for transmission scenario B is shown in Figure 6.11. For this computation and all the following, the noise power spectral density N_0 has been computed for a temperature of 37 °C and an additional noise figure of 20 dB has been applied as defined in (5.3). Thus, the noise is the same as for the channel capacity calculations. Furthermore, all communication links $\mathbf{t}_i \rightarrow \mathbf{r}_j$ for each phantom are considered, i.e. the random placement of a single receive antenna. It can be seen that – apart from Alvar – for all of the phantoms the shape of the probability density function (PDF) is similar. The average received $\frac{E_b}{N_0}$ varies between −6.17 dB for Hanako to 9.61 dB for Alvar. The

Table 6.3: The number of communication links that have the given number of channel taps for the discrete time equivalent baseband channel model that preserves 99.99 % of the energy.

Model	1 Tap	2 Taps	Model	1 Tap	2 Taps
Alvar	269 999	1	Golem	159 296	0
AustinMan 1	323 985	15	Hanako	273 996	4
AustinMan 2	311 976	24	Helga	321 230	5
AustinWoman 1	303 989	11	Irene	193 775	0
AustinWoman 2	293 996	4	Taro	217 998	2
Donna	124 959	1	VisibleHuman	405 980	20

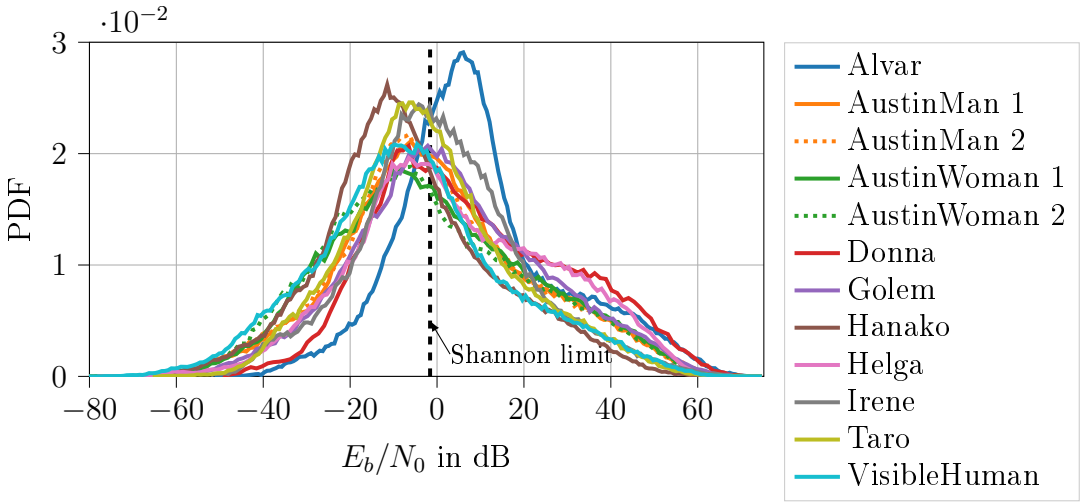

Figure 6.11: The probability density function (PDF) of the received $\frac{E_b}{N_0}$ in dB at the sampling instants for scenario B.

percentage of communication links that result in an $\frac{E_b}{N_0}$ smaller than the Shannon limit of −1.6 dB is 27.2 % for Alvar and 64.4 % for Hanako. Thus, it is evident that many communication links exhibit a very poor performance which will not be usable for any data transmission. If scenario A is used instead of scenario B, the PDFs in Figure 6.11 move by 14.98 dB to the left. Hence, the received $\frac{E_b}{N_0}$ deteriorates even more. The value of 14.98 dB follows from the $\frac{E_b}{N_0}$ to SNR conversion in (6.6). With that, even for Alvar 66.2 % of all communications links result in an $\frac{E_b}{N_0}$ smaller than −1.6 dB. These results show again that it is necessary to use a large number of antennas distributed on the abdominal surface to establish a connection to all the transmitter locations.

6.3 Performance Evaluation

As the transmission takes place in an AWGN channel, the bit error probability can be computed directly from (6.9) using the received $\frac{E_b}{N_0}$. Thus, no simulations are necessary to evaluate the performance of the ultra wideband capsule endoscope system. In the following sections, the two transmission scenarios A and B will be compared for all the phantoms using the same antenna configurations already employed for the capacity computations in Section 5.2. The performance will be measured in terms of the transmitter coverage. The transmitter coverage is the percentage of all transmitter locations $\mathbf{t}_i$ in the digestive tract that can establish a connection to the on-body receive antennas with a certain bit error probability. Due the length of the small intestine of 6 m to 8 m [KCB10] high coverage values are needed. If the coverage is 99.9 %, only 0.1 % of the transmitter locations are not covered. However, that means there is a part of 6 mm to 8 mm that is missing in the transmitted image material which could already mean that important parts cannot be diagnosed. The transmitter coverage will be investigated for target bit error probabilities P_b smaller than 10^{-2}, 10^{-3} and 10^{-4}. The bit error probability P_b can directly be mapped to $\frac{E_b}{N_0}$ values using (6.9). This mapping is given in Table 6.4. The investigation of forward error correcting schemes is out of scope of this thesis. Hence, all bit error probabilities shown in the following refer to uncoded transmission.

Unless noted otherwise all the following results are retrieved using maximum ratio combining at the receiver and the modulation parameters are set according to transmission scenario B (3 Mbit/s, see Table 6.2). The transfer function including free space losses will be used as channel model. The dielectric properties of the underlying layer model will always be taken from Gabriel *et al.* [Gab96]. However, as shown in Sections 2.1 and 5.4 there is a large uncertainty on the actual values of the dielectric properties and, thus, also for the communication performance.

The resulting performance will be analyzed for different configurations. First, it will be investigated how the transmitter coverage behaves for different target bit error probabilities. Second, the dependence on the number and the placement of receive antennas will be determined. Moreover, it will be shown how the choice of the data rate influences the coverage. Finally, the influence of the combining scheme on the resulting coverage is analyzed.

Table 6.4: Relationship of the investigated bit error probability values P_b to $\frac{E_b}{N_0}$.

$P_b <$	10^{-2}	10^{-3}	10^{-4}
	⇕	⇕	⇕
$\frac{E_b}{N_0} >$	1.86 dB	3.25 dB	4.24 dB

6.3.1 Transmitter Coverage for Different Target Bit Error Probabilities

As it is known from the capacity investigations, multiple antennas will be needed to achieve any improvement over existing narrowband solutions. Thus, for this first analysis of the transmitter coverage the five optimally placed receive antennas in terms of the 10 %-outage channel capacity determined in Section 5.2 were selected.

Figure 6.12 shows the transmitter coverage for the different target bit error probabilities. The coverage for Alvar reaches up to 99.9 % at a bit error probability P_b smaller than 10^{-2} as well as 10^{-3}. For a target bit error probability of 10^{-4} the coverage reduces just by 0.1 percent points to 99.8 %. In the worst case, for Hanako, the coverage is 91.1 % for $P_b < 10^{-2}$ down to 90.4 % for $P_b < 10^{-4}$. Thus, there are – as expected from the capacity computations – large differences between the phantoms regarding the achievable coverage.

Additionally, it can be observed that the coverage does not vary much for the different target bit error probabilities. The difference in coverage on any phantom between $P_b < 10^{-4}$ and $P_b < 10^{-2}$ is only up to 1.2 percent points. This might stem

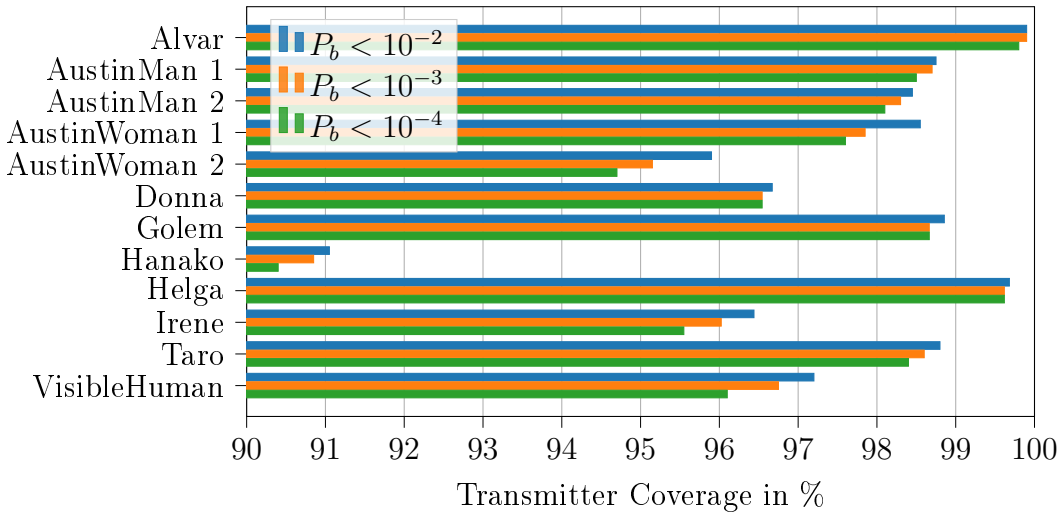

Figure 6.12: The transmitter coverage for different target bit error probabilities for five receive antennas at the optimum locations determined in Section 5.2.

from the fact that the bit error probability curve shown in Figure 6.3 is rather steep for a 512-PPM. Moreover, it could be observed that by using more receive antennas the loss in coverage from $P_b < 10^{-4}$ to $P_b < 10^{-2}$ becomes smaller.

In general, the coverage is at least 90.4 % for all phantoms at a target bit error probability of 10^{-4}. The coverage increases by at most 1.2 percent points for a target bit error probability of 10^{-2}. Thus, for most of the remaining 9.6 % of transmitter locations the bit error probability is *larger* than 10^{-2}. For complexity reasons, a target bit error probability of 10^{-2} is considered as boundary in the following. A larger uncoded bit error probability would require very complex error correcting codes which are not suitable due to hardware constraints of the capsule. The results in this chapter – in contrast to the channel capacity evaluations – give a worst case estimation of the performance for ultra wideband capsule endoscopy. Further influences on the bit error probability and the resulting quality of service are studied in Section 6.4.

6.3.2 Dependence on Number and Position of Receive Antennas

As it was found from the channel capacity analysis in Section 5.2 using only a small number of antennas at their optimized positions is not feasible as already small deviations from this optimum position lead to severe degradation. Hence, the same antenna grid already proposed in Section 5.2.3 will be used here to investigate how dense the antennas need to be placed on the abdominal surface. Figure 6.13 shows the worst case and best case transmitter coverage across all phantoms for the different antenna grid configurations to achieve $P_b < 10^{-2}$ for scenario B (3 Mbit/s). Shown are the number of phantoms that achieve at most the transmitter coverage shown on the abscissa. Table 6.5 gives the number of receive antennas that can be placed on any phantom for a given grid distance. More details can be found in Section 5.2.3. The blue dashed line in Figure 6.13, for a grid distance of $d_{\text{grid}} = 30\,\text{mm}$, refers to the maximum number of receive antennas $N_{\text{RX,max}}$ placed on the abdomen. In this case, only for three of the phantoms the coverage is smaller than 100 %, i.e. for nine of the phantoms a communication link with a bit error probability smaller than 10^{-2} can be established to all possible transmitter locations $\mathbf{t}_i$ in the digestive tract. The three phantoms for which this is not possible are AustinMan 2 (coverage of 99.95 %), Irene (99.88 %), and Hanako (96.75 %).

Table 6.5: Minimum and maximum number of receive antennas placed on any phantom for a given grid distance and the check pattern. This is a summary of Table 5.1.

d_{grid} in mm	30	60	90	120	Check pattern
No. of Antennas	109–203	24–56	9–28	4–17	54–103

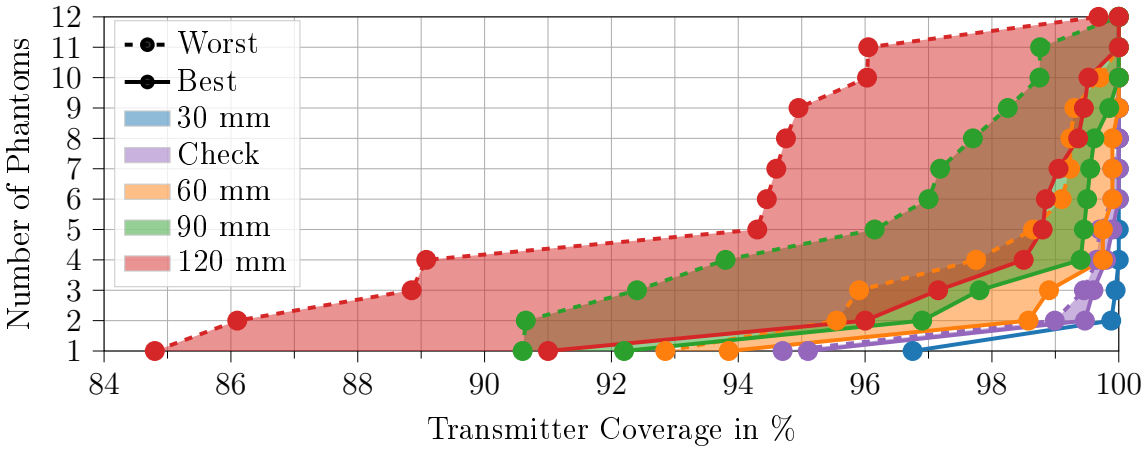

Figure 6.13: The transmitter coverage for $P_b < 10^{-2}$ in transmission scenario B (3 Mbit/s). The legend gives the distance between adjacent receive antennas on the antenna grid. See Table 6.5 for the corresponding number of antennas.

The transmitter coverage decreases as the antenna grid distance increases. Already for a grid distance of 60 mm, which corresponds to 24 to 56 antennas, only four of the phantoms (Alvar, Donna, Golem, and Helga) achieve 100 % coverage in their optimum position. Only for Alvar and Helga the coverage remains 100 % in this case independent of the relative position of the antenna grid. For Donna and Golem the coverage reduces to 99.23 % and 99.24 %, respectively, in the worst case.

Once the antenna distance is incresed even further, the coverage degrades severely. However, for Alvar and Helga it is possible to achieve a coverage of 100 % also for an antenna grid with distance of 120 mm between the antennas at its optimum position. This corresponds to approximately 4 to 17 receive antennas (cf. Table 6.5). Whereas, this antenna grid would result in a transmitter coverage between 84.8 % to 99.7 % in the worst case on any phantom.

In Figure 6.14 the coverage results for scenario A (94.3 Mbit/s) are shown. Comparing this figure to Figure 6.13, it can be seen that the resulting coverage is much smaller. This is because of the reduced energy per bit that is allowed as the data rate is increased from 3 Mbit/s to 94.3 Mbit/s. In this scenario only for Helga a coverage of 100 % for an antenna grid with $d_{\text{grid}} = 30$ mm (blue dashed line) can be

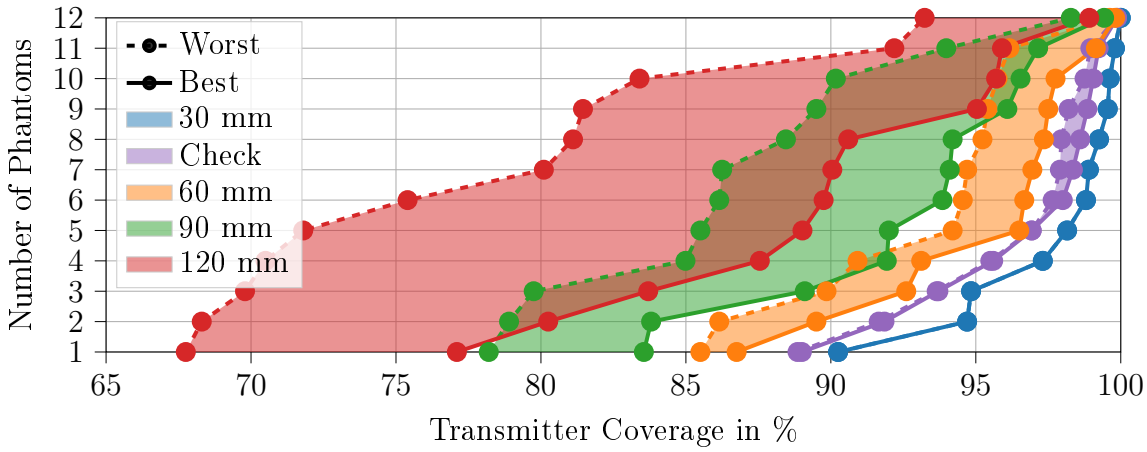

Figure 6.14: The transmitter coverage for $P_b < 10^{-2}$ in transmission scenario A (94.3 Mbit/s). The legend gives the distance between adjacent receive antennas on the antenna grid. See Table 6.5 for the corresponding number of antennas.

achieved. For the same antenna grid the worst performance is achieved for Hanako, namely a coverage of only 90.25 %. The coverage for all other phantoms is affected by a quite large degradation compared to Figure 6.13.

Up to now, all computations in this section are made based on the transfer function $\tilde{\mathcal{H}}_{\mathbf{t}_i \to \mathbf{r}_j}(f; c_0)$ including free space losses (see Section 4.1.5). As it was found in Section 4.2, using $\tilde{\mathcal{H}}_{\mathbf{t}_i \to \mathbf{r}_j}(f; c_0)$ leads to an underestimation of the path loss that is observed in a more realistic numerical wave simulation. It could be seen that using the transfer function $\tilde{\mathcal{H}}_{\mathbf{t}_i \to \mathbf{r}_j}(f; c_e)$ including effective tissue losses instead gives an upper bound on the actual path loss.

Figure 6.15 shows the resulting reduction in transmitter coverage, if instead of $\tilde{\mathcal{H}}_{\mathbf{t}_i \to \mathbf{r}_j}(f; c_0)$ $\tilde{\mathcal{H}}_{\mathbf{t}_i \to \mathbf{r}_j}(f; c_e)$ is used in transmission scenario B. It can be seen that the degradation is dependent on the phantom and on the distance between the antennas on the grid. The largest reduction of 22.65 percent points is observed for Taro and an antenna grid distance of 120 mm, closely followed by Irene with 22.43 percent points. The highest reduction for $d_{\text{grid}} = 90$ mm is seen for AustinWoman 1 with 11.9 percent points. Moreover, for $d_{\text{grid}} = 60$ mm it is largest for AustinWoman 2 with 7.45 percent points and for $d_{\text{grid}} = 30$ mm the largest reduction is seen for Hanako with 6.1 percent points. The smallest reduction for all antenna configurations is observed for Helga, which is at most 5.30 percent points. Only for Helga a coverage of 100 % is still possible using $d_{\text{grid}} = 30$ mm, i.e. the reduction is zero. Hence, for phantoms that already exhibit a quite low overall path loss, considering this upper bound on the attenuation leads only to small degradation. However, for those phantoms that on average have a larger path loss the reduction is even

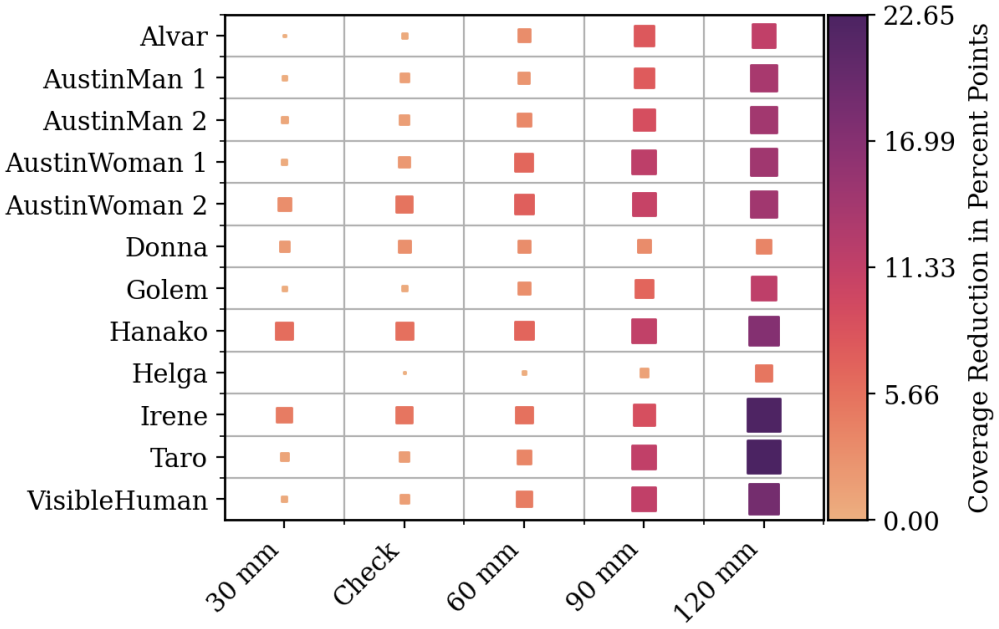

Figure 6.15: The reduction in transmitter coverage in percent points for $P_b < 10^{-2}$ in transmission scenario B. Compared are the optimum placements of the antenna grids for transfer functions including free space losses to transfer functions including effective tissue losses. The size of the markers is proportional to the values.

larger. Thus, for these cases it is even more important to have accurate estimations of the actual path loss to predict the suitability of using ultra wideband communication. Furthermore, this again supports earlier statements that it is necessary to place as much antennas on the abdominal surface as possible to reliably support ultra wideband communication. A larger number of antennas allows to compensate for the high attenuation.

6.3.3 Influence of the Combining Scheme

Up to now, in all the results in this section a maximum ratio combining scheme was implemented. As a selection combining scheme is easier to implement and requires less channel knowledge, the degradation due to this non-optimum combining is also of interest. Another commonly used combining scheme is equal gain combining. However, for equal gain combining it is not possible to derive a closed form solution for the received $\frac{E_b}{N_0}$ [Gol05]. Hence, it is not considered in the following comparison. Nevertheless, the performance of equal gain combining will lie between selection combining and maximum ratio combining, usually quite close to the performance of maximum ratio combining [Gol05].

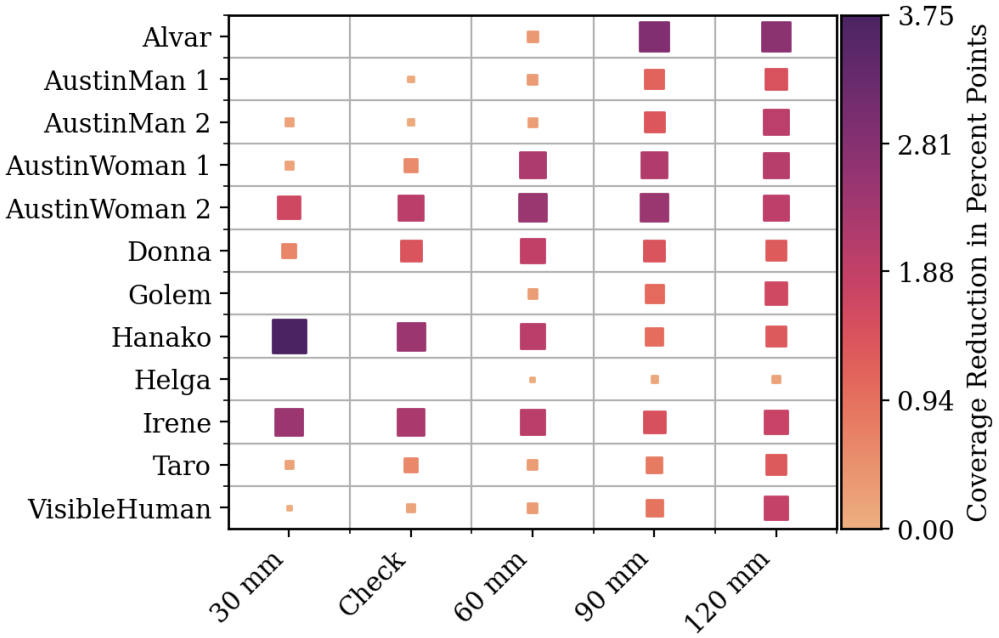

Figure 6.16: The reduction of the transmitter coverage in percent points for $P_b < 10^{-2}$ in transmission scenario B. Shown are the largest possible losses if instead of maximum ratio combining selection combining is implemented. The size of the markers is proportional to the values.

Figure 6.16 shows the reduction in transmitter coverage in percent points if instead of maximum ratio combining selection combining is used. For some phantoms, e.g. Alvar, Golem and Helga in some of the antenna grid configurations there is no coverage reduction at all. Hence, in these cases the coverage is independent of the combining scheme. However, there is a reduction for others. In some cases the reduction decreases with increasing antenna distance, e.g. for Hanako, and in other it increases with increasing antenna distance, e.g. for VisibleHuman. Hence, there seems to be no clear correlation. Overall it can be seen that the reduction is concentrated to values around 1 percent point. This agrees well to the results already obtained in [BKB19]. There only a negligible difference between all the combining schemes was found. However, it can happen that depending on the phantom and the exact location of the receive antennas the reduction in transmitter coverage is up to 3.75 percent points.

A more detailed investigation of the weighting factors used for maximum ratio combining revealed that there is usually one very dominant factor. All other weighting factors are most commonly several dB smaller than the maximum. Hence, in this scenario maximum ratio combining reduces in most of the communication links to selection combining.

6.4 Further Influences on the Bit Error Probability

The results on the transmitter coverage for uncoded transmission from the last sections show that the bit error probability strongly depends on various factors. Viewing it from an application point-of-view the relevant performance metric is the image or video quality of the retrieved material from the capsule endoscope. At the end, the physician is only interested in the fact that the Quality of Service (QoS) is better than with existing capsules. However, the uncoded bit error probability alone is not sufficient to estimate the QoS. The effective $\frac{E_b}{N_0}$ and the packet error rate can be affected by different aspects. A few will be discussed in the following.

Forward Error Correction. As the computing power of the capsule is limited, it is important to select an error correcting code that has a low encoding complexity. Nevertheless, results in this chapter have shown that the uncoded bit error probability is larger than 10^{-2} for a non-negligible percentage of communication links. Thus, the error correcting codes should have strong correction capabilities in addition to a low encoding complexity. The only two ultra wideband communication standards that exist to the best of our knowledge are the Body Area Network standard IEEE 802.15.6 and the low-rate wireless networks standard IEEE 802.15.4. In IEEE 802.15.6 a variant of PPM is deployed and a BCH(63, 51) code is applied for forward error correction. Moreover, in IEEE 802.15.4 [Ins20] an outer Reed-Solomon code is combined with an inner half-rate convolutional code. Again, a variant of pulse position modulation is used. However, no simulations of the resulting bit or packet error rate for pulse position modulation using any forward error correction scheme could be found in literature.

Image Compression and Correction. As mentioned in Section 3.1, there are algorithms that compress capsule endoscope images by factors of 20 to 50. These are supposed to be implemented easily and efficiently on a capsule endoscope. Because the image material will also have large similarities between individual frames, it will be possible to restore lost parts of an image at the receiver. This would allow the physical layer to operate at a higher bit error probability. Hence, allowing some errors to remain in the image, which can be corrected on the application layer afterwards.

Retransmission Schemes. Between the physical layer and the application layer usually an automatic retransmission query (ARQ) scheme is implemented in case

the information in any packet could not be decoded correctly. However, this works only if a retransmission is required for a small percentage of packages. The exact implementation of the automatic repeat request scheme influences the QoS. As it was shown in the previous sections the channel characteristics are very much location dependent. One possibility to increase the success rate of a retransmission would be to add a small memory element into the capsule to store some frames for later retransmission.

6.5 Summary

In this chapter the channel modeling approach introduced in Chapter 4 has been used to investigate the bit error probability of an ultra wideband impulse radio system. Due to the advantageous property of pulse position modulation (PPM), that the power efficiency increases with the modulation order, PPM was selected as the modulation scheme. For an average transmit power constraint the energy per pulse, i.e. per symbol, may be increased as the symbol duration T_s increases with the modulation order M if the pulse shape is kept constant. This leads to the nice property that the bit error probability for larger M decreases. Hence, it is advantageous to use a modulation order that is as large as possible.

Based on the choice of the modulation scheme, a modulated Gaussian pulse was identified as the best solution for the PPM pulse shape. It was found that for the power spectral density of the transmit pulse to fit in the spectral mask for ultra wideband communication a carrier frequency of $f_c = 3.575\,\mathrm{GHz}$ should be used. The parameter τ should be set to 1.35 ns to achieve a 10 dB bandwidth of approximately 500 MHz. With these settings each slot for the pulse position modulation should have a length of 5.3 ns to conserve 99.99 % of the pulse's energy. Moreover, based on the UWB spectral mask and the maximum allowed specific absorption rate, the maximum transmit power that may be used in each of the phantoms was determined. It was found that the maximum transmit power varies by two orders of magnitude depending on the physiology of the phantom. Furthermore, the pulse based specific absorption was found to comply with the regulatory limits. Based on these parameters two transmission scenarios were identified. The highest data rate can be achieved with scenario A, which allows transmission at a rate of 94.3 Mbit/s using a modulation order $M = 4$. It was found in Section 3.1 that a data rate of 3 Mbit/s would be required for substantial improvements of the diagnostic quality of capsule endoscopy. This is incorporated in scenario B, which uses a

modulation order $M = 512$ and can, thus, achieve a data rate of 3 Mbit/s. All the results summarized in the following are based on scenario B unless noted otherwise.

In a next step the channel characteristics of the resulting discrete time equivalent baseband channel were analyzed. It was found that the resulting channels for scenario A and B are frequency flat and can, hence, be described solely by the path loss and AWGN. Thus, for all the following performance results the bit error probability could be determined from the analytic expression for pulse position modulation in AWGN channels.

Furthermore, the performance in terms of the transmitter coverage was determined. The transmitter coverage is the percentage of transmitter locations that can establish a communication link with at most a certain target bit error probability $P_{b,\mathrm{target}}$. First, it was shown that for five optimally placed receive antennas the transmitter coverage for all phantoms and for $P_{b,\mathrm{target}} = 10^{-4}$ is always larger than 90 %. The coverage is increased by at most 1.2 percent points when increasing the target bit error probability from 10^{-4} to 10^{-2}. Hence, for more than 90 % of all transmitter locations it is possible to achieve $P_b < 10^{-4}$ using five optimally placed receive antennas. However, for the remaining transmitter locations the bit error probability will most likely be larger than 10^{-2}. For a larger number of receive antennas, the reduction of the coverage, when increasing the target bit error probability from 10^{-4} to 10^{-2}, is smaller than 1.2 percent points.

Moreover, the dependence of the transmitter coverage on the number and the position of the receive antennas was investigated. It could be shown that for all phantoms the transmitter coverage for $P_{b,\mathrm{target}} = 10^{-2}$ is larger than 99.8 %, when a grid with antenna distance of 30 mm is placed on the abdominal surface. This corresponds to the maximum investigated amount of receive antennas, i.e. between 109 and 205 receive antennas. As expected the coverage decreases as the antenna distance increases, as fewer antennas can be placed on the abdomen. Only for two of the phantoms (Alvar and Helga) the coverage remained at 100 % even for an antenna grid with $d_{\mathrm{grid}} = 120$ mm at its optimum position. This corresponds to 4 to 17 receive antennas on the abdominal surface. Whereas the coverage goes down to only 84.8 % in the worst case for this antenna grid.

Additionally, it was found that increasing the data rate for scenario A leads to a severe degradation of the coverage due to the reduced energy per pulse that can be spent in this scenario. In this case only Helga can achieve a coverage of 100 % for the most dense antenna grid, i.e. 205 antennas. The coverage for all other phantoms is affected by a quite large degradation in the order of approximately 10 percent points.

In contrast to this severe degradation it could be shown that the combining scheme does only play a negligible role for the transmitter coverage. A reduction in the order of only 1 percent point could be observed when using selection combining instead of maximum ratio combining. Due to the high attenuation in tissue, maximum ratio combining reduces to selection combining in this scenario.

In Section 4.2 it was found that using a transfer function including free space losses leads to an underestimation of the actual path loss and a transfer function including effective tissue losses instead gives an upper bound on the actual path loss. This uncertainty in the layer modeling results in an uncertainty about the resulting transmitter coverage. All previously mentioned results in this summary are based on the transfer function including free space losses, i.e. the lower bound on the path loss. If instead the upper bound is used, the transmitter coverage degrades drastically by up to 22.65 percent points for an antenna grid with 120 mm distance between the antennas, i.e. 4 to 17 antennas. For the more dense antenna grids the degradation is smaller. Hence, if the actual path loss follows this upper bound an even denser antenna grid would be necessary to achieve the same desired transmitter coverage. Only for Helga a coverage of 100 % could be achieved using the most dense antenna grid in this case.

Chapter 7

Conclusion

In this work, ultra wideband communication for the use case of capsule endoscopy was studied in-depth. Specifically, it was the goal to determine upper limits on the possible data rate, i.e. to compute the channel capacity for this setup. In the course of this thesis a detailed but simplified channel model was introduced to compute the necessary transfer functions for the communication links.

In a first step, the fundamentals for wireless in-body communication were reviewed. The frequency dependency of human tissue for electromagnetic radiation and differences in the measurements for different tissue types were discussed. Moreover, the safety of using electromagnetic radiation in the ultra wideband frequency region inside the body was assessed. Especially, upper limits for the average transmit power and the pulse energy of ingested wireless sensors were summarized. Twelve different digital human phantoms were presented in detail, which were used throughout this work as references. Additionally, existing solutions for in-body communication systems have been reviewed. The evolution of the wireless sensor capsules began in 1957 with simple radio transmitters that could only transmit pressure and temperature. It lead to the development of the capsule endoscope in 2000, which was equipped with camera, lighting and a radio transmitter. Current devices are capable of transmitting images with a rather limited image resolution and small video frame rate. State of the art in-body communication to ingested or implanted sensors is nowadays usually based on narrowband communication in the UHF band. These schemes have the disadvantage of limited spectral resources. Much higher bandwidths are allowed in the ultra wideband frequency range. Hence, it is expected that the data rate can be increased using ultra wideband communication. The feasibility of this was shown in various experiments in literature. A review of existing ultra wideband channel

models showed that there are great variations in the resulting path loss models depending on the exact setup. Moreover, the inherent frequency dependency of the tissues was not included in any of them, which is unsuitable to investigate signals with bandwidths of more than 500 MHz.

The main contribution of this thesis is a simplified channel model for ultra wideband communication, which can easily be adapted to different setups and extended to different digital human phantoms. Moreover, as the frequency dependencies are included it is possible to investigate different transmission and reception strategies using the same channel model. The general idea is to model the propagation path of an electromagnetic wave by a multi-layered dielectric resembling the tissue structure on the path between transmitter and receiver. It was found by a numerical simulation of the actual wave propagation in CST Microwave Studio that it is not enough to approximate the in-body to on-body link with just one direct path. Instead the sum of two paths is considered for the final layer modeling approach. One path is the direct connection from transmitter to receiver and the second is the path along the shortest direction from the transmitter out of the body and then along the body surface to the receiver. This second indirect path becomes more dominant as the distance between transmitter and receiver increases. Furthermore, it was shown that the resulting path loss, power delay profile and the frequency dependency of the transfer functions are well recreated by the layer modeling approach.

A second major contribution of this work is the computation of the channel capacity based on the proposed layer modeling technique. The goal was to systematically assess various influences on the communication performance. The first observation was that due to the frequency dependent nature of the communication channel, it is not beneficial to increase the transmission bandwidth arbitrarily. It should rather be kept at the minimum value allowed to comply with UWB regulations, i.e. a bandwidth of 500 MHz should be used. Moreover, it was shown that the exact placement of the receive antennas on the abdominal surface plays a crucial role for the channel capacity. For five optimally placed receive antennas a 10 %-outage capacity of 217.5 Mbit/s to 1.5 Gbit/s could be achieved on the twelve investigated phantoms. However, as soon as this optimum placement is not met exactly, the 10 %-outage capacity deteriorates drastically by around one order of magnitude. Hence, a suboptimal placement scheme was investigated, where the antennas were placed on a rectangular grid on the abdominal surface. It was shown that using a grid of antennas the same performance as with five optimally placed antennas can be achieved. However, to achieve nearly the same performance, 24 to 56 antennas are needed in that case, depending on the abdominal surface area of the phantom. Due to the large

differences in anatomy and physiology of the phantoms, no general rule to place the antennas could be derived. As mentioned above, the differences in capacity between the phantoms are significant. For some antenna configurations this difference turned out to be larger than one order of magnitude. The main reason for this difference is the difference in waist circumference and body mass index. Additionally, also the ratio of muscle to fat tissue in the abdomen influences the capacity, as the attenuation in muscle tissue is much higher than in fat. In most of the current literature, the dielectric properties of human tissue is taken from measurements from Gabriel *et al.* [Gab96]. However, their data mostly comes from ex-vivo measurements. Recent in-vivo experiments in [FCF+19] have revealed substantially different values. Using the latter values for the dielectric properties, it was shown that these have a huge impact on the channel capacity. The computations of the 10 %-outage capacity revealed a reduction by a factor of 1.2 to 30 compared to the capacity obtained using the results from [Gab96], depending on the phantom. Hence, there is a large uncertainty about the actual values of the dielectric properties and its influence on the communication performance. To reliably predict the communication performance, more work is needed to accurately describe the dielectric properties of human tissue and its range of fluctuation.

In the final chapter an exemplary ultra wideband communication system using pulse position modulation is designed and its bit error probability is analyzed. Based on the layer modeling approach, the effective discrete time equivalent baseband transfer function was derived to be frequency flat. Two scenarios were considered using the same pulse shaping parameters. One with a data rate of 94.3 Mbit/s (modulation order $M = 4$) and the other with 3 Mbit/s ($M = 512$). It was found that for five optimally placed receive antennas on all phantoms a communication link to more than 90 % of the transmitter locations can be established with an uncoded bit error probability lower than 10^{-4} for a data rate of 3 Mbit/s. By far the most of the remaining 10 % of the links exhibit a bit error probability larger than 10^{-2}. If the complete abdomen is covered with an antenna grid, i.e. the distance between adjacent antennas is 30 mm, 109 to 205 antennas would be needed depending on the phantom. In this case a bit error probability of at least 10^{-2} could be achieved in 99.8 % of all communication links for any phantom. By increasing the distance between the antennas, the coverage reduces. Only for two of the phantoms (Alvar and Helga) the coverage remains at 100 % even if the antennas are 120 mm apart, which relates to only up to 17 receive antennas. However, in that case the coverage drops to 84.8 % in the worst case on the other phantoms. For the higher data rate of 94.3 Mbit/s, a severe degradation could be observed because the energy per pulse is reduced. The degradation is in the range of approximately 10 percent points for

all the phantoms.

Of course, the final bit error probability of the transmission depends on the usage of a suitable forward error correction scheme. Nevertheless, it can be seen from the results presented in this thesis that all the values that were determined in this work are highly dependent on the specific assumptions. To the best of our knowledge, this is the first time that a direct comparison of the communication performance of multiple phantoms was investigated. To precisely predict the communication performance in a real application, future work should further investigate the exact values of the dielectric properties. Moreover, the variability of the dielectric properties of the same tissue in different humans should be taken into account in future models.

Appendix A

Channel Model

A.1 Mapping of Tissue Properties

Shown in Table A.1 are the tissue names used in this work in the first column. The second column shows the name of the tissue types as used in [Gab96] from which the parameters of the Cole-Cole model were taken. For tissues not contained in [Gab96] mappings from [And18] and [ITI18] were used. The third column shows the properties of the tissue which were investigated in [FCF+19]. For the computations in this thesis, the other remaining tissues were substituted by the ones from [Gab96].

Table A.1: Mapping of tissue properties from [Gab96] and [FCF+19] to the ones used in this work.

Tissue name	Name in [Gab96]	Name in [FCF+19]
Aorta	Aorta	Aorta
Bladder	Bladder	Bladder
Blood	Blood	Blood
Blood vessel	Aorta	Aorta
Body fluid	Vitreous humor	
Bone cancellous	Bone (cancellous)	
Bone cortical	Bone (cortical)	
Bone marrow	Bone marrow (not infiltrated)	
Brain grey matter	Grey matter	
Brain white matter	White matter	
Breast fat	Breast fat	
Cartilage	Cartilage	
Cerebellum	Cerebellum	

Table A.1: Mapping of tissue properties from [Gab96] and [FCF+19] to the ones used in this work.

Tissue name	Name in [Gab96]	Name in [FCF+19]
Cerebro spinal fluid	Cerebro spinal fluid	
Cervix	Cervix	
Colon	Colon	Colon
Cornea	Cornea	
Duodenum	Stomach	Stomach
Dura	Dura	
Eye sclera	Eye (sclera)	
Fat	Fat (not infiltrated)	Fat
Gall bladder	Gall bladder	Gallbladder
Gall bladder bile	Gall bladder bile	
Gland	Thyroid	
Heart	Heart	Heart
Kidney	Kidney	Kidney
Lens	Lens cortex	
Liver	Liver	Liver
Lung deflated	Lung deflated	Lung deflated
Lung inflated	Lung inflated	Lung inflated
Lymph	Thyroid	
Mucous membrane	Skin (wet)	
Muscle	Muscle (transverse)	Muscle
Nail	Bone (cortical)	
Nerve	Nerve (spinal cord)	
Oesophagus	Stomach	Esophagus
Ovary	Ovary	Ovary
Pancreas	Thyroid	Pancreas
Prostate	Testis	
Retina	Eye (sclera)	
Skin dry	Skin (dry)	Skin
Skin wet	Skin (wet)	Skin
Small intestine	Small intestine	Small intestine
Spinal cord	Nerve (spinal cord)	
Spleen	Spleen	Spleen
Stomach	Stomach	Stomach
Tendon	Tendon	

Table A.1: Mapping of tissue properties from [Gab96] and [FCF+19] to the ones used in this work.

Tissue name	Name in [Gab96]	Name in [FCF+19]
Testis	Testis	
Thymus	Thyroid	
Thyroid	Thyroid	
Tongue	Tongue	
Tooth	Bone (cortical)	
Trachea	Trachea	
Uterus	Uterus	Uterus
Vitreous humor	Vitreous humor	
Lens cortex	Lens cortex	
Lens nucleus	Lens nucleus	
GI contents	Muscle	Muscle
Stomach contents	Muscle	Muscle

A.2 Derivation of the Relationship between Transmission and Scattering Parameters

In this section the derivation of the transfer function S_{21} of a plane wave propagating through a multi-layered dielectric will be shown. Furthermore, the reflection coefficient S_{11} of an inbound wave will be derived. The general setup is shown in Figure 4.3.

General Introduction

Starting from the definition of the inbound and outbound waves from (4.18) to (4.21) and the fact that the electric and magnetic field at the transmitter (TX) and the receiver (RX) can be split up in forward and backward traveling waves, the fields can be written as follows

$$E_{TX} = E_{TX+} + E_{TX-} = \frac{1}{\sqrt{\mathrm{Re}(\eta_s)}} (a_1\eta_s + b_1\eta_s) \tag{A.1}$$

$$E_{RX} = E_{RX+} + E_{RX2-} = \frac{1}{\sqrt{\mathrm{Re}(\eta_l)}} (b_2\eta_l + a_2\eta_l) \tag{A.2}$$

$$H_{TX} = H_{TX+} - H_{TX-} = \frac{1}{\sqrt{\mathrm{Re}(\eta_s)}} (a_1 - b_1) \tag{A.3}$$

$$H_{RX} = H_{RX+} - H_{RX-} = \frac{1}{\sqrt{\mathrm{Re}(\eta_l)}} (b_2 - a_2)\ . \tag{A.4}$$

Inserting now (A.1) to (A.4) into (4.11) using (4.17) yields

$$\frac{a_1\eta_s + b_1\eta_s}{\sqrt{\mathrm{Re}(\eta_s)}} = A\frac{b_2\eta_l + a_2\eta_l}{\sqrt{\mathrm{Re}(\eta_l)}} + B\frac{b_2 - a_2}{\sqrt{\mathrm{Re}(\eta_l)}} \tag{A.5}$$

$$\frac{a_1 - b_1}{\sqrt{\mathrm{Re}(\eta_s)}} = C\frac{b_2\eta_l + a_2\eta_l}{\sqrt{\mathrm{Re}(\eta_l)}} + D\frac{b_2 - a_2}{\sqrt{\mathrm{Re}(\eta_l)}}\ . \tag{A.6}$$

Equations (A.5) and (A.6) can now be used as a starting point to derive the entries S_{ij} of the scattering matrix $\mathbf{S}$.

Deriving the Transfer Function

The transfer function S_{21} of the multi-layered dielectric can be obtained from (4.22) as

$$S_{21} = \left.\frac{b_2}{a_1}\right|_{a_2=0} . \tag{A.7}$$

Setting now $a_2 = 0$ in (A.5) and (A.6) leads to

$$\frac{a_1\eta_s + b_1\eta_s}{\sqrt{\mathrm{Re}(\eta_s)}} = A\frac{b_2\eta_l}{\sqrt{\mathrm{Re}(\eta_l)}} + B\frac{b_2}{\sqrt{\mathrm{Re}(\eta_l)}} \tag{A.8}$$

$$\frac{a_1 - b_1}{\sqrt{\mathrm{Re}(\eta_s)}} = C\frac{b_2\eta_l}{\sqrt{\mathrm{Re}(\eta_l)}} + D\frac{b_2}{\sqrt{\mathrm{Re}(\eta_l)}} . \tag{A.9}$$

Solving (A.9) for b_1 and inserting it into (A.8) yields

$$2a_1\eta_s = C\frac{b_2\eta_l\eta_s\sqrt{\mathrm{Re}(\eta_s)}}{\sqrt{\mathrm{Re}(\eta_l)}} + D\frac{b_2\eta_s\sqrt{\mathrm{Re}(\eta_s)}}{\sqrt{\mathrm{Re}(\eta_l)}} + A\frac{b_2\eta_l\sqrt{\mathrm{Re}(\eta_s)}}{\sqrt{\mathrm{Re}(\eta_l)}} + B\frac{b_2\sqrt{\mathrm{Re}(\eta_s)}}{\sqrt{\mathrm{Re}(\eta_l)}}$$

$$\Leftrightarrow 2a_1\eta_s = b_2\frac{\sqrt{\mathrm{Re}(\eta_s)}}{\sqrt{\mathrm{Re}(\eta_l)}}\left(\eta_l A + B + \eta_l\eta_s C + \eta_s D\right) . \tag{A.10}$$

Now (A.7) can be used together with (A.10) to get the final result

$$S_{21} = \left.\frac{b_2}{a_1}\right|_{a_2=0} = \frac{\sqrt{\mathrm{Re}(\eta_l)}}{\sqrt{\mathrm{Re}(\eta_s)}}\frac{2\eta_s}{\eta_l A + B + \eta_l\eta_s C + \eta_s D} . \tag{A.11}$$

In a similar way S_{12} can be derived as

$$S_{12} = \left.\frac{b_1}{a_2}\right|_{a_1=0} = \frac{\sqrt{\mathrm{Re}(\eta_s)}}{\sqrt{\mathrm{Re}(\eta_l)}}\frac{2\eta_l}{\eta_l A + B + \eta_l\eta_s C + \eta_s D} . \tag{A.12}$$

However, note that $S_{21} \neq S_{12}$. This is due to the complex source and load impedance. The system is nevertheless reciprocal [MW92].

Derivation of the Reflection Coefficient

From (4.22) it follows that

$$S_{11} = \left.\frac{b_1}{a_1}\right|_{a_2=0} . \tag{A.13}$$

Setting $a_2 = 0$ in (A.5) and (A.6) results again in (A.8) and (A.9). However, now (A.9) needs to be solved for b_2 and inserted into (A.8). This yields

$$\frac{a_1\eta_s + b_1\eta_s}{\sqrt{\mathrm{Re}(\eta_s)}} = \frac{A\eta_l}{\sqrt{\mathrm{Re}(\eta_l)}} \cdot \frac{\frac{a_1-b_1}{\sqrt{\mathrm{Re}(\eta_s)}}}{\frac{C\eta_l}{\sqrt{\mathrm{Re}(\eta_l)}} + \frac{D}{\sqrt{\mathrm{Re}(\eta_l)}}} + \frac{B}{\sqrt{\mathrm{Re}(\eta_l)}} \cdot \frac{\frac{a_1-b_1}{\sqrt{\mathrm{Re}(\eta_s)}}}{\frac{C\eta_l}{\sqrt{\mathrm{Re}(\eta_l)}} + \frac{D}{\sqrt{\mathrm{Re}(\eta_l)}}} \tag{A.14}$$

$$\Leftrightarrow a_1\eta_s - a_1\frac{A\eta_l + B}{C\eta_l + D} = -b_1\eta_s - b_1\frac{A\eta_l + B}{C\eta_l + D}\,. \tag{A.15}$$

Hence, it follows that

$$S_{11} = \frac{\eta_l A + B - \eta_s\eta_l C - \eta_s D}{\eta_l A + B + \eta_s\eta_l C + \eta_s D}\,. \tag{A.16}$$

Appendix B

Definition of Statistic Measures

B.1 Correlation of Complex-Valued Data

This section is mainly based on the work from Schreier and Scharf [SS10] unless indicated otherwise. In general the correlation coefficient between two random variables X and Y is defined as

$$\rho_{XY} = \frac{E\left\{\left(X - E\{X\}\right)\left(Y - E\{Y\}\right)^*\right\}}{\sqrt{E\left\{\left|X - E\{X\}\right|^2\right\} E\left\{\left|Y - E\{Y\}\right|^2\right\}}} = \frac{R_{XY}}{\sqrt{R_{XX}R_{YY}}}\,. \tag{B.1}$$

Real-Valued Data

For real valued random variables X and Y the correlation coefficient ρ_{XY} computed from (B.1) is a real number with $-1 \leq \rho_{XY} \leq 1$. The correlation coefficient gives an indication of how well the relationship between X and Y can be described as a linear function. Computing the correlation coefficient ρ_{XY} is directly related to the linear minimum mean-squared error (MMSE) estimate $\hat{X}(Y)$ of X from Y, which is

$$\hat{X}(Y) = \frac{R_{XY}}{R_{YY}} \cdot Y\,. \tag{B.2}$$

The mean-squared error of this estimate is

$$E\left\{\left|\hat{X}(Y) - X\right|^2\right\} = R_{XX}(1 - |\rho_{XY}|^2)\,. \tag{B.3}$$

Hence, for $|\rho_{XY}| = 1$ the mean-squared error is zero and it is sure that there is a linear relationship between X and Y and $\frac{R_{XY}}{R_{YY}}$ gives the slope. The closer $|\rho_{XY}|$ is to zero, the larger is the uncertainty of the linear MMSE estimate.

Complex-Valued Data

For complex random variables X and Y the correlation coefficient ρ_{XY} computed using (B.1) is a complex number with $|\rho_{XY}| \leq 1$. Similar to the real-valued case above, the correlation coefficient is related to the linear MMSE estimate $\hat{X}(Y)$, which in the complex case is also given by

$$\hat{X}(Y) = \frac{R_{XY}}{R_{YY}} \cdot Y \,. \tag{B.4}$$

Though, in this case R_{XY} is a complex number. Hence, now the estimate $\hat{X}(Y)$ is not only scaled but also rotated in the complex plane. The mean-squared error of this estimate is again

$$E\left\{\left|\hat{X}(Y) - X\right|^2\right\} = R_{XX}(1 - |\rho_{XY}|^2) \,. \tag{B.5}$$

From this relationship it can be concluded that the magnitude of the correlation coefficient ρ_{XY} from (B.1) indicates how well X can be represented as linear function of Y.

However, for complex-valued data the relation ship between X and Y may not only be linear but also *conjugate linear*. This conjugate linear MMSE estimate is of the form

$$\hat{X}(Y^*) = \frac{\tilde{R}_{XY}}{R_{YY}} \cdot Y^* \,, \tag{B.6}$$

where $\tilde{R}_{XY}$ describes the complementary covariance, which is defined as

$$\tilde{R}_{XY} = E\left\{\big(X - E\{X\}\big)\big(Y - E\{Y\}\big)\right\} \,. \tag{B.7}$$

Hence, for the conjugate linear estimate the correlation coefficient is

$$\tilde{\rho}_{XY} = \frac{\tilde{R}_{XY}}{\sqrt{R_{XX}R_{YY}}} = \frac{E\left\{\big(X - E\{X\}\big)\big(Y - E\{Y\}\big)\right\}}{\sqrt{E\left\{\left|X - E\{X\}\right|^2\right\} E\left\{\left|Y - E\{Y\}\right|^2\right\}}} \,. \tag{B.8}$$

In general, also a *widely linear* MMSE function could be fitted to the data. A widely linear estimate has the general form of

$$\hat{X}(Y, Y^*) = \alpha Y + \beta Y^* . \tag{B.9}$$

Thus, it is a combination of linear and conjugate linear estimation. However, it was found that the relationship between the data from the transfer functions as discussed in 4.2.4 and 4.3 is mostly linear and in rare cases only conjugate linear. A widely linear estimate could not be determined in any of the investigated cases. For more details on widely linear MMSE estimation see [SS10].

To determine a single value for the correlation between complex X and Y, either the value of $|\rho_{XY}|$ or $|\tilde{\rho}_{XY}|$ will be taken as the correlation coefficient. Depending on which value is larger. The resulting complex correlation coefficient is denoted as ρ_{XY} in this thesis.

B.2 The Dvoretzky-Kiefer-Wolfowitz Inequality

The Dvoretzky-Kiefer-Wolfowitz inequality gives an upper bound on the probability of error for the difference between an empirical cumulative distribution function (CDF) F_n to the actual CDF $F(x)$ defined on $\mathbb{R}$. The empirical CDF F_n is assumed to be computed using n samples drawn from a real valued random variable X with CDF F. For any $\epsilon > 0$, the inequality reads [Dud14]

$$\mathrm{P}\left(\sup_x \left|(F_n - F)(x)\right| > \epsilon\right) \leq 2e^{-2n\epsilon^2} . \tag{B.10}$$

This result can be used to determine the upper and lower confidence interval of the empirical CDF which contains the real CDF with a certain probability $1 - \alpha$. From (B.10) it follows for the probability α of an error larger than ϵ:

$$\mathrm{P}\left(\sup_x \left|(F_n - F)(x)\right| > \epsilon\right) \leq 2e^{-2n\epsilon^2} \tag{B.11}$$

$$\alpha \leq 2e^{-2n\epsilon^2} \tag{B.12}$$

$$\epsilon \leq \sqrt{\frac{\ln \frac{2}{\alpha}}{2n}} \tag{B.13}$$

Hence, for $\epsilon = \sqrt{\frac{\ln \frac{2}{\alpha}}{2n}}$ the true CDF $F(x)$ lies within the interval $[F_n - \epsilon, Fn + \epsilon]$ with probability $1 - \alpha$.

Appendix C

Path Loss Model Parameters

Table C.1: Modeling parameters for the path loss model from (4.41) where the transfer function was computed either including free space losses (0) or effective tissue losses (e). All values are given in dB. The definition of the communication channels is given in Table 4.3.

			Channel				
Phantom	RL		1	2	3	4	5
Alvar	(0)	PL_0	49.30	56.75	63.96	53.77	51.32
		n	8.42	8.27	8.11	8.36	8.41
	(e)	PL_0	62.59	69.91	77.02	67.01	64.63
		n	8.47	8.35	8.20	8.42	8.46
AustinMan 1	(0)	PL_0	44.93	53.40	62.03	49.80	47.03
		n	10.50	10.43	10.29	10.46	10.48
	(e)	PL_0	58.92	67.22	75.73	63.74	61.04
		n	10.53	10.48	10.36	10.50	10.50
AustinMan 2	(0)	PL_0	43.65	52.12	60.76	48.53	45.80
		n	10.58	10.47	10.29	10.53	10.55
	(e)	PL_0	57.65	65.96	74.45	62.47	59.81
		n	10.61	10.51	10.36	10.56	10.56
AustinWoman 1	(0)	PL_0	34.52	42.44	50.57	39.21	36.69
		n	11.51	11.50	11.43	11.48	11.46
	(e)	PL_0	47.22	54.95	62.89	51.83	49.39
		n	11.49	11.50	11.45	11.47	11.44
AustinWoman 2	(0)	PL_0	35.44	43.55	51.86	40.19	37.53
		n	11.26	11.19	11.05	11.21	11.23
	(e)	PL_0	48.40	56.32	64.42	53.06	50.48
		n	11.18	11.12	11.01	11.14	11.15

Table C.1: Modeling parameters for the path loss model from (4.41) where the transfer function was computed either including free space losses (0) or effective tissue losses (e). All values are given in dB. The definition of the communication channels is given in Table 4.3.

			Channel				
Phantom	RL		1	2	3	4	5
Donna	(0)	PL_0	33.79	41.51	49.61	38.40	35.97
		n	11.95	11.85	11.57	11.90	11.91
	(e)	PL_0	46.38	53.97	61.91	50.94	48.56
		n	11.99	11.89	11.63	11.95	11.95
Golem	(0)	PL_0	47.71	55.31	62.88	52.26	49.83
		n	9.55	9.48	9.35	9.51	9.52
	(e)	PL_0	61.43	68.85	76.26	65.90	63.56
		n	9.50	9.46	9.36	9.47	9.47
Hanako	(0)	PL_0	53.67	60.77	67.63	57.96	55.68
		n	7.89	7.66	7.41	7.80	7.88
	(e)	PL_0	68.01	74.98	81.73	72.24	70.01
		n	7.82	7.61	7.37	7.74	7.82
Helga	(0)	PL_0	28.90	37.65	46.86	33.95	31.08
		n	12.02	11.98	11.82	11.99	11.98
	(e)	PL_0	41.54	50.10	59.09	46.53	43.74
		n	12.00	11.99	11.85	11.98	11.96
Irene	(0)	PL_0	56.61	63.59	70.25	60.83	58.56
		n	7.38	7.26	7.17	7.36	7.41
	(e)	PL_0	72.41	79.30	85.88	76.59	74.36
		n	7.34	7.23	7.14	7.32	7.37
Taro	(0)	PL_0	56.44	63.78	70.81	60.81	58.39
		n	8.12	7.99	7.83	8.08	8.14
	(e)	PL_0	70.62	77.87	84.80	74.94	72.56
		n	8.13	8.00	7.85	8.09	8.14
VisibleHuman	(0)	PL_0	45.91	55.06	64.22	50.98	47.89
		n	10.18	10.02	9.85	10.12	10.16
	(e)	PL_0	60.13	69.12	78.15	65.15	62.13
		n	10.21	10.08	9.93	10.16	10.19

List of Acronyms and Abbreviations

ARQ	Automatic retransmission query
AWGN	Additive white Gaussian noise
BAN	Body area network
BER	Bit error rate
BMI	Body mass index
CDF	Cumulative distribution function
CDMA	Code division multiple access
CT	Computer tomography
EIRP	Effective isotropic radiated power
ERP	Effective radiated power
ETSI	European Telecommunications Standards Institute
FCC	US Federal Communications Commission
FDA	US Food and Drug Administration
FDTD	Finite difference time domain
FIT	Finite integration technique
FSK	Frequency shift keying
GI	Gastrointestinal
GSM	Global System for Mobile Communications
HBC	Human body communication
ICNIRP	International Commission on Non-Ionizing Radiation Protection

IR	Impulse radio
ISM	Industrial, scientific and medical band
MAC	Medium access control
MICS	Medical Implant Communication Service
MMSE	Minimum mean-squared error
MRI	Magnetic resonance imaging
MSE	Mean-squared error
NICT	National Institute of Information and Communications Technology
OFDM	Orthogonal frequency divison multiplex
PDF	Probability density function
PDP	Power delay profile
PPM	Pulse position modulation
PSD	Power spectral density
PSK	Phase shift keying
QAM	Quadrature amplitude modulation
QoS	Quality of Service
RF	Radio frequency
RMS	Root mean square
SA	Specific absorption
SAR	Specific absorption rate
TEM	Transverse electromagnetic
UHF	Ultra high frequency (300 MHz to 3 GHz)
UWB	Ultra wideband
WC	Waist circumference
WHO	World Health Organisation
WtHR	Waist-to-height ratio

Bibliography

[ACG+16] C. Andreu, S. Castello-Palacios, C. Garcia-Pardo, A. Fornes-Leal, A. Valles-Lluch, and N. Cardona, "Spatial In-Body Channel Characterization Using an Accurate UWB Phantom", *IEEE Transactions on Microwave Theory and Techniques*, vol. 64, no. 11, pp. 3995–4002, 2016. DOI: 10.1109/TMTT.2016.2609409.

[Ack98] M. J. Ackerman, "The Visible Human Project", *Proceedings of the IEEE*, vol. 86, no. 3, pp. 504–511, 1998. DOI: 10.1109/5.662875.

[AFP97] D. Andreuccetti, R. Fossi, and C. Petrucci. (1997). An Internet resource for the calculation of the dielectric properties of body tissues in the frequency range 10 Hz - 100 GHz, http://niremf.ifac.cnr.it/tissprop/. Accessed: 2021-10-05.

[AGC+18] C. Andreu, C. Garcia-Pardo, S. Castello-Palacios, A. Valles-Lluch, and N. Cardona, "Frequency Dependence of UWB In-Body Radio Channel Characteristics", *IEEE Microwave and Wireless Components Letters*, pp. 1–3, 2018. DOI: 10.1109/LMWC.2018.2808427.

[AGF+17] C. Andreu, C. Garcia-Pardo, A. Fomes-Leal, M. Cabedo-Fabres, and N. Cardona, "UWB In-Body Channel Performance by Using a Direct Antenna Designing Procedure", in *11th European Conference on Antennas and Propagation (EUCAP)*, IEEE, 2017, pp. 278–282. DOI: 10.23919/EuCAP.2017.7928416.

[AHY+06] A. Alomainy, Y. Hao, Y. Yuan, and Y. Liu, "Modelling and Characterisation of Radio Propagation from Wireless Implants at Different Frequencies", in *The 9th European Conference on Wireless Technology*, Piscataway, NJ: IEEE Service Center, 2006, pp. 119–122. DOI: 10.1109/ECWT.2006.280449.

[AKC+14] D. Anzai, K. Katsu, R. Chávez-Santiago, Q. Wang, D. Plettemeier, J. Wang, and I. Balasingham, "Experimental Evaluation of Implant UWB-IR Transmission With Living Animal for Body Area Networks",

IEEE Transactions on Microwave Theory and Techniques, vol. 62, no. 1, pp. 183–192, 2014. DOI: 10.1109/TMTT.2013.2291542.

[AM11] S. N. Adler and Y. C. Metzger, "PillCam COLON capsule endoscopy: recent advances and new insights", *Therapeutic Advances in Gastroenterology*, vol. 4, no. 4, pp. 265–268, 2011. DOI: 10.1177/1756283X11401645.

[And16] D. Andreuccetti, *Dielectric Properties of Tissues: Correspondence per E-Mail*, Jan. 8, 2016.

[And18] D. Andreuccetti, *Dielectric Properties of Body Tissues: Correspondence per E-Mail*, Jun. 18, 2018.

[APG+18] M. Awan, S. Perez-Simbor, C. Garcia-Pardo, K. Kansanen, and N. Cardona, "Experimental Phantom-Based Security Analysis for Next-Generation Leadless Cardiac Pacemakers", *Sensors*, vol. 18, no. 12, p. 4327, 2018. DOI: 10.3390/s18124327.

[ATK+09] T. Aoyagi, K. Takizawa, T. Kobayashi, J. Takada, and R. Kohno, "Development of a WBAN channel model for capsule endoscopy", in *Antennas and Propagation Society International Symposium*, 2009, pp. 1–4. DOI: 10.1109/APS.2009.5172160.

[ATT+08] T. Aoyagi, J. Takada, K. Takizawa, H. Sawada, N. Katayama, K. Y. Yazdandoost, H.-B. Li, and R. Kohno. (2008). Channel model for wearable and implantable WBANs, https://mentor.ieee.org/802.15/dcn/08/15-08-0416-04-0006-channel-models-for-wearable-and-implantable-wbans.pdf. Accessed: 2014-08-06.

[BB16] J.-C. Brumm and G. Bauch, "Optimum Receiver Location for Ultra Wideband In-Body Communication Based on Channel Capacity Calculation", in *11th International Conference on Body Area Networks*, Turin, Italy, 2016.

[BB17a] J.-C. Brumm and G. Bauch, "Channel Capacity and Optimum Transmission Bandwidth of In-Body Ultra Wideband Communication Links", in *11th International ITG Conference on Systems, Communications and Coding 2017 (SCC'2017)*, Hamburg, Germany, 2017.

[BB17b] J.-C. Brumm and G. Bauch, "On the Placement of On-Body Antennas for Ultra Wideband Capsule Endoscopy", *IEEE Access*, vol. 5, pp. 10 141–10 149, 2017. DOI: 10.1109/ACCESS.2017.2706300.

[BB17c] J.-C. Brumm and G. Bauch, "On the Shadowing Distribution for Ultra Wideband In-Body Communication Path Loss Modeling", in

IEEE AP-S Symposium on Antennas and Propagation and USNC-URSI Radio Science Meeting, San Diego, CA, USA, 2017. DOI: 10.1109/APUSNCURSINRSM.2017.8072445.

[BB19] J.-C. Brumm and G. Bauch, "Influence of Physiological Properties on the Channel Capacity for Ultra Wideband In-Body Communication", in *13th International Symposium on Medical Information and Communication Technology (ISMICT)*, Oslo, Norway, 2019. DOI: 10.1109/ISMICT.2019.8743876.

[BB20] J.-C. Brumm and G. Bauch, "Verification of a Simplified Channel Modeling Technique for Ultra Wideband In-Body Communication with Simulations", in *European Conference on Antennas and Propagation (EuCAP'2020)*, Kopenhagen, 2020.

[BKB19] J.-C. Brumm, J. Kohagen, and G. Bauch, "Improving Ultra Wideband In-Body Communication Using Space Diversity", in *12th International ITG Conference on Systems, Communications and Coding 2019 (SCC'2019)*, Rostock, Germany, 2019. DOI: 10.30420/454862027.

[BLM04] J. R. Barry, E. A. Lee, and D. G. Messerschmitt, *Digital Communication*, 3rd ed. Boston, MA: Springer US, 2004.

[BMA+16] H. Bahrami, S. A. Mirbozorgi, R. Ameli, L. A. Rusch, and B. Gosselin, "Flexible, Polarization-Diverse UWB Antennas for Implantable Neural Recording Systems", *IEEE Transactions on Biomedical Circuits and Systems*, vol. 10, no. 1, pp. 38–48, 2016. DOI: 10.1109/TBCAS.2015.2393878.

[BMR+14] H. Bahrami, S. A. Mirbozorgi, L. A. Rusch, and B. Gosselin, "BER Performance of Implant-to-Air High-Speed UWB Data Communications for Neural Recording Systems", in *36th Annual International Conference of the IEEE Engineering in Medicine and Biology Society (EMBC'2014)*, vol. 2014, Chicago, IL, 2014, pp. 3961–3964. DOI: 10.1109/EMBC.2014.6944491.

[Bra07] P. D. Bradley, "Implantable ultralow-power radio chip facilitates in-body communications", *RF Design*, vol. 30, no. 6, p. 20, 2007.

[Bru20] J.-C. Brumm. (2020). LayerModel_lib: A Python toolkit to compute the transmission behaviour of plane electromagnetic waves through human tissue, https://doi.org/10.5281/zenodo.3507609. Accessed: 2023-05-26.

[BSB19] J.-C. Brumm, H. Strohm, and G. Bauch, "A Stochastic Channel Model for UWB In-Body Communication", in *41st Annual International Conference of the IEEE Engineering in Medicine and Biology Society (EMBC'2019)*, Berlin, Germany, 2019.

[Bun19a] Bundesnetzagentur, *Allgemeinzuteilung von Frequenzen für die Nutzung durch Ultrabreitbandgeräte (UWB): Vfg. Nr. 135/2019*, 2019.

[Bun19b] Bundesnetzagentur, *Allgemeinzuteilung von Frequenzen für Funkanlagen kleiner Leistung im Gesundheitsbereich: Vfg. Nr. 134/2019*, 2019.

[Cap16a] CapsoVision, Inc. (2016). CapsoCam Plus, `https://www.nicolai-medizintechnik.de/dokumente/CapsoCamPlus.pdf`. Accessed: 2022-01-21.

[Cap16b] CapsoVision, Inc. (2016). CapsoCam Plus: See More. Diagnose Smarter., `http://www.nicolai-medizintechnik.de/dokumente/CapsoCam_2016.pdf`. Accessed: 2017-04-13.

[CB14] R. Chávez-Santiago and I. Balasingham, "Radio propagation models for in-body sensors", in *2014 XXXIth URSI General Assembly and Scientific Symposium (URSI GASS)*, 2014, pp. 1–4. DOI: `10.1109/URSIGASS.2014.6930106`.

[CBB+13] R. Chávez-Santiago, I. Balasingham, J. Bergsland, W. Zahid, K. Takizawa, R. Miura, and H.-B. Li, "Experimental implant communication of high data rate video using an ultra wideband radio link", in *35th Annual International Conference of the IEEE Engineering in Medicine and Biology Society (EMBC'2013)*, 2013, pp. 5175–5178. DOI: `10.1109/EMBC.2013.6610714`.

[CBB12] R. Chávez-Santiago, I. Balasingham, and J. Bergsland, "Ultrawideband Technology in Medicine: A Survey", *Journal of Electrical and Computer Engineering*, vol. 2012, no. 15, pp. 1–9, 2012. DOI: `10.1155/2012/716973`.

[CGF+15] R. Chávez-Santiago, C. Garcia-Pardo, A. Fornes-Leal, A. Valles-Lluch, G. Vermeeren, W. Joseph, I. Balasingham, and N. Cardona, "Experimental Path Loss Models for In-Body Communications within 2.36-2.5 GHz", *IEEE Journal of Biomedical and Health Informatics*, 2015. DOI: `10.1109/JBHI.2015.2418757`.

[CGF+16] S. Castello-Palacios, C. Garcia-Pardo, A. Fornes-Leal, N. Cardona, and A. Valles-Lluch, "Tailor-Made Tissue Phantoms Based on Acetonitrile Solutions for Microwave Applications up to 18 GHz", *IEEE Transactions on Microwave Theory and Techniques*, vol. 64, no. 11, pp. 3987–3994, 2016. DOI: `10.1109/TMTT.2016.2608890`.

[Cha14] R. Chandra, "Antennas, Wave Propagation, and Localization in Wireless Body Area Networks", Dissertation, Lunds Universitet, Lund, Sweden, 2014.

[CKB+09] R. Chávez-Santiago, A. Khaleghi, I. Balasingham, and T. A. Ramstad, "Architecture of an Ultra Wideband Wireless Body Area Network for Medical Applications", in *2nd International Symposium on Applied Sciences in Biomedical and Communication Technologies (ISABEL)*, 2009, pp. 1–6. DOI: 10.1109/ISABEL.2009.5373624.

[CMD11] G. Ciuti, A. Menciassi, and P. Dario, "Capsule endoscopy: From current achievements to open challenges", *IEEE Reviews in Biomedical Engineering*, vol. 4, pp. 59–72, 2011. DOI: 10.1109/RBME.2011.2171182.

[CSK+13] R. Chávez-Santiago, K. Sayrafian-Pour, A. Khaleghi, K. Takizawa, J. Wang, I. Balasingham, and H.-B. Li, "Propagation Models for IEEE 802.15.6 Standardization of Implant Communication in Body Area Networks", *IEEE Communications Magazine*, vol. 51, no. 8, pp. 80–87, 2013. DOI: 10.1109/MCOM.2013.6576343.

[CWB13] R. Chávez-Santiago, J. Wang, and I. Balasingham, "The Ultra Wideband Capsule Endoscope", in *IEEE International Conference on Ultra-Wideband (ICUWB)*, Institute of Electrical and Electronics Engineers, Ed., 2013, pp. 72–78. DOI: 10.1109/ICUWB.2013.6663825.

[DAA+16] A. F. Demir, Z. E. Ankarali, Q. H. Abbasi, Y. Liu, K. Qaraqe, E. Serpedin, H. Arslan, and R. D. Gitlin, "In Vivo Communications: Steps Toward the Next Generation of Implantable Devices", *IEEE Vehicular Technology Magazine*, vol. 11, no. 2, pp. 32–42, 2016. DOI: 10.1109/MVT.2016.2520492.

[Dan11] M. V. Dancsisin, "Characterization of Tissue Mimicking Materials for Testing of Microwave Medical Devices", Master Thesis, Mississippi State University, Mississippi, 2011.

[Das20] Dassault Systèmes. (2020). CST Studio Suite 3D EM simulation and analysis software, https://www.3ds.com/products-services/simulia/products/cst-studio-suite/. Accessed: 2020-05-04.

[Di 06] M.-G. Di Benedetto, Ed., *UWB Communication Systems: A Comprehensive Overview*, ser. EURASIP book series on signal processing and communications. New York, NY: Hindawi Publ, 2006, vol. 5.

[Dud14] R. M. Dudley, *Uniform central limit theorems*, Second edition, ser. Cambridge studies in advanced mathematics. Cambridge: Cambridge University Press, 2014, vol. 142. DOI: 10.1017/CBO9781139014830.

[Dum20] G. Dumphart, "Magneto-Inductive Communication and Localization: Fundamental Limits with Arbitrary Node Arrangements", PhD thesis, PhD Thesis, ETH Zurich, 2020.

[EU 19] EU Commision, "Commission Implementing Decision (EU) 2019/785 on the harmonisation of radio spectrum for equipment using ultra-wideband technology in the Union and repealing Decision: 2007/131/EC", *Official Journal of the European Union L127*, vol. 62, pp. 23–33, May 14, 2019.

[Eur16a] European Telecommunications Standards Institute, *Short Range Devices (SRD) using Ultra Wide Band (UWB); Part 3: Worldwide UWB regulations between 3.1 and 10.6 GHz*, V1.1.1, ETSI TR 103 181-3, 2016.

[Eur16b] European Telecommunications Standards Institute, *Short Range Devices (SRD) using Ultra Wide Band technology (UWB); Harmonised Standard covering the essential requirements of article 3.2 of the Directive 2014/53/EU; Part 1: Requirements for Generic UWB applications*, V2.1.1, ETSI TR 302 065-1, 2016.

[Eur16c] European Telecommunications Standards Institute, *Ultra Low Power Active Medical Implants (ULP-AMI) and associated Peripherals (ULP-AMI-P) operating in the frequency range 402 MHz to 405 MHz*, 2.1.1, ETSI EN 301 839, 2016.

[Eur19] European Telecommunications Standards Institute, *Ultra Low Power (ULP) wireless medical capsule endoscopy devices operating in the band 430 MHz to 440 MHz; Harmonised Standard for access to radio spectrum*, 1.2.1, ETSI EN 302 520, 2019.

[FCB+15] P. A. Floor, R. Chávez-Santiago, S. Brovoll, O. Aardal, J. Bergsland, O.-J. Grymyr, P. S. Halvorsen, R. Palomar, D. Plettemeier, S.-E. Hamran, T. A. Ramstad, and I. Balasingham, "In-Body to On-Body Ultrawideband Propagation Model Derived from Measurements in Living Animals", *IEEE Journal of Biomedical and Health Informatics*, vol. 19, no. 3, pp. 938–948, 2015. DOI: 10.1109/JBHI.2015.2417805.

[FCF+19] A. Fornes-Leal, N. Cardona, M. Frasson, S. Castello-Palacios, A. Nevarez, V. P. Beltran, and C. Garcia-Pardo, "Dielectric Characterization of In Vivo Abdominal and Thoracic Tissues in the 0.5 – 26.5 GHz Frequency Band for Wireless Body Area Networks", *IEEE Access*, p. 1, 2019. DOI: 10.1109/ACCESS.2019.2903481.

[FCK+19] P. A. Floor, R. Chavez-Santiago, A. N. Kim, K. Kansanen, T. A. Ramstad, and I. Balasingham, "Communication Aspects for a Measurement Based UWB In-Body to On-Body Channel", *IEEE Access*, vol. 7, pp. 29 425–29 440, 2019. DOI: 10.1109/ACCESS.2019.2902104.

[FCP+18] J. Faerber, G. Cummins, S. K. Pavuluri, P. Record, A. R. A. Rodriguez, H. S. Lay, R. McPhillips, B. F. Cox, C. Connor, R. Gregson, R. E. Clutton, S. R. Khan, S. Cochran, and M. P. Y. Desmulliez, "In Vivo Characterization of a Wireless Telemetry Module for a Capsule Endoscopy System Utilizing a Conformal Antenna", *IEEE Transactions on Biomedical Circuits and Systems*, vol. 12, no. 1, pp. 95–105, 2018. DOI: 10.1109/TBCAS.2017.2759254.

[For07] A. Fort, "Body Area Communications: Channel Characterization and Ultra-Wideband System-Level Approach for Low Power", Dissertation, Vrije Universiteit Brussel, Brussels, 2007.

[Fos00] K. R. Foster, "Thermal and Nonthermal Mechanisms of Interaction of Radio-Frequency Energy with Biological Systems", *IEEE Transactions on Plasma Science*, vol. 28, no. 1, pp. 15–23, 2000. DOI: 10.1109/27.842819.

[Fri46] H. T. Friis, "A Note on a Simple Transmission Formula", *Proceedings of the IRE*, vol. 34, no. 5, pp. 254–256, 1946. DOI: 10.1109/JRPROC.1946.234568.

[FZP+04] U. A. Fill, M. Zankl, N. Petoussi-Henss, M. Siebert, and D. Regulla, "Adult Female Voxel Models of Different Stature and Photon Conversion Coefficients for Radiation Protection", *Health Physics*, vol. 86, no. 3, 2004.

[Gab96] C. Gabriel, "Compilation of the Dielectric Properties of Body Tissues at RF and Microwave Frequencies", *Brooks Air Force Technical Report*, no. AL/OE-TR-1996-0037, 1996.

[GCC+15] C. Garcia-Pardo, R. Chávez-Santiago, N. Cardona, and I. Balasingham, "Experimental UWB Frequency Analysis for Implant Communications", in *37th Annual International Conference of the IEEE Engineering in Medicine and Biology Society (EMBC'2015)*, vol. 2015, 2015, pp. 5457–5460. DOI: 10.1109/EMBC.2015.7319626.

[GFC+16] C. Garcia-Pardo, A. Fornes-Leal, N. Cardona, R. Chavez-Santiago, J. Bergsland, I. Balasingham, S. Brovoll, O. Aardal, S.-E. Hamran, and R. Palomar, "Experimental Ultra Wideband Path Loss Models for Implant Communications", in *27th IEEE International Symposium*

on Personal, Indoor, and Mobile Radio Communications (PIMRC), Valencia, Spain, 2016, pp. 1–6. DOI: 10.1109/PIMRC.2016.7794780.

[GGC96] C. Gabriel, S. Gabriel, and E. Corthout, "The dielectric properties of biological tissues: I. Literature survey", *Physics in Medicine and Biology*, vol. 41, no. 11, pp. 2231–2249, 1996. DOI: 10.1088/0031-9155/41/11/001.

[GLG96a] S. Gabriel, R. W. Lau, and C. Gabriel, "The dielectric properties of biological tissues: II. Measurements in the frequency range 10 Hz to 20 GHz", *Physics in Medicine and Biology*, vol. 41, no. 11, pp. 2251–2269, 1996. DOI: 10.1088/0031-9155/41/11/002.

[GLG96b] S. Gabriel, R. W. Lau, and C. Gabriel, "The dielectric properties of biological tissues: Part III. Parametric models for the dielectric spectrum of tissues", *Physics in Medicine and Biology*, vol. 41, no. 11, pp. 2271–2293, 1996. DOI: 10.1088/0031-9155/41/11/003.

[GMB15] L. M. Gonzalez, A. J. Moeser, and A. T. Blikslager, "Porcine models of digestive disease: The future of large animal translational research", *Translational Research*, vol. 166, no. 1, pp. 12–27, 2015. DOI: 10.1016/j.trsl.2015.01.004.

[GMH+02] M. Ghavami, L. B. Michael, S. Haruyama, and R. Kohno, "A Novel UWB Pulse Shape Modulation System", *Wireless Personal Communications*, vol. 23, no. 1, pp. 105–120, 2002. DOI: 10.1023/A:1020953424161.

[GMK07] M. Ghavami, L. B. Michael, and R. Kohno, *Ultra Wideband Signals and Systems in Communication Engineering*. Chichester, UK: John Wiley & Sons, Ltd, 2007. DOI: 10.1002/9780470060490.

[Gol05] A. Goldsmith, *Wireless Communications*. Cambridge University Press., 2005.

[Gol49] M. J. E. Golay, "Note on the Theoretical Efficiency of Information Reception with PPM", *Proceedings of the IRE*, vol. 37, no. 9, p. 1031, 1949.

[GZ11] A. C. Gordillo and K. Zhou, "Design Considerations for Implant — On-Body UWB Communication for Medical Applications", in *2nd National Conference on Telecommunications (CONATEL)*, Piscataway, NJ: IEEE, 2011, pp. 1–5. DOI: 10.1109/CONATEL.2011.5958662.

[Hel16] Helmholtz Zentrum München Deutsches Forschungszentrum für Gesundheit und Umwelt. (2016). Virtual Human Database, https://www.helmholtz-muenchen.de/irt/service/virtual-human-download-

portal/virtual-human-database/index.html. Accessed: 2016-06-23.

[Höh13] P. A. Höher, *Grundlagen der digitalen Informationsübertragung: Von der Theorie zu Mobilfunkanwendungen*, 2., überarb. u. erw. Aufl., ser. Lehrbuch. Wiesbaden: Springer Vieweg, 2013.

[IMG+00] G. Iddan, G. Meron, A. Glukhovsky, and P. Swain, "Wireless capsule endoscopy", *Nature*, vol. 405, no. 6785, p. 417, 2000. DOI: 10.1038/35013140.

[Ins05] Institute of Electrical and Electronics Engineers, *IEEE Standard for Safety Levels with Respect to Human Exposure to Radio Frequency Electromagnetic Fields, 3 kHz to 300 GHz*, 2005. DOI: 10.1109/IEEESTD.2006.99501.

[Ins12] Institute of Electrical and Electronics Engineers, *IEEE Std 802.15.6-2012, IEEE Standard for Local and metropolitan area networks - Part 15.6: Wireless Body Area Networks*, 2012.

[Ins20] Institute of Electrical and Electronics Engineers, *IEEE Std 802.15.4–2020. IEEE Standard for Low-Rate Wireless Networks*, Piscataway, NJ, USA, 2020. DOI: 10.1109/IEEESTD.2020.9144691.

[Int02] International Telecommunication Union, *RS.1346 : Sharing between the meteorological aids service and medical implant communication systems (MICS) operating in the mobile service in the frequency band 401-406 MHz*, 2002.

[Int13a] International Agency for Research on Cancer, *Non-ionizing radiation: Part 2: radiofrequency electromagnetic fields (volume 102)*, ser. IARC monographs on the evaluation of carcinogenic risks to humans. 2013, vol. 102.

[Int13b] IntroMedic. (2013). MiroCam Capsule Endoscope: User Manual, https://apps.fcc.gov/oetcf/eas/reports/ViewExhibitReport.cfm?mode=Exhibits&RequestTimeout=500&calledFromFrame=N&application_id=lDzQpmMw1wlbe%2Bu%2BnArgNg%3D%3D&fcc_id=VAXINTROMEDIC5. Accessed: 2022-01-21.

[Int15] IntroMedic. (2015). MiroCam, http://intromedic.com/eng/sub_products_2.html. Accessed: 2015-02-09.

[Int20] International Commission on Non-Ionizing Radiation Protection, "ICNIRP Note: Critical Evaluation of Two Radiofrequency Electromagnetic Field Animal Carcinogenicity Studies Published in 2018", *Health Physics*, vol. 118, no. 5, pp. 525–532, 2020. DOI: 10.1097/HP.0000000000001137.

[Int98] International Commission on Non-Ionizing Radiation Protection, "Guidelines for Limiting Exposure to Time-Varying Electric, Magnetic and Electromagnetic Fields (Up to 300GHz)", *Health Physics*, vol. 74, no. 4, pp. 494–522, 1998.

[ITI18] IT'IS Foundation, *Tissue Properties Database V4.0*, 2018. DOI: 10.13099/VIP21000-04-0.

[JDM75] C. C. Johnson, C. H. Durney, and H. Massoudi, "Electromagnetic Power Absorption in Anisotropic Tissue Media (Short Papers)", *IEEE Transactions on Microwave Theory and Techniques*, vol. 23, no. 6, pp. 529–532, 1975. DOI: 10.1109/TMTT.1975.1128617.

[JKK+10] J.-H. Jung, S.-W. Kim, Y.-S. Kim, and S.-Y. Kim, "Electromagnetic Propagation From the Intestine-Ingested Source in the Human Body Model", *IEEE Transactions on Antennas and Propagation*, vol. 58, no. 5, pp. 1683–1688, 2010. DOI: 10.1109/TAP.2010.2044338.

[KB09] A. Khaleghi and I. Balasingham, "Improving In-Body Ultra Wideband Communication Using Near-Field Coupling of the Implanted Antenna", *Microwave and Optical Technology Letters*, vol. 51, no. 3, pp. 585–589, 2009. DOI: 10.1002/mop.24126.

[KCB10] A. Khaleghi, R. Chávez-Santiago, and I. Balasingham, "Ultra-wideband pulse-based data communications for medical implants", *IET Communications*, vol. 4, no. 15, p. 1889, 2010. DOI: 10.1049/iet-com.2009.0692.

[KCL+10] A. Khaleghi, R. Chávez-Santiago, X. Liang, I. Balasingham, Leung, Victor C. M., and T. A. Ramstad, "On Ultra Wideband Channel Modeling for In-Body Communications", in *IEEE 5th International Symposium on Wireless Pervasive Computing 2010*, 2010, pp. 140–145. DOI: 10.1109/ISWPC.2010.5483804.

[KFR+12] A. N. Kim, P. A. Floor, T. A. Ramstad, and I. Balasingham, "Communication using Ultra Wide-band Pulse Position Modulation for In-body Sensors", in *Proceedings of the 7th International Conference on Body Area Networks*, Oslo, Norway: ICST, 2012, pp. 159–165.

[KHT08] T. Karacolak, A. Z. Hood, and E. Topsakal, "Design of a Dual-Band Implantable Antenna and Development of Skin Mimicking Gels for Continuous Glucose Monitoring", *IEEE Transactions on Microwave Theory and Techniques*, vol. 56, no. 4, pp. 1001–1008, 2008. DOI: 10.1109/TMTT.2008.919373.

[KKS14] M. Kanaan, C. Kocer, and M. Suveren, "On the Relationship Between Antenna Parameters and Near-Field Effects for UWB Implant Body

Area Networks", in *8th International Symposium on Medical Information and Communication Technology (ISMICT)*, 2014, pp. 1–5. DOI: 10.1109/ISMICT.2014.6825231.

[KLN+07] C. Kim, T. Lehmann, S. Nooshabadi, and I. Nevat, "An ultra-wideband transceiver architecture for wireless endoscopes", in *International Symposium on Communications and Information Technologies (ISCIT)*, Institute of Electrical and Electronics Engineers, Ed., Piscataway, NJ: IEEE Service Center, 2007, pp. 1252–1257. DOI: 10.1109/ISCIT.2007.4392209.

[KLP+08] J. Kim, H. S. Lee, J. K. Pack, and T. H. Kim, *Channel Modeling for Medical Implanted Communication Systems by Numerical Simulation*, 2008.

[KN14] A. Kiourti and K. S. Nikita, "Numerical and Experimental Techniques for Body Area Electromagnetics", in *Handbook of Biomedical Telemetry*, ser. IEEE Press Series on Biomedical Engineering, K. S. Nikita, Ed., Wiley-IEEE Press, 2014, pp. 133–173. DOI: 10.1002/9781118893715.ch6.

[KN17] A. Kiourti and K. S. Nikita, "A Review of In-Body Biotelemetry Devices: Implantables, Ingestibles, and Injectables", *IEEE Transactions on Biomedical Engineering*, vol. 64, no. 7, 2017. DOI: 10.1109/TBME.2017.2668612.

[KPN14] A. Kiourti, K. A. Psathas, and K. S. Nikita, "Implantable and Ingestible Medical Devices With Wireless Telemetry Functionalities: A Review of Current Status and Challenges", *Bioelectromagnetics*, vol. 35, no. 1, pp. 1–15, 2014. DOI: 10.1002/bem.21813.

[KRB11] A. N. Kim, T. A. Ramstad, and I. Balasingham, "Very low complexity low rate image coding for the wireless endoscope", in *Proceedings of the 4th International Symposium on Applied Sciences in Biomedical and Communication Technologies*, S. Frattasi, Ed., New York, NY: ACM, 2011, pp. 1–5. DOI: 10.1145/2093698.2093788.

[KSK+19] C. Kissi, M. Särestöniemi, T. Kumpuniemi, M. Sonkki, S. Myllymaki, M. N. Srifi, and C. Pomalaza-Raéz, "Directive Low-Band UWB Antenna for In-body Medical Communications", *IEEE Access*, pp. 149 026–149 038, 2019. DOI: 10.1109/ACCESS.2019.2947057.

[KSS13] M. Kanaan, M. Suveren, and O. Saracoglu, "On The Bandwidth Dependency of Near-Field Effects in UWB Implant Body Area Networks", in *Proceedings of the 8th International Conference on Body*

Area Networks, ser. ACM Digital Library, Boston, Massachusetts, United States, 2013. DOI: 10.4108/icst.bodynets.2013.253926.

[Laa18] I. Laakso. (2018). Alvar: Adult whole-body anatomic phantom for computational dosimetry, https://version.aalto.fi/gitlab/ilaakso/alvar. Accessed: 2020-03-25.

[LIS+18] P. Leelatien, K. Ito, K. Saito, M. Sharma, and A. Alomainy, "Channel Characteristics and Wireless Telemetry Performance of Transplanted Organ Monitoring System Using Ultra-wideband Communication", *IEEE Journal of Electromagnetics, RF and Microwaves in Medicine and Biology*, vol. 2, no. 2, pp. 94–101, 2018. DOI: 10.1109/JERM.2018.2827779.

[Mac59] R. S. Mackay, "Radio Telemetering from Within the Human Body", *IRE Transactions on Medical Electronics*, vol. ME-6, no. 2, pp. 100–105, 1959. DOI: 10.1109/IRET-ME.1959.5007926.

[MBC+05] A. F. Molisch, D. C. Balakrishnan, C.-C. Chong, S. Emami, A. Fort, J. Karedal, J. Kunisch, H. G. Schantz, U. Schuster, and K. Siwiak. (2005). IEEE 802.15.4a channel model - final report, https://mentor.ieee.org/802.15/dcn/04/15-04-0662-04-004a-channel-model-final-report-r1.pdf. Accessed: 2020-09-10.

[MCC+06] A. F. Molisch, D. Cassioli, C.-C. Chong, S. Emami, A. Fort, B. Kannan, J. Karedal, J. Kunisch, H. G. Schantz, K. Siwiak, and M. Z. Win, "A Comprehensive Standardized Model for Ultrawideband Propagation Channels", *IEEE Transactions on Antennas and Propagation*, vol. 54, no. 11, pp. 3151–3166, 2006. DOI: 10.1109/TAP.2006.883983.

[Mel20] R. Melnick, "Regarding ICNIRP'S Evaluation of the National Toxicology Program's Carcinogenicity Studies on Radiofrequency Electromagnetic Fields", *Health Physics*, vol. 118, no. 6, pp. 678–682, 2020. DOI: 10.1097/HP.0000000000001268.

[MFT+09] N. Mitsuhashi, K. Fujieda, T. Tamura, S. Kawamoto, T. Takagi, and K. Okubo, "BodyParts3D: 3D structure database for anatomical concepts", *Nucleic Acids Research*, vol. 37, no. Database, pp. D782–D785, 2009. DOI: 10.1093/nar/gkn613.

[MHM11] D. Manteuffel, P. A. Höher, and M. Mehdorn, "Evaluation of RF Localization for Deep Brain Implants", in *5th European Conference on Antennas and Propagation (EuCAP)*, 2011, pp. 2372–2376.

[Mic14] Microsemi Corporation. (2014). ZL70103 Medical Implantable RF Transceiver Datasheet, http://www.microsemi.com/document

-portal/doc_download/134304-zl70103-datasheet. Accessed: 2015-05-26.

[MKP+04] T. Matila, M. Kosamo, T. Patana, P. Jakkula, T. Hirvonen, and I. Oppermann, "UWB Antennas", in *UWB Theory and Applications*, I. Oppermann, M. Hämäläinen, and J. Iinatti, Eds., Chichester, UK: John Wiley & Sons, Ltd, 2004. DOI: 10.1002/0470869194.ch6.

[MMD+09] A. Moglia, A. Menciassi, P. Dario, and A. Cuschieri, "Capsule endoscopy: Progress update and challenges ahead", *Nature Reviews Gastroenterology & Hepatology*, vol. 6, no. 6, pp. 353–361, 2009. DOI: 10.1038/nrgastro.2009.69.

[MNY+17] S. Makarov, G. Noetscher, J. Yanamadala, M. W. Piazza, S. Louie, A. Prokop, A. Nazarian, and A. Nummenmaa, "Virtual Human Models for Electromagnetic Studies and Their Applications", *IEEE Reviews in Biomedical Engineering*, vol. 10, pp. 95–121, 2017. DOI: 10.1109/RBME.2017.2722420.

[Mol06] A. F. Molisch, "Introduction to UWB Signals and Systems", in *Ultra-Wideband: Antennas and Propagation for Communications, Radar and Imaging*, B. Allen, M. Dohler, E. E. Okon, W. Q. Malik, A. K. Brown, and D. J. Edwards, Eds., Chichester, UK: John Wiley & Sons, Ltd, 2006, pp. 1–17. DOI: 10.1002/0470056843.ch1.

[MRF+12] B. Moussakhani, T. A. Ramstad, J. T. Flåm, and I. Balasingham, "On Localizing a Capsule Endoscope using Magnetic Sensors", in *34th Annual International Conference of the IEEE Engineering in Medicine and Biology Society (EMBC'2012)*, vol. 2012, IEEE, 2012, pp. 4058–4062. DOI: 10.1109/EMBC.2012.6346858.

[MSP+19] G. Maenhout, A. Santorelli, E. Porter, I. Ocket, T. Markovic, and B. Nauwelaers, "Effect of Dehydration on Dielectric Measurements of Biological Tissue as Function of Time", *IEEE Journal of Electromagnetics, RF and Microwaves in Medicine and Biology*, p. 1, 2019. DOI: 10.1109/JERM.2019.2953401.

[MW92] R. B. Marks and D. F. Williams, "A General Waveguide Circuit Theory", *Journal of Research of the National Institute of Standards and Technology*, vol. 97, no. 5, pp. 533–562, 1992.

[MY16] J. W. Massey and A. E. Yilmaz, "AustinMan and AustinWoman: High-fidelity, anatomical voxel models developed from the VHP color images", in *38th Annual International Conference of the IEEE Engineering in Medicine and Biology Society (EMBC'2016)*, Florida, USA, 2016, pp. 3346–3349. DOI: 10.1109/EMBC.2016.7591444.

[MY20a] J. W. Massey and A. E. Yilmaz. (2020). AustinMan > Methodology > Coarsening and Extrusion, http://sites.utexas.edu/austinmanaustinwomanmodels/am-coarsening-and-extrusion/. Accessed: 2020-04-16.

[MY20b] J. W. Massey and A. E. Yilmaz. (2020). AustinMan and AustinWoman Human Body Models, http://sites.utexas.edu/austinmanaustinwomanmodels/. Accessed: 2020-03-26.

[Nat17] National Institute of Information and Communications Technology. (2017). Biomedical EMC: Japanese adult male and female whole-body voxel human models, http://emc.nict.go.jp/bio/model/model01_1_e.html. Accessed: 2020-03-26.

[Nat18] National Toxicology Program, *Toxicology and carcinogenesisstudies in Hsd:Sprague Dawley SD rats exposed to whole-body radio frequency radiation at a frequency (900 MHz) and modulations (GSM and CDMA) used by cell phones*, ed. by National Institutes of Health, NTP TR 595, 2018.

[Nat20] National Toxicology Program. (2020). Cellphone Radio Frequency Radiation Studies: Fact sheet. National Institute of Environmental Health Sciences, Ed., https://www.niehs.nih.gov/health/materials/cell_phone_radiofrequency_radiation_studies_508.pdf. Accessed: 2020-02-04.

[NAW18] K. Nomura, D. Anzai, and J. Wang, "Experimental evaluation of 30 MHz band implant communication using automatic equalisation technique", *IET Microwaves, Antennas & Propagation*, vol. 12, no. 13, pp. 2089–2093, 2018. DOI: 10.1049/iet-map.2018.5211.

[NM03] Y.-P. Nakache and A. F. Molisch, "Spectral Shape of UWB Signals: Influence of Modulation Format, Multiple Access Scheme and Pulse Shape", in *The 57th IEEE Semiannual Vehicular Technology Conference.*, 2003, pp. 2510–2514. DOI: 10.1109/VETECS.2003.1208843.

[NON+20] M. Newville, R. Otten, A. Nelson, A. Ingargiola, T. Stensitzki, D. Allan, A. Fox, F. Carter, Michał, D. Pustakhod, Y. Ram, Glenn, C. Deil, Stuermer, A. Beelen, O. Frost, N. Zobrist, Mark, G. Pasquevich, A. L. R. Hansen, T. Spillane, S. Caldwell, A. Polloreno, Andrewhannum, J. Fraine, Deep-42-Thought, B. F. Maier, B. Gamari, A. Persaud, and A. Almarza, *Lmfit/lmfit-py 1.0.1*, 2020. DOI: 10.5281/ZENODO.3814709.

[NRB12] H. T. Nguyen, T. A. Ramstad, and I. Balasingham, "Coded Pulse Position Modulation Communication System Over the Human Abdominal Channel for Medical Wireless Body Area Networks", in *23rd IEEE International Symposium on Personal, Indoor, and Mobile Radio Communications (PIMRC)*, IEEE, 2012, pp. 1992–1996.

[NWS+04] T. Nagaoka, S. Watanabe, K. Sakurai, E. Kunieda, S. Watanabe, M. Taki, and Y. Yamanaka, "Development of realistic high-resolution whole-body voxel models of Japanese adult males and females of average height and weight, and application of models to radio-frequency electromagnetic-field dosimetry", *Physics in Medicine and Biology*, vol. 49, no. 1, pp. 1–15, 2004. DOI: 10.1088/0031-9155/49/1/001.

[OHI04] I. Oppermann, M. Hämäläinen, and J. Iinatti, Eds., *UWB Theory and Applications*. Chichester, UK: John Wiley & Sons, Ltd, 2004. DOI: 10.1002/0470869194.

[Oly13] Olympus Europa SE & Co KG. (2013). Endocapsule 10 System: More than a capsule. A comprehensive system for capsule endoscopy., http://www.olympus.de/medical/en/medical_systems/hidden/download_jsp.jsp?link=/medical/rmt/media/en/content/content_1/documents_1/brochures_1/Final_EC10_1210~1.pdf. Accessed: 2017-04-24.

[PAG+19] S. Perez-Simbor, C. Andreu, C. Garcia-Pardo, M. Frasson, and N. Cardona, "UWB Path Loss Models for Ingestible Devices", *IEEE Transactions on Antennas and Propagation*, p. 1, 2019. DOI: 10.1109/TAP.2019.2891717.

[PBG+18] S. Perez-Simbor, M. Barbi, C. Garcia-Pardo, S. Castello-Palacios, and N. Cardona, "Initial UWB In-Body Channel Characterization Using a Novel Multilayer Phantom Measurement Setup", in *2018 IEEE Wireless Communications and Networking Conference Workshops (WCNCW)*, IEEE, 2018, pp. 384–389. DOI: 10.1109/WCNCW.2018.8369011.

[Per19] S. Perez-Simbor, "In-body to On-body Experimental UWB Channel Characterization for the Human Gastrointestinal Area", PhD thesis, Universitat Politecnica de Valencia, Valencia, Spain, 2019.

[PW12] G. Pan and L. Wang, "Swallowable Wireless Capsule Endoscopy: Progress and Technical Challenges", *Gastroenterology Research and Practice*, vol. 2012, p. 841 691, 2012. DOI: 10.1155/2012/841691.

[PZF+02] N. Petoussi-Henss, M. Zanki, U. Fill, and D. Regulla, "The GSF family of voxel phantoms", *Physics in Medicine and Biology*, vol. 47, no. 1, pp. 89–106, 2002. DOI: 10.1088/0031-9155/47/1/307.

[SAC+17] Y. Shimizu, D. Anzai, R. Chavez-Santiago, P. A. Floor, I. Balasingham, and J. Wang, "Performance Evaluation of an Ultra-Wideband Transmit Diversity in a Living Animal Experiment", *IEEE Transactions on Microwave Theory and Techniques*, vol. 65, no. 7, pp. 2596–2606, 2017. DOI: 10.1109/TMTT.2017.2669039.

[SAL+18] A. Santorelli, B. Abbasi, M. Lyons, A. Hayat, S. Gupta, M. O'Halloran, and A. Gupta, "Investigation of Anemia and the Dielectric Properties of Human Blood at Microwave Frequencies", *IEEE Access*, vol. 6, pp. 56 885–56 892, 2018. DOI: 10.1109/ACCESS.2018.2873447.

[SAW12a] J. Shi, D. Anzai, and J. Wang, "Channel Modeling and Performance Analysis of Diversity Reception for Implant UWB Wireless Link", *IEICE TRANSACTIONS on Communications*, vol. E95-B, no. 10, pp. 3197–3205, 2012.

[SAW12b] J. Shi, D. Anzai, and J. Wang, "Diversity Performance of UWB Low Band Communication over In-body to On-body Propagation Channel", in *Proceedings of the 6th European Conference on Antennas and Propagation (EuCAP)*, 2012, pp. 535–539. DOI: 10.1109/EuCAP.2012.6206576.

[SCB10a] S. Støa, R. Chávez-Santiago, and I. Balasingham, "An Ultra Wideband Communication Channel Model for Capsule Endoscopy", in *3rd International Symposium on Applied Sciences in Biomedical and Communication Technologies*, 2010, pp. 1–5. DOI: 10.1109/ISABEL.2010.5702854.

[SCB10b] S. Støa, R. Chávez-Santiago, and I. Balasingham, "An Ultra Wideband Communication Channel Model for the Human Abdominal Region", in *IEEE Globecom Workshops*, 2010, pp. 246–250.

[SFK+10] H. J. Schneider, N. Friedrich, J. Klotsche, L. Pieper, M. Nauck, U. John, M. Dörr, S. Felix, H. Lehnert, D. Pittrow, S. Silber, H. Völzke, G. K. Stalla, H. Wallaschofski, and H.-U. Wittchen, "The predictive value of different measures of obesity for incident cardiovascular events and mortality", *The Journal of clinical endocrinology and metabolism*, vol. 95, no. 4, pp. 1777–1785, 2010. DOI: 10.1210/jc.2009-1584.

[Sha48] C. E. Shannon, "A mathematical theory of communication", *The Bell System Technical Journal*, vol. 27, no. 4, pp. 623–656, 1948. DOI: 10.1002/j.1538-7305.1948.tb00917.x.

[SHI17] M. Särestöniemi, M. Hämäläinen, and J. Iinatti, "An Overview of the Electromagnetic Simulation Based Channel Modeling Techniques for Wireless Body Area Network Applications", *IEEE Access*, vol. 5, pp. 10 622–10 632, 2017. DOI: 10.1109/ACCESS.2017.2708161.

[SM04] K. Siwiak and D. McKeown, *Ultra–Wideband Radio Technology*. Wiley, 2004. DOI: 10.1002/0470859334.

[SML+13] D. B. Smith, D. Miniutti, T. A. Lamahewa, and L. W. Hanlen, "Propagation Models for Body-Area Networks: A Survey and New Outlook", *IEEE Antennas and Propagation Magazine*, vol. 55, no. 5, pp. 97–117, 2013. DOI: 10.1109/MAP.2013.6735479.

[SO19] A. Santorelli and M. O'Halloran, "Patient-Specific Debye Parameters for Human Blood", in *41st Annual International Conference of the IEEE Engineering in Medicine and Biology Society (EMBC'2019)*, Berlin, Germany, 2019.

[SPB+19] M. Särestöniemi, C. Pomalaza-Raéz, M. Berg, C. Kissi, M. Hämäläinen, and J. Iinatti, "In-Body Power Distribution for Abdominal Monitoring and Implant Communications Systems", in *2019 16th International Symposium on Wireless Communication Systems (ISWCS)*, 2019, pp. 457–462. DOI: 10.1109/ISWCS.2019.8877274.

[SRF+10] A. Sani, M. Rajab, R. Foster, and Y. Hao, "Antennas and Propagation of Implanted RFIDs for Pervasive Healthcare Applications", *Proceedings of the IEEE*, vol. 98, no. 9, pp. 1648–1655, 2010. DOI: 10.1109/JPROC.2010.2051010.

[SS10] P. J. Schreier and L. L. Scharf, *Statistical signal processing of complex-valued data: The theory of improper and noncircular signals*, 1. publ. Cambridge: Cambridge University Press, 2010.

[SV87] A. Saleh and R. Valenzuela, "A Statistical Model for Indoor Multipath Propagation", *IEEE Journal on Selected Areas in Communications*, vol. 5, no. 2, pp. 128–137, 1987. DOI: 10.1109/JSAC.1987.1146527.

[SW10] J. Shi and J. Wang, "Channel Characterization and Diversity Feasibility for In-Body to On-Body Communication using Low-band UWB Signals", in *3rd International Symposium on Applied Sciences in Biomedical and Communication Technologies*, 2010, pp. 1–4. DOI: 10.1109/ISABEL.2010.5702784.

[SYH+09] K. Sayrafian-Pour, W.-B. Yang, J. Hagedorn, J. Terrill, and K. Y. Yazdandoost, "A Statistical Path Loss Model for Medical Implant Communication Channels", in *20th IEEE International Symposium on Personal, Indoor and Mobile Radio Communications (PIMRC)*, 2009, pp. 2995–2999. DOI: 10.1109/PIMRC.2009.5449869.

[TAH+09] K. Takizawa, T. Aoyagi, K. Hamaguchi, and R. Kohno, "Performance Evaluation of Wireless Communications Through Capsule Endoscope", in *31st Annual International Conference of the IEEE Engineering in Medicine and Biology Society (EMBC)*, 2009, pp. 6897–6900. DOI: 10.1109/IEMBS.2009.5333613.

[The20] The National Library of Medicine. (2020). The National Library of Medicine's Visible Human Project, https://www.nlm.nih.gov/research/visible/visible_human.html. Accessed: 2020-03-25.

[TP05] D. Turgis and R. Puers, "Image compression in video radio transmission for capsule endoscopy", *Sensors and Actuators A: Physical*, vol. 123-124, pp. 129–136, 2005. DOI: 10.1016/j.sna.2005.05.016.

[TRY14a] K. M. S. Thotahewa, J.-M. Redouté, and M. R. Yuce, "A UWB wireless capsule endoscopy device", in *36th Annual International Conference of the IEEE Engineering in Medicine and Biology Society (EMBC'2014)*, Chicago, IL, 2014, pp. 6977–6980. DOI: 10.1109/EMBC.2014.6945233.

[TRY14b] K. M. S. Thotahewa, J.-M. Redouté, and M. R. Yuce, *Ultra Wideband Wireless Body Area Networks*. Springer, 2014. DOI: 10.1007/978-3-319-05287-8.

[TRY15] K. M. S. Thotahewa, J.-M. Redouté, and M. R. Yuce, "Propagation, Power Absorption, and Temperature Analysis of UWB Wireless Capsule Endoscopy Devices Operating in the Human Body", *IEEE Transactions on Microwave Theory and Techniques*, vol. 63, no. 11, pp. 3823–3833, 2015. DOI: 10.1109/TMTT.2015.2482492.

[TTT+12] P. Theilmann, M. A. Tassoudji, E. H. Teague, D. F. Kimball, and P. M. Asbeck, "Computationally Efficient Model for UWB Signal Attenuation Due to Propagation in Tissue for Biomedical Implants", *Progress In Electromagnetics Research B*, vol. 38, pp. 1–22, 2012. DOI: 10.2528/PIERB11112111.

[Tur59] G. L. Turin, "The Asymptotic Behavior of Ideal M-ary Systems", *Proceedings of the IRE*, vol. 47, no. 1, pp. 93–94, 1959.

[Val02] J. Valentin, "Basic anatomical and physiological data for use in radiological protection: Reference values: ICRP Publication 89", *Annals*

of the ICRP, vol. 32, no. 3, pp. 1–277, 2002. DOI: 10.1016/S0146-6453(03)00002-2.

[vdBdLH15] C. van de Bruaene, D. de Looze, and P. Hindryckx, "Small bowel capsule endoscopy: Where are we after almost 15 years of use?", *World Journal of Gastroenterology : WJG*, vol. 7, no. 1, pp. 13–36, 2015. DOI: 10.4253/wjge.v7.i1.13.

[Wen07] D. D. Wentzloff, "Pulse-Based Ultra-Wideband Transmitters for Digital Communication", PhD Thesis, Massachusetts Institute of Technology, 2007.

[WFP16] Q. Wang, X. Fang, and D. Plettemeier, "Impedance Characteristics and Field Separation of Body Implanted Antennas", in *11th International Conference on Body Area Networks*, Turin, Italy, 2016.

[WFW06] J. Wang, O. Fujiwara, and S. Watanabe, "Approximation of Aging Effect on Dielectric Tissue Properties for SAR Assessment of Mobile Telephones", *IEEE Transactions on Electromagnetic Compatibility*, vol. 48, no. 2, pp. 408–413, 2006. DOI: 10.1109/TEMC.2006.874085.

[WLS+15] J. Wang, J. Liu, K. Suguri, and D. Anzai, "An In-Body Impulse Radio Transceiver With Implant Antenna Miniaturization at 30 MHz", *IEEE Microwave and Wireless Components Letters*, vol. 25, no. 7, pp. 484–486, 2015. DOI: 10.1109/LMWC.2015.2429112.

[WMW09] Q. Wang, K. Masami, and J. Wang, "Channel modeling and BER performance for wearable and implant UWB body area links on chest", in *IEEE International Conference on Ultra-Wideband, 2009 (ICUWB)*, 2009, pp. 316–320. DOI: 10.1109/ICUWB.2009.5288734.

[WNN+18] J. Wang, K. Nomura, H. Narita, F. Ito, D. Anzai, J. Bergsland, and I. Balasingham, "Development and In Vivo Performance Evaluation of 10–60-MHz Band Impulse-Radio-Based Transceiver for Deep Implantation Having 10 Mbps", *IEEE Transactions on Microwave Theory and Techniques*, vol. 66, no. 9, pp. 4252–4260, 2018. DOI: 10.1109/TMTT.2018.2854165.

[Wor00] World Health Organisation, "Obesity: Preventing and managing the global epidemic: Report of a WHO Consultation", *WHO Technical Report Series*, no. 894, 2000.

[WRM12] C. J. Willmott, S. M. Robeson, and K. Matsuura, "A refined index of model performance", *International Journal of Climatology*, vol. 32, no. 13, pp. 2088–2094, 2012. DOI: 10.1002/joc.2419.

[WS06] J. Wang and D. Su, "Design of an Ultra Wideband System for In-Body Wireless Communications", in *4th Asia-Pacific Conference on*

Environmental Electromagnetics, Institute of Electrical and Electronics Engineers, Ed., Dalian, China, 2006, pp. 565–568. DOI: 10.1109/CEEM.2006.258019.

[WW13] J. Wang and Q. Wang, *Body Area Communications: Channel Modeling, Communication Systems, and EMC*. Singapore: John Wiley & Sons, Ltd, 2013.

[WW80] C. J. Willmott and D. E. Wicks, "An Empirical Method for the Spatial Interpolation of Monthly Precipitation within California", *Physical Geography*, vol. 1, pp. 59–73, 1980.

[WWP10] Q. Wang, K. Wolf, and D. Plettemeier, "An UWB Capsule Endoscope Antenna Design for Biomedical Communications", in *3rd International Symposium on Applied Sciences in Biomedical and Communication Technologies*, 2010, pp. 1–6. DOI: 10.1109/ISABEL.2010.5702832.

[XMR+09] L. Xu, M.-H. Meng, H. Ren, and Y. Chan, "Radiation Characteristics of Ingestible Wireless Devices in Human Intestine Following Radio Frequency Exposure at 430, 800, 1200, and 2400 MHz", *IEEE Transactions on Antennas and Propagation*, vol. 57, no. 8, pp. 2418–2428, 2009. DOI: 10.1109/TAP.2009.2024459.

[YD12] M. R. Yuce and T. Dissanayake, "Easy-to-Swallow Wireless Telemetry", *IEEE Microwave Magazine*, vol. 13, no. 6, pp. 90–101, 2012. DOI: 10.1109/MMM.2012.2205833.

[YHM09] M. R. Yuce, Ho Chee Keong, and Moo Sung Chae, "Wideband Communication for Implantable and Wearable Systems", *IEEE Transactions on Microwave Theory and Techniques*, vol. 57, no. 10, pp. 2597–2604, 2009. DOI: 10.1109/TMTT.2009.2029958.

[YK07] K. Y. Yazdandoost and R. Kohno, "An antenna for medical implant communications system", in *European Microwave Conference 2007*, Institute of Electrical and Electronics Engineers, Ed., 2007, pp. 968–971. DOI: 10.1109/EUMC.2007.4405356.

[Yoo16] E.-G. Yoo, "Waist-to-height ratio as a screening tool for obesity and cardiometabolic risk", *Korean Journal of Pediatrics*, vol. 59, no. 11, p. 425, 2016. DOI: 10.3345/kjp.2016.59.11.425.

[YS10] K. Y. Yazdandoost and K. Sayrafian-Pour. (2010). Channel Model for Body Area Network, https://mentor.ieee.org/802.15/dcn/08/15-08-0780-12-0006-tg6-channel-model.pdf. Accessed: 2014-05-05.